Université de Lille 1 Sciences et Technologies

UFR de Physique

Unité Matériaux et Transformations (UMR CNRS 8207)

Thèse

En vue de l'obtention du grade de

Docteur en physique de l'Université de Lille 1 Sciences et Technologies

Spécialité : Sciences des matériaux

Présentée et soutenue publiquement

le 16 novembre 2015

par GERGES Joseph

Numerical study of the physical factors responsible for the ability to vitrify / crystallize of model materials of pharmaceutical interest

Composition du jury:

CORMIER Laurent	Directeur de recherche CNRS à l'Université Pierre et Marie Curie-Sorbonne	Rapporteur
PETIT Samuel	Professeur à l'Université de Rouen	Rapporteur
LINDFORS Lennart	Chercheur à AstraZeneca R&D Mölndal (Suède)	Examinateur
YU Lian	Professeur à l'Université de Wisconsin - Madison (Etats-Unis)	Examinateur
DESCAMPS Marc	Professeur à l'Université de Lille 1	Examinateur
AFFOUARD Frédéric	Professeur à l'Université de Lille 1	Directeur de thèse

"Learning by doing, peer-to-peer teaching, and computer simulation are all part of the same equation"

Nicholas Negroponte

Acknowledgements

All the work done in this thesis was held in the MMT (Matériaux Moléculaire et Thérapeutique) group which is part of the UMET (*Unité Matériaux et Transformations* - UMR CNRS 8207) laboratory directed by Pr. LEGRIS Alexandre.

First of all, I would like to thank my advisor Pr. AFFOUARD Frédéric. It was a privilege working with him for nearly three years. He provided me with the guidance that I needed to perform all of the simulation work. Furthermore, he offered me lots of significant advices and ideas that made my Ph.D experience more productive and motivating.

I would like to thank all the members of the MMT group. They welcomed me from the first day as a member of their group which created a supportive environment for my research work.

I am grateful for the fruitful discussions with Pr. DESCAMPS Marc. His remarks and insights made me understand more the nucleation and growth mechanisms on the fundamental level.

I am very much thankful to CORREIA Natalia and VALDES Laurent-Charles for reviewing the manuscript and providing many valuable corrections.

I am deeply grateful to all members of the jury: CORMIER Laurent, PETIT Samuel, LINDFORS Lennart and YU Lian for agreeing to read my thesis and for the time and the effort they dedicated in order to examine the scientific work and to participate in the defense of this thesis.

I wish to acknowledge the use of the facilities of the IDRIS (Orsay, France) and the CRI (Villeneuve d'Ascq, France) where some calculations were carried out.

I acknowledge the funding source that made my Ph.D possible. I was funded by the French ministry of research.

I was lucky to be surrounded by awesome friends, in Lille and in my home country, which provided me with the moral support. From farther distances, the absolute love from my parents and family has been the source of joy and happiness during my tough times. In addition, I would not be here without their sacrifices for me during my school and university years. It is them to whom I dedicate this thesis.

Résumé

La tendance naturelle d'un matériau à cristalliser ou à vitrifier est très difficilement prévisible. Il s'agit d'un problème très fondamental de la science des matériaux avec aussi des implications très importantes dans le développement pharmaceutique et en particulier pour des formulations basées sur l'état amorphe. La cristallisation se décompose en général en deux étapes principales de nucléation et de croissance au cours desquelles les mêmes ingrédients physiques fondamentaux apparaissent: i) la mobilité moléculaire mesurée par exemple par la constante de diffusion ou indirectement par la viscosité, ii) la force motrice, c'est à dire la différence d'énergie libre de Gibbs entre l'état liquide et cristallin, et iii) l'énergie libre d'interface γ entre le liquide et le cristal. La connaissance de ces trois paramètres couplée à l'utilisation d'approches théoriques comme la théorie classique de la nucléation et certains modèles de croissance (continue, 2d, dislocation vis) peut fournir a priori une estimation de la facilité d'un matériau à cristalliser ou pas. La mobilité moléculaire et la force motrice sont relativement accessibles. La détermination expérimentale de l'énergie libre interfaciale représente par contre un vrai défi. La modélisation moléculaire offre une alternative très intéressante pour pallier cette difficulté.

Au cours de ce travail, à l'aide de simulations de dynamique moléculaire nous avons déterminé les principaux paramètres impliqués dans la nucléation et la croissance de différents matériaux de complexité croissante : des systèmes atomiques modèles de type Lennard-Jones et plusieurs polymorphes de composés moléculaires d'intérêt pharmaceutique (felodipine, nifedipine et indométacine). Ces investigations nous ont permis d'analyser les tendances à la cristallisation de ces matériaux et notamment de souligner le rôle fondamental de l'énergie libre interfaciale solide-liquide. Les études menées sur les systèmes modèles ont mis en

évidence l'importance de la partie attractive des potentiels d'interactions vis-à-vis de la cristallisation. Dans le cas des matériaux pharmaceutiques, les valeurs de l'énergie libre interfaciale cristal-liquide à la température de fusion ont été déterminées pour la première fois. Le recouvrement des zones de nucléation et de croissance qui sont particulièrement bien reproduites a été étudié. Cette analyse permet de comprendre l'origine qui était jusqu'à présent mal comprise de la cristallisation préférentielle de certains polymorphes métastables. Les travaux réalisés apparaissent clairement comme un premier pas vers le développement d'un outil numérique pour prédire les transformations d'état de matériaux pharmaceutiques complexes.

Abstract

The natural tendency of a material to crystallize or to vitrify is not easily predicted. It is a fundamental problem in material science with many implications in the pharmaceutical developments in particular in the formulation of drugs in the amorphous state. The crystallization occurs in general in two steps of nucleation and growth during which the same fundamental factors appear: i) the molecular mobility measured for example by the diffusion or indirectly by the viscosity, ii) the driving force which is the difference in the Gibbs free energy between the liquid and the crystalline states and iii) the interfacial free energy γ between the liquid and the solid. The knowledge of these three parameters coupled with theoretical approaches like the classical nucleation theory and some growth models (normal, 2d, screw dislocation) can provide an estimation of the ability of a material to crystallize or not. The molecular mobility and the driving force are relatively accessible. However, the experimental determination of the interfacial free energy presents a real challenge. Molecular modeling offers a very interesting alternative to overcome this challenge.

In this work, by means of molecular dynamic simulations, we determined the main factors involved in the nucleation and the growth of different materials with increasing complexity: Lennard-Jones model atomic systems and some molecular polymorphs having a pharmaceutical interest (felodipine, nifedipine and indomethacin). These investigations enabled us to analyze the crystallization tendency of these materials and especially emphasis the role of the crystal-liquid interfacial free energy. The study held on the model systems enabled to show the importance of the attractive part of the interaction potential towards the crystallization. In the case of the pharmaceutical materials, the values of the

crystal−liquid interfacial free energy at the melting temperature have been determined for the first time. The overlap of the nucleation and growth zones, which are accurately reproduced, was studied. This analyze allowed to clarify the preferential crystallization of certain metastable polymorphs. This work is a rational step towards the development of a numerical tool in order to predict the phase transformation of complex pharmaceutical materials.

To my family…

Table of Contents

Introduction

Upon cooling, there are two basic ways for a liquid to solidify: it may form a crystalline solid in which atoms are arranged in an orderly manner on a lattice; or it may form a glass characterized by an atomic disorder and the absence of a long-range order. The latter can only be formed if the liquid is cooled rapidly enough with respect to the kinetics associated to crystallization. Although thermodynamically unstable, a solid can remain amorphous for a long time until its transformation into a stable crystalline state having a lower Gibbs free energy because the atoms do not have enough mobility to rearrange[1, 2]. Despite considerable attention and great importance to both basic science and applications for processing materials, the tendency for a given material to crystallize, vitrify, or revert to the more stable crystalline state from the amorphous state remains poorly understood[3-5]. This fundamental issue has initiated intense activity. Recent developments and approaches in many different fields particularly focus on predicting and possibly controlling the conditions that will favor/unfavor the crystallization/vitrification depending if it is desirable or not. For example, these transformations have been extensively studied and reviewed throughout the metallurgic literature[6, 7]. Indeed, understanding glass-forming ability of metallic glasses is a long-standing fundamental problem[6-9]. The possibility to obtain excellent glass-forming ability at a very low cooling rate for complex multicomponent alloys has clearly aroused much interest. In pharmaceutical industries, many substances are preferably developed in the crystalline state for evident reasons of stability. However, either by accident or design, they may also exist in a total or partially amorphous state. This situation is encountered more and more frequently due to the increasing complexity of synthesized molecules. The amorphous state has thus become increasingly important in pharmaceutical

applications owing to its higher apparent solubility and faster dissolution rate. Most pharmaceuticals are composed of small organic molecules showing a high contrast between intra and inter molecular forces with respect to other classes of materials. Motivated by the need to predict if crystallization/vitrification will occur or not for a large number of materials including pharmaceuticals, many attempts have been made to derive general rules from easily accessible structural, dynamical or thermodynamical experimental properties and thus define some quantitative predictors. For example, it was suggested that good glass-forming ability (GFA) is linked to the complex composition of molecules such as metallic alloys[10] where various of Fe-based alloys have been developed with a large GFA combined with other high physical, chemical and mechanical properties (high strength and hardness, good corrosion and excellent soft magnetic properties). It was also suggested that the low molecular symmetry and high flexibility due to a high number of internal degrees of freedom[11] could be used as an indicator to a good GFA. Figure 1 represents an example of two isomers of xylene: meta-xylene and para-xylene. Even though both isomers have the same chemical formula ($C_6H_4(CH_3)_2$), similar melting and boiling points, the molecular structure difference allows the meta-xylene (having a lower molecular symmetry) to have a much better GFA than the para-xylene[11].

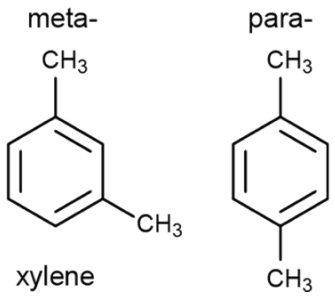

Fig.1.1: Two different isomers of xylene (meta- and para- xylene).

The role of the molecular mobility and its temperature dependence has been also pointed out. The mobility versus the steepness of the temperature curve is usually measured by the so-called fragility parameter defined as the slope at the glass transition temperature T_g of the viscosity or the primary relaxation time obtained from dielectric relaxation experiments[12]. Liquids can be thus classified either as strong or fragile depending if their molecular mobility shows an Arrhenius or a non-Arrhenius behavior respectively. The role of the fragility in crystallization/vitrification has been highly debated. It has been particularly shown that a large number of good glass-formers belong to the strong liquids having a lower molecular mobility in the supercooled regime[13-16]. However, the situation seems quite different for some other materials such as isomers of monohydroxy alcohols or alkanes[17] or some pharmaceuticals showing the same molecular dynamics but completely different crystallization tendencies[18, 19]. For polymers, it has been observed that the crystallization tendency increases with increasing fragility[20]. These results suggest a weak correlation between the glass forming ability and the fragility which could be also highly dependent on the considered class of materials. While this correlation seems accurate in metallic materials, it seems more questionable in other molecular glass-formers. Correlations are also difficult to clearly assess due to the inconsistency of the fragility values for the same sample determined from different techniques such as calorimetry and dielectric relaxation spectroscopy[15]. Thermodynamically, a low melting entropy ΔS_m and a limited range between the melting temperature T_m and the glass transition temperature T_g appear to be an advantage for glass formation[11, 13, 16, 21]. For a long time, it is well known that the ratio $\frac{T_g}{T_m} > \frac{2}{3}$ may provide a fair prediction of the glass-forming ability[22, 23] but there are some counter examples[24, 25]. No predictors can be unfortunately considered as fully reliable[21, 26-28]

since the structure, the dynamics and the thermodynamics seem interrelated. Moreover, in order to really investigate the influence of one specific parameter, the others should be the same which is not the case in general.

From a fundamental point of view, crystallization in the undercooled melt is a phenomenon involving complex nucleation and growth stages both having their own specific properties[26]. Nucleation is the first stage. It can be described in the framework of the classical nucleation theory (CNT) which provides a reliable basic description despite significant shortcomings amply reviewed in the literature[1, 2, 29-31]. Nucleation is related to the stochastic spontaneous formation of small crystalline nuclei made of few molecules in the liquid. The appearance of a nucleus of the new phase implies the creation of an interface between liquid and solid phases. Growth is the second stage in which the supercritical nuclei formed will grow within the liquid phase[1, 2, 29-32]. It occurs by aggregation of molecules of the phase undergoing a transformation.

Overall the phase transformation induced by cooling is the interplay of the nucleation rate N and growth rate G which are basically determined to some extent by three main physical ingredients: i) the driving force ΔG, ii) the diffusivity D and iii) the interfacial free energy γ [26, 33]. The first two parameters can be estimated without major difficulty from experimental data. The driving force ΔG can be usually obtained either from the temperature dependencies of the heat capacities of the liquid and crystalline phases if experimental data are available with enough accuracy or from analytical expressions derived from the melting enthalpy and temperature such as Turnbull or Hoffman equations[34, 35]. Experimental diffusivity data are often scarce but assuming the validity of the Stokes-Einstein relation, the diffusion coefficient D can be replaced by the much more experimentally

accessible shear viscosity, although this replacement is questionable due to possible decoupling of diffusion and relaxation[2, 36].

However, the experimental determination of the last parameter i.e. the crystal-liquid interfacial free energy really remains problematic. Despite its importance to theoretical models and to practical applications, accurate data for γ are in general not known, even for simple cases[6, 7]. Only a few interfacial free energies values are available in the literature for pharmaceuticals and more generally for molecular compounds[30, 37-39]. The determination of the parameter γ from simulation thus presents a clear interest as revealed by recent works[6, 7, 40, 41]. In recent years, several approaches based on Molecular Dynamics (MD) simulations have been particularly proposed but validated mostly on simple systems composed of hard spheres, Lennard-Jones particles, metal atoms or small molecules such as water.

This thesis is motivated by the need to develop a numerical tool in order to predict the phase transformation of complex materials. The question ‘‘why some liquids form a glass easily but others do not?’’ is still the matter of active debates[6, 23, 42]. Understanding the microscopic origin of the tendency for a given material to vitrify/crystallize is highly desirable for both fundamental researches or from the perspective of materials designs. Clear explanations have not been yet suggested for the origin of the good glass forming ability of some bulk metallic glasses [6]. In pharmaceutical developments, a basic understanding of the principles underlying molecular properties in the amorphous state and disordered crystalline materials is essential for stability studies for any type of bulk drug manufacturing or solid dosage design[19, 43, 44].

By combining guidance from the available theories of nucleation (CNT) and growth with calculations of fundamental parameters (driving force ΔG, diffusivity D and interfacial free energy γ) obtained from MD simulations there is an interesting opportunity to investigate the conditions that will favor crystallization/vitrification of some materials.

In this work, two different classes of systems of increasing complexity were investigated: i) simple Lennard-Jones (LJ) atomic systems in which the attractive part of the interaction potential can be tuned and ii) some molecular polymorphs having a pharmaceutical interest (felodipine, nifedipine and indomethacin). These investigations enabled us to analyze the crystallization tendency of these materials and especially emphasis the interplay of the crystal-liquid interfacial free energy and driving force on the nucleation barrier.

Investigations performed on simple LJ models have clearly served as a rational step before studying real molecular pharmaceutical compounds. Methods and validity of some theories were tested. The simplicity of the LJ models particularly allowed us to observe directly the crystallization phenomena and thus to obtain nucleation rates without any theory. Such results were compared with predictions from the classical nucleation theory (CNT) on steady-states rates and the induction periods at small and large undercooling. It revealed in which temperature domain either the transient/induction regime dominates. From a fundamental point of view, these studies also enabled us to analyze the importance of the attractive part of the interaction potential towards the crystallization. The need for a temperature-dependent interfacial free energy $\gamma(T)$ was also pointed out from different tests performed.

Then, we have studied three well-known pharmaceuticals nifedipine, felodipine and indomethacin which usually serve as model systems for studying the crystallization of organic compounds. All three drugs exhibit a rich crystalline polymorphism and polymorphic selectivity of crystallization is observed depending on temperature. Nifedipine and felodipine are known to have different remarkable crystallization tendencies[45-48] from the melt which were not understood. The availability of some experimental estimations of the interfacial free energy of indomethacin polymorphs was another motivation of investigation of this material. The values of the crystal−liquid interfacial free energy at the melting temperature have been determined for the first time for the different polymorphs of these pharmaceuticals. The overlap of the nucleation and growth zones was studied. This analysis allowed us to clarify the preferential crystallization of certain metastable polymorphs.

The thesis manuscript is organized in four chapters.

In the first chapter, we introduce the general framework along with a short review of the actual experimental and numerical developments in the field. This introduction includes the description of the mechanisms of nucleation and growth, the concepts related to polymorphism and glass transition, the experimental and numerical determinations of the crystal-liquid interfacial free energy and some examples of recent experimental approaches to predict crystallization and vitrification of pharmaceuticals.

The second chapter is dedicated to the numerical methods and algorithms associated with molecular dynamic simulations along with the methods used to determine the different thermodynamical and dynamical properties. The capillary

fluctuation method is detailed in this chapter since it is the numerical method applied in order to obtain the crystal-liquid interfacial free energy in chapter three and four. Simulation details are also reported in this chapter.

In chapter three, recent works performed on simple modeled liquids with tunable interaction potentials are reviewed. The construction of tunable LJ-potential is described. The calculation of the interfacial free energy at the melting temperature for the different potentials is presented. A comparison between the estimated nucleation time and the nucleation times obtained directly from MD simulations is shown in order to validate the method.

In Chapter four, a comparative study of the crystallization tendency from the melt of felodipine (I and II), nifedipine (α and β) and indomethacin polymorphs (α and γ) is reported. A detailed description of each compound is given including some comparisons between properties obtained by MD simulations with experimental values. We particularly focused our investigations on the calculations of the Gibbs free energy difference between the liquid and the crystal ΔG, the diffusivity D and the crystal-liquid interfacial free energy γ. The determination of these parameters enables the estimation of the nucleation/growth rates of each compound.

In the final part, we summarize our main results and present some perspectives that might be done in order to improve this work.

Chapter 1: General framework

This chapter presents the scientific context of this thesis. General concepts and properties involved in crystallization and glass formation processes are described.

This chapter has four distinct parts. Section 1 deals with notions of nucleation and growth for which the contribution of the main physical ingredients (kinetics and thermodynamics) are given as well as a brief presentation of the classical nucleation theory and some models of growth. Section 2 specifically focuses on the definition of the solid-liquid interfacial free energy, its main properties and its experimental and numerical characterization. In section 3 some recent approaches for the prediction of the glass-forming ability of pharmaceuticals are presented.

The general framework given in this chapter aims to facilitate understanding of the results and discussions presented in the next chapters.

1 Crystallization and glass formation

1.1 Nucleation

Two main stages are involved in the crystallization process from the undercooled melt: nucleation and growth[26]. The nucleation process has been well described in the framework of the classical nucleation theory (CNT). Although this theory is far from being perfect, it offers a rational framework to understand nucleation[1, 2, 29-31]. Nucleation occurs via the formation of small embryos of the crystalline phase inside the large volume of the liquid phase. This transformation is thermodynamically controlled by a subtle balance between a favorable term, the

so-called "driving force" for the phase transformation, ΔG_v, which is the difference between the Gibbs free energy of the liquid and the solid per unit volume (Fig.1.2) and an unfavorable term, the crystal-liquid interfacial free energy γ, that is the resistance to the creation of the solid-liquid interface. This latter mainly originates from an entropy loss due to the increased ordering of the liquid as the crystal nucleus surface is approached[33].

The Gibbs free energy needed to form a spherical crystalline germ with a radius r may be written as follows[2, 49]:

$$\Delta G(r) = -\frac{4}{3}\pi r^3 \Delta G_v + 4\pi r^2 \gamma \qquad 1.1$$

The evolution of the function $\Delta G(r)$ as function of the radius r is shown in Fig. 1.3. From the analysis of equation 1.1, it can be demonstrated that $\Delta G(r)$ has a maximum value $\Delta G^* = \frac{16\pi}{3}\frac{\gamma^3}{{\Delta G_v}^2}$ and at the radius $r^* = \frac{2\gamma}{\Delta G_v}$.

The balance between "driving force" (ΔG_v) and resistance to the creation of the solid-liquid interface (γ) thus gives rise to an activation energy barrier (ΔG^*) that needs to be overcome to produce a nucleus having a size larger than a minimum critical size (r^*) needed for the nucleus to expand, otherwise it will shrink (see Fig.1.3). In other words, the formation of a small solid nucleus in the liquid generates a negative volume contribution to the Gibbs free energy due to the lowest free energy of the solid with respect to the liquid, and a positive surface contribution due to the creation of a solid-liquid interface[49-51].

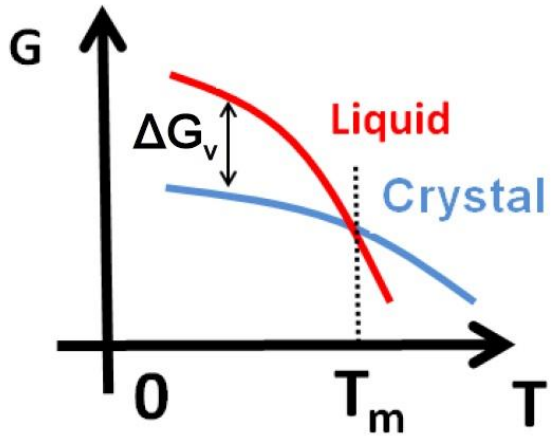

Fig.1.2: A schematic representation of the Gibbs free energy as function of the temperature. The liquid and the crystal are represented respectively by red and blue lines. Both lines cross at the melting point at the temperature T_m. The driving force for transformation i.e. the Gibbs free energy difference ΔG_v between the liquid and the crystal is also represented.

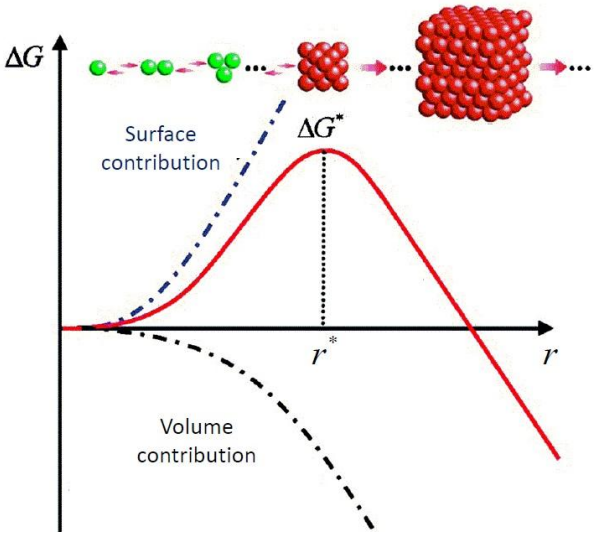

Fig.1.3: A schematic representation of the Gibbs free energy ΔG(r) as function of the nucleus radius r (extracted from ref. [52]). The volume and the surface contributions are also represented. Combining these two contributions ($-\frac{4}{3}\pi r^3 \Delta G_v$ and $4\pi r^2 \gamma$) we obtain a maximum value at r^*. For $r<r^*$, the system can lower its free energy by the dissolution of the germ while if $r>r^*$ it can lower its free energy by the growth of the germ.

In addition, diffusion is also required to make the nucleation process possible since molecules have to aggregate to form the nucleus. Nucleation is often characterized by the nucleation rate N (unit $m^{-3}s^{-1}$) which is the number of formed critical nuclei per unit of volume and time. It depends on the product of two activated processes: i) the number of critical size nuclei $\sim exp[-\Delta G^*/k_BT]$, and ii) the probability of an atom to migrate across the interface separating the critical size nucleus and the liquid (thus forming a supercritical size nucleus) which is roughly proportional to the diffusivity $D \sim exp[-A/k_BT]$ where A is the energy barrier associated to atomic motion. Both probabilities behave in opposite ways as a function of temperature and thus give rise to the bell-shaped dependence of the nucleation rate. Diffusion thus allows the nucleation phenomenon to occur but also modulates its kinetics[53, 54]. The steady-state nucleation rate N can be estimated from the expression[2, 49] :

$$N = A_N(T) \cdot exp\left[-\frac{\Delta G^*}{k_BT}\right] \qquad 1.2$$

where $A_N(T)$ is the kinetic pre-factor that is usually expressed as $A_N(T) = Zn_{lq}\frac{24Dn^{*\frac{2}{3}}}{\lambda^2}$ where λ is the atomic jump distance approximated to $1/{n_{lq}}^{1/3}$ in the following, n^* is the number of atoms in the critical nucleus, n_{lq} is the number density of liquid, $Z = (\Delta G_v/6\pi k_BTn^*n_{cx})^{1/2}$ is the Zeldovich factor and n_{cx} is the number density of the solid. We could write as well $n^* = \left(\frac{4}{3}\right)(\pi r^{*3}n_{cx})$ [55]. The Zeldovich factor describes the fluctuations of the cluster around the critical size and the probability for a stable nucleus to redissolve. This factor was not taken into consideration in the initial expression of the nucleation rate derived by Volmer & Weber[56] and Farkas[57] which led to an overestimation. It should be mentioned that in most cases the steady-state regime occurs after the so-called transient time or incubation time which is also described by the CNT[19] (see chapter 3).

1.2 Growth

Once a small crystal seed has formed during the nucleation step, it will continue to grow by advancing the crystal/liquid interface[1, 2, 29-32]. Growth occurs by aggregation of molecules of the phase undergoing a transformation. Crystal-growth velocity G (unit ms^{-1}) is a measure of the growing of the crystal surface of the supercritical nuclei. Similarly to the nucleation rate, the growth velocity G depends on the product of a thermodynamic term that describes the probabilities of attachment/detachment of the molecules to/from the nuclei $(1 - exp[-\Delta G/k_B T])$ and the probability of the diffusion of the molecules across the interface which is also roughly proportional to the diffusivity D. The net effect combining these two terms is that the growth rate must go through a maximum and thus also gives rise to a bell-shaped dependence as a function of temperature. The general mathematical form for the crystal growth rate can be summarized as follows:

$$G = k \cdot A_G(T) \cdot f(T) \cdot \left[1 - exp\left(-\frac{\Delta G}{k_b T}\right)\right] \qquad 1.3$$

where k is a temperature independent constant, $A_G(T)$ (unit : $m.s^{-1}$) describes the molecular mobility and has been approximated by $\frac{D \cdot a}{\lambda^2}$ in the following where a is the average width of the crystal lattice spacing ($a \approx 1/{n_{cx}}^{1/3}$). The last two terms represent thermodynamics of the growth process. $f(T)$ is a dimensionless function depending on the growth mechanism at the interface. The last term represents the probability of attachment/detachment of molecules to the crystal nucleus. It only plays a significant role at relatively small undercooling and it approaches unity at large undercooling. The establishment of the mechanism of growth i.e. the mathematical form of $f(T)$ is far from being trivial[30, 58]. Three main general models have been classically proposed[2]: i) normal or continuous growth, ii) growth determined by two-dimensional nucleation and iii) growth originating from screw

dislocations. In the simplest model, i.e. normal growth, all liquid-like molecules from the melt are able to join the crystal surface to become solid-like. Growth thus proceeds from any point along a direction normal to the surface. This behavior could be expected from a rough interface where on average all site are equivalent[2, 33, 59]. In that case, $f \approx 1$ and growth at deep undercooling is mainly controlled by dynamics. In contrast, for perfect smooth surfaces, growth requires the formation of two dimensional nuclei on the interface. Such surface nucleation mediated growth proceeds via lateral aggregation. Models are based on two-dimension treatment of nucleation similar to the three-dimensional theory[2, 33, 59]. The function is given by $f = exp\left[-\frac{\pi \cdot a \cdot \gamma^2}{k_b T \cdot \Delta G_v}\right]$. However, crystal often possesses defects such as dislocations that may induce continuous steps on their surface. The dislocation thus also provides a perpetual ledge and there is no longer need for the nucleation of new layers as in the previous two-dimensional model. Steps form spiral on the surface and f is given by the number of growth sites where the spiral has developed on the crystal surface which is inversely proportional to the spacing between spiral steps[2, 33, 59]. For dislocation-controlled growth, it can be shown that $f = a \cdot \Delta G_v/\gamma$. It can be mentioned that it is believed that specific treatment to eliminate lattice defects are required in order to observe surface nucleation mediated growth as shown for molecular compounds such as salol[2, 33].

The maximum of the growth rate can be different to the maximum associated with the nucleation rate. In other words, the curves representing their temperature dependencies can either overlap or not. When the curves representing the temperature dependencies of nucleation and growth rate do not significantly overlap, good glass-forming ability is to be expected (Fig.1.4). Poor glass formers would have a large temperature overlap in which both nucleation and growth rates

are high. The knowledge of the two nucleation and growth rates as function of temperature thus provides a guide to predict the crystallization tendency.

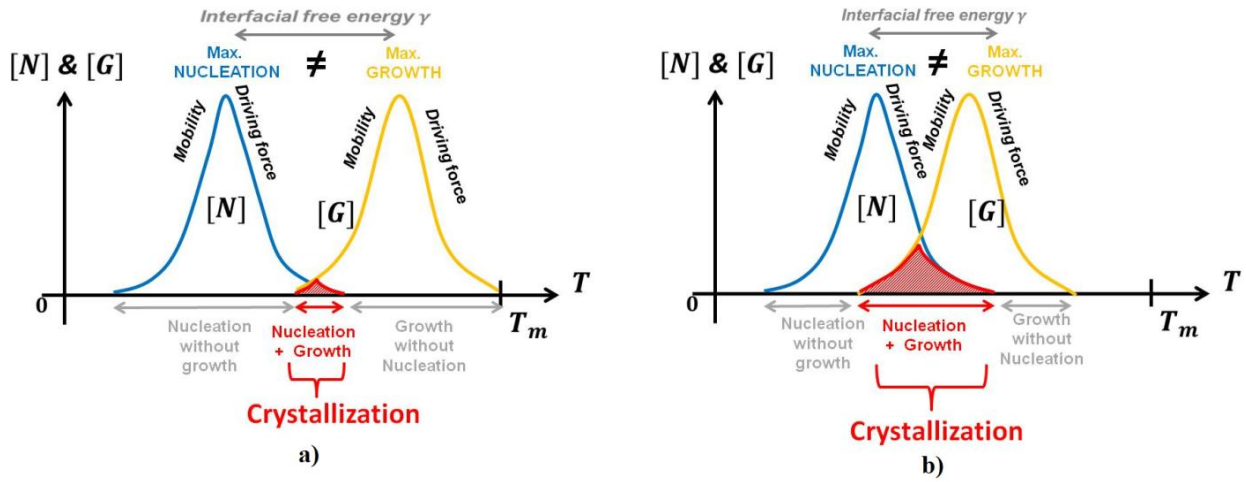

Fig.1.4: A schematic representation of the nucleation and the growth rates as function of temperature. In the figure a) the overlap of the two curves is small and a good glass forming ability is expected. In figure b), a bad glass forming ability is expected since the two curves have a large overlap. This can be explained by a large and small interfacial free energy respectively[26].

It could be noted that from the combination of both nucleation and growth rates (assuming a constant variation as function of time), it would be possible to determine the so-called TTT (Time-Temperautre-Transformation) curve for a given crystallized volume fraction as it is frequently done in metallurgy[21, 60]. Each point of this C-shaped curve (Fig.1.5) corresponds to the time required to observe a fixed extent of crystallization that occurred in a sample at a given temperature. The nose of this curve represents the minimum time required to observe the crystallization below T_m [61]. Therefore, the glass-forming ability can directly be determined from the position of the 'nose' of the TTT curve. In Fig.1.5, the cooling rates ($-dT/dt$) are represented by the lines (1 and 2). In order to obtain a

glass, the cooling rate should bypass the cone of crystallization enabling the supercooled melt to vitrify. The tangent line to the TTT curve (line 1) gives the critical cooling rate R_c required for vitrification. If the cooling rate is slower (line 2 in Fig. 1.5 that has a smaller steepness than line 1) the crystallization is expected since an intersection occurred with the TTT curve.

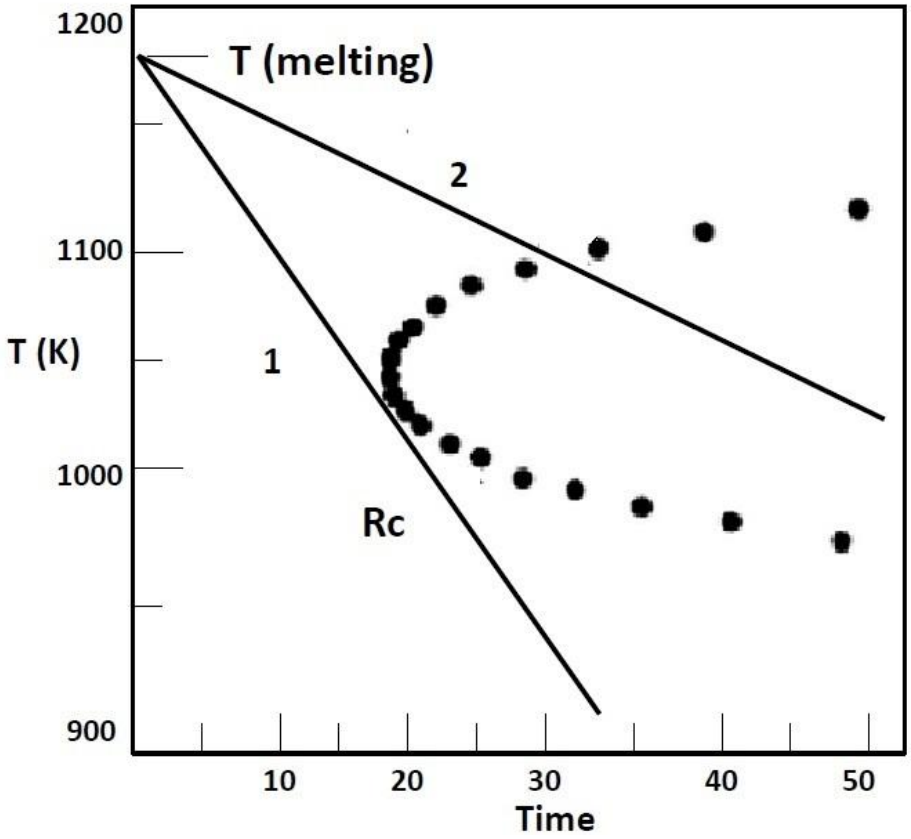

Fig.1.5: A TTT curve of a GeO_2 system[61]. Line 1 gives the critical cooling rate for glass formation and line 2 shows a slower cooling rate (having a smaller steepness).

1.3 Polymorphism

The capability of a solid material to exist in more than one form or crystal structure is called polymorphism. Pseudopolymorphism is a term used when the changes in the crystalline arrangements appears in the presence of solvent molecules as an integral part of the structure[62]. The difference between two polymorphs can be detected by the variation of their physical and chemical properties such as their solubility, hardness, color, melting temperature, stability, solubility, heat of fusion, density and conductivity.

In the pharmaceutical industry, the phenomenon of polymorphism is certainly the most important because of its impact on the biodisponibility and the toxicity of the active ingredients and the excipients[50]. For example, the hardness of a crystal form can promote the stage granulation or the conversion into pills[63]. The quality of the final product can be affected due to the unwanted crystallization of excipients into formula during freeze-drying[50]. The drug effectiveness can be influenced as well if the polymorph in use is not fully identified. The biodisponibility is linked directly to the solubility which itself depends on the type of polymorph. So a drug can become ineffective if the amount of substance initially designed to enter the body is reduced. While in some cases, a high solubility can increase the side effects[64, 65].

The key question concerning polymorphic systems is the relative stability of the different crystal conformations and the alterations in the thermodynamic properties accompanying phase changes and the different domains of temperature, pressure and other conditions. Let's consider two polymorphs (1 and 2). Their relative stability depends on their free energy, the most stable phase has the lowest

free energy (phase 1 in our case). At a constant temperature (T) and pressure (P), the relative stability of a system is given by the Gibbs free energy (G):

$$G = H - TS \qquad 1.4$$

where H is the enthalpy and S is the entropy. The thermodynamic conditions that define the equilibrium between phases and the possible phase transformation at constant pressure for a system having two polymorphs that exists in amorphous and crystalline states are shown in the Gibbs free energy plot or the phase diagram (Fig 1.6 a and b). In Fig. 1.6 a), the polymorph 1 is more stable than 2, since the transformation from polymorph 2 to 1 is possible ($\Delta G = G_1 - G_2 < 0$). While the amorphous form of the same system has a higher free energy than the crystalline phases due mainly to the higher enthalpy and entropy of the glass. The temperature T_m in the diagram represent the melting points: coexisting between the crystal state (either 1 or 2) and the liquid state. The point T_t,1-2 corresponds to the transformation between the two crystalline states. The temperature T_g is the glass transition temperature at which the supercooled liquid leaves equilibrium.

The system shown in Fig.1.6 a) is a monotropic system where at all temperatures below the melting point, phase 1 is more stable. In other words, the free energy curves of the different polymorphs do not cross as it is seen in the case of indomethacin for example[30]. An enantiotropic system is represented in Fig. 1.6 b) where a crystal-crystal transition temperature exists between two polymorphs below the melting points. Carbamazepine[66] and flufenamic acid[67] are two examples of enantiotropic systems where above and below the transition temperature T_t,1-2 the stability order is reversed.

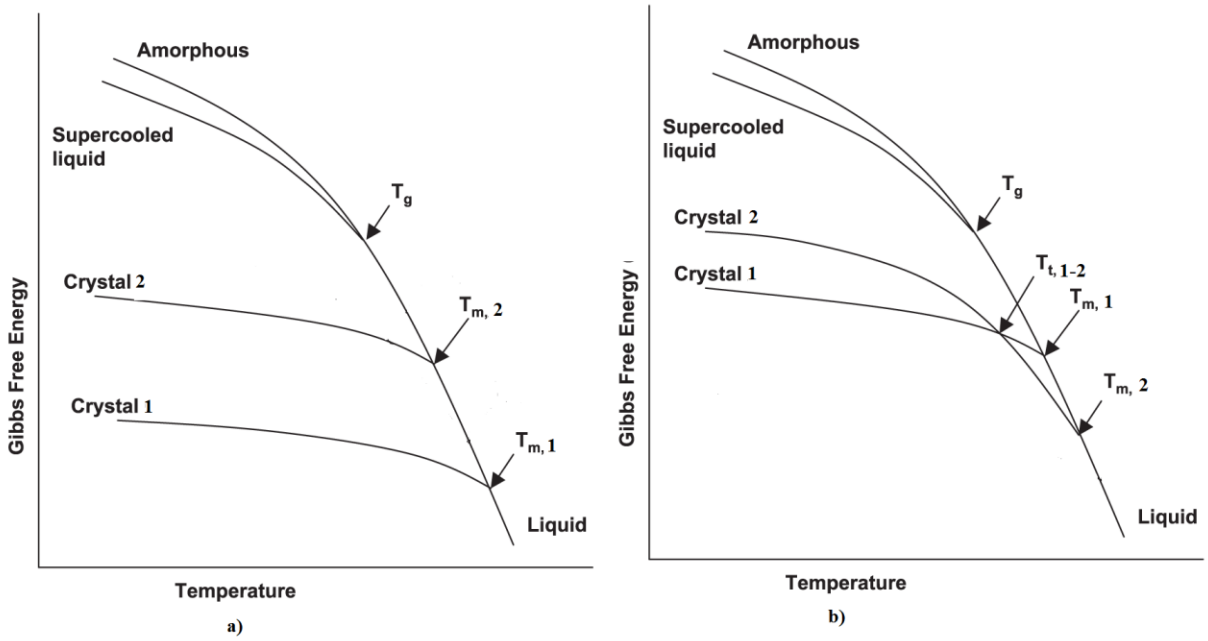

Fig.1.6: Schematic phase diagram for a monotropic system (a) and an enantiotropic system (b) that exhibits crystalline (crystal 1 and 2) and amorphous phases. The melting temperatures T_m, the crystal-crystal transition temperature T_t and the glass transition temperature T_g are represented by the intersections of the crystalline and the liquid curves, the intersection of the crystalline curves and the intersections of the supercooled liquid and the amorphous curves respectively.

1.4 Supercooled liquid and glass transition

A liquid maintained below its melting temperature T_m is said to be supercooled[68] (see Fig.1.7). This state is thermodynamically metastable with respect to the most stable crystalline state. The most striking feature of some supercooled liquids is the dramatic decrease in the mobility by several orders of magnitude, with slight decrease in temperature (see Fig.1.8). When the structural relaxation time reaches 100 s or the viscosity 10^{12} Poise, dynamics is extremely

slow and actually coincides with the experimental timescale[69]. Thus inevitably results in the loss of equilibrium. The supercooled liquid then transforms to an amorphous solid material, i.e., a glass. The corresponding temperature at which this event happens is called as the glass transition temperature T_g (see Fig.1.7).

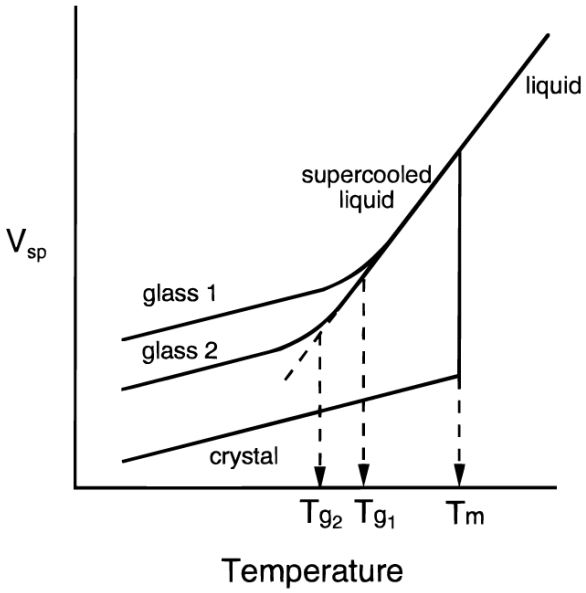

Fig.1.7: The specific volume as function of temperature represented schematically for a liquid that can either crystallize at the temperature T_m or vitrify at the temperature T_{g_1} or T_{g_2} depending on the cooling rate. A slower cooling rate was applied to form glass 2 compared to glass 1.

The glass transition represents a change from equilibrium to non-equilibrium conditions on cooling or the reverse process on heating. The temperature at which glass transition takes place reflects the kinetic behaviour of the system and not a thermodynamically driven process[68]. Changes in volume that occur on liquid supercooling and glass formation are shown graphically in Fig.1.7. As shown in Fig. 1.7, the value of the temperature T_g is different for different cooling rates. A smaller cooling rate allows the system to remain in equilibrium until lower temperatures. However, for a variation of about an order of magnitude of the

cooling rate, T_g varies only by 3-5 K. T_g is thus really an important characteristic of the material[1].

In Fig.1.8, the viscosity of several materials is represented as function of $\frac{T_g}{T}$ (Angell plot[70]). Using this representation of the viscosity, the liquids can be classified into two categories: 'strong' or 'fragile' liquids. The formers have a viscosity that is described by the Arrhenius functionality $\eta = \eta_0 exp\left(\frac{E_a}{RT}\right)$ where η_0 is the viscosity at infinitely high temperature, E_a is the activation energy and R is the universal gas constant. This kind of behavior is generally encountered in systems having short range and strong interactions like covalent bonds (ex: SiO_2 in Fig.1.8). The fragile liquids show a clear deviation from the Arrhenius behavior where the viscosity increases sharply near T_g . These materials are well represented by the Vogel-Tammann-Fulcher-Hesse (VTFH) equation[71-73] $\eta = \eta_0 exp\left(\frac{B}{T-T_0}\right)$ where B is a characteristic constant of each material and $T_g > T_0 > 0$. Complex organic systems (as many pharmaceutical materials[25]) are considered as fragile (ex: o-terphenyl in Fig.1.8). Their apparent activation energy is also high near the glass transition temperature compared to the strong liquids. The fragility index m, which characterizes the slope of the viscosity versus the temperature as we approach the glass transition temperature, can be used to distinguish between fragile and strong liquids. It can be written as follow: $m = \left(\frac{\partial log_{10}\eta}{\partial\left(\frac{T_g}{T}\right)}\right)_{T_g}$. Fragile liquids have high m (m =107 for sorbitol[74]) whereas strong liquids have low m (m=18 for SiO_2)[1, 12].

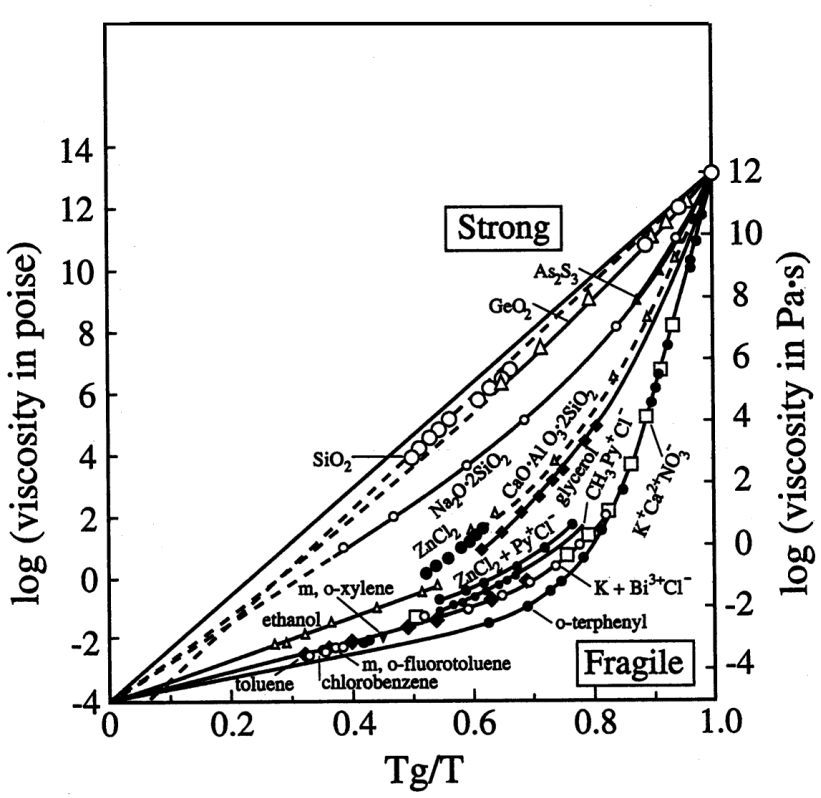

Fig.1.8: Angell classification of liquids (strong/fragile)[70]. Strong liquids show Arrhenius behavior (a straight line in the $log\ (\eta)$ vs $\frac{T_g}{T}$ plot) while fragile liquids present a sharp increase in viscosity near T_g .

2 Solid-Liquid interfacial free energy

The solid-liquid interfacial free energy is one of the fundamental parameters of nucleation and it is involved in several mechanisms of growth[6, 7, 33]. Three types of interfaces are fundamentally important in most systems: i) free surfaces of a crystal (solid/vapor interface), ii) grain boundary interfaces (between two solid phases) and iii) the interphase interfaces (between two different phases, i.e. the crystal-liquid interface). The solid/vapor interface is essential in all the vaporization and the condensation processes. The grain boundary interface, which

is the interface that separates two crystals having the same composition and structure but different orientation, plays an important role in the recrystallization mechanism from a highly deformed crystal into a new undeformed crystal[31]. One of the most important thermodynamic factors that influence nearly all of the processes involving the nucleation and growth of crystals from the melt is the crystal-liquid interfacial free energy γ. It determines the morphology of growth and also leads the solidifications in preferred crystallographic orientations[31]. In addition, crystal-melt energies dictate to a large extent the temperature at which solids nucleate, homogenously or heterogeneously, from their liquids[34]. In indomethacin, it was shown that the interface term has a different value for each polymorph[30]. This might be an additional reason for the difference in the energy barrier between polymorphs. Indeed, since at the crystal-liquid interface, the surface of a less stable phase is likely to be more disordered than the surface of a most stable one, hence the interfacial free energy is likely to be smaller. This trend is also well in line with the well-known Ostwald rule of stages[75] suggesting that the crystal phase that nucleates is not the most thermodynamically stable phase but rather another metastable phase that is closest in Gibbs free energy to the parent phase.

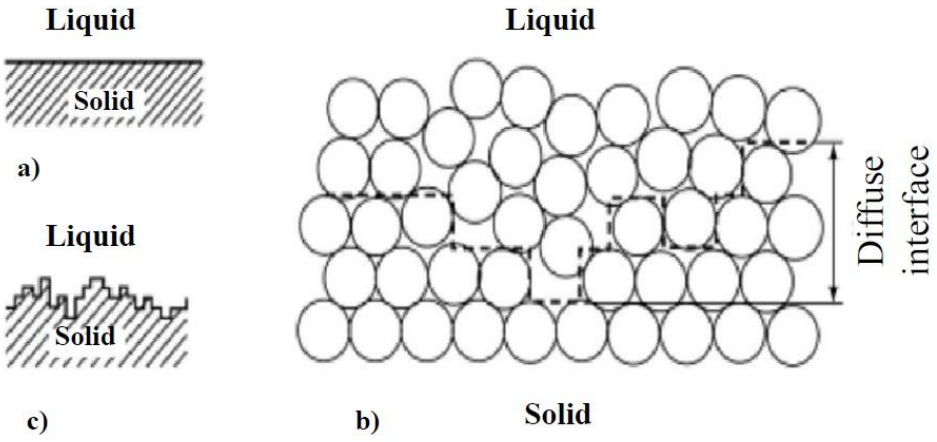

Fig.1.9: Crystal-liquid interface for a flat interface (a), and a rough interface (b) and (c)[31]. The dotted line in (b) represent the rough nature of the interface by dividing the atoms into solid-like and liquid-like.

Two types of solid-liquid interfaces exist. The first type is described by a smooth interface (also called faceted, flat or sharp) (Fig.1.9 a) where the transition from the liquid to the solid phase takes place in a narrow region with a thickness of one atom layer. The second type is the diffuse interface (also called rough or non-faceted) as shown in Fig.1.9 b and c. The transition between solid and liquid in such interfaces takes place over quite a few atom layers[31, 33]. The change in the thermodynamic parameters (enthalpy and entropy) will thus occur gradually across the interface from the bulk solid to the bulk liquid as presented schematically in Fig.1.10. At equilibrium and at the melting temperature, the higher enthalpy of the liquid compared to the solid is compensated by the higher entropy so the two phases have the same free energy. Nevertheless, at the interface the balance is dispersed generating an excess free energy γ.

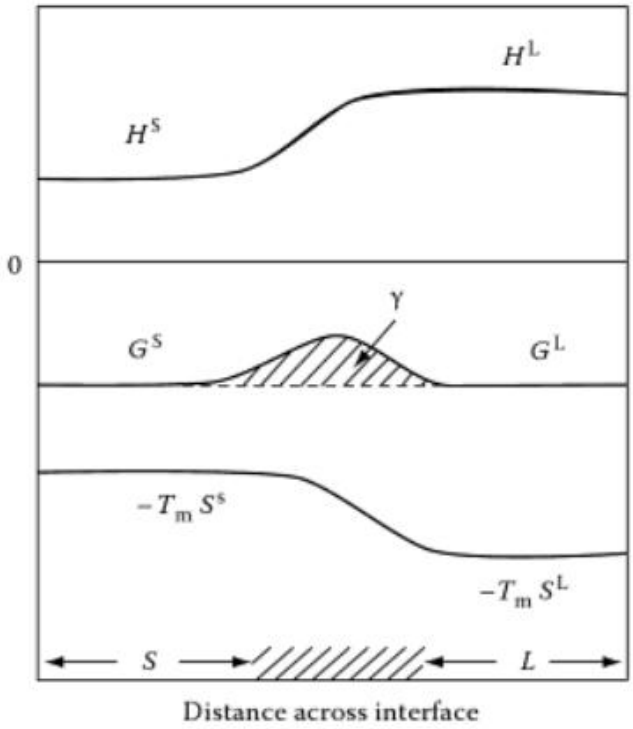

Fig.1.10: The origin of the crystal-liquid interfacial free energy γ shown by the variation of the thermodynamic parameters (enthalpy H, entropy S and free energy G) across the solid-liquid interface at the melting temperature T_m [49]. The superscripts S and L correspond to the solid and liquid phases respectively.

Spaepen[76] stated that this excess free energy should be basically of entropic origins. He showed that surface free energy is produced by the decrease of the configurational entropy S_{conf} caused by the adjustment of liquid particles to a crystal surface in pursuance of minimizing its density and energy. In other words, liquid atoms at the crystal-liquid interface do not have as much available configurations as the bulk due to the special boundary conditions of the crystal plane. It is possible to show for a model interface that the interfacial free energy can estimated as[6, 76]:

$$\gamma \approx \Delta H_m \left[\frac{\Delta S_{config}(bulk) - \Delta S_{config}(interface)}{\Delta S_m}\right] \quad 1.5$$

where ΔS_m is the total entropy of fusion which consists of two components: a configurational term ΔS_{config} and a vibrational term ΔS_{vib} due to the increasing in the local available volume to the liquid atoms around their average position. In Spaepen's model, ΔS_{vib} is considered to be the same in the bulk liquid and at the interface since the atomic volume is approximately constant up to the interface. Fig.1.11 shows a schematic representation of the entropies as a function of the distance normal to the interface.

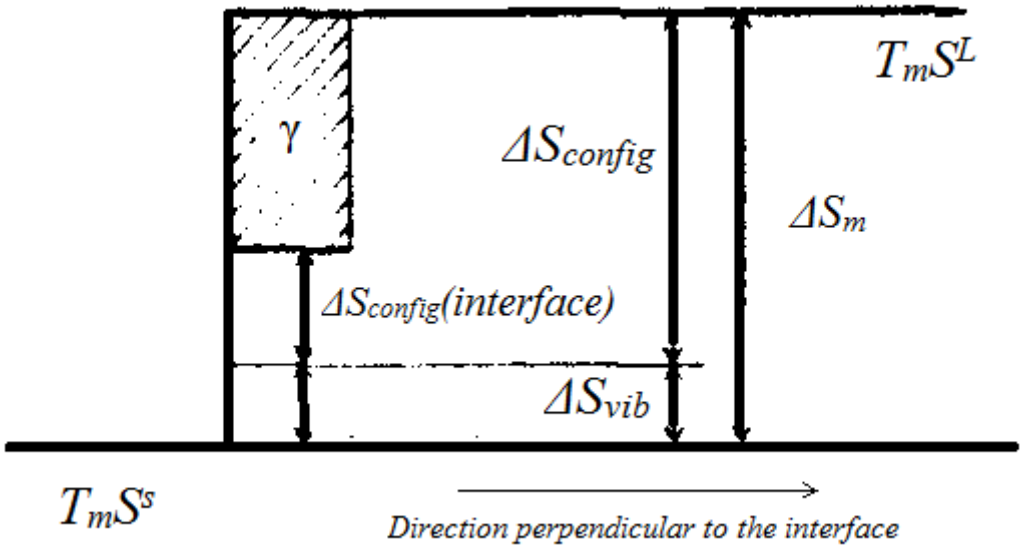

Fig.1.11: Schematic representation of the entropy change as function of the distance normal to the interface. The interfacial free energy γ is thus proportional to $\Delta S_{config}(bulk) - \Delta S_{config}(interface)$.

A correlation between γ with both the melting enthalpy ΔH_m (consistent with equation 1.5) and the atomic density in the crystal state ρ_{cx} was first established by Turnbull [34] on the basis of experimental data on metallic systems (Fig.1.12). It is

usually expressed as $\gamma_m = C_T \cdot \Delta H_m \cdot \rho_{cx}^{2/3}$ where C_T is the Turnbull coefficient which was found to be about 0.45 for most metals and 0.32 for semi metals and water[38]. Other studies showed that this coefficient, for metallic alloys, range from 0.13 to 1[77] or from 0.21 to 0.77[39] for other variety of materials (camphene, benezene, lauric acid, stearic acid, dibromobenzene…). Therefore, the value of C_T seems to change with the type of materials. For hard-sphere model a proportionality with the melting temperature T_m [78], $\gamma_m \propto k_b T_m \cdot \rho_{cx}^{2/3}$, has been suggested which is consistent with the Turnbull relation since for all fcc metals the ratio $\Delta H_m / k_B T$ is roughly the same. Alternative rules to the Turnbull relation have been also proposed in which the interfacial free energy varies with temperature [79, 80] such as $\gamma(T) = \gamma_m \frac{T}{T_m}$.

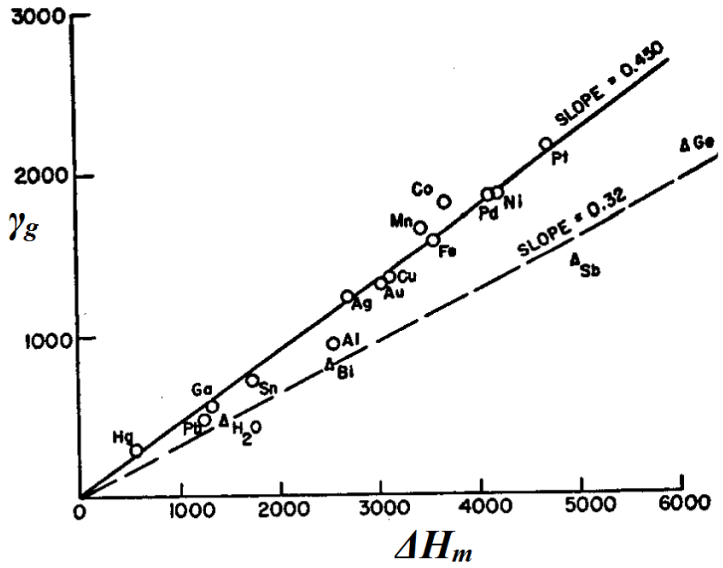

Fig.1.12: The gram-atomic interfacial free energy (γ_g) versus the enthalpy of fusion for various substances extracted from ref. [34].

Reported interfacial free energies values are very scarce in literature[16, 23] especially for molecular materials due to the difficulty to determine this parameter with high accuracy from experiments[30, 37-39]. A further difficulty is that, unlike a liquid-gas interface, the crystal-liquid interfacial free energy may show anisotropy and dependence on the orientation of the crystalline face in contact with the liquid. There are few experimental techniques capable of measuring this fundamental quantity. One of the oldest and most widely used technologies proposed in the early 1950s by Turnbull[34] to estimate γ is based on the nucleation rate measurements of the formation of solid particles in the liquid from microscopy followed by a subsequent treatment using the classical nucleation theory (CNT). In this approach, γ emerges as a fitting parameter (Fig.1.13)[81]. The values thus measured have also a large degree of uncertainty due to the heterogeneous nucleation that may occur close to material defects (impurities)[2, 81]. Moreover, as previously mentioned, nucleation is also a difficult phenomenon to study in-situ due to the very small critical nuclei of a few nanometers.

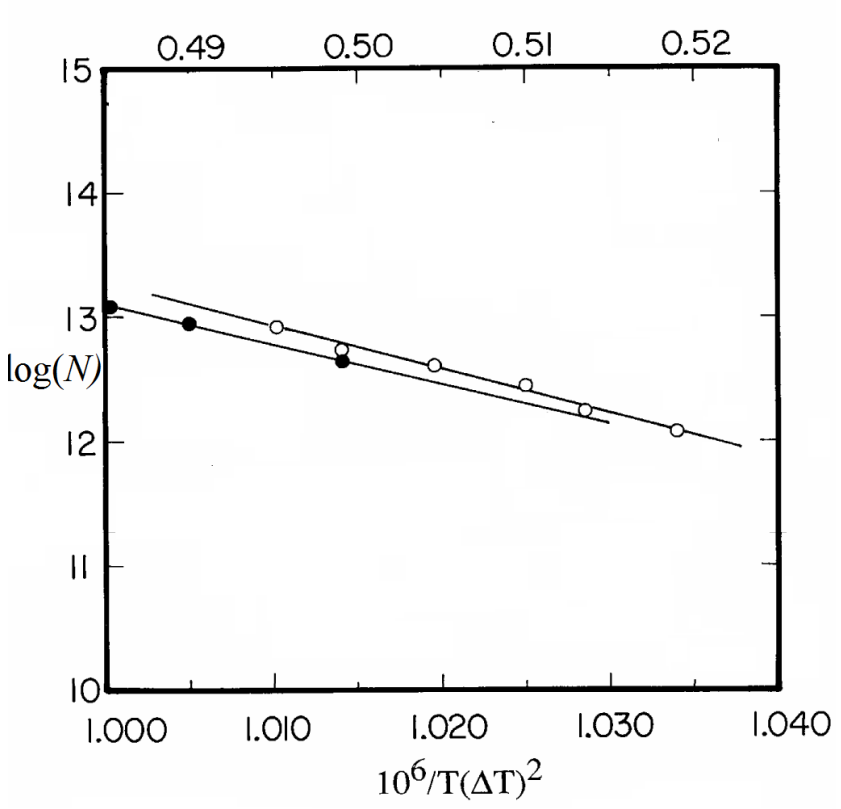

Fig.1.13: The steady state nucleation rate $\log(N)$ *(m*$^{-3}$ *s*$^{-1}$*) for liquid Hg as function of* $\frac{10^6}{T(\Delta T)^2}$ *where* ΔT *represents the undercooling. The figure was extracted from ref.*[82]*. The two sets of data correspond to two different droplet size distributions: black circles correspond to the data obtained from the nucleation of droplets having a slightly bigger diameter. The solid lines correspond to the linear fit since* $\log(N)$ *vs* $(T(\Delta T)^2)^{-1}$ *should be linear. The slope is proportional to* γ^3 *which enables the determination of the interfacial free energy. For Hg,* γ *was found to be 0.031 J/m*^{2}*.*

Another alternative experimental approach, called the grain boundary groove method (GBG), is widely used to determine γ as well as the Gibbs-Thomson coefficient. The first report of its application was by Jones and Chadwick[83] for some transparent materials and it was later extended by Gunduz and Hunt[84, 85] to measure γ for metallic alloys. It is based on the application of the Gibbs-Thomson equation. To observe the grain boundary groove, a thin liquid layer will be melted

and the specimen will be annealed in a constant temperature gradient for enough time to observe the grain boundary groove shapes via CCD digital cameras. Even though this method has a wide application on multi-component systems as well as pure materials, for opaque and transparent materials, it lacks of accuracy since the total error in the determination of the Gibbs-Thomson coefficient is about 10 %. Another method was introduced by Glicksman and Vold[86, 87] to study the free energy of extended crystal-liquid interfaces. It employs measurements of the equilibrium dihedral angle of a groove on the solid-liquid interface by a low angle tilt boundary (DA). The measurements were done in situ by an electron microscope and then using Herring analysis[88] to extract the crystal-liquid interfacial free energy. Good agreement was found between the values of γ derived from this method and the values obtained by Turnbull's method but there are some difficulties encountered in analyzing the data obtained from the tilt boundaries for some wide angles. It is therefore not surprising that the values determined experimentally differ considerably depending on the specific technique used[86, 89] (see some examples in Table 1).

	γ (mJ/m^2)	Method of measurement
Bismuth	61.3	DA[86]
	54.4	Turnbull's method[34]
Ice-water	44	GBG[89]
	45	DA[89]
	32	Turnbull's method[34]
Succinonitrile	7.86	GBG[39]
	8.94	GBG[39]
Al	158	DA[90]
	93	Turnbull's method[34]

Table 1: A comparison between the experimental crystal-melt interfacial free energies obtained from different methods.

In recent years, several techniques based on Molecular Dynamics (MD) simulations have been proposed for the determination of the solid-liquid interfacial free energy[6, 7, 40, 41]. Broughton and Gilmer[91] proposed a method called "adiabatic cleaving" based on the fact that the free energy of interface is a thermodynamic state function. Using this approach, they were able to calculate the reversible work required to create a solid-liquid interface *i.e.* the interfacial free energy for a set of particles interacting via a Lennard-Jones potential. This approach has been extended by Davidchack and Laird[92, 93] to take into account the anisotropy of the crystal interface of the compounds mainly made either of hard spheres[92] or Lennard-Jones particles[93]. Handel et al[94] extended the cleaving method to a molecular system where they performed direct calculations of the ice-water interfacial free energy for the TIP4P model. Moreover, the critical nucleus method (CNM)[95] is based on the classical nucleation theory (CNT). γ is estimated from the Gibbs-Thomson effect and from the determination of the critical undercooling corresponding to a given critical radius. An alternative approach proposed by Hoyt, Asta, and Karma[96, 97], called "the capillary fluctuation method" (CFM) has been successfully validated in recent years for monatomic[98] and binary atomic simple systems[99] and more realistic models such as metallic compounds[40, 100], alloys[101] and molecular materials such as water[102] and succinonitrile[38]. In this approach the interface is intrinsically treated as "rough". The amplitude of the fluctuations of the position of the crystal-liquid interface is used as a measure of its roughness in order to determine its stiffness - soft interface have more fluctuations – which can be directly correlated to the interfacial free energy. All these methods will be detailed in chapter 2 along with the CFM which is the method employed in the present work in order to obtain the crystal-melt interfacial free energy γ.

3 Some approaches for the prediction of the glass-forming ability of pharmaceuticals

There has been a considerable amount of work on the so-called amorphous solid dispersions aiming to predict the persistence of the active pharmaceutical ingredients (API) in the amorphous state as function of temperature[103-105]. The main motivation is to prevent recrystallization upon long-term storage since this transformation would obviously negate advantages of using the amorphous state (higher solubility)[19, 45, 46, 106-108]. In other words, it is essential for the drug to remain in the amorphous state for the life time of the product (2-3 years). Since it is not practical to wait all this time in order to verify if crystallization will occur, it is necessary to widen the understanding of the crystallization tendency. This understanding will enable to differentiate between the compounds that have a high risk for crystallization and those who do not.

The reduced glass transition temperature T_g/T_m [22, 23] is the most common used estimation of the GFA of organic molecules. Compounds with higher T_g/T_m values are most probably more resistant to crystallization. However, there are compounds that have similar values of T_g/T_m, like chlorpropamide and ketoconzazole[25], but exhibit different crystallization rates indicating that T_g/T_m is not a good predictor of the GFA.

The viscosity η, when it is used to represent the diffusion, is considered as a key factor that governs the crystallization tendency since both nucleation and growth are dependent on η[25]. It can be thus used as a predictive factor to the crystallization/vitrification tendency. The compounds that have a steeper increase in viscosity upon cooling might be more resistant to crystallization (good GFA).

This correlation between the viscosity and crystallization is not always valid since: i) other thermodynamics factors ($\gamma, \Delta G$) varies between compounds which make the comparison more difficult, and ii) the viscosity may not accurately reproduce the diffusion upon deep cooling owing to the breakdown of the Stokes-Einstein relations[2, 36].

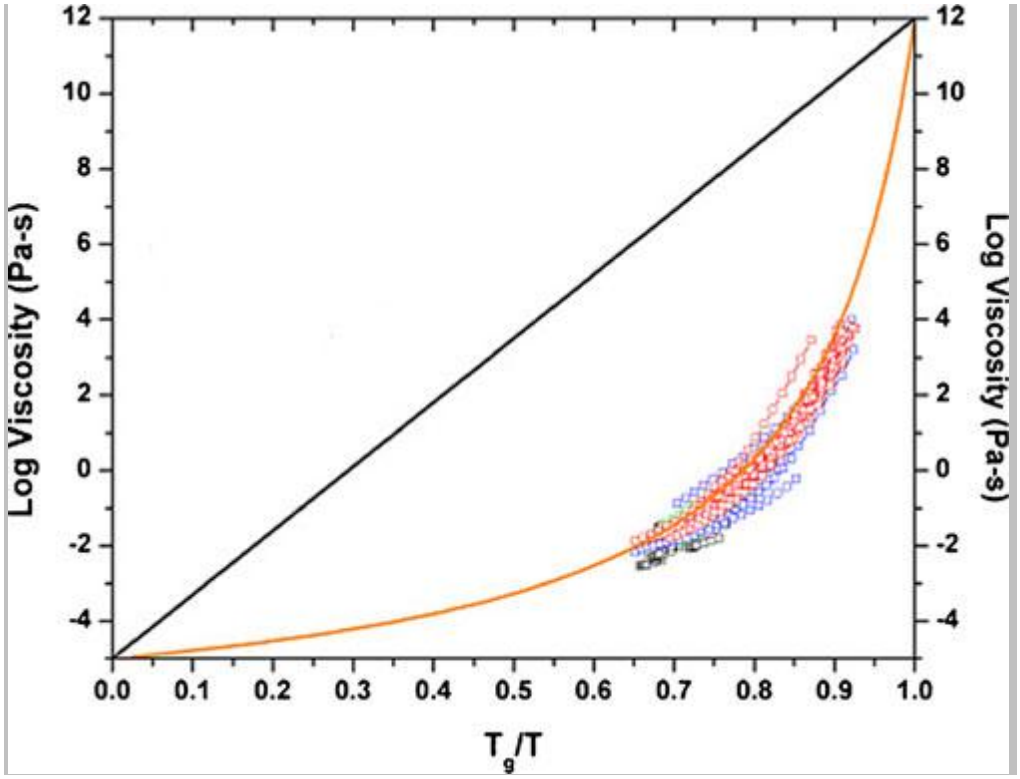

Fig.1.14: T_g-scaled viscosity for different pharmaceutical organic compounds (circles) extracted from ref. [25] exhibiting a similar non-Arrhenius behavior (fragile liquids) which is represented by the solid orange line (m=134). The black solid line represents an Arrhenius behavior (Strong liquids, m=16).

Furthermore, the fragility was used for polymers to distinguish between good and bad GFA's[20]. But for several pharmaceutical compounds[25], this parameter is not able to predict their crystallization/vitrification tendencies since they possess similar fragile behavior as shown in Fig.1.14 where $\log(\eta)$ vs T_g/T_m is

represented. It can be noted that all compounds, good and bad glass formers, exhibit a similar non-Arrhenius behavior. Hence, "Angell" plot as presented in Fig.1.14 gives us minimal information on the GFA of organic compounds.

Since it is difficult to obtain a good prediction of the crystallization/vitrification tendency while knowing only one (or more) parameter that influence the crystallization and nucleation rates, it is obviously more advantageous to use directly the nucleation/crystallization rates to predict the good/bad GFA. A method combining several types of experiments (DSC, hot stage microscopy) can be applied to obtain the growth rate by melt quenching and subsequently reheating the compound in question[16, 28]. The crystallization tendencies observed by this method depend on the experimental conditions (heating/cooling rates) and more importantly on the temperature dependence of the nucleation and growth rates (N and G). As mentioned before, both N and G have a bell-shaped form as function of the temperature where the maximum in the growth rate occurs generally at higher temperatures than the maximum in the nucleation rate[30]. As shown schematically in Fig.1.4, a compound that has a good crystallizing ability should have a considerable growth rate in a region where the nucleation is thermodynamically and kinetically favorable. In contrast, compounds that exhibit a good GFA upon cooling and a good crystallizing ability upon reheating might form nuclei upon cooling in a region where the crystal growth is slower. Hence, these compounds will crystallize upon heating when a more favorable temperature region for growth is obtained. Many possible explanations can be presented for compounds that do not crystallize neither upon cooling nor upon heating. Both nucleation and growth rates might be low or the system might have a high crystallization rate but a low nucleation rate. This method[16] cannot thus provide fundamental understanding for recrystallization of similar compounds since the

study is limited to the growth rate which is easily accessible compared to the nucleation rate[46, 48, 58]. However, Trasi et al[28] used the crystallization behavior from DSC experiments from ref.[16] to include the nucleation rate effects and compounds were classed in 5 classes (Fig.1.15): class IA where compounds have high nucleation and growth rates with a temperature range where the two rates overlap which explains their high nucleation tendency upon cooling from the melt, class IB has high nucleation/growth rates but a minimal overlapping which is explained by a good GFA ability but once a nuclei is formed there is a high probability of crystallization (low glass stability), class II represent the compounds that have a high growth rate but low nucleation rate which explains there good GFA but poor glass stability once a nuclei is formed, class III encompasses compounds that have high nucleation rates but low growth rate while class IV compounds have slow nucleation and growth rates. It can be noted that the highest risk compounds for formulation in the amorphous form are compounds from the class I followed by class II.

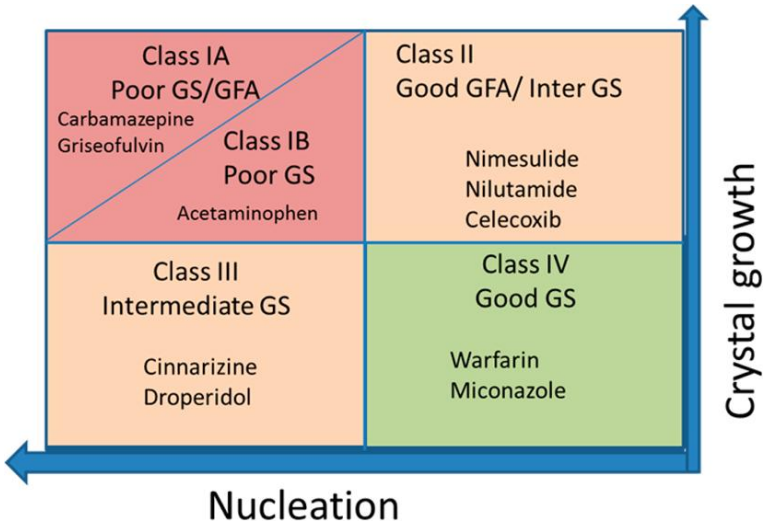

Fig.1.15: Classification of compounds based on their crystallization and growth rates (figure extracted from ref.[28]).

Chapter 2 Simulations details and methods

The aim of this chapter is to present the different numerical methods used to calculate all the parameters under investigation in this thesis.

First, we will present brief highlight on the numerical methods and algorithms associated with the molecular dynamics (MD) simulations (additional details can be also found in the annex section) followed by the possibilities and limits of MD simulations in calculating the different thermodynamic and kinetic parameters.

Secondly, the estimation of the interfacial free energy via MD simulations will be discussed. A more detailed description will be given to the capillary fluctuations method being the method used in this work to determine the crystal-liquid interfacial free energy.

Finally, the details of the simulations used in this work will be presented. The general simulation parameters (simulation time, integration time step, …) and the details of the construction of the simulation boxes (size, shape…) will be shown.

1 Introduction to MD simulations

Simulations cover a large ensemble of numerical techniques that enable the determination of the properties of a certain material on different time and length scales. The choice of the simulation method relies on the choice of the desired temporal and spatial scales (Fig.2.1). The atomic radius spatial scale and the femto/picosecond temporal scale are covered by Quantum Mechanics calculations such as the Density Functional Theory (DFT)[109] describing the

evolution of the electronic clouds. MD simulations treat the interactions on an atomic level (nanometer scale) with time scales ranging from picoseconds to a few nanoseconds[110]. Mesoscopic methods use coarse-grain approaches in which molecular groups such as CH_3 or monomers in polymers are treated as a single 'super' atom. It thus reduces the number of atoms and allows simulations of systems having the size of nanometers to micrometers with microseconds time scales[111]. For larger systems (centimeters) and on a larger time scale (seconds), finite element simulations are applied[112]. It can be noticed that numerical simulations may thus intervene in all the constituent of matter: electrons, atoms, molecules, macromolecules and micro-structures.

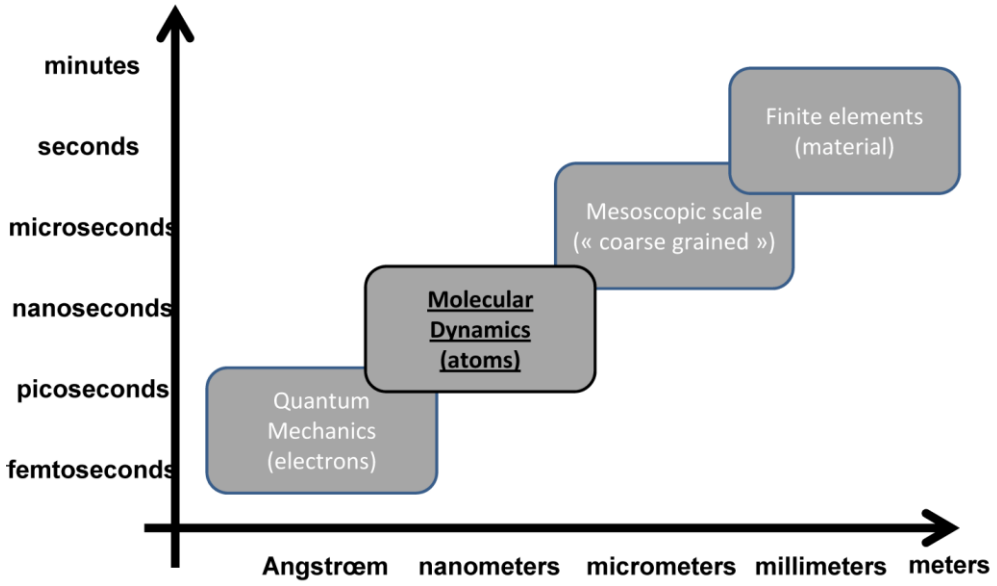

Fig.2.1: Different numerical approaches as function of the time/spatial scales.

Molecular dynamics simulations was our chosen numerical method since our study consist of understanding the mechanisms involved in crystallization, recrystallization, vitrification processes (and in particular the role of the crystal-

liquid interfacial free energy γ) by simulating crystalline and amorphous materials at the microscopic level.

It should be mentioned that MD simulation is a very powerful technique which has been playing an important role, not only in physics but in biology and chemistry as well, in the understanding of the different physical mechanisms involved in the studied systems. Therefore, numerous works have been published in various domains in order to study biomolecular systems[113-115], predictions of molecular properties[116, 117], rheological properties[118, 119], etc ...

MD simulations can be described as a bridge between the microscopic parameters, like positions, velocities and accelerations of an atom or a group of atoms, and the macroscopic properties, which we can mainly use to depict the tangible world such as density, enthalpy, and viscosity. Essentially MD simulations consist of resolving Newton's second law that is expressed as

$$\vec{F}_i(t) = m_i \frac{d^2\vec{r}_i(t)}{dt^2} \qquad 2.1$$

where $\vec{F}_i(t)$ is the force exerted on an atom i at time t, m_i is its mass and $\frac{d^2\vec{r}_i(t)}{dt^2}$ its acceleration vector. By a step by step integration using a time step of about $\delta t \approx 1$ fs, it is possible to follow the evolution of the position of each atom in the studied system as function of time. $\vec{F}_i(t)$ is obtained by the use of an empirical complex force field that describes all the interactions between each atom (van der Waals forces, electrostatic forces, covalent bonds…). Using this technique, we have access to a complete knowledge of the simulated material and it is thus possible to calculate different experimental properties like the dipole moment, enthalpy, etc…[110, 120].

1.1 Force fields

The force field is one of the most essential ingredients in MD simulations that enable the calculations of the forces exerted on atoms. The accuracy of the calculations is strongly related to the accuracy of the force field itself and its ability to reproduce experimental data. Its main role is to describe the potential energy of an assembly of atoms. It is composed of an empirical and analytical expression of the interatomic potential energy $U(\vec{r}_1, \vec{r}_2, \vec{r}_3 \ldots . \vec{r}_N)$ where the $\vec{r}_i$'s are the coordinates of the N atoms contained in the system, and some other parameters like the spring constant, van der Waals radius, electrostatic charges, … . Those parameters are obtained generally by quantum mechanics calculations or by fitting experimental data such as X-ray diffraction, NMR … [121]. The molecules are usually modeled as a group of atoms linked together by harmonic oscillators where no chemical reaction can take place. The significant development of force fields started in the end of the 1960's when the first computers became available[122]. The first force fields were very simple and optimized to determine structural properties and vibrational spectra and enthalpies of isolated molecules such as hydrocarbons[123] and alcohols[124]. Improvements of force fields (and computer power) made possible first atomistic simulations of a protein[125] in the native state, denaturation of a protein using a coarse grained model[126], or even study of enzymatic reactions from QM-MM (Quantum Mechanics/Molecular Mechanics)[127]. In the early 1980's, many force fields were developed like AMBER[128], CHARMM[129] and OPLS[130]. Since then, those force fields have been improved and are still used nowadays. A good review of available force fields can be found in refs.[131-133].

Each force field has its own applications that are highly dependent on the system studied that makes it hard to compare the performance of existing force

fields. The force field used in this work is the General Amber Force Field (GAFF[134, 135]) which is a generalization of the AMBER force field to a variety of small organic molecules and the OPLS force field[130] where its functional form is also very similar to the AMBER force field.

In general, the force field can be written as the summation of 6 contributions (see eq. 2.2) to the total potential energy[110, 120, 132, 136]:

$$U = V_{Bond} + V_{Angular} + V_{Dihedral} + V_{Improper} + V_{L-J} + V_{elec} \qquad 2.2$$

These contributions can be classified into 2 groups:

i) the intramolecular interactions which model the flexibility of the molecule V_{Bond}, $V_{Angular}$, $V_{Dihedral}$ and $V_{Improper}$ describe respectively the interactions linked to the chemical bond between two atoms, the deformation of the angles between covalent bonds, the torsions and the planarity of molecules.

ii) the intermolecular contributions such as the van der Waals interactions modeled by the Lennard-Jones potential V_{L-J} and Coulomb interactions V_{elec}. The Lennard-Jones potential models the combination of two opposite forces: a repulsive force describing Pauli repulsion at short ranges due to the overlapping of electron orbitals and an attractive force describing the attraction at long-ranges (van der Waals forces). Each term is detailed in the annex at the end of this manuscript. Ab-initio calculations are performed in order to calculate the point charges needed by the electrostatic potential V_{elec}. For the force field GAFF, Hartree-Fock method is recommended to obtain charges. The angle and bond parameters can be adjusted using the crystalline structures data from X-ray and neutronic diffraction experiences while dihedral angles can be obtained using quantum mechanics calculations[110, 120, 132, 136].

1.2 Algorithms and principles

A system of N point particles in a classical system is characterized by 6N variables. 3N variables relative to the positions of the particles and 3N variables relative to the momentum. Hence, a phase space is formed by these variables and each position in this system is called a microstate. All the needed quantities can be obtained by averaging their corresponding values in each microstate. To do so, an exploration of the phase space must be done. This exploration can be made by a stochastic approach (like Monte Carlo simulations) or a deterministic approach. MD simulations study the phase space by integrating step by step the Newton equation. This equation cannot be solved analytically as it is since it consists of solving 3N coupled equations of the 2nd order (equation 2.1). These equations are hence an N-body problem that has not an analytical solution. Several numerical algorithms have been developed for integrating the equations of motion such as Verlet algorithm[137] and Verlet leap-frog[138] that are discussed in the annex. Furthermore, in order to run MD simulations in an NPT (constant number of particles, pressure and temperature) or an NVT (constant volume) ensemble, barostats and/or thermostats must be used such as the Berendsen[139] barostat/thermostat (see annex). These algorithms are employed to maintain the temperature and the volume/pressure constant during a MD run.

2 MD simulations: possibilities and limits

In recent years, the application of MD simulations to condensed matter sciences has made it an essential analysis tool that sheds the light on information that is hardly accessible by other methods[119]. We can “naively” classify the information provided by MD simulations in two categories: the easily estimated

parameters that can be directly obtained by the outputs of the simulations and the more difficult parameters that demand additional efforts in order to acquire them.

2.1 Easily accessible properties

The first category includes the density of the system, the total volume, the internal energy E obtained from the force field inter and intra interactions and the enthalpy ($H = E + PV$). The self-diffusion coefficient D is also in this category and it can be calculated by the mean square displacement (MSD) $< r^2(t) >$. By definition, MSD is defined as

$$MSD = \frac{1}{N}\sum_i < |\vec{r}_i\,(t) - \vec{r}_i(0)|^2 > \qquad 2.3$$

where the <> symbol denotes the average over time, $\vec{r}_i(t)$ is the position of the center of mass i at a given time t and $\vec{r}_i(0)$ is the tagged particle's initial position. Using Einstein-Smoluchowski relation of motion[140], one can relate the self-diffusion coefficient D, which is a macroscopic transport coefficient, to the MSD which is a microscopic property (for long t):

$$D = lim_{t\to\infty} \frac{MSD\ (t)}{6t} \qquad 2.4$$

For each temperature the long time behavior of $MSD\ (t)$ can be fitted using the linear relation (equation 2.4) in order to obtain D as function of the temperature. An example is shown in Fig.2.2 for felodipine.

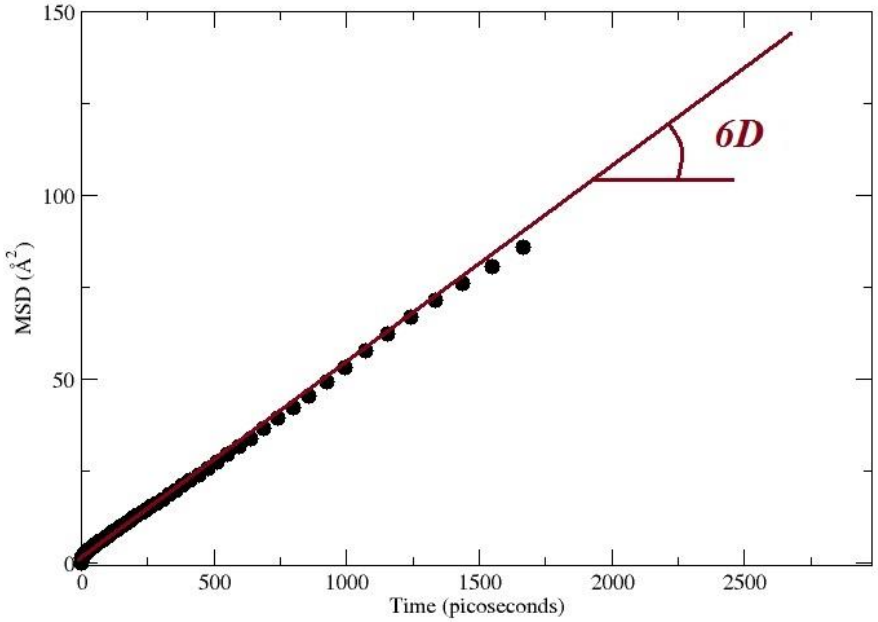

Fig.2.2: An example of the evolution of the MSD as function of time for a felodipine system at 500 K. The diffusion coefficient obtained from the fitting (solid line) is D=8.1 10^{-11} m^2/s.

The shear viscosity η can be also calculated without difficulty. Using the Green-Kubo (GK) expression[120], η can be estimated by integrating the stress-stress autocorrelation function :

$$\eta = lim_{t\to\infty} \frac{V}{k_B T} \int_0^\infty < P_{\alpha\beta}(t) P_{\alpha\beta}(0) > dt \qquad 2.5$$

where V is the volume of the system, T is the temperature, k_B is Boltzman's constant and $P_{\alpha\beta}$ refers to an off-diagonal element of the stress tensor. The brackets in equation 2.5 refer to an average over time (see Fig.2.3). The calculation can be performed at different temperatures enabling the determination of the shear viscosity as function of the temperature $\eta(T)$.

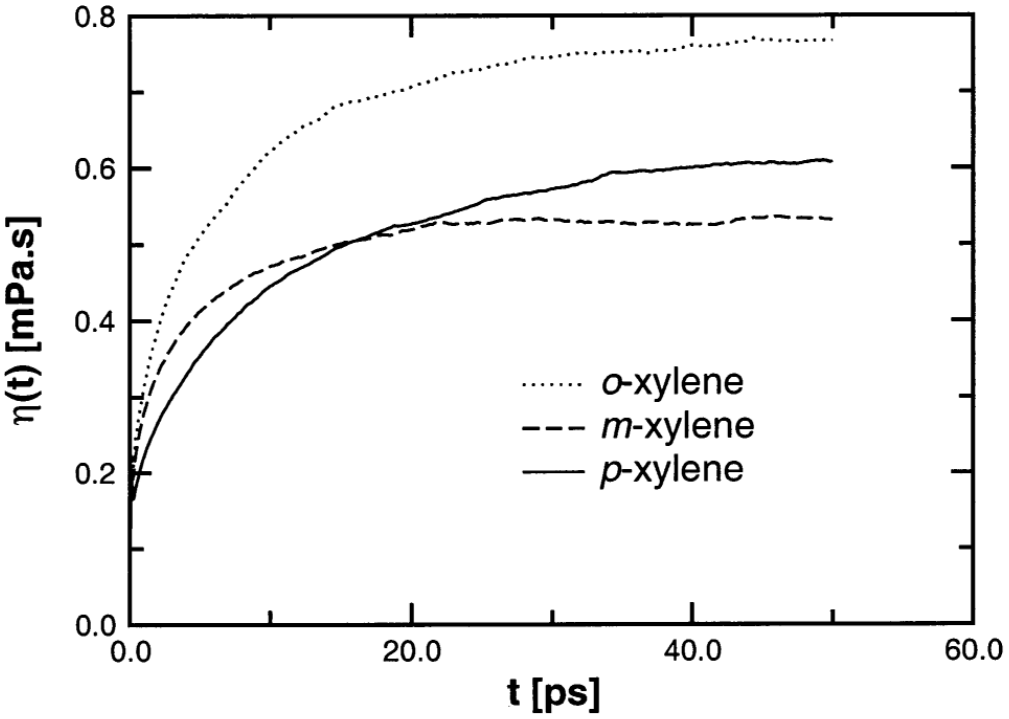

Fig.2.3: The shear viscosity of the different xylene isomers as function of time at T=298 K and P=0.1 MPa taken from ref[141]. The shear viscosity is given by the value of η when $t \to \infty$. The values of η at T=298 K and P=0.1 MPa are thus 0.76 mPa.s, 0.53 mPa.s and 0.60 mPa.s for o-xylene, m-xylene and p-xylene respectively.

The calculation of D and η requires evidently sufficient mobility. To access this mobility via MD simulations while avoiding very long simulations, the temperature of the system where the transport property is calculate should be high ($T \gg T_g$). At lower temperatures, D and η can be estimated using extrapolations from equations that fit their behavior at different "high" temperatures such as the VFTH (Vogel-Fulcher-Tamman-Hesse) equation[71-73] or the model proposed by Mauro et al[142].

The radial distribution function (RDF) is easily obtained as well by the means of MD simulations. To calculate the RDF, also referred to as $g(r)$, one needs to

calculate the probability of finding a particle between a distance r and $r + dr$ away from a given reference particle (Fig.2.4). This probability is then normalized by the expected value for a homogenous system.

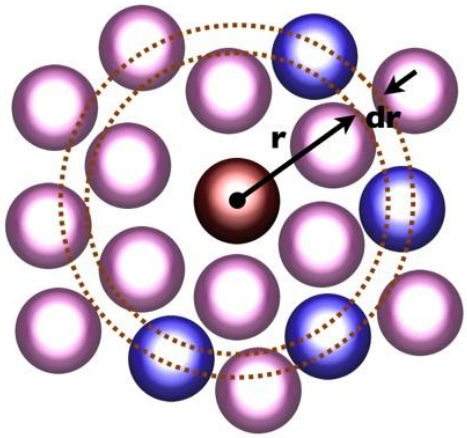

Fig.2.4: A schematic representation of the enumeration of the particles localized between a distance r and $r + dr$ away from a given reference particle. The central particle represents the reference particle (see text).

The RDF parameter $g(r)$ is linked by a Fourrier transformation to the experimentally measurable structure factor $S(k)$. Both $g(r)$ and $S(k)$ thus provide additional information on the spatial correlations between atoms[110]. An example is shown in Fig.2.5. The RDF of a solid phase is distinguished by several peaks while only a few broad peaks are found for the liquid phase.

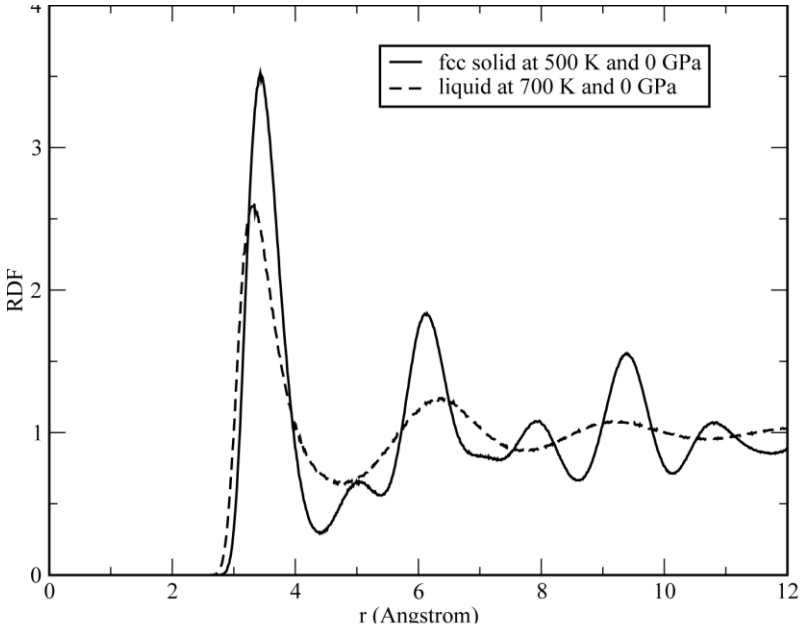

Fig.2.5: RDF calculated for Pb taken from ref [143]. The solid phase of the fcc system is showed at 500 K and at 700 K for the liquid.

2.2 More difficult properties to determine from MD

In the second category, we can find some thermodynamic parameters such as the melting temperature. The melting point, or more generally the melting line, has a fundamental interest leading to the understanding of the equilibrium properties of both liquid and solid phases[144]. The calculation of the Gibbs free energy of both phases led traditionally to determination of the melting line[145] by using the relationship

$$g_s(P, T_m) = g_l(P, T_m) \qquad 2.6$$

where $g(P, T)$ is the Gibbs free energy per particle at the melting temperature T_m corresponding to the pressure P. The subscripts s and l corresponds to the solid and liquid phases respectively. Many simulations are needed to calculate the

difference in free energy from a reference system to the system of interest at certain temperature and pressure and then to plot the Gibbs free energy as a function of temperature and pressure[144]. The Gibbs free energy itself presents a significant difficulty to compute directly since it requires calculations to estimate the entropy of the simulated system. Determining the entropy of the simulated system ($S = k_B \ln(\Omega)$) by estimating the number of microstates Ω from the positions and the velocities linked to each atom is impossible[110]. Therefore, the application of some approximations is necessary, such as harmonic and quasi-harmonic approximations[146], which can limit the use of these methods on some systems or in a range of temperature.

Alternatively, the crystal-liquid coexistence can be simulated directly by combining the two phases in question, and then monitoring the evolution of this biphasic system at different temperatures[144, 147]. While performing several MD simulations at several temperatures, either the crystallization of the system or the melting can be observed. The melting temperature will be the temperature where the system stays in equilibrium, i.e. when the system neither melts nor crystallizes. The melting/crystallizing of the system can be examined by the density or the total energy change at each temperature[148, 149] (Fig.2.6), by calculating an order parameter[150] or by probing the crystal-melt interfacial position[149]. The microcanonical ensemble (NVE) has been the natural choice in the direct simulation of the liquid-solid coexistence[148, 150, 151], but other studies showed that such calculation are possible in the NPT ensembles[148, 149, 152]. This method is widely used for the study of fluid-solid coexistence in LJ systems[144], hard spheres[151], metals[147, 152-154], alloys[149], fluids[155], ionic systems[156], and water[157, 158]. All these works share the same approach of the calculation of the melting properties from direct simulations either by using MD simulations or Monte Carlo. Both

simulation techniques are valid and show good results compared to experimental data. The accuracy of the method is mainly affected by the potential parameters, specially the potential cutoff, and other finite-size effects[159].

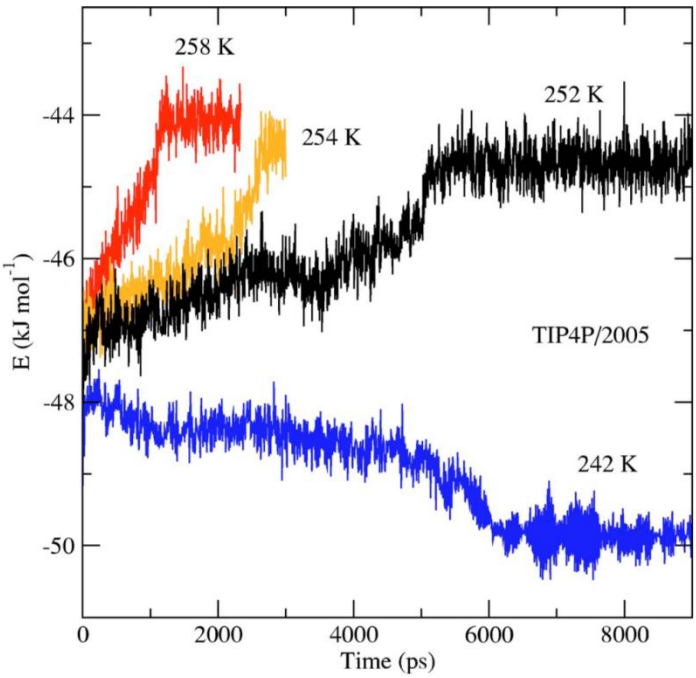

Fig.2.6: The evolution of the total energy (per mole of molecules) of an ice and liquid water system for the TIP4P/2005 model at P=1 bar[148]. The increase (at T = 252, 254 or 258 K) or decrease (at T = 242 K) of the total energy indicates melting and crystallization respectively.

The thermodynamic integration based on the coupling parameter of Kirkwood[160] is largely employed in numerical simulations. It consists of determining the difference in the Gibbs free energy between two phases along a fictive path linking these two phases. This path consists of an ensemble of states where the potential energy of each state (V_1 and V_2) is equal to the summation of the potential energies of each phase (phase 1 and 2) weighted by a coupling constant λ that varies between 0 and 1 ($V = \lambda V_1 + (1-\lambda)V_2$). This description assumes that at the extreme cases (λ=0 and λ=1), we retrieve the potential energies of each phase.

Given that in the NVT ensemble the variation of the free energy along the fictive path is similar to the variation of the spatial average of the potential energy, the difference in the free energy between the two phases could be obtained by integrating the spatial average of the potential energy compared to the coupling parameter $\Delta F = \int_0^1 \langle \frac{\partial V}{\partial \lambda} \rangle \, d\lambda$ [145]. This method was able to determine the thermodynamic properties of systems composed of single chemical entities and of a mixture of binary systems as well having different concentrations[161]. This method was recently used to determine the melting temperature of atomic and ionic systems. The melting temperatures were underestimated by 1 to 20 K compared to experimental data for Argon and 1-Butyl-3-methylimidazolium chloride respectively[162]. The difficulty of applying this method to molecular systems (such as pharmaceuticals) comes from the complexity of constructing a reversible fictive path from the liquid to the crystal[162]. In order to apply this method on polymorphic systems, the fictive and reversible path should be simulated between each phase of the system and all the other polymorphic forms at different temperatures.

The two-phase model[163, 164] is a method that can provide the thermodynamic parameters such as entropy of the system in a given state from its vibrational density of state. The use of complex reversible paths is then avoided. Therefore, just one MD simulation at a given temperature is needed to obtain the thermodynamic parameters. The vibrational density of state of the system is divided into two components, a fluid-like component and a solid-like component, and used subsequently to determine the different thermodynamical properties since the entropy can be theoretically determined from these two types of vibrational density of state. This method was able to determine accurately the entropy in a large range of temperatures of hard spheres system[163], small molecules used as

solvents[165] and the entropy as well as the coexistence curves of different models of water[164].

3 Interfacial free energy

For a few years, due the importance of the determination of γ, several new theoretical approaches have been developed to tackle the issue of the interfacial free energy via computer simulations[166]. The most recent approaches are based on metadynamics[167], superheating-supercooling method[168], Gibbs-Cahn integration[169], entropy/energy changes across the interface[166], Gibbs-Thomson approach[41, 170, 171], thermodynamic integration scheme[172, 173] and mold integration method[174]. All these methods have been successfully checked in general for model systems so far. Only few data exist[30, 37-39] in literature for complex systems which makes validation of numerical approaches even more difficult. In the following, the estimation of the crystal-liquid interfacial free energy via MD simulations will be discussed exploring the different methods used in order to determine this parameter.

In this section, we will focus mainly on three methods that use molecular dynamics simulations.

3.1 The cleaving method (CM)

Taking into consideration that γ is the reversible work needed to form a unit area of interface between a crystal and its melt, the cleaving method introduced by Broughton & Gilmer[91] and then developed by Davidchack & Laird[92, 93] determines γ by thermodynamic integration along a reversible path that begins with the separation of crystal and liquid bulk systems maintained at the coexistence conditions and ends with one system containing a crystal-melt interface surrounded by two bulk phases. To achieve such a path, a procedure

should be used in order to reversibly cleave the simulation box into two systems that does not interact. This procedure consists of 4 consecutive steps:

Step 1: Choose a cleaving potential to cleave (separate) the crystal bulk while maintaining the periodic boundary conditions.

Step 2: Cleave the liquid bulk in the same way

Step 3: Join the crystal and the liquid systems together while rearranging the periodic boundary conditions. In this step, the cleaving potentials are maintained.

Step 4: Remove the cleaving potential from the final system.

The interfacial free energy is obtained by calculating the total work needed to perform the 4 steps above and dividing it by the area of the created interface.

The cleaving of the systems is achieved by cleaving potentials. The choice of these potentials influences significantly the reversibility and the precision of the thermodynamic integration process. It is required from a cleaving potential to perturb the system as little as possible. Consequently the potential in step 2 should bring in some structure to the cleaved liquid making it compatible with the structure of the crystal. In addition, the cleaving potential should be able to prevent any particle from crossing the cleaving planes. If this requirement is not fulfilled the rearrangement of the periodic boundary conditions in step 3 cannot be achieved.

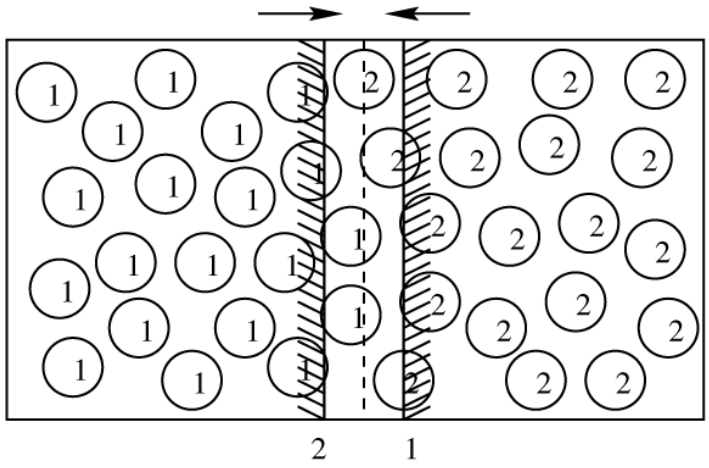

Fig.2.7: An illustration of the cleaving of the system by two moving walls as shown in ref.[92].

A series of cleaving potentials was first designed by Broughton & Gilmer[91] but it was mainly optimized to the truncated LJ system of their work. Later Davidchack and Laird[92, 93] proposed a different approach adaptable to systems with different interparticle interaction potentials and different crystal structures. Fig.2.7 shows the idea of this approach. First, to cleave the system at a cleaving plane the particles in the system are assigned by types 1 and 2 relative to their position to the plane. Then, two assigned walls (1 and 2) are placed on the opposite sides of the cleaving plane. The goal of assigning the walls and the spheres is to specify the interaction between them in a way that the walls interact only with the spheres having a similar type. It should be noted that if the distance between the walls and the cleaving plane is bigger than the sphere radius, the walls do not interact with the spheres. The system will be cleaved when the walls move towards each other (arrows in Fig.2.7), from an initial position z_i, where the walls have no interaction with the system, till z_f where the spheres of different types no longer collide. The average pressure on the wall $P(z)$ will be measured, during the

progression of the walls, as a function of the wall position. Finally the total work per unit area needed to perform the cleaving is given by the following integral:

$$w = \int_{z_i}^{z_f} P(z)\, dz \qquad 2.7$$

This work can be calculated for the 4 steps mentioned above, and since γ is the reversible work needed to form a unit area of interface between a crystal and its melt, γ is given by:

$$\gamma = w_1 + w_2 + w_4 \qquad 2.8$$

The w_3 is missing from equation 2.8 because in Davidchack & Laird's approach, no work is done on the system in the third step.

This method proved its efficiency to obtain the magnitude of the crystal-melt interfacial free energy but it is still complicated and not straightforward to implement[41], and it is restricted to hard-spheres and Lennard-Jones systems.

3.2 The critical nucleus method (CNM)

This method was inspired by Turnbull's experiments that were mentioned earlier (see chapter 1). The classical nucleation theory (CNT)[49] states that the change in the Gibbs free energy $\Delta G(r)$ to form a small crystal sphere of radius r from the undercooled melt is expressed as :

$$\Delta G(r) = -\frac{4}{3}\pi r^3 \Delta G_v + 4\pi r^2 \gamma \qquad 2.9$$

where ΔG_v is the Gibbs free energy difference per unit volume between the liquid and crystal phases at temperature T. ΔG_v can be approximated as:

$$\Delta G_v \cong \Delta H_{m,v} \frac{\Delta T}{T_m} \qquad 2.10$$

where $\Delta T = Tm - T$ is the undercooling temperature. Using equation 2.9, the critical radius can be obtained:

$$r^* = \frac{2\gamma}{\Delta G_v} \cong \left(\frac{2\gamma T_m}{\Delta H_{m,v}}\right)\frac{1}{\Delta T} \qquad 2.11$$

and the critical nucleation barrier is:

$$\Delta G^* = \frac{16\pi\gamma^3}{3(\Delta G_v)^2} \cong \left(\frac{16\pi\gamma^3 T_m^2}{3\Delta H_{m,v}^2}\right)\frac{1}{\Delta T^2} \qquad 2.12$$

For a given undercooling temperature, there exist a critical radius r^* associated with ΔG^*. If $r < r^*$ the crystal sphere melts lowering the free energy of the system; if $r > r^*$ it grows. In the case where $r = r^*$ can be obtained, the sphere will be in equilibrium (but unstable) with the surrounding liquid. Fig.2.8 presents an example of a germ of iron nanoparticles[95].

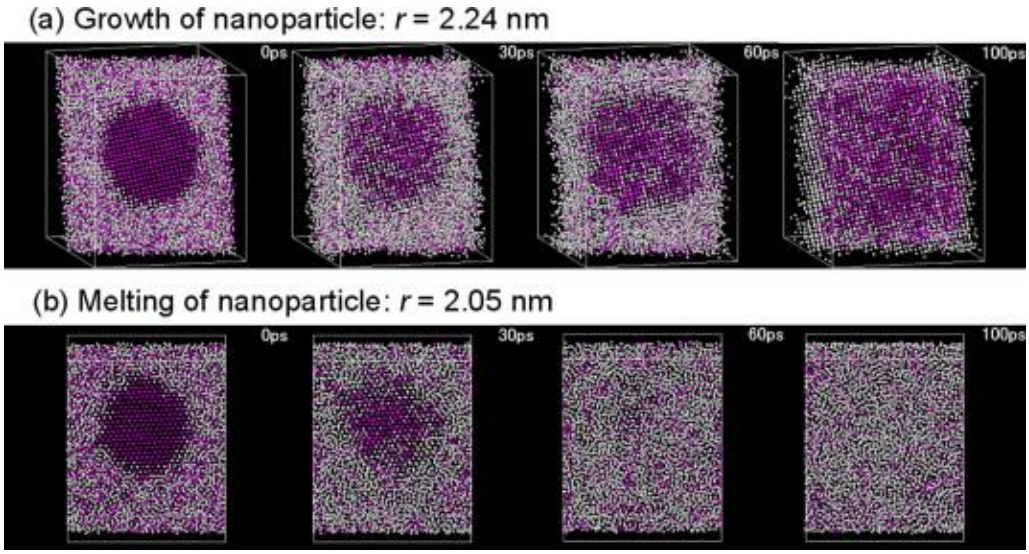

Fig.2.8: Snapshots of the calculation cell containing two different germs of iron nanoparticle. In the case where r=2.24nm (>r) the growth of the nanoparticle is observed and if r=2.05nm (<r*) the melting is observed* [95].

In this method[41, 95, 170, 171], the critical undercooling temperature ΔT^* is found for a given critical radius r^*. So, if $\Delta T < \Delta T^*$ the crystal sphere dissolves into the surrounding liquid, if $\Delta T > \Delta T^*$, it grows. Since the critical nucleus radius r^* is proportional to the reciprocal of the undercooling ΔT (equ. 2.11), γ can be found by the slope of the curve of r^* versus 1/ ΔT^* (Fig.2.9). The melting temperature T_m and the enthalpy of fusion ΔH_m can be calculated by the coexistence temperature of the crystal and the melt and by comparing the enthalpy difference of the bulk solid and liquid phases at T_m.

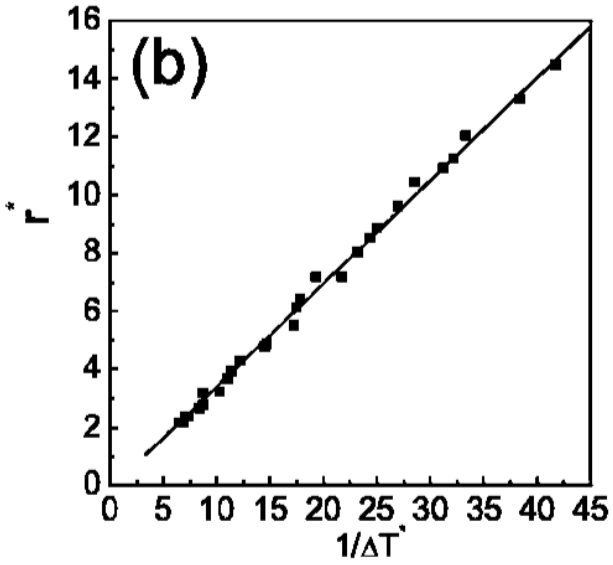

Fig.2.9: The critical nucleus size r^* as function of the inverse of the critical undercooling temperature ΔT^* for a LJ system[41]. The value of γ was found to be 0.302 (in standard LJ units).

This method showed its accuracy in the calculation of the interfacial free energy[171], but since the γ calculated here is an average value over different crystallographic orientations this method is not able to detect the anisotropy of the interfacial free energy. Furthermore, its application on more complex systems might be difficult since the crystallization time of a molecular system will be much longer than that of an atomic liquid[27].

3.3 The capillary fluctuation method (CFM)

In the following, the capillary fluctuation method, the method used in this work, will be described. By definition, the capillary fluctuations are waves on an interface between two bulk regions excited by thermal noise[175]. This method is widely used in literature[38, 96-98, 176-178] where the interfacial stiffness is determined from the power spectrum of the fluctuations of the interfacial position. The stiffness is defined as $\gamma + \gamma''$ where $\gamma'' = d^2\gamma/d^2\theta$ and θ is the angle between the growth direction and the direction normal to the interface. The anisotropy of this quantity is an order of magnitude larger than that of γ [179] giving an advantage to the capillary fluctuation method to detect more accurately the anisotropy of the interfacial free energy than the other methods described above. It is usually reported in many model systems[97, 99, 100, 178, 179] and realistic molecular systems[38] that the anisotropic effect is usually relatively weak being of the order of few percent. For succinonitrile[38] for example, the interfacial free energies for the orientations (100)[001], (110)[001] and (111)[1-10] were found to be 7.06 mJ/m^2, 7.00 mJ/m^2 and 7.01 mJ/m^2 respectively. For the LJ system[178], γ(100), γ (110) and γ (111) were estimated to be 0.369, 0.361 and 0.355 respectively (in standard LJ units).

3.3.1 Demonstration of the equilibrium fluctuation spectrum expression

Considering two infinite phases in equilibrium at pressure P and temperature T, their minimum free energy corresponds to a flat interface, but due to the thermodynamic fluctuation near the equilibrium, the interface of all configurations of the system is not planar[179]. Consequently, for non flat interfaces, the assumption of fluctuating interface can be reasonably used in order to extract the interfacial free energy[180]. In addition, the fluctuations magnitudes are of the

order of nanometer and the growth and time scale for the decay of the interface waves are of the order of picosecond which make the molecular dynamics techniques suitable to this kind of studies.

To identify the relation between the fluctuation of the interface position and the interfacial free energy, a form of the free energy of the interface should be established. To do so, the energy cost of the distortion of the interface should be considered.

Let us consider S the area of an interface, and dS the infinitesimal variation of its area. The minimum work needed to form this interface is proportional to the quantity dS[181, 182]:

$$W = \gamma \, dS \qquad 2.13$$

Monge parameterization[175] is used in order to define the dS term. Fig.2.10 shows a schematic representation of a 2 dimensional interface: the x and z directions are along the interface, and the y direction is normal to the interface. In this representation the height, y, is equal to $h(z, x)$ [183].

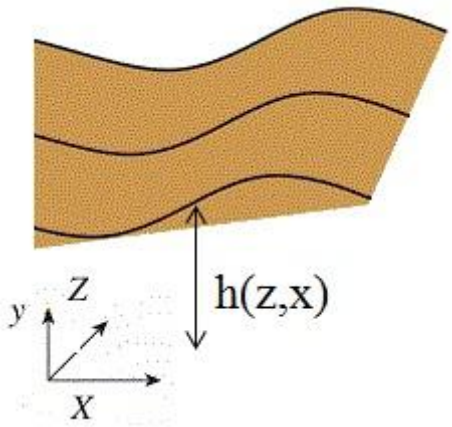

Fig.2.10: Monge representation of a surface defined by a set of cartesian coordinates x,y and z.

Therefore the position of the interface is given by

$$\vec{R} = (x, h(z,x), z) \qquad 2.14$$

We can take a slice of surface in the x direction (i.e. at constant z), and construct a tangent vector $\vec{r}_x$ in this direction by making a unit step in the x-direction, and a step $\partial h/\partial x$ in the y direction (Fig.2.11a). The same procedure is applied to the z direction giving the pair of tangent vectors: $\vec{r}_x$ = (1, $\partial h/\partial x$,0) and $\vec{r}_z$ = (0, $\partial h/\partial z$,1). (i.e. $h_x = \partial h/\partial x$, $h_z = h/\partial z$).

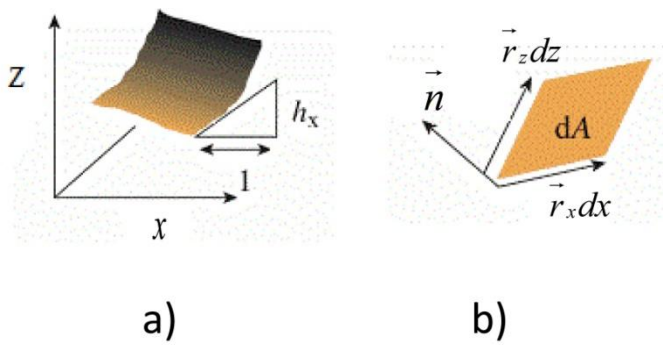

Fig.2.11 (a) For a line tangent to the surface and lying in the xy plane, a step $\Delta x = 1$ *corresponds to* $\Delta y = \frac{\partial}{\partial x}$ *, resulting in a tangent vector* $\vec{r}_x = (1, \frac{\partial}{\partial x}, 0)$ *. (b) An area element* $dx\ dz$ *on the xz plane corresponds to an element* $ds = |\vec{r}_x \wedge \vec{r}_z|\ dx\ dz$ *on the surface. The unit normal to the surface is* $\vec{n} = \vec{r}_x \wedge \vec{r}_z / |\vec{r}_x \wedge \vec{r}_z|$

As shown in Fig.2.11b, a segment of length dx along the x axis corresponds to a vector $\vec{r}_x dx$ along the surface. The cross product of the vector $\vec{r}_x dx$ and $\vec{r}_z dz$ gives the area element dS on the surface which is

$$dS = |\vec{r}_x \wedge \vec{r}_z| dx dz = (1 + h_x^2 + h_z^2)^{1/2} dx dz \qquad 2.15$$

Replacing equation 2.15 in equation 2.13 and summing on all the area:

$$W = \gamma \int_0^b \int_0^L (1 + h_x^2 + h_z^2)^{\frac{1}{2}} dx dz \qquad 2.16$$

For a system with a quasi-2D boundary, where b is the width and L is the length ($b << L,\ h_z \sim 0$), which is our case, equation 2.16 will take the following form

$$W = \gamma b \int_0^L (1 + h_x^2)^{\frac{1}{2}} dx \qquad 2.17$$

If we consider that γ does not depend on the orientation, we can extract it from the integral, and if we consider the approximation that the fluctuations are small ($h_x << 1$), W will be equal to:

$$W = \gamma b \int_0^L \left(1 + \frac{1}{2} h_x^2\right) dx \qquad 2.18$$

The energy of a flat interface is given by $W_0 = \gamma b L$ so the additional interfacial free energy of the undulated interface over that of the flat interface (dW) is given by

$$dW = W - W_0 \quad = \gamma b \int_0^L \frac{1}{2} h_x^2 dx \qquad 2.19$$

To solve this integral, the local interface position is expressed as Fourier series

$$h(x) = a_0 + \sum_{n=1}^{\infty} \left(a_n \cos\frac{n\pi x}{L} + b_n \sin\frac{n\pi x}{L}\right) \qquad 2.20$$

Deriving $h(x)$ over x:

$$h_x = \frac{\partial h(x)}{\partial x} = 0 + \sum_{n=1}^{\infty} (-a_n \, \mathrm{q_n} \sin(\mathrm{q_n x}) + b_n \, \mathrm{q_n} \cos(\mathrm{q_n x})) \qquad 2.21$$

with $q_n = n\pi/L$ as the wave vector,

$$h_x^2 = \left(\sum_{n=1}^{\infty} -a_n \, \mathrm{q_n} \sin(\mathrm{q_n} x) + b_n \mathrm{q_n} cos(\mathrm{q_n} x)\right)^2 \qquad 2.22$$

$$h_x^2 = \sum_1^{\infty} a_n^2 \, \mathrm{q_n}^2 \sin(\mathrm{q_n} x)^2 + \sum_1^{\infty} b_n^2 \, \mathrm{q_n}^2 \cos(\mathrm{q_n} x)^2 + 2\sum \ldots \sum \ldots \qquad 2.23$$

Using $sin^2(x) + cos^2(x) = 1$, and the fact that for $h(x) \sim 0$ then $q \sim 0$, so we eliminate the final term in equation 2.23 and h_x^2 becomes:

$$h_x^2 = \sum_{n=1}^{\infty} (a_n^2 + b_n^2) \, q_n^2 \qquad 2.24$$

Replacing 2.24 in equation 2.19

$$dW = \frac{1}{2}\,\gamma b \int_0^L \sum_{n=1}^{\infty}(a_n^2 + b_n^2)\, q_n^2\; dx \qquad 2.25$$

$$dW = \frac{1}{2}\gamma bL \sum_{n=1}^{\infty}(a_n^2 + b_n^2)\, q_n^2 \qquad 2.26$$

We can use the equipartition theorem (each normal mode, when configurationally averaged, contributes $k_BT/2$ for the energy of the system[179] where k_B is Boltzmann constant and T is temperature),

$$dW = \frac{1}{2}\,k_BT = \frac{1}{2}\gamma bL\langle h_q^2\rangle q^2 \qquad 2.27$$

where $\langle h_q^2\rangle = a^2 + b^2$, and q denotes the magnitude of the wave vector.

Finally we obtain the usual form of the interface fluctuation spectrum:

$$< h_q^2 >= \frac{k_BT}{bL\gamma q^2} \qquad 2.28$$

The typical geometry of the required system needed to perform such calculations is shown in Fig.2.12. The longest direction is perpendicular to the average interfacial plane. The other two directions parallel to the plane are the thickness b and the width L where $b << L$ in order to obtain a quasi-one-dimensional height function $h(x)$ measuring the position of the interface (see Fig.2.12). Details about how we can obtain the shape of the system used to extract the fluctuation spectrum via molecular dynamics simulation will be provided at the end of this chapter.

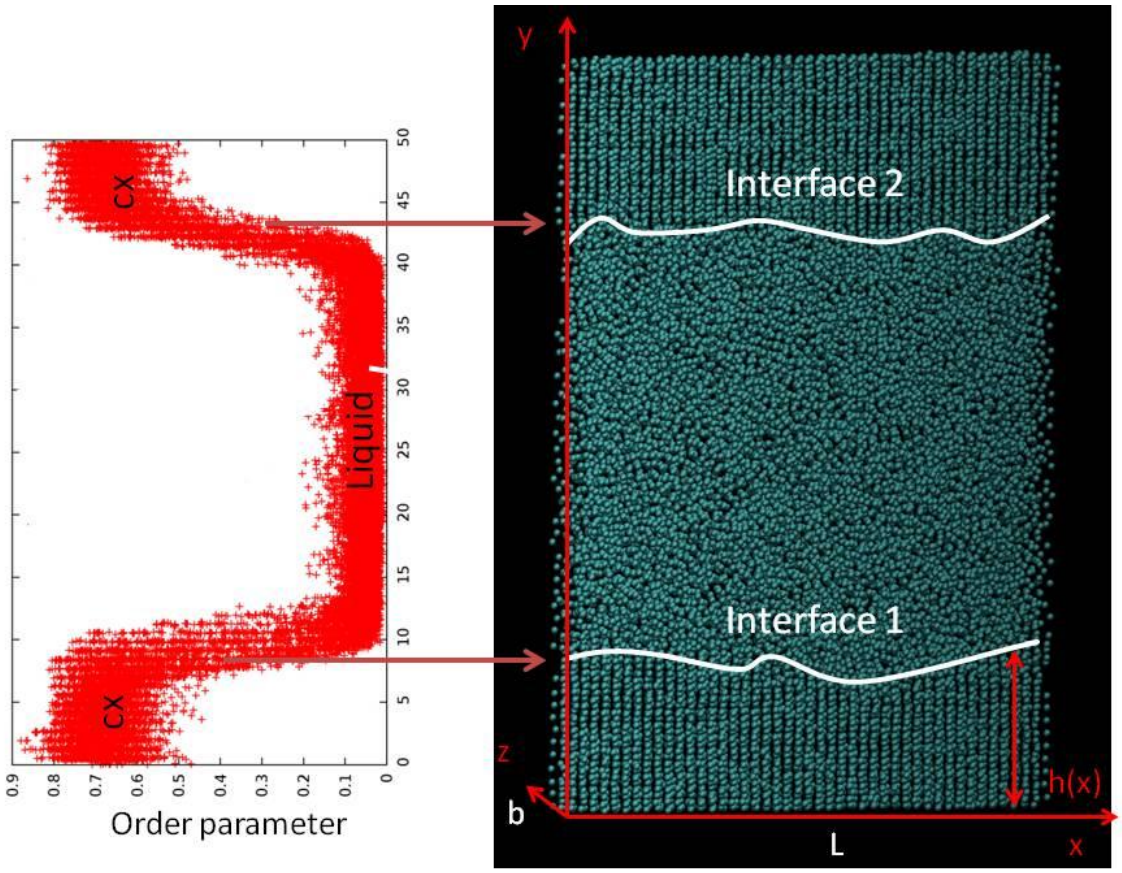

Fig.2.12: A snapshot of a simulation box used to determine the interfacial stiffness of an LJ system. The interface is parallel to the (xz) plane. The system size is as follow: L = Lx = 165.98 Å, b = Lz = 21.83 Å and Ly = 225.91 Å. Lx, Ly and Lz are the dimensions of the whole simulation box along the x, y an z directions. The left part of the figure represents the evolution of the local order parameter (see section 3.3.4) that enabled the determination of the height function h(x). For solid-like particles the local parameter should be equal to 1 and for liquid-like particles it should be equal to 0 (see chapter 3).

3.3.2 The analysis of the CFM

The first step of the capillary fluctuation method is to analyze the different configurations of the equilibrated system obtained during the production. For each

configuration the interface position is determined using a local order parameter as described in the next section. The interfacial profile thus obtained has the following form $y = h(x)$ where x is the direction along the interface. The values of the function $h(x)$ are measured at a discrete set of points $x_n = n\Delta$ where $n = 1, \dots N$ and $\Delta = L/N$.

The fluctuating height profiles are then Fourier transformed to obtain the instantaneous values of the height amplitudes h_q which are averaged over all the configurations to yield $< h_q^2 >$. Using equation 2.28, the plot of $ln(< h_q^2 >)$ versus $ln(q)$ should be linear with a slope of -2. The interfacial free energy is then extracted from the intercept of this plot.

The capillary fluctuation method was chosen in this study because it was shown that it can be applied accurately to obtain the crystal-melt interfacial free energies for molecular systems[38, 102]. On the computational level, this method is easy to implement compared to the cleaving method since it does not require external cleaving potentials that should be chosen carefully since the cleaving process should be reversible. Table 2.1 represents some interfacial free energy values obtain by using different simulation methods. It can be noticed that, for some cases, the orientationally averaged interfacial free energy varies significantly as function of the method employed (up to 16 % for example in the case of the Lennard-Jones systems).

Computational Method	System studied	Orientationally averaged interfacial free energy
CFM[178]	LJ system	0.362 ε/σ^2
CM[93]		0.360 ε/σ^2
CNM[41]		0.302 ε/σ^2
CFM[102]	Water	27 mJ/m^2
CM[94]		23.8 mJ/m^2
CFM[171]	Cu	149 mJ/ m^2
CNM[171]		136 mJ/ m^2

Table 2.1: Comparative table for some orientationally averaged interfacial free energies obtained from the different methods described in the text.

3.3.3 Order parameters

A major issue in most methods is the definition of a local parameter at the molecular scale that can distinguish very clearly between the liquid and the solid phases in order to obtain the position of the interface[41, 97, 100, 184]. Due to the complexity of molecular systems and their crystalline symmetries, a simple rotational-invariant order parameter $\langle q_6 \rangle$ [40, 184-188] is used. It is defined as a combination of spherical harmonic functions that interfere constructively when the system has the correct symmetry (crystal form), and destructively when the system is disordered (liquid form)[189]. Generally this order parameter is used for systems

having a cubic symmetry and allows distinguishing between different crystal cubic systems but it can be used as well for non-cubic symmetries[187, 188]. In this work, this parameter allows us to distinguish the liquid and the solid phases in order to obtain the position of the interface. The order parameter for a molecule i is given by[186]:

$$\langle q_l(i)\rangle = \sqrt{\frac{4\pi}{2l+1}\sum_{m=-l}^{l}|\langle q_{lm}(i)\rangle|^2} \qquad 2.29$$

where q_{lm} is defined in terms of $q_{lm}(k)$

$$\langle q_{lm}(i)\rangle = \frac{1}{N_b(i)}\sum_{k=0}^{N_b(i)} q_{lm}(k) \qquad 2.30$$

The complex vector $q_{lm}(k)$ of the particle k is defined as

$$q_{lm}(k) = \frac{1}{N_b(k)}\sum_{j=1}^{N_b(k)} Y_{lm}(\vec{r}_{kj}) \qquad 2.31$$

$N_b(i)$ is the number of nearest neighbors of particle i, $Y_{lm}(\vec{r}_{kj})$ are the spherical harmonics and $\vec{r}_{kj}$ is the vector from particle k to particle j. l is a free integer parameter and m runs from $m = -l$ to $m = l$. l is considered to be equal 6 in the following. Two molecules are considered as neighbors if the distance between their center of mass is smaller than the distance that corresponds to the first minimum of the radial pair distribution function of the bulk-liquid phase at the melting temperature. Therefore to obtain $\langle q_l(i)\rangle$ of particle i, the local orientational vector $\langle q_{lm}(i)\rangle$ is used and averaged over the particle i and its surroundings. Fig.2.13 shows an example of the evolution of $\langle q_6\rangle$ along the direction perpendicular to the interface for one instantaneous configuration of the felodipine II system for a given layer $[x, x + \Delta x]$. This figure shows clearly the existence of two domains allowing the identification of a crystal part (high values roughly above $\langle q_6\rangle$~0.115) and a

liquid part (low values below $\langle q_6 \rangle$~0.06) separated by an interface. In order to precisely determine the position of the interface $h(x)$, the evolution of $\langle q_6 \rangle$ has been fitted to an hyperbolic tangent function[40] :

$$\langle q_6 \rangle(y) = \frac{q_s+q_l}{2} + \frac{q_s-q_l}{2}\left(tanh\left(\frac{y-h_1(x)}{\delta_1}\right) + tanh\left(\frac{y-h_2(x)}{\delta_2}\right)\right) \qquad 2.32$$

This function describes the shape of a flat interface with effective width δ, q_s and q_l are the average value of the $\langle q_6 \rangle$ parameter in the solid and the liquid domains respectively and $h_1(x)$ and $h_2(x)$ are the mean positions of the two interfaces created due to the boundary conditions (Fig.2.12).

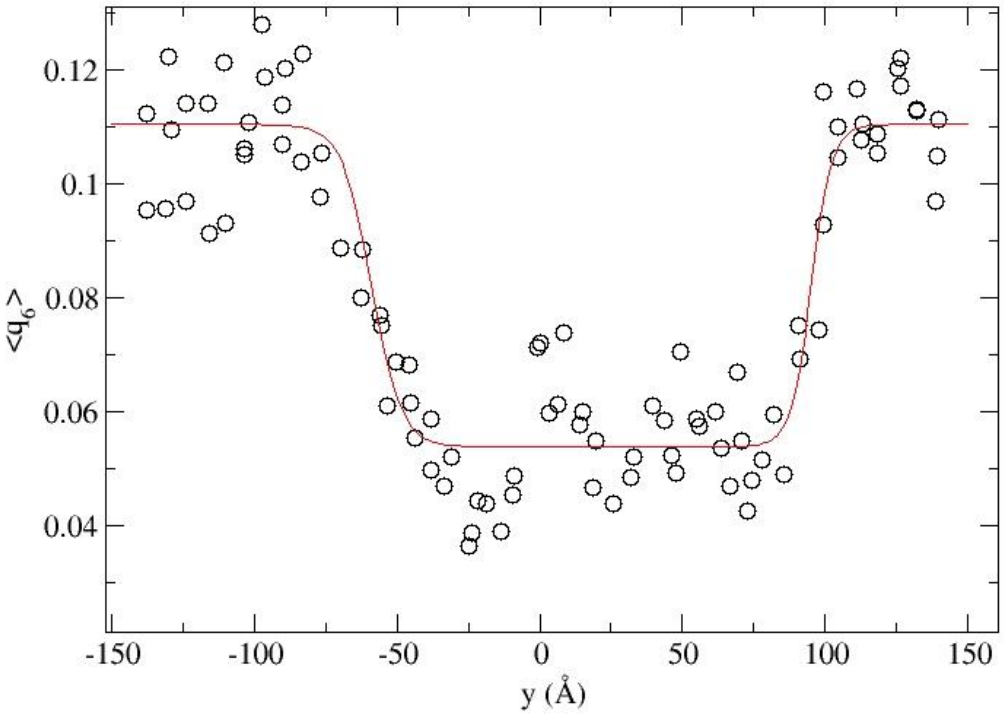

Fig.2.13: Evolution of the order parameter $\langle q_6 \rangle$ along the direction orthogonal to the interface (y). The line indicates the fitting using equ. 2.32.

3.3.4 Limitations of the equilibrium fluctuation spectrum expression

The interpretation of the form of the fluctuation spectrum discussed above is based essentially on the assumption that $h_x = \partial h/\partial x << 1$. So equation 2.28 is limited to $q \sim 0$.

By the mean of this theory, we could define two regions where the fluctuation spectrum of equation 2.28 is no longer valid:

- For long wave lengths, corrections must be made to the γ form. Higher order terms must be taken into consideration (like the bending rigidity of the interface κ)

$$\gamma(q) = \gamma(0) + \kappa q^2 + O(q)^4 \qquad 2.33$$

$\gamma(0)$ is the macroscopic interfacial tension.

- For short wave length, the interface is probed on single-particle (or molecule) length scale and smaller, and will be very rough as a result, so the concept of a smooth interface breaks down[180].

Note that the two final remarks were made for fluid-fluid or polymer-polymer interfaces. But the breakdown of equation 2.28 in the case of the interfacial free energy of a solid-liquid system is also probable[40, 98, 100, 152, 190-193] and deviations are expected in those kinds of systems for large and small q as it is shown in Fig.2.14:

-For small q (large wave length) the relaxation time could be larger than the simulation time[98] which gives larger uncertainties in the results.

-For large q (small wave length), the wave length becomes commensurate with the crystal lattice spacing and the uncertainty will be amplified by morphological instabilities[193].

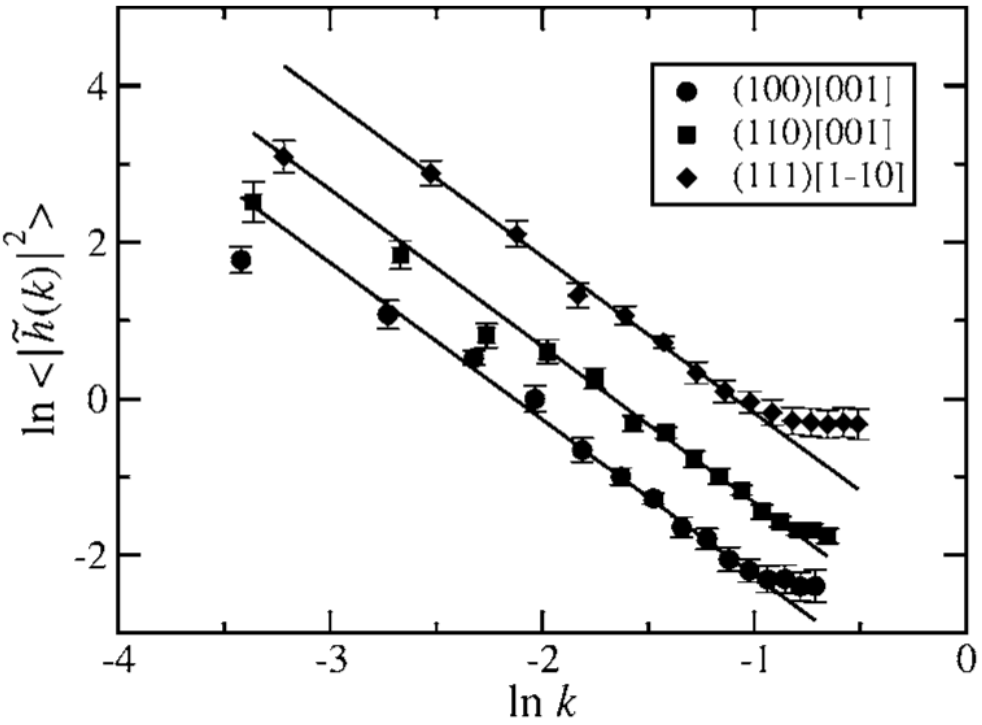

Fig.2.14: An example of the fluctuation spectrum of the quasi-one-dimensional interface height of a succinonitrile system[38] for three different orientations. The deviations of equation 2.28 are shown for large and small values of the wave vector k.

3.4 Simulation details

In chapter 3, MD simulations were performed on simple "Lennard-Jones"-like liquids and the specific simulation details, especially the force fields, are detailed in this chapter. In chapter 4, MD simulations were performed on different polymorphs, in their crystalline and liquid states, of felodipine, nifedipine and indometacin using the DLPOLY package[194] . For felodipine and nifedipine, the force field GAFF[134] (General Amber Force Field) was employed. For Indometacin, the OPLS[130] force field was used since the GAFF force field failed to stabilize the crystal structure of the metastable α phase at temperatures close to the melting

temperatures. The charge distribution of felodipine and nifedipine molecules were determined using the Gaussian software[195] with the HF/6-31G* basis set. For indomethacin, the charges used were those of the OPLS force field. Simulations were conducted either in the statistical ensemble NPT or NVT where N is the number of molecules, P the pressure, T the temperature and V is the volume. The number of molecules was fixed in the simulations and pressure and temperature were controlled with a Berendsen barostat and thermostat respectively with the relaxation time of 2 ps and 0.2 ps. The length of all the covalent bonds of each molecule was considered to be fixed using SHAKE algorithm[196]. All NPT simulations were realized at atmospheric pressure. The time step to integrate Newton's equation of motion was chosen to 0.001 ps. A cutoff radius of 10 Å was used to calculate short range van der Waals interactions. Ewald summation was employed in order to calculate the long range electrostatic interactions with the same cutoff radius. Periodic boundary conditions were applied in all directions.

The starting configurations of the crystal form of each system were obtained from the Cambridge Crystallographic data center[197]. The systems were then heated gradually to 450 K with a step of 50 K. 200 ps MD simulation runs were performed in the NPT ensemble at each step.

The starting configurations of the liquid form were achieved by melting the crystal forms at high temperatures (~800 K). A gradual quench to 100 K is then applied, using a step of 50 K, to the starting configuration which was stabilized at 750 K. Each simulation was done using the NPT ensemble during 200 ps.

The densities, the averaged cell parameters of the boxes and the enthalpies of each simulation in the NPT ensemble were determined using the corresponding average values of the final 100 ps of the simulation.

The numerical melting temperature $T_m(sim)$ was estimated using solid-liquid coexistence simulations as it was mentioned before. This method requires MD simulations of a biphasic crystal-liquid structure. For each polymorph, a large crystalline simulation box was generated from the experimental crystallographic data but with a larger number of molecules ranging from about 1200 to 1700. Each system was first equilibrated at the known experimental melting temperature for 100 ps in the statistical ensemble NPT, then for another 100 ps in the NVT ensemble using the equilibrated volume obtained from the NPT simulation. This crystalline box was then melted at high temperature (~800 K) and subsequently cooled at the experimental melting temperature then equilibrated at this temperature using first NPT then NVT simulation for 100 ps each. Both crystal and liquid boxes are combined together in order to form only one biphasic system (similar to Fig. 2.12). For all investigated systems, the total number of atoms was about 120 000 and the interface orientation in contact with the liquid was [100](010) [along the interface] (normal to the interface). A small gap was initially set between the crystalline and liquid parts in order to avoid overlapping between the atoms. The whole system was then equilibrated for 10 ps in order to remove this gap. Due to the periodic boundary conditions (Fig. 2.12); a solid-liquid-solid structure was finally obtained. Finally, this biphasic system was simulated at different temperatures above and below the experimental melting temperature. The melting temperature was estimated to be the temperature at which the density remains roughly stable as function of simulation time, in other words at the temperature where the liquid and crystals coexist. The determination of the melting temperature allowed us to estimate the enthalpy of melting from the difference of the enthalpy of the crystal and the liquid according to the MD simulation data.

The crystal-melt biphasic system that was used to obtain γ was constructed as follows. First the crystal and liquid phases were equilibrated separately at the melting temperature with similar cross section $b \times L$ (Fig. 2.12). Then the two systems were joined together along the y direction to form an interface where a small gap region is created to avoid overlapping. The total system is then equilibrated in a NPT ensemble for 50 ps while atomic positions of solid molecules were fixed leaving the melt molecules to fill in the gaps. 100 ps run was then conducted to equilibrate the whole system freeing the solid molecules. These simulations were followed by a 100 ps NVT simulation for additional equilibration where the averaged cell parameters of the final configuration of the NPT simulation were imposed. A 500 ps production run was finally executed in which 5000 configurations were stored for analysis. This procedure leads to the formation of two crystal-melt interfaces due to boundary periodic conditions for which profile is described by a function $h(x)$.

In order to reduce the computational effort, in the following we will identify the interfacial stiffness $\tilde{\gamma}$ determined using one single orientation to an isotropic interfacial free energy γ. It is usually reported in many model systems[97, 99, 100, 178] and realistic molecular systems[38, 94, 102, 198] that the anisotropic effect is usually relatively weak of the order of few percent and smaller than the uncertainties of the employed method. For example, for the cubic molecular solid (succinonitrile)[38], the interfacial free energy has been estimated to 7.06 $\pm$ 0.4 mJ/m^2 , 7.0 $\pm$ 0.4 mJ/m^2 and 7.01 $\pm$ 0.4 mJ/m^2 for the (100), (110) and (111) orientations respectively. For the hexagonal Ice Ih-water interface system in which molecules may form a high number of hydrogen bonds, the anisotropy was also found to be relatively weak: 23.3 $\pm$ 0.8 mJ/m^2, 23.6 $\pm$ 1 mJ/m^2 and 24.7 $\pm$ 0.8 mJ/m^2 for the basal, prism and (11-20) orientations respectively[94]. Moreover, it can

be mentioned that in the present work the chosen crystal orientation in contact with the liquid, [100](010), has approximately the same planar density for all polymorphs (1.2, 1.4, 1.4 and 1.3 x 10^{-2} molecules/Å^2 for nifedipine α, nifedipine β, felodipine I and felodipine II respectively and 2.0 x 10^{-2} molecules/Å^2 for both indomethacin polymorphs) which made possible the comparison of the different interfacial free energies. It should be also noted that this property is not completely verified by some of the other faces for which PD may reach 0.9 to 2 x 10^{-2} molecules/Å^2 depending on the considered face and polymorph. These other faces may possibly possess a different interfacial free energy. It is supposed that the difference remains within the uncertainties of the method as shown for succinonitrile and water. Note that the systems anisotropy is a very important issue and it would clearly deserve further studies.

The method used to estimate the diffusion coefficient D is described as follows. The systems were first equilibrated in the NPT ensemble for 1 ns and then a production run was performed in the NVT ensemble for another 3 ns at the equilibrated volume. These longer runs allowed us to obtain the self-diffusion coefficient from the calculation of the mean square displacement $< r^2(t) >$. For each temperature the long time behavior of $< r^2(t) >$ was fitted using the linear relation $< r^2(t) >=6Dt$ in order to obtain D. The diffusion coefficient at lower temperatures was extrapolated using equation 2.34 as described in reference[142]:

$$ln\left(\frac{1}{D}\right) = A_1 + \frac{A_2}{T} exp\left(\frac{A_3}{T}\right) \qquad 2.34$$

where A_1, A_2, and A_3 are adjustable parameters. It has been suggested that this relation was particularly able to reproduce very well both high and low temperatures ranges[142].

Chapter 3: Investigation of the crystallization in simple Lennard-Jones (LJ) systems

In the present Chapter, as a rational step before studying real molecular pharmaceutical compounds, we have investigated from MD simulations crystallization properties of model systems composed of simple atoms interacting through “Lennard-Jones”-like potentials. This study allowed us to obtain a fundamental understanding to address the dependence of diffusion, relative stabilities of liquid and crystal phases, solid-liquid interfacial free energy and nucleation rates on a specific controllable property i.e. the attractive part of the interaction potential for the same atomic system. The simplicity of the models also allowed us to observe the crystallization phenomena and thus to obtain directly nucleation rates. Such results were compared with predictions from the classical nucleation theory (CNT) on steady-states rates and the induction periods of small and large undercooling.

This chapter is organized as follow. The main motivations of this study on simple modelled liquids with tunable interaction potentials as well as recent works performed in the field are presented in the introduction. Then, the parameterization of the LJ-potential is firstly introduced followed by the description of the λ-integration method used to calculate the Gibbs free energy difference between the liquid and the crystalline state. The calculation of the interfacial free energy at the melting temperature for the different potentials is then presented. The interfacial stiffness was estimated for three orientations for each potential in order to compute the interfacial free energy. Finally, a comparison between the estimated nucleation

time and the nucleation times obtained directly from MD simulations is represented in order to validate the method.

This work was done with the collaboration of Dr. Valdes L.-C. and Dr. Mizuguchi T. (UMET-University of Lille 1-France).

1 Introduction

In many materials: metallic alloys, minerals, ceramics, polymers, molecular compounds,… it is clear that the interaction potential, $V(r)$ between the different components, determines ultimately all structural, dynamical or thermodynamical at all temperatures both below and above T_g [199]. An important aspect of the glass-forming ability may be thus elucidating how specific features of molecular interactions, such as the attractive and the repulsive forces, influence the rich variety of phenomena associated with the glass transition[200].

Computer simulations are ideally suited to the pursuit of this question because they allow interactions between particles to be varied in a systematic manner, thereby enabling the investigation of the effects of changes in individual variables to be conducted with a level of specificity not generally possible in experiments[201]. However, there are still clearly many challenges for narrowing the gap between practical experimental issues on real macroscopic materials, and results based on simulations performed at the microscopic levels[27].

Due to very limited computer power, first numerical MD studies of crystallization that were performed in the 1960s focused on simple liquids i.e. argon-like made of simple atoms interacting by pairwise hard-sphere or Lennard-

Jones potentials [202]. More than 40 years later, it might be surprising that these very simple systems are still of interest[203]. They remain relevant to model the properties of much complex materials due to their ability to approximate real interactions relatively well. Simple pair-wise interactions studied in this context include the hard sphere, inverse power law, large family of Lennard-Jones-type, Yukawa, Gaussian, and other model potentials[151, 192, 204]. Significant progresses of computers allow nowadays performing very extensive numerical simulations of such simple models. It particularly enable: i) to obtain much more accurate data by limiting size effects (larger systems made of billions of atoms) or ii) to access to properties that were not possible to obtain in the 70' such as mobility (fragility) in very deep undercooled situations or to discuss stability from direct determination of the Gibbs energy and crystal-melt interfacial properties[203].

In the following, we will mainly focus on the interest of tuning pair-wise interaction potentials $V(r)$ in MD simulations to induce (or modify) certain liquid properties of molecular and atomic systems. The idea of such tuning interaction potentials, has been around for some time[201, 205] but had not been exploited for the specific purpose of determining the conditions for vitrification/crystallization until rather recently.

In the recent decades, MD simulations on tunable interactions have been particularly performed aiming to identify the key features of the potential such as softness, attractivity, well depth or well location that might influence glass-forming/crystallization ability.The intrinsic "duality"glass formation/crystallization has obviously motivated two types of complementary investigations. Those mostly related to simple liquids that:

- do not crystallize "easily" on computation time scales with a strong focus on the temperature-dependence of the mobility in the supercooled regime (as measured by the so-called fragility index) which is one of the main ingredients involved in crystallization processes.
- do crystallize "easily" on computation time scales for which interfacial thermodynamics, nucleation barrier, structure of the crystalline phase, phase diagrams were analyzed.

It is a formidable challenge to avoid spontaneous crystallization on cooling of single component atomic simple liquid such as a Lennard-Jones liquid. This is why most of investigations performed on the glass formation issue have been mainly conducted on mixtures composed of different atoms. The viscous regime of the binary mixed Lennard-Jones system – the so-called Kob-Andersen (KA) model[206, 207] and its numerous derivatives[199] have been particularly investigated many times. One may note a few exceptions to this general rule. For example, the model proposed by[208] is a single-component atomic liquid that may be deeply supercooled. However, the inability to vitrify is induced by the very specific form of the interaction potential possessing two characteristic distances. This model thus actually corresponds to a quasi-binary mixture of soft spheres with two different diameters.

The accepted liquid-state picture whereby repulsive forces play a dominant role in determining the structure, with attractive forces providing a uniform cohesive background[209] underlies important recent works on viscous liquids. To date, relatively few investigations have explored systematically the effects of changes in the interaction potential[210, 211] and the precise role of the repulsive and attractive interactions in the viscous regime of some model systems.

One may particularly mention investigations by Berthier and Tarjus[212] in which the authors made a comparison of the structure and the dynamics of a standard Lennard-Jones glass-forming liquid mixture with (KA model)[207] and without (WCA model)[209] the attractive tail of the interaction potentials. The viscous slowing down of the two systems was found to be different, whereas the static pair correlations remain close. It was concluded that the common assumption that the behavior of dense non-associated liquids is determined by the short-ranged repulsive part of the intermolecular potentials dramatically breaks down for the relaxation in the viscous liquid regime. For the same systems, Banerjee et al.[213] recently shown that the differences in the interaction potentials may have a modest effect on structure, but a more significant effect on the thermodynamics (configurational entropy), and the Adam-Gibbs (AG) relation could hence capture the quantitative differences seen in the dynamics. We may also mention MD investigations by Coslovich and Roland[214] on modified LJ mixtures with different pair potentials defined by the exponent n of the repulsive term ($\sim 1/r^n$). The authors have shown an invariance of some physical parameters such as the fragility under isobaric conditions which suggests that the variations in fragility seen among different real materials have their origin in other aspects of the intermolecular potentials. In further MD studies[200] performed on Lennard-Jones-like glass-forming binary mixtures interacting via pair potentials with variable softness, fixed well depth, and fixed well depth location, it was also shown that softening of the potential leads to a modest increase in fragility.

Of course, the converse question of glass formation is the crystallization tendency. There have been important developments examining the influence of some specific aspects of the interparticle interactions on structural, dynamical and thermodynamical properties of simple systems that do crystallize “easily” on

computation time scales. A few examples are given below. Ahmed and Sadus[215] determined properties of fluids interacting via n-6 Lennard-Jones potentials, where n=11, 10, 9, 8, and 7 instead of the classical value n=12. The complete solid-liquid equilibria for these systems were obtained and the influence of the interatomic repulsive forces on the melting temperatures discussed. It could be noted that universality of melting curves for a wide range of interparticle interactions (Inverse power law, Yukawa, Weeks-Chandler-Anderson, Lennard-Jones and modified Lennard-Jones, Buckingham) have been suggested by A. Khrapak[216] from simple considerations. Interaction potentials and their effects on crystal nucleation and symmetry have been studied by Hsu and Rahman[217] in order to further clarify the effect of the interaction potential on the forming crystalline structure. By playing with the interaction potential, it was shown that the symmetry of the nucleated phase could be changed to bcc instead fcc as seen in classical Lennard-Jones. Davidchack and Laird[218] performed MD studies on the dependence of the crystal-melt interfacial free energy on molecular interaction and crystal structure (fcc vs bcc) for simple systems interacting with inverse-power repulsive potentials $V(r) = \varepsilon\left(\frac{\sigma}{r}\right)^n$ for different n approaching the hard-sphere limit ($n \to \infty$). Both the magnitude and anisotropy were found to increase as the range of the potential increases. Main aim of this work was to develop a generic microscopic understanding of the interfacial thermodynamics of simple materials. Molinero et al.[219] examined what happened to the melting points and the liquid state properties, of atomic systems as the parameter determining the strength of the "tetrahedrality" parameter in the three-body part of the Stillinger-Weber silicon potential was changed. Auer and Frenkel[220] performed numerical study of crystal nucleation in a system of weakly charged colloids in which interaction between the colloids is approximated by a simple repulsive hard-core Yukawa potential. It was shown that

the softness of the potential has a pronounced direct effect on the nucleation barrier through a lowering of the solid–liquid surface free energy. Most recently, the effects of the softness of the pairwise repulsive core, pairwise non-additivity, and the form of the pairwise intermediate-range repulsion interactions have been investigated from MD simulations on the glass-forming ability of metallic alloys. It has been particularly shown that hard-core interactions play the dominant role in setting the glass-forming ability of such materials but the crystal structure that competes with glass formation (and thus the glass-forming ability) also depends sensitively on the form of the repulsive interactions[221].

In the present literature on tunable interactions investigated from MD simulations, some results strongly support the possibility that, contrary to our common understanding, some properties such as mobility in liquids in the supercooled regime are mostly controlled by other properties of the potential, more than by the hard core repulsion. The possible significant role of the attractive part of the interaction has been discussed. To our knowledge, no detailed investigation on the precise role of the attractive part alone has been realized so far neither on mobility nor on crystallization tendency.

In the following, we will present some results obtained on three simple models composed of monoatomic Lennard-Jones atoms which have been recently investigated. Slight changes of the attractive part of the interaction potential were made in order to probe its influence on the crystallization capability. It will be particularly shown how the relative stabilities of liquid and crystal phases may be influenced by this change.

The three main physical ingredients involved in the nucleation process as described in the classical nucleation theory (CNT) have been directly calculated:

- The diffusion coefficient D has been calculated at different temperatures from atomic displacements.

- The driving force (ΔG) i.e. the Gibbs energy difference between the liquid and the crystalline state has been computed at different temperatures close to the melting point using the thermodynamics integration method (i.e. λ-integration method. See annex)

- The crystal-liquid interfacial free energy (γ) has been obtained from the capillary fluctuation method (see chapter 2 for a full description) which required the simulation of the interface in equilibrium at the melting point and the calculation of the fluctuations of the position of the crystal-liquid interface. The advantages of this method allowed calculating the anisotropy and the magnitude of the interfacial free energy accurately.

Such studies allowed us to obtain predictions from the classical nucleation theory (CNT) which is one of the simplest and most widely used theory that describes a nucleation process[1, 2, 31]. The non steady-state (time-lag for nucleation) and steady-state were predicted. Since crystallization can be directly observed in such simple liquids, it enabled us to analyze the nucleation kinetics at different undercooling and to compare with CNT predictions.

2 Simulation Details

2.1 Development of the interaction potentials with controlled attractivity

The simplest mathematical model that approximates the interaction between a pair of neutral atoms or molecules is the Lennard-Jones (LJ) potential. The first proposition of this interatomic potential was in 1924 by John Lennard-Jones [222]. The typical form of this potential is expressed as:

$$E_{LJ}(r) = \epsilon \left[\left(\frac{r_0}{r}\right)^{12} - 2\left(\frac{r_0}{r}\right)^{6} \right] \quad 3.1$$

where r is the distance between two atoms, r_0 is the distance where the potential well attends its minimum and ε is the depth of the well. Another representation might be used:

$$E_{LJ}(r) = 4\epsilon \left[\left(\frac{\sigma}{r}\right)^{12} - \left(\frac{\sigma}{r}\right)^{6} \right] \quad 3.2$$

where $\sigma = 2^{-\frac{1}{6}} r_0$ represents the cross section.

In order to show the effect of the attractive part of the LJ potential on the different factors that influence crystallization, the repulsive part of the potential is fixed and the attractive part is parameterized. Hence, the whole potential is defined as the classic LJ repulsive part and a family of parameterized attractive potentials described below.

The potential is defined on three successive intervals: $0 < r \leq r_0, r_0 < r < r_c$ and $r_c \leq r$. Two conditions of continuity of the potential and its derivatives are added in r_0 (between the attractive and the repulsive parts) and in r_c i.e. the cutoff radius (see chapter 2). In the following, this family of potentials is denoted

by $E_l(r)$ and its parameter l is defined as the root of the equation $E_l(l) = 0$ $(l \neq r_c)$. The family of potentials is thus controlled by the six conditions below:

$$\left\{\begin{array}{c} E_l(r_0) = -\varepsilon \\ \frac{dE_l}{dr}(r_0) = 0 \\ \frac{d^2E_l}{dr^2}(r_0) = 72\frac{\varepsilon}{r_0^2} \\ E_l(r_c) = 0 \\ \frac{dE_l}{dr}(r_c) = 0 \\ E_l(l) = 0 \end{array}\right\} \qquad 3.3$$

In order to simplify the numerical calculations, we first thought to take a polynomial form of degree 5 because of the six conditions (3.3), but this solution must be dismissed since the potential cannot have for certain values, for $r > r_0$, the S-shape characteristic of the Lennard-Jones as reference. The easiest non polynomial form compatible with fast numerical calculations is, otherwise, the rational fraction. Rational fractions with a number of coefficients compatible with the number of conditions (3.3) have all been analyzed and the choice of degrees of the numerator and denominator was decided to respect a look of attractive potential similar to the Lennard-Jones potential for $r > r_0$.

In the following, the family of the interaction potentials investigated in this study has the following form:

$$E_l(r) = \left\{\begin{array}{ll} \varepsilon\left[\left(\frac{r_0}{r}\right)^{12} - 2\left(\frac{r_0}{r}\right)^{6}\right] & for\ 0 < r \leq r_0 \\ \varepsilon\frac{(r-A)^2(r-B)}{C(r-r_0)^2+D(r-r_0)+E} & for\ r_0 < r < r_c \\ 0 & for\ r_c \leq r \end{array}\right\} \qquad 3.4$$

The expressions of constants A, B, C and D can be deduced from the conditions (3.3). By taking:

$$\begin{Bmatrix} \rho = \frac{r_c}{r_0} - 1 \\ \lambda = \frac{l}{r_0} - 1 \end{Bmatrix} \quad 3.5$$

it comes

$$\begin{Bmatrix} A = r_c \\ B = l \\ C = (36\rho^2\lambda + 2\rho + \lambda)r_0 \\ D = -(\rho + 2\lambda)\rho r_0^2 \\ E = \rho^2\lambda r_0^3 \end{Bmatrix} \quad 3.6$$

It has been verified that the potential is similar to that of the Lennard-Jones potential for all values of the parameter l below a certain upper bound l_{max}, function of r_0 and r_c. Fig.3.1 shows some examples of potentials where l_{max}=1.1038 σ for $r_0 = 2^{1/6}$ σ and $r_c = 3\sigma$.

In the following, we investigated properties of four interaction potentials: the classical Lennard-Jones potential given by equation 3.1 and three potentials E_{l^*} for $l^* = 0.10$, 0.95 and 1.05 where the subscript $*$ denotes the reduced parameter $l^* = \frac{l}{\sigma}$. The increasing l^* corresponds to the increasing attractiveness of the potential $E_{l^*}(r)$ (Fig.3.2).

It could be also mentioned that an additional merit of these potentials including several continuity conditions (see above) is to leave open the possibility of using this family of potentials for the search of minima of potential energy surface by gradient methods and possible analyses of the potential energy landscape[1, 200, 211] .

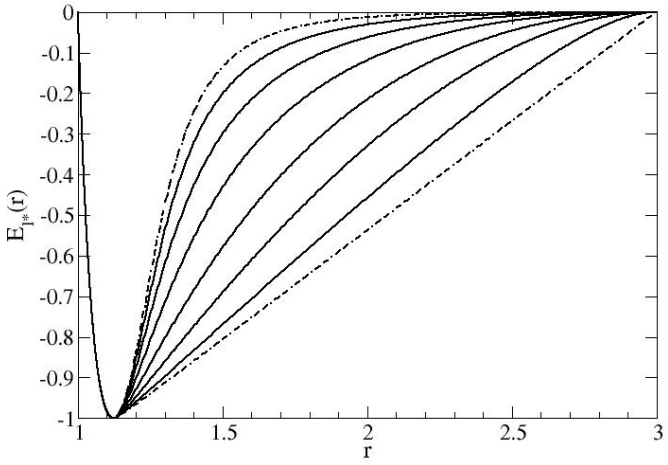

Fig.3.1: Some examples of the parametrized potentials $E_{l^*}(r)$. From left to right: l^*=-10[9] , 0.50 , 0.90 , 1.02 , 1.07 , 1.09 , 1.10 , 1.1038 (upper limit).

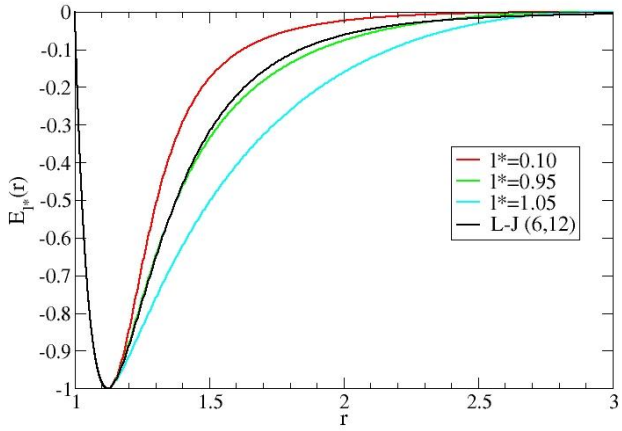

Fig.3.2 : Potentials with increasing attractivity $E_{0.10}(r), E_{0.95}(r), E_{1.05}(r)$ and investigated in the present study. The classical LJ potential $E_{LJ}(r)$ is also represented to show its similarity with the $E_{0.95}(r)$ potential.

2.2 Simulation parameters

The Molecular Dynamics simulations are performed using the software DLPOLY-classic[136] on systems composed of 864 particles. The following parameters, in argon units, are used: m_{Ar}=6.642.10^{-26} kg, a cross section of σ_{Ar}

=3.405 10^{-10} m and a minimum potential value ε_{Ar} =1.6605.10^{-21} J. The simulation box is cubic with periodic boundary conditions in all directions. Calculations are performed with the time step Δt =0.005.10^{-12} s and the cut-off distance r_c=10.215.10^{-10} m. The pressure used in this work correspond to P =4.206.10^{7} Pa. The results are presented in the system of units of the argon atom σ_{Ar} , m_{Ar}, ε_{Ar} and the Boltzmann constant k_B =1.3807.10^{-23} J.K^{-1}. With these quantities, we constructed time units $t_{Ar} = \sqrt{\frac{m_{Ar}}{\varepsilon_{Ar}}}.\sigma_{Ar}$ = 2.153.10^{-12} s, pressure $P_{ar} = \frac{\varepsilon_{Ar}}{\sigma_{Ar}^3}$ = 420.6.10^{5} Pa and temperature $T_{Ar} = \frac{\varepsilon_{Ar}}{k_B}$ =120.27 K. In the following, an asterisk superscript denotes the value of the physical quantity expressed in this system of units. Hence, $\Delta t^* = 0.005$, r_c^* =3, $P^* = 1$ and $r_0^* = 1.122$.

3 Diffusion coefficient and crystal and liquid densities

The variation of the liquid and crystal volumes (V^*) as function of the temperature was obtained from the simulation of systems containing 864 particles at various temperatures. All simulations were conducted at $P^* = 1$ for the three studied potentials. The volumes of the systems during heating and quenching are represented in Fig.3.3. An initial crystalline box (fcc) was first generated and equilibrated at T^*= 0.3. The system was then heated from T^*= 0.3 to T^*= 1.3 with a temperature step of ΔT^*= 0.1. At each temperature, the MD simulation runs last for t^*=464.5. Upon heating, the melting of the system is clearly observed from the sudden jump of the volume (see Fig.3.3). At T^*= 1.3, the system was then cooled to T^*= 0.3 at the same rate as in the heating process. Crystallization is detected by a clear volume drop. The melting and crystallization phenomena are characterized by a marked hysteresis in this heating/quenching cycle. Indeed, it is usually

reported that periodic boundary conditions used in MD simulation may contribute to reinforce artificially the stability of the crystalline state. It thus allows the system to be overheated. Fast quench/cooling rates certainly also contribute to maintain the system in a metastable state compared to the most stable state at a given temperature. From Fig.3.3, we may also notice that after quenching the system does not reach the initial volume corresponding to a perfect fcc lattice. Upon crystallization, several defects are formed. The solid state obtained upon quenching the liquid is thus more disordered which explains the observed increased in volume. The change of the attraction in the interaction potential has also clearly an influence on the volume of the crystal and the liquid phase. One may notice that the volume decreases with the increasing attractive part of the potential which can be logically understood from just an increase in cohesivity since the repulsive part is kept constant.

From Fig. 3.3, the density $\left(\rho^* = \frac{N}{V^*}\right)$ evolution as function of the temperature was estimated by fitting the liquid density by $\rho_{lq}^*(T) = a_{lq}T^* + b_{lq}$ and the solid density by $\rho_{cx}^*(T) = a_{cx}T^{*2} + b_{cx}T^* + c_{cx}$ at high and low temperatures respectively. Table 3.1 summarizes the values of the fitting parameters a_{lq}, b_{lq}, a_{cx}, b_{cx} and c_{cx} .

The coefficient of diffusion was estimated from the long term evolution of the mean square displacement $< r^2(t) > \sim 6D^*t$ (see Chapter 2) calculated at different temperatures in the liquid states. The simulation results of D^* at each temperature T^* are represented in Fig.3.4. It shows that the attractive part of the potential also has an influence on D^*: the coefficient of diffusion decreases with the increasing of the attractive part of the potential. This behavior certainly just

originates from the increase in density as it is known for purely van der Waals liquids. Same trend has been reported in a recent MD study[223].

It can be noticed that the coefficient of diffusion of classical Lennard-Jones potential and the l^*= 0.95 potential are roughly the same. This behavior was expected since the two potentials are almost identical (Fig.3.2). In order to fit D^* at high temperatures in the liquid domain, an Arrhenius law ($D^* = \exp\left(\frac{a_D}{T^*} + b_D\right)$) was used. The different parameters obtained by the fits are reported in the caption of Fig.3.4.

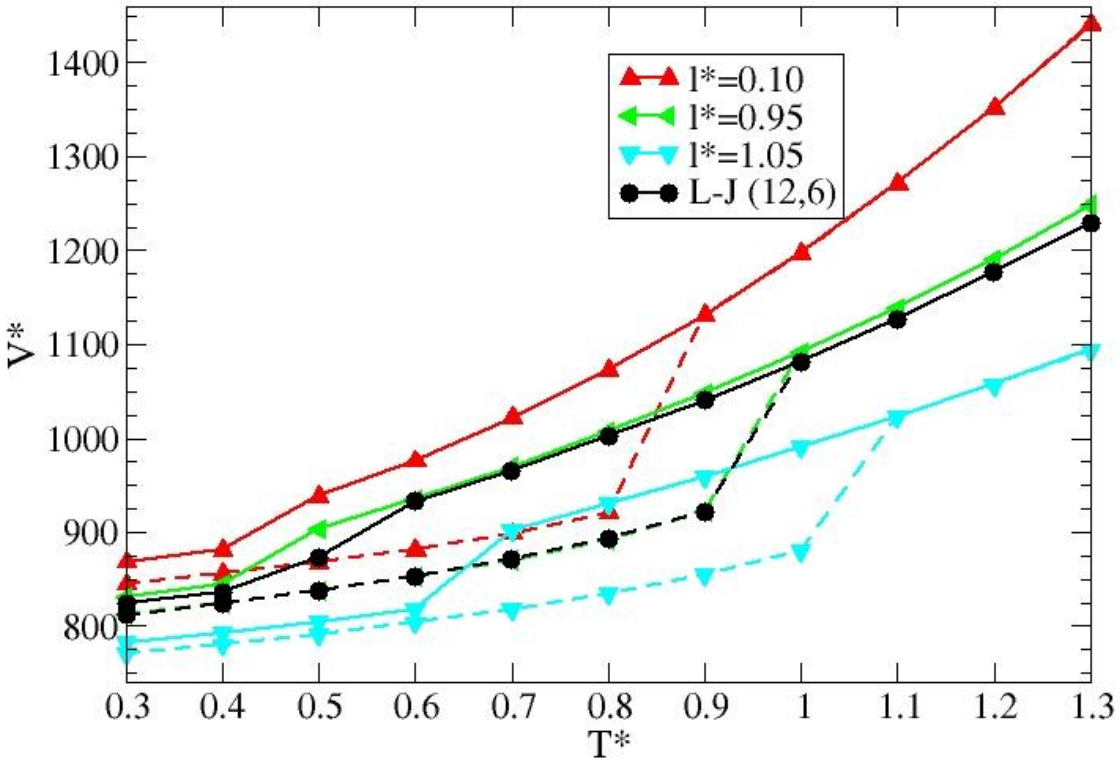

Fig.3.3: Evolution of the volume V^* as function of the temperature T^* for the different investigated systems upon heating (dashed lines) and cooling (solid lines).

l^*	0.10	0.95	1.05
a_{lq}	- 0.413	- 0.330	- 0.282
b_{lq}	1.135	1.122	1.155
a_{cx}	- 0.107	- 0.911	- 0.811
b_{cx}	- 0.051	- 0.090	- 0.083
c_{cx}	1.048	1.099	1.153

Table 3.1: The fitting parameters obtained for the liquid and crystal density for the three different studied potentials (see text).

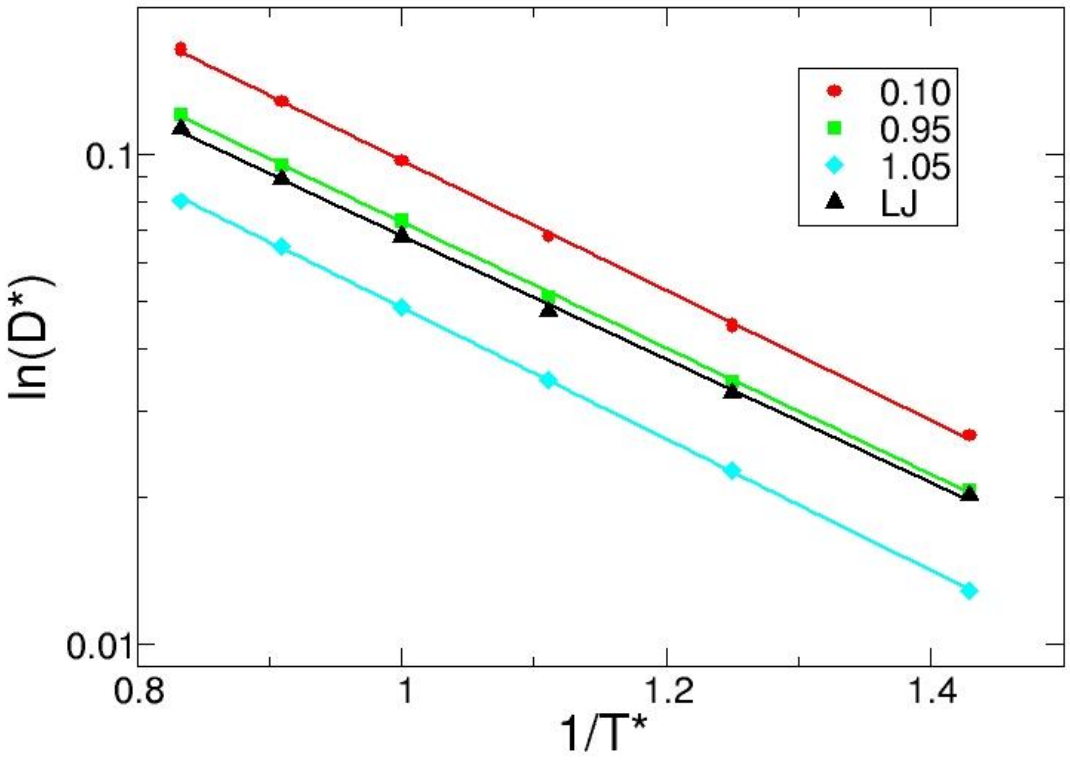

Fig.3.4: The influence of the attractive part of the potential on the coefficient of diffusion D^*. The fitting parameters (a_D, b_D) are: -0.49, 0.57 ; -0.35, 0.41 ; -0.25, 0.29 and -0.32, 0.38 for $E_{0.10}(r), E_{0.95}(r), E_{1.05}(r)$ and $E_{LJ}(r)$ respectively (see text).

4 Gibbs free energy calculations

The Gibbs free energy difference between the solid and the liquid for the three different potentials ($l^* = 0.1$, 0.95 and 1.05) and the classical LJ potential was calculated directly using the constrained fluid λ-integration approach [224]. This method relies on the construction of reversible and integrable paths to connect the solid and the liquid states (see annex).

As previously described, the melting and the solidifying hysteresis curves are obtained by progressively heating and quenching, crystal and liquid cells, using an NPT ensemble at $P^* = 1$ for each of the three tunable potentials described previously and the classical LJ. Four temperatures in the hysteresis loop are chosen at which both liquid and crystalline states can be stabilized. The Helmholtz free energy differences between the crystal and the liquid states are calculated using the constrained fluid λ-integration approach (see annex). The Gibbs free energy differences ΔG between the liquid and the solid is calculated as function of the Helmholtz free energy F differences using the relation $\Delta G = \Delta F + p\Delta V$.

The evolution of the Gibbs energy difference as function of the temperature is represented in Fig.3.5 for the three studied potentials and the classical LJ potential. The Gibbs free energy can be modeled at different temperatures using the following quadratic form:

$$\Delta G^* = a_G T^{*2} + b_G T^* + c_G \qquad 3.15$$

Table 3.2 represents the values of the fitting of equation 3.15 to the calculated data of ΔG^*. The melting temperature can thus be easily obtained by solving the equation $\Delta G^* = 0$ (see Table 3.4). Table 3.3 summarizes all the values

of the melting temperature, the enthalpy of fusion and the crystal/liquid densities at the melting point for all the three studied potentials.

Potential	$E_{LJ}(r)$	$E_{0.10}(r)$	$E_{0.95}(r)$	$E_{1.05}(r)$
a_G	-0.201725	- 0.890225	- 0.326893	- 0.195025
b_G	-1.14799	- 0.421411	- 1.015459	- 1.160909
c_G	1.01603	0.784140	0.978890	1.180715

Table 3.2: The fit coefficients of the Gibbs free energy by equation 3.15 for the three studied potentials and for the classical Lennard-Jones potential obtained from the λ-integration approach.

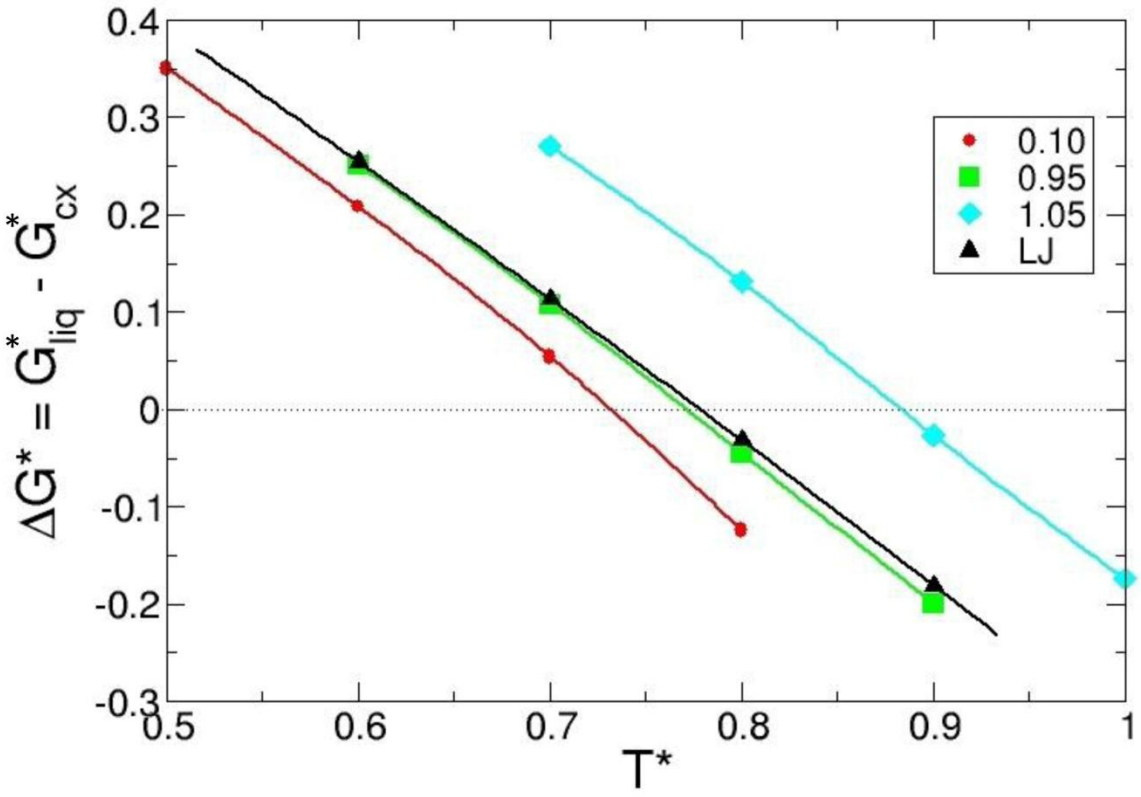

Fig.3.5: The Gibbs free energy difference calculated at four different temperatures for the four studied potentials. The dotted line indicates the position of the melting ($\Delta G^* = 0$)

l^*	LJ	0.10	0.95	1.05
T_m^*	0.778	0.731	0.772	0.885
ΔH_m^*	1.118	1.260	1.172	1.333
$\rho_{cx}^*(T_m)$	0.984	0.958	0.993	1.058
$\rho_{lq}^*(T_m)$	0.871	0.831	0.867	0.904

Table 3.3: Melting temperature, enthalpy of fusion and crystal/liquid densities at the melting point for the three studied potential and the classical LJ potential

The evolutions reported in Table 3.3 of densities and melting temperatures which increase from potential $l^* = 0.1$ to 1.05 can be understood quite easily. Density increase is a direct consequence from the increase in cohesivity of the system which just originates from the increase of the attractive part of the potential while maintaining the repulsive part constant as described above (see Fig.3.3). Melting temperature increase is the result of the higher heat required to overcome cohesive forces that held atoms together in the crystal lattice. For strong forces, one needs more heat, and thus, the melting temperature is higher. For melting enthalpies, the situation is more complex since ΔH_m^* does not follow a monotonic trend as function of the attraction of the potential as it could be expected. The potential l^*=0.95 (as well as the classic LJ potential) possesses the lowest enthalpy of fusion (ΔH_m^*=1.172) compared to the other potentials (1.26 for l^* = 0.10 and 1.33 for l^* = 1.05). This behavior can be clarified at least partially from the evolution of the enthalpy difference between the liquid and the solid state as function of the temperature $\Delta H^*(T^*)$ shown in Fig.3.6. It can be noticed that the three curves do not follow parallel evolution in temperature. The $\Delta H^*(T^*)$ curve of the l^*=0.10 potential particularly intersects the other curves in two distinct points. Since melting temperatures are different for the different potentials, the values $of\ \Delta H_m^*$

do not follow a regular evolution from the potential with the lowest attraction to the potential with the highest attraction. We have no clear explanation at the moment for the marked difference observed on $\Delta H^*(T^*)$ for the potential the l^*=0.10.

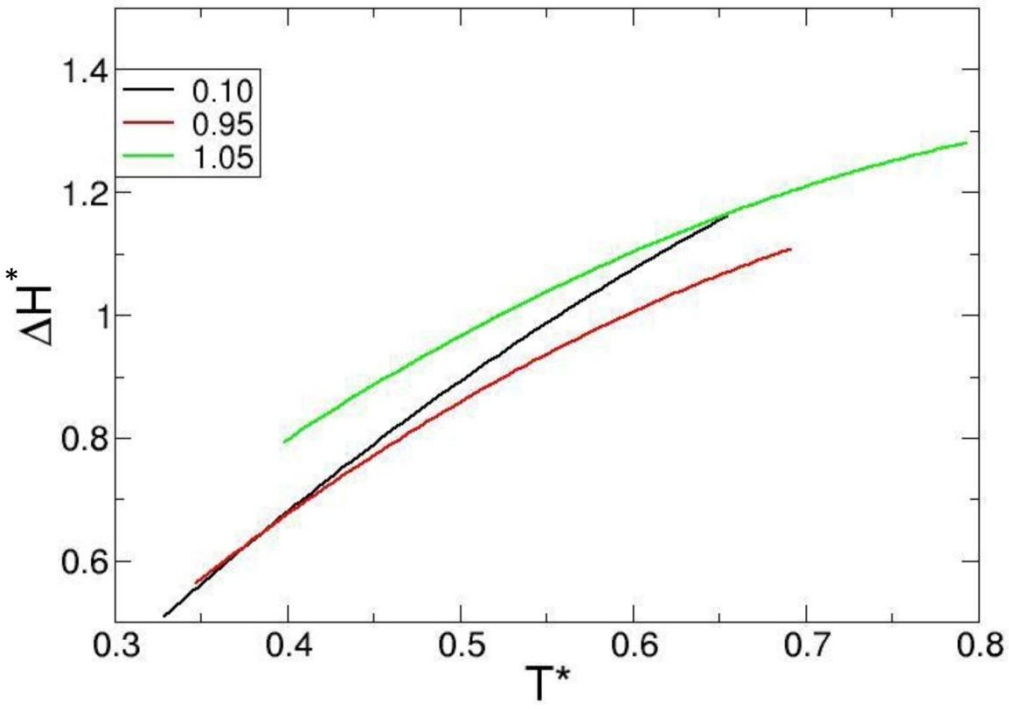

Fig.3.6: The evolution of the enthalpy difference between the liquid and the crystal as function of the temperature T^* for the three investigated potentials.

5 Interfacial free energy calculations

The capillary fluctuation method has been used in this work. A biphasic (crystal-liquid) system has been constructed and we followed the fluctuations of the crystal-liquid interface in equilibrium at the melting temperature (see chapter 2). In order to obtain the fluctuation spectrum which is related to the interfacial stiffness, we proceeded as follows.

We first equilibrate crystal and liquid phases separately at constant temperature $T^* = T_m^*$ (see Table 3.3) and pressure P^*=1.0 and calculate the density of each phase in equilibrium (see Table 3.3). With these density values, slab-shaped crystal and liquid samples are prepared separately, with the identical cross sections bW *(*see Fig.3.7*)*. The melting temperature T_m^* has been determined by coexistence simulations (see chapter 2). The melting temperatures for our systems for P^*=1 are given in Table 3.4. Note that the melting temperatures were obtained as well by the constrained λ-integration method [224] and compared to the melting temperatures obtained directly from the coexisting simulations (Table 3.4). We can notice that the values are different but within error bars, proving the validity of both methods.

After joining crystal and liquid boxes, the system is equilibrated at constant temperature $T^* = T_m^*$ and pressure P^*=1.0. A snapshot of an instantaneous configuration is given in Fig.3.7 The number of particles is reported in Table 3.5. The system is then equilibrated at constant temperature $T = T_m$ and volume (400,000 time steps). The run for data collection was one million time steps. During this run, atomic positions were stored every 500 time steps.

Potential	T_m^* (constrained λ-integration method)	T_m^* (coexistence simulation)
0.1	0.731	0.77 +/- 0.03
0.95	0.772	0.81 +/- 0.03
1.05	0.885	0.89 +/- 0.03
LJ	0.778	0.79 +/- 0.03

Table 3.4: The melting temperatures obtained via coexisting simulation and via the constrained λ-integration method for the 3 different potentials and for the classic LJ potential.

In order to determine the interfacial height $h(x)$ derived from atomic configurations, it is necessary to distinguish between crystal and liquid atoms (see Figure 3.7). Hence, we first define a local order parameter[100, 178] Ψ for each atom:

$$\Psi = \left| \frac{1}{N_{\vec{q}}} \frac{1}{Z} \sum_{\vec{r}} \sum_{\vec{q}} \exp\left(i\vec{q}\vec{r}\right) \right|^2 \qquad 3.16$$

where $N_{\vec{q}}$ represents a set of wave vectors $\vec{q}_i$ such that $\exp(i\vec{q}\vec{r}) = 1$ for any vector $\vec{r}$ connecting the neighbors (Z) in a perfect fcc lattice. The summation over $\vec{r}$ runs over each of the neighboring particles found within a distance d_c from an atom chosen between the first and the second neighbor shell in the perfect fcc lattice. The antiparallel vectors are omitted so $N_{\vec{q}}$= 6. Thus, for a perfect fcc lattice, the order parameter will be equal 1 and less than 1 in all the other cases. In order to improve the discrimination between liquid and solid atoms, the order parameter will then be averaged over the neighboring values:

$$|\Psi_i| = \frac{1}{Z+1}\left(\Psi_i + \sum_j \Psi_j\right) \qquad 3.17$$

where j runs over all the Z neighboring atoms i. This average eliminates the isolated atoms and clusters that might have a significantly different order parameter than their surroundings.

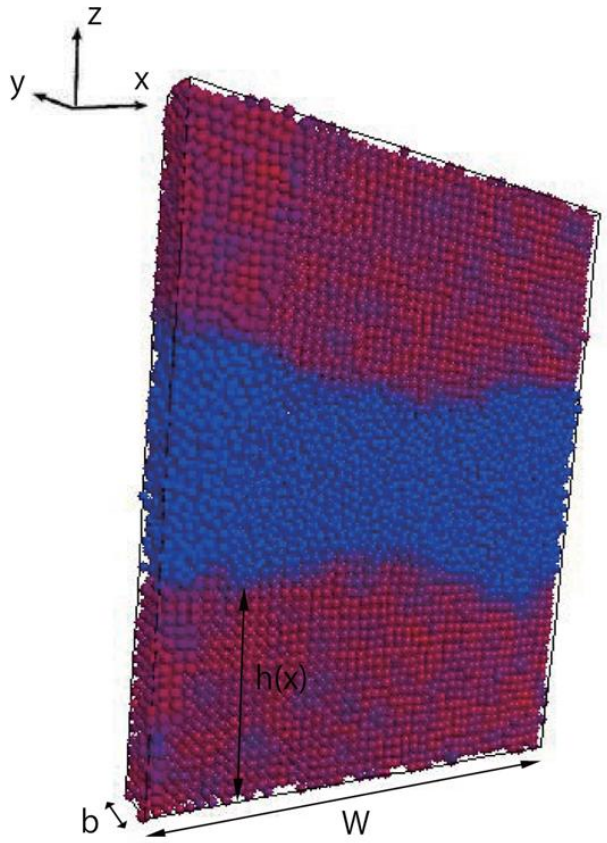

Fig.3.7: A snapshot of the system with two (110) interfaces for the potential 0.95. Liquid-like particles have a blue color whereas solid-like particles have a red color.

Figure 3.8 shows the averaged local order parameter $|\Psi|$ for each atom for the $(110)[1\bar{1}0]$ interface of the potential 0.95. To define the interfacial particles, we take the following procedure. We first define a threshold value $|\Psi_s|$ of the order parameter $|\Psi|$ for the solid phase, that is, the particles that satisfy $|\Psi| > |\Psi_s|$ is considered to belong to the solid phase. We can calculate the number of the nearest

neighboring solid particles Z_{nns} for each atom using the threshold value $|\Psi_s|$. Figure 3.9 shows the order parameter Z_{nns} for each atom calculated for the same configuration as Fig.3.8. We also define a threshold value Z_s for the order parameter Z_{nns}, and consider the particles that satisfy $Z_{nns} \geq Z_s$ as solid particles. We can determine $h(x)$ using these two order parameters. In Fig.3.7, the solid atoms have darker color than the liquid atoms. We can notice an important difference between crystalline and disordered regions. For instance, we may define $|\Psi_s|$=0.47 and Z_s=10 with Fig.3.8 and 3.9 for this configuration. The interfacial particles are thus determined as the particles that satisfy $|\Psi_i| < |\Psi_s|$ and $0<Z_{nns}<Z_s$. From the height function found earlier, we can calculate the fluctuation spectrum $h\,(q)$ which is obtained by the Fourier transform of $h(x)$ (see Chapter 2).

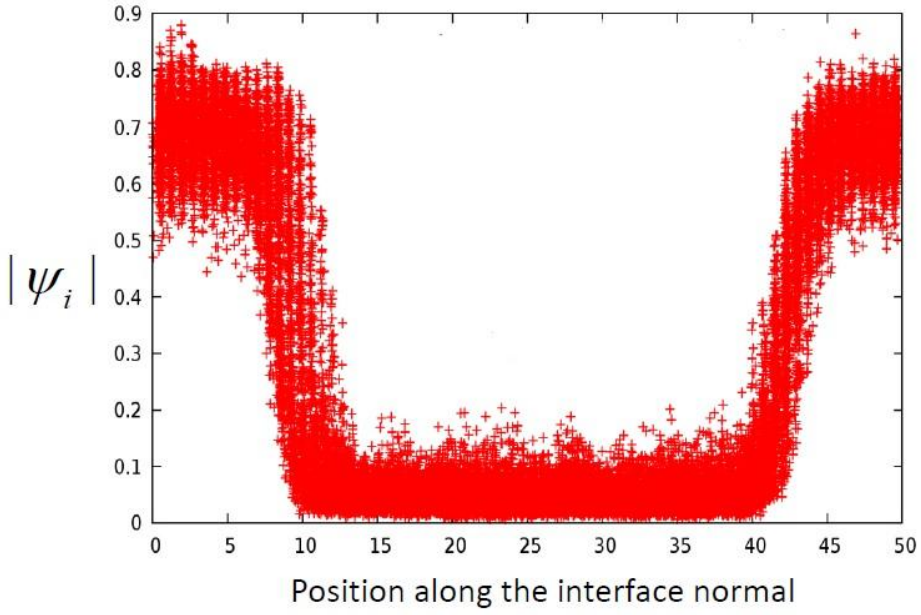

Fig.3.8: The order parameter $|\Psi|$ for each atom in an instantaneous configuration of the $(110)[1\bar{1}0]$ *interface for the potential 0.95, as a function of atomic position measured along the interface normal.*

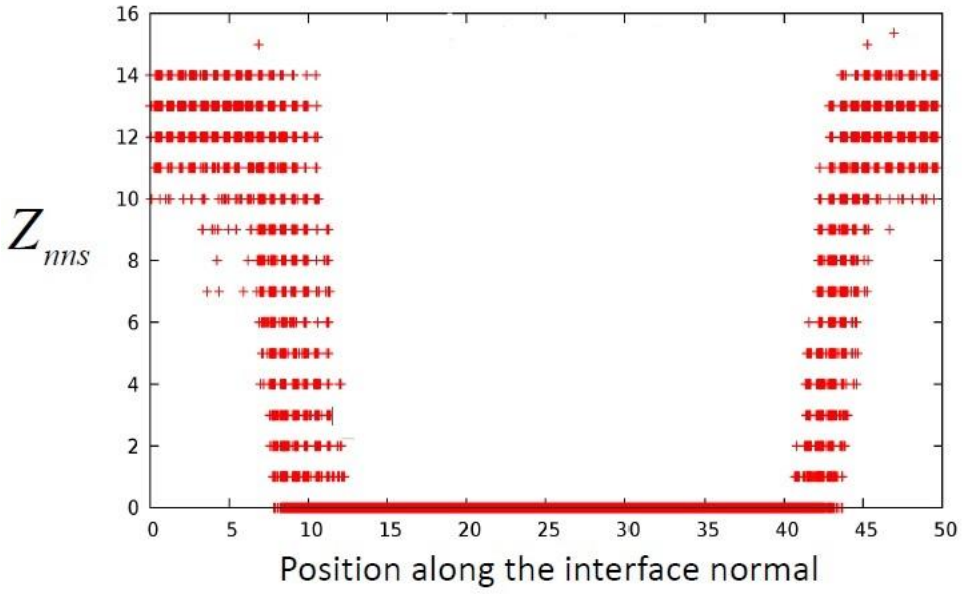

Fig.3.9: The order parameter Z_{nns} for each atom in the same configuration as Fig. 3.8.

The interfacial stiffness is expected to be more anisotropic than the interfacial free energy[38, 97, 100, 178, 179, 225]. For a weak anisotropic system, the orientation-dependent expressions for the interfacial free energy can be represented by the cubic harmonic expansion[225]

$$\gamma(\vec{n}) = \gamma_0 \left[1 + \varepsilon_1 \left(\sum_i n_i^4 - \frac{3}{5}\right) + \varepsilon_2 \left(3\sum_i n_i^4 + 66 n_1^2 n_2^2 n_3^2 - \frac{17}{7}\right)\right] \quad 3.18$$

where $\vec{n} = (n_1, n_2, n_3)$ is the unit vector normal to the interface, γ_0 is the orientationally averaged interfacial free energy, and ε_1 and ε_2 are the anisotropy parameters. From this equation, we can derive similar expressions for the interfacial stiffness. A minimum of three interface orientations are needed to determine the values of $\varepsilon_1, \varepsilon_2$ and γ_0. We calculated the parameters using the three stiffnesses of $(100)[001], (210)[001]$ and $(110)[1\bar{1}0]$ where the numbers in parentheses are Miller indices for the interface normal and the numbers in square

bracket are those for the short direction tangent to the interface. The anisotropic interfacial stiffnesses for these three orientations are given by

$$\tilde{\gamma}_{(100)[001]} = \gamma_0 \left(1 - \frac{18}{5}\varepsilon_1 - \frac{80}{7}\varepsilon_2\right) \quad 3.19$$

$$\tilde{\gamma}_{(110)[1\bar{1}0]} = \gamma_0 \left(1 - \frac{21}{10}\varepsilon_1 + \frac{365}{14}\varepsilon_2\right) \quad 3.20$$

$$\tilde{\gamma}_{(210)[001]} = \gamma_0 \left(1 + \frac{6}{5}\varepsilon_1 - \frac{274}{35}\varepsilon_2\right) \quad 3.21$$

From these equations and the stiffness values derived from MD, we obtain the orientationally averaged free energy γ_0.

Fig.3.10 shows $< |h(q)^2| >$ for each of the geometries and for different potentials. According to Eq.2.28 (see Chapter 2), a plot of $ln(< |h(q)^2| >)$ against *ln*(q) should be linear with a slope of -2 and the determination of the interfacial stiffness $\tilde{\gamma}$ can be done from the intercept of this plot (Fig. 3.10). We can notice that the fluctuations follow this behavior for small q indicating the roughness of the interface[178]. For large q (small wave length), a deviation occurs. The wave length becomes commensurate with the crystal lattice spacing and the uncertainty will be amplified by morphological instabilities. Using these stiffness values and Eq. 3.19-3.21, we can calculate the orientationally averaged interfacial free energy γ_0. The values of γ_0 for the three potentials and the classical 12-6 Lennard-Jones potential are shown in Table 3.5.

Potential	Number of particles	Orientation	γ_0 (ϵ/σ^2)	$\tilde{\gamma}$ (ϵ/σ^2)
0.1	16384 18920 17748	(100)[001] (110)[$1\bar{1}0$] (210)[001]	*0.35*	0.33 0.38 0.33
0.95	16384 18920 17748	(100)[001] (110)[$1\bar{1}0$] (210)[001]	*0.37*	0.38 0.43 0.36
1.05	16384 18920 17748	(100)[001] (110)[$1\bar{1}0$] (210)[001]	*0.43*	0.41 0.52 0.40
LJ	16384 18920 17748	(100)[001] (110)[$1\bar{1}0$] (210)[001]	*0.37*	*0.38* 0.43 0.35

Table 3.5: The orientationally averaged interfacial free energy for the three potentials and the classical 12-6 Lennard-Jones potential. The number of atoms and the interfacial stiffnesses for three orientations for the same potentials are also listed.

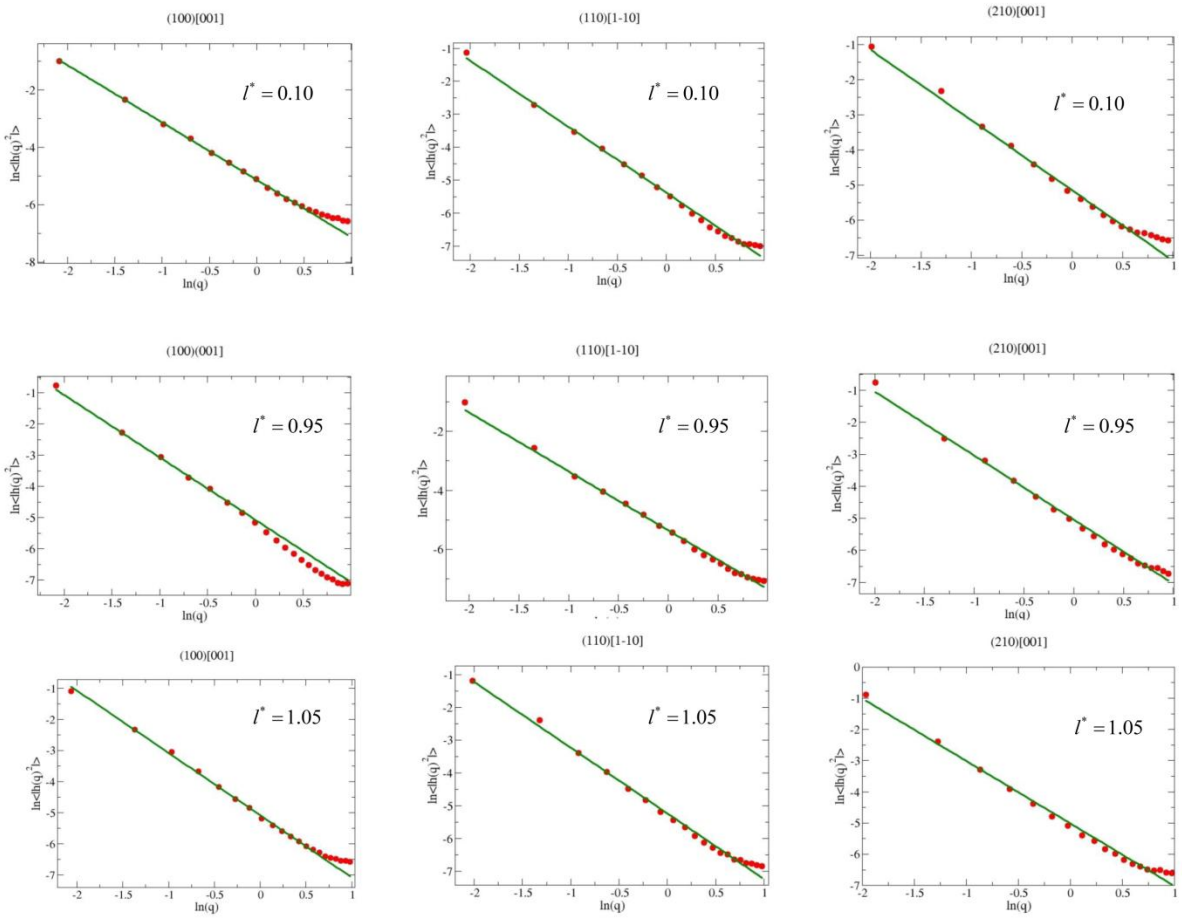

Fig.3.10 : Fluctuation spectra for the three orientations of the three potentials. The plot $ln(< |h(q)|^2 >)$ vs $ln(q)$ is represented (red dots) with the linear fit (solid green line).

The values of the solid-liquid interfacial free energy are reported in Table 3.5. As expected, the value of γ_0 for the potential l^*=0.95 and the classic LJ potential are close due to the similarities of the two potentials. To our knowledge, the effect of the attractive part of the Lennard-Jones potential was not studied before. So we could not compare our values to other published data. However, the melting temperature and the interfacial free energy of Lennard Jones system was already obtained for a pressure of P^* = -0.01 [91, 93, 178]. The value of the orientationally average interfacial stiffness γ_0 was found to be 0.362 [178] and

0.360 [93]. In this work, and for the classic LJ system, a slightly higher value was obtained (0.372). A slightly higher value of the melting temperature was obtained as well (0.770) compared to the existing data (0.620[178] and 0.617[93]). Note that at $P^* = 1$ in ref.[224], T_m^* was found to be equal to 0.7. These higher values could be caused by the higher pressure used in the present work (P^*=1). Furthermore, in ref.[93], the coexistence conditions were studied for a Lennard-Jones system with different P^*. It can be noticed from Table 3.6 that our value for the melting temperature seems consistent with the reported values since it can be situated between the melting temperatures found in literature for pressures above and below the pressure used in this work.

T_m^*	P^*
0.61	-0.02
0.77 (this work)	1 (this work)
1.0	4.95
1.5	12.9

Table 3.6: The coexistence conditions (the melting temperatures T_m^* corresponding to the pressure P^*) obtained for the LJ potential from ref. [93], and the coexistence condition obtained in this work at P=1.*

Both the interfacial stiffness $\tilde{\gamma}$ and the interfacial free energy γ_0 values are reported in Table 3.5. The interfacial free energy $\tilde{\gamma}$ is clearly interesting since its anisotropy is an order of magnitude larger than the anisotropy of the interfacial free energy[97, 178]. The values reported in Table 3.5 reveal an increase of γ_0 and $\tilde{\gamma}$ upon increasing the attractive part of the potential. We may particularly notice a significant increase of 23% in the interfacial free energy γ_0 from the increase of

the attraction term from l^*= 0.1 to l^*= 1.05 potential (see Fig. 3.2). This increase is also coupled to an increase of anisotropy. We also found for all the studied potentials that $\tilde{\gamma}_{(210)[001]} < \tilde{\gamma}_{(100)[001]} < \tilde{\gamma}_{(110)[1\bar{1}0]}$ except for the l^*= 0.1 potential where $\tilde{\gamma}_{(210)[001]} = \tilde{\gamma}_{(100)[001]}$.

This result is in line with the values obtained by Morris et al.[178] for the (210)[001] and $(110)[1\bar{1}0]$ orientations. However, in their study they found that (100)[001] has the smallest value of $\tilde{\gamma}$. It should be mentioned that Broughton et al.[91] also obtained different values of the anisotropy than of those of Morris et al.[178] which indicates the delicacy of the calculation of this parameter.

6 A comparative insight on the nucleation and induction times as obtained from the CNT equations and from direct MD simulations

At a first step, the nucleation times were calculated by the equations provided by the CNT as described in chapter 1 since all the parameters needed were determined ($\Delta G, \gamma, D, T_m, \rho_{cx}, \rho_{lq}$). We defined an estimated steady state nucleation time t^*_{nuc} by the time needed to form one critical nucleus in a system. This time can be calculated from:

$$t^*_{nuc} = \frac{1}{NV^*} \qquad 3.22$$

where $N = A(T) \cdot exp\left[-\frac{\Delta G^*}{k_b T}\right]$ is the steady-state nucleation rate (see Chapter 1) and V^* is the volume of the system.

Most of theoretical estimations of the nucleation rates are often restricted to the steady-state regime. However, as described in the CNT, the steady-state nucleation takes place after the so-called incubation time or transient time noted t^*_{trans} in the following. This time is required for the system to reach the steady-

state equilibrium after a quench[81] and during this regime nucleation becomes time-dependent. The overall characteristic time of the nucleation is thus controlled by the addition of the steady state nucleation time t^*_{nuc} and the transient time t^*_{trans}. Some disagreement between experimental measurements and CNT predictions may originate from this transient time[55, 79, 80] that is often overlooked.

From the CNT, the transient time can be expressed as[55]:

$$t^*_{trans} = \frac{n^{*2}}{4\beta^*} \qquad 3.24$$

where n^* is the number of atoms in the critical nucleus and $\beta^* = 24Dn^{*2/3}\rho_{lq}^{2/3}$ (see Chapter 1).

In this work, t^*_{nuc} and t^*_{trans} were calculated for the three studied potentials and compared to the nucleation times $\langle t^*_{cx} \rangle$ obtained directly from MD simulations. Since the crystallization can be observed due to the simplicity of the models, the nucleation time $\langle t^*_{cx} \rangle$ was determined by quenching large systems (108 000 particles) at different temperatures and waiting the necessary time for a germ to appear. The appearance of a crystalline germ was detected by the sudden decrease of the potential energy of the system (Fig.3.11). This procedure was repeated 10 times at different temperatures T^* in order to obtain an average value of the simulated nucleation time $\langle t^*_{cx} \rangle$. Fig.3.12 shows $\langle t^*_{cx} \rangle$ for the three studied potentials as function of $(T_m - T)/T_m$.

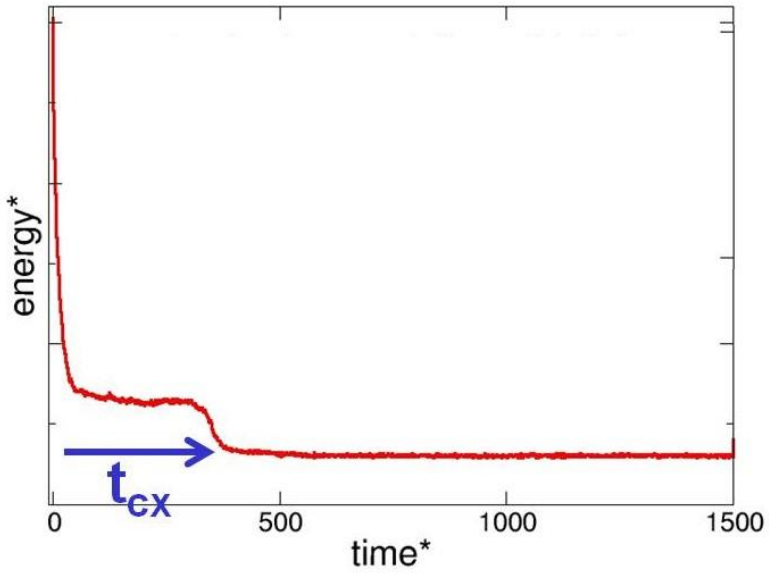

Fig.3.11: An example of the evolution of the potential energy as function of the simulation time after a rapid quench from a high temperature to a low temperature below the melting temperature. Nucleation time $\langle t_{cx}^* \rangle$ is estimated from the sudden drop of the potential energy. Note that the first drop at very short time is just due to the sudden change of temperature.

The shape of the curves indicates the existence of a minimum nucleation time. It is the analogous in time of a bell shaped nucleation rate (chapter 1). The three curves show a minimum $\langle t_{cx}^* \rangle$ for an approximate undercooling of $0.38T_m$ as expected for Lennard-Jones systems[79, 80]. For moderate undercoolings, from $0.28T_m$ to $0.35T_m$, the simulated nucleation times $\langle t_{cx}^* \rangle$ change by about 2 orders of magnitude whereas the variation of $\langle t_{cx}^* \rangle$ varies only by one order of magnitude between $0.35T_m$ and $0.6T_m$. It can also be noted that a change in the attractive of the interaction potential also slightly influence the nucleation times. Indeed, Fig.3.12 shows that the nucleation times decrease with the attractiveness of the potential i.e. $\langle t_{cx}^* \rangle$ decreases from the less attractive potential l* = 0.10 to the most attractive one l*=1.05. This trend does not fit with the behavior observed for the evolution of the interfacial free energy γ (see table 3.5) which increases upon increasing the

interaction potential. Unlikely, this trend of the interfacial free energy would suggest the opposite and an enhanced difficulty to crystallize. However, the evolution of $\langle t_{cx}^* \rangle$ is well in line with the evolution of the driving force ΔG_v (see Fig.3.5). Indeed, a higher driving force is found for the more attractive potential. The overall crystallization trend can be explained by the fact that the nucleation barrier $\Delta G^* \sim \frac{\gamma^3}{\Delta G_v^2}$ depends on the interplay between the interfacial free energy γ and the driving force ΔG_v. This latter physical ingredient thus seems to dominate the crystallization process for the investigated systems. Its variations are more important from one potential to the other compared to the change found for the values of the interfacial free energies between the different potentials which are actually quite close (γ_0=0.35 ϵ/σ^2, 0.37 ϵ/σ^2 and 0.43 ϵ/σ^2 for l^*=0.1, 0.95 and 1.05 respectively).

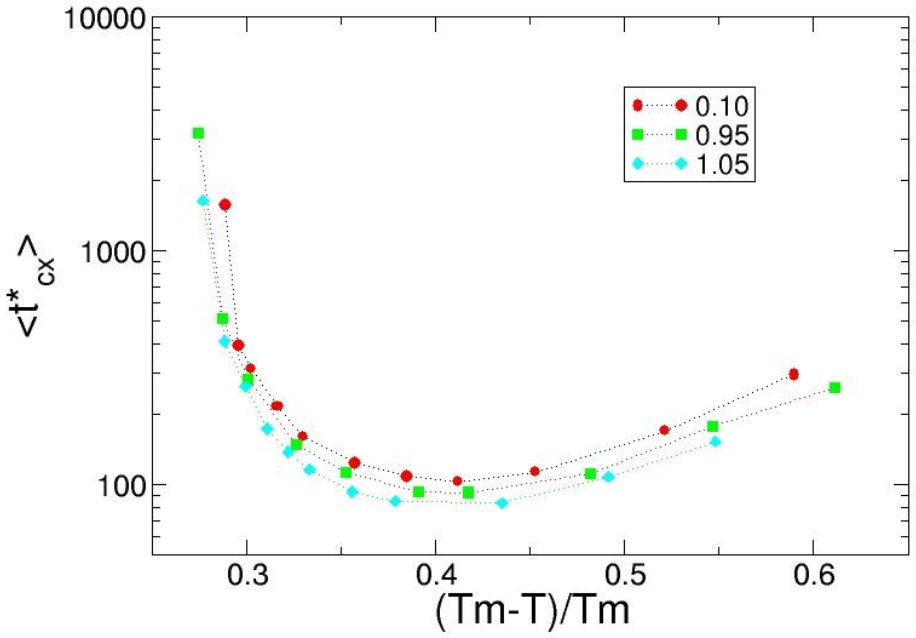

Fig.3.12: The average nucleation time $\langle t_{cx}^* \rangle$ as obtained from MD simulations for the three studied potentials.

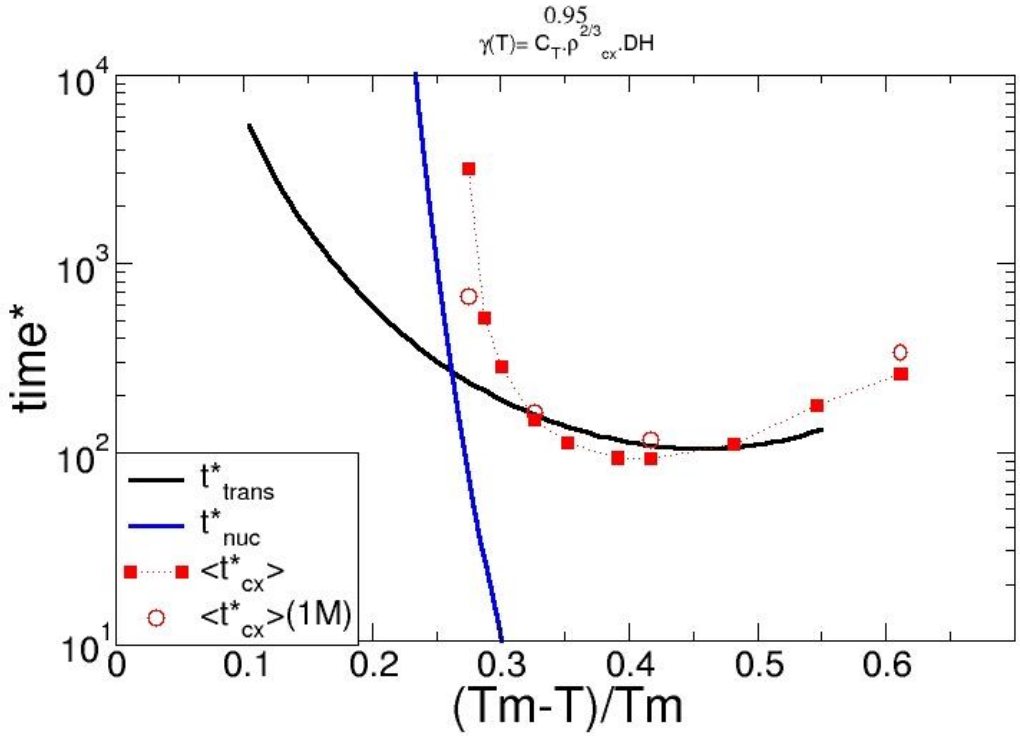

Fig.3.13: Comparison of the calculated transient t^*_{trans} and steady-state t^*_{nuc} nucleation times with the simulated nucleation times $\langle t^*_{cx} \rangle$ for the 0.95 potential using the temperature dependant mode $\gamma(T) = C_t \Delta H(T) \rho^{\frac{2}{3}}_{cx}(T)$ as function of the reduced undercooling $(T_m - T)/T_m$. The system size was also studied by comparing the simulated times for nucleation of a system containing 1 million atoms (empty red circles) and a system containing 108 00 atoms (red squares).

The overall shape of the evolution of $\langle t^*_{cx} \rangle$ will be analyzed in the following by a comparison with the transient t^*_{trans} and steady-state t^*_{nuc} times. In Fig.3.13, we compare the steady-state nucleation time t^*_{nuc} and the transient time t^*_{trans} to the simulated time $\langle t^*_{cx} \rangle$ for the l^*= 0.95 potential. It can be noticed that two main important regimes are represented. The first regime is observed at

low undercoolings where the steady state nucleation time t^*_{nuc} is longer than the transient time t^*_{trans} which can be neglected in this region. However, in deep and intermediate undercoolings, t^*_{trans} is longer indicating that it is going to dominate the nucleation process. The crossover between the two domains occurs approximately at a reduced undercooling of 0.27 which is well in line with 0.33 which is the value obtained from the calculations done for LJ sytems[79]. A similar behavior was observed for the other potentials and the other modes of the interfacial free energy but we presented the 0.95 potential here in order to compare it to the LJ potentials studied in the literature[79, 80]. This figure might also explain the discrepancies between the experimental data and the theoretical predictions of the CNT[7, 226, 227] that does not take into account the transient time which dominates at intermediate and deep undercoolings. It can be also mentioned that the size effect was studied by calculating $\langle t^*_{cx} \rangle$ for a system containing 1 million atoms (red circles). No major differences were found between the two sizes tested.

Test of some models for the temperature dependence of the interfacial free energy

Three different models describing possible evolution of the temperature-dependent interfacial free energy have been checked by comparing the t^*_{trans} and $\langle t^*_{cx} \rangle$ for the three tunable interaction potentials (Fig.3.14). We made a comparison using the transient time t^*_{trans} instead of the steady-state time t^*_{nuc}, since t^*_{trans} dominates t^*_{nuc} over a larger domain in the investigated temperature range. In the following, we have compared: a temperature independent model $\gamma(T) = \gamma(T_m)$, a model of linear dependence of temperature $\gamma(T) = \gamma(T_m) \cdot T/T_m$ and a temperature dependent model inspired from the Turnbull equation $\gamma(T) = C_t \Delta H(T) \rho_{cx}^{2/3}(T)$[79, 80] . For this latter potential, the constant C_t is determined from

the value calculated at the melting temperature i.e. $C_t = \frac{\gamma(T_m)}{H(T_m)\rho_{cx}^{2/3}(T_m)}$. In the present study, we found C_t= 0.26, 0.29 and 0.31 for l^* = 0.10, 0.95 and 1.05 respectively.

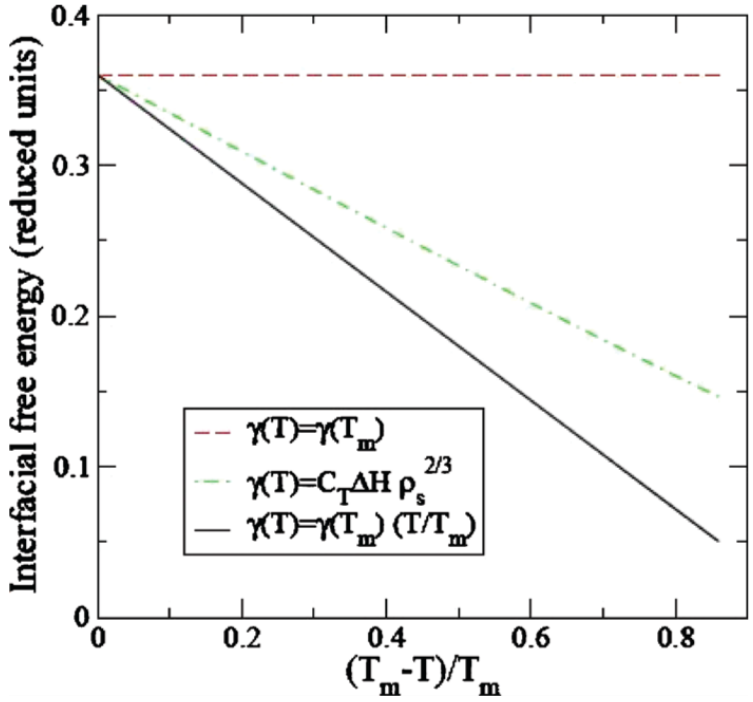

Fig.3.14: The three temperature dependant modes used in this study to compare $\langle t_{cx}^* \rangle$ to the calculated transient and steady-state nucleation times[79, 80].

The transient times for nucleation t_{trans}^* of the three different potentials are compared to the simulated nucleation times $\langle t_{cx}^* \rangle$ in Fig.3.15 for the different temperature-dependent interfacial free energy. The overall behavior of the different curves t_{trans}^* is found similar with the presence of a minimum close to the temperature at which the nucleation time $\langle t_{cx}^* \rangle$ shows a minimum too. We may also clearly notice that for the $\gamma(T) = \gamma(T_m)$ model (no temperature dependence) the nucleation t_{trans}^* are significantly longer compared to the other models as expected. For the two other models, the interfacial free energy decreases when temperature decreases which facilitates nucleation. We found that the linear

temperature dependence model $\gamma(T) = \gamma(T_m) \cdot T/T_m$ seems to produce a better agreement with $\langle t_{cx}^* \rangle$. This temperature-dependence model was particularly able to reproduce the decreasing nucleation times t_{trans}^* with the increasing of the potentials attraction at the minimum. This is not the case for the two other studied models. The use of the model inspired from the Turnbull relation $\gamma(T) = C_t \Delta H(T) \rho_{cx}^{2/3}(T)$ gives the opposite trend. This may be understood from the peculiar evolution of the difference in enthalpy $\Delta H(T)$ between the enthalpy of the liquid and solid state that crosses unexpectedly for the different interaction potentials described previously (see Fig.3.6).

7 Conclusion

In this chapter, we studied the effect of the attractive part of the inter-particle interaction potential on the crystallization capability of some simple LJ-like potentials models. The construction of tunable potentials allowed us to investigate specifically the influence of the attractive part of the potential while fixing the repulsive part. The simplicity of these systems also enabled us to observe directly crystallization. It was thus possible to compare crystallization rates with predictions from the classical nucleation theory in both the transient and steady-state regimes. This work has required MD simulations of the liquid and crystalline phases separately and also biphasic systems to calculate interfacial properties. The main parameters involved in the CNT were directly computed such as driving force ΔG, melting temperature T_m, interfacial free energy γ, densities of the crystalline and liquid phase (ρ_{cx}, ρ_{lq}) and the coefficient of diffusion D.

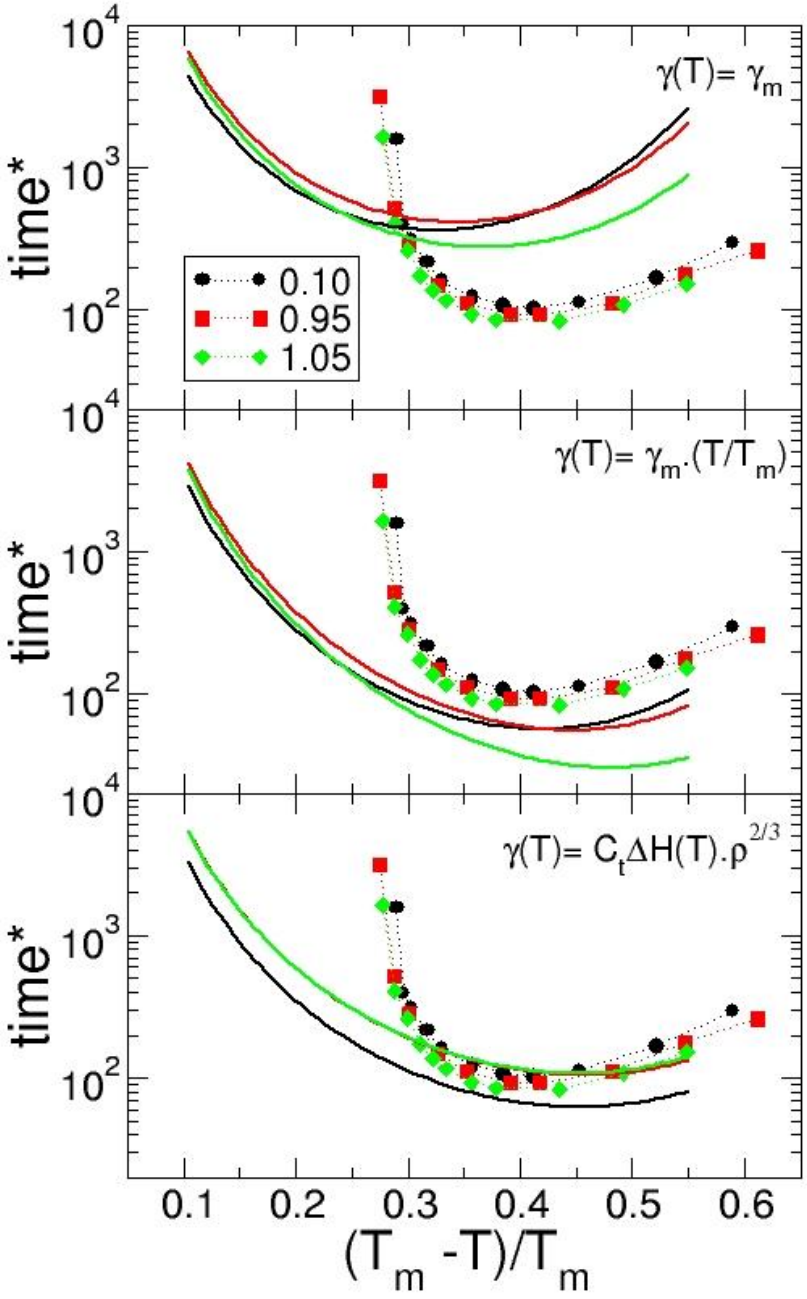

Fig.3.15: The calculated transient times from the CNT for nucleation t^*_{trans} (solid lines) of the three studied potentials compared to the simulated nucleation times $\langle t^*_{cx} \rangle$ obtained directly (symbols) as function of the reduced undercooling $(T_m - T)/T_m$ using the three interfacial temperature dependent models: $\gamma(T) = \gamma(T_m)$, $\gamma(T) = \gamma(T_m) \cdot T/T_m$ and $\gamma(T) = C_t \Delta H(T) \rho_{cx}^{2/3}(T)$[79, 80].

We found that the attractive part of the potential has an influence more or less significant on all calculated parameters. As expected for a pure van der Waals system, the increase of the attractive part of the potential results in an increase of density for both liquid and crystalline phases. Accordingly, diffusion thus also logically decreases. The increasing of the attraction increases the driving force ΔG and shifts the melting temperature to higher values due to the need to bring more heat to the system to break forces responsible for the cohesivity of the crystal. It is found that the interfacial free energy at the melting temperature, which is comparable to a form of tension, reasonably increases when the attractive part of the potential increases. All these parameters monotonically evolve with the variation of the form of the potential. The difference in enthalpy between liquid and crystal $\Delta H(T^*)$ was shown to exhibit a non-monotonic behavior but we have no clear explanation at the moment for this marked difference.

We have pointed out that a change in the attractive part of the interaction potential slightly influences the nucleation times. The nucleation times decrease with the attractiveness of the potential. This trend matches well with the evolution of the driving force ΔG_v but not with the interfacial free energy γ which behaves in an opposite trend. This result highlights the importance of the relative interplay of each parameters on the nucleation barrier $\Delta G^* \sim \frac{\gamma^3}{\Delta G_v^2}$. The driving force seems to dominate in the present study.

An overall fair agreement is found between the direct estimation of the nucleation times and prediction of the nucleation times from the CNT. The need for a temperature-dependent interfacial free energy $\gamma(T)$ is revealed from different tests performed. Calculation of both characteristic times of the transient and steady-state regimes allowed providing a thorough analysis of the directly

determined nucleation times. Two different behaviors of the nucleation times were observed as function of the undercooling. For small undercoolings, the steady state nucleation time is much longer than the transient time for nucleation while at intermediate and deep undercooling the transient time is much longer. It can be noted, that at small undercoolings, the result point out to the possibility of reaching the experimental regime where the transient time can be neglected. However, at intermediate and deep undercoolings, the transient time should not be neglected while predicting the homogeneous nucleation times since it dominates over the steady-state nucleation time. At small undercoolings, the nucleation time, i.e. the steady state nucleation time, increases abruptly which make it difficult to simulate due to the long simulation times needed. Overall, the transient time seems to dominate mostly the investigated temperature range. This may explain, at least partially, the disagreement found between predictions from CNT and direct measurements of the crystallization times.

This investigation thus demonstrates the possibility to obtain reasonable crystallization tendencies from CNT predictions by computations of the main involved physical ingredients (driving force, interfacial free energy and diffusion). Hence, in the following chapter, we will apply the same method on more realistic systems like pharmaceuticals while avoiding a direct simulation of the crystallization which can be very time consuming (or even impossible on computer time scales) specially for complex systems.

Chapitre 4 Prediction of the crystallization tendencies of pharmaceutical products

Despite its importance to theoretical models and practical applications, predicting the ability of a given material to vitrify or crystallize remains a challenging problem. This is a very important issue for the development of amorphous pharmaceuticals which particularly requires a fundamental physical understanding of the stability of the amorphous state against crystallization. In this chapter, we will investigate the crystallization tendencies of three different polymorphic pharmaceutical products (nifedipine, felodipine and indomethacin). These drugs usually serve as model systems for studying the crystallization of organic compounds. In addition, they exhibit a rich crystalline polymorphism and polymorphic selectivity of crystallization is observed depending on temperature[228]. Using the methods described in the previous chapters, we will estimate the different thermodynamic and kinetic factors influencing the nucleation/growth rates via MD simulations and guidance by the classical nucleation theory (CNT) predictions and different growth mechanism models (normal, two-dimensional, and screw dislocation). Such numerical predictions are not very common in the literature.

This chapter is divided into two main sections. Section 1 provides a comparative study of the crystallization tendency from the melt of felodipine (I and II) and nifedipine (α and β) polymorphs. In section 2, the study of the crystallization tendency of indomethacin polymorphs (α and γ) is reported. In each section a detailed description of each compound is given including some comparisons between structural, dynamical and thermodynamical properties

obtained by our MD simulations with the experimental values. For each system, we particularly focused our investigations on the calculations of the Gibbs free energy difference between the liquid and the crystal ΔG, the coefficient of diffusion D and the crystal-liquid interfacial free energy γ. A comparative study of the nucleation/growth rates of each compound is then discussed followed by a general conclusion.

The main results obtained for nifedipine and felodipine have been published in The Journal of Physical Chemistry B **2015**, *119*, 10768−10783.

1 Crystallization tendencies of nifedipine and felodipine

1.1 Description of the nifedipine and felodipine systems

Nifedipine $C_{17}H_{18}N_2O_6$ [3,5-dimethyl 2,6-dimethyl-4-(2-nitrophenyl)-1,4-dihydropyridine-3,5-dicarboxylate] (Fig.4.1) is a calcium-channel blocker used in the treatment of cardio-vascular diseases[5, 229], for the long-term treatment of hypertension, angina pectoris[230] and as vasodilating drug of the dihydropyridine type[231].

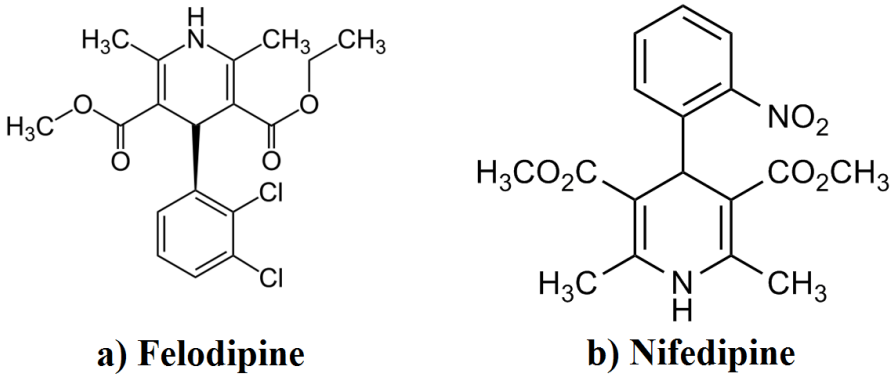

Fig.4.1: Chemical structure of felodipine (a) and nifedipine (b).

Confusion still remains in the literature on the polymorphism of nifedipine even thought it has been studied for more than a decade[5, 45, 47, 229, 232-236]. It is characterized by a high photosensitivity, a low aqueous solubility[235], a suitable product for crystallization growth rate studies[47], and a model for studying the crystallization of organic compounds[5, 229, 236]. Eckert et al[234] first identified three monotropically polymorphs (I-II-III) where the form I is the most thermodynamically stable polymorph. Chan et al[236] identified three other polymorphs noted (α, β, γ) as well as Grooff et al[235] (A,B,C). The agreement exists only for the thermodynamically stable polymorph (I=α=A)[5] (Fig.4.2). The confusion comes mainly from the lack of structural data on nifedipine polymorphs[5] and the complex phase transformations during thermal treatment[229, 235]. It should be noted that the nifedipine system still represents an exceptional unsolved problem in pharmaceutical polymorphism.

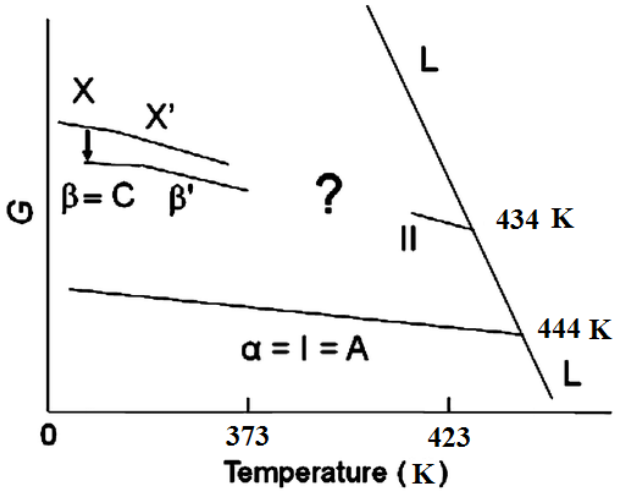

Fig.4.2: A partial phase diagram of the nifedipine polymorphs extracted from ref. [5]. The X indicates a newly obtained polymorph at 353 K which has a different crystalline structure from the β form (N_β). The question mark represents the zone of confusion. The arrow from the X polymorph to the β polymorph indicates the conversion observed at room temperature. The kinks in the β and X lines mark the reversible transitions to β' and X' respectively. The β' is likely to be the form II identified by Zhou et al[229] or the form C reported by Groof et al[235].

From the melt, three crystalline polymorphs can be obtained: a metastable form, noted β (N_β) that is preferentially obtained from the glassy state, and another metastable polymorph (the polymorph X in Fig.4.2) that crystallizes concomitantly with N_β from the supercooled melt and transforms to the β form at room temperature. The most stable form noted α (N_α) only grows preferentially above 120°C[5, 45, 47, 48].

The nucleation is a challenging task to study experimentally due to the small size of embryos and the transient nature of the nucleation process. However, Marsac et al[45] were able to obtain the nucleation rate of nifedipine and felodipine in a narrow range of temperature (294 K to 357 K) using optical microscopic observation. At different temperatures, spin-coated samples were stored inside desiccators and then removed at each time point where the determination of the nucleation site number density was made. Crystal growth on the other hand is more easily studied due to the fact that the clusters are bigger and can be spotted without any difficulties. Ishida et al[48] obtained the crystal growth rate of nifedipine (N_α and N_β) by storing a liquid film at the desired temperatures in a desiccator and tracking the growth of the crystalline particles by polarizing light microscopy. The growth rate thus reported was the average growth of at least three crystalline particles. X-Ray powder diffraction was subsequently used to identify each polymorph.

In the present work, nifedipine polymorphs N_α and N_β were studied. According to ref.[5] the melting temperature of N_α was found to be 444 K with a density of 1.379 g/cm^3 and a monoclinic crystalline structure with a space groups $P2_1/c$ while N_β has a density of 1.382 g/cm^3 and a triclinic crystalline structure with a space group $P\bar{1}$. A 434 K melting polymorph of nifedipine is well established[5, 233] (Fig.4.2) but it is still unclear which polymorph is identified with

this melting point[5]. The glass transition temperature was found to be 315 - 318 K [45, 48].

Felodipine $C_{18}H_{19}Cl_2NO_4$ [ethyl 5-methyl 4-(2,3-dichlorophenyl)-2,6-dimethyl-1,4-dihydropyridine-3,5-dicarboxylate] (Fig.4.1) is a calcium-channel blocking agent just like nifedipine. It is also widely used for hypertension treatment and prevention of angina[4]. Felodipine is characterized by its insolubility in water but also by a good permeability and a good absorption by the gastrointestinal tract[237]. Srčič et al[238] stated for the first time that felodipine possess several polymorphs, then Rollinger et al[239] characterized the two forms (F I and F II). However F II lacked of reproducibility and they weren't able to obtain any crystal structure[4, 240]. Finally, Lou et al[241] described a method to obtain single crystals of form II suitable for determination of its crystalline structure. Additional crystallization studies[4] later on discovered two more felodipine polymorphs (F III and F IV) obtained from co-crystallization in solution where F III is almost iso-energetic to F I and F IV being obtained only as isolated single crystals.

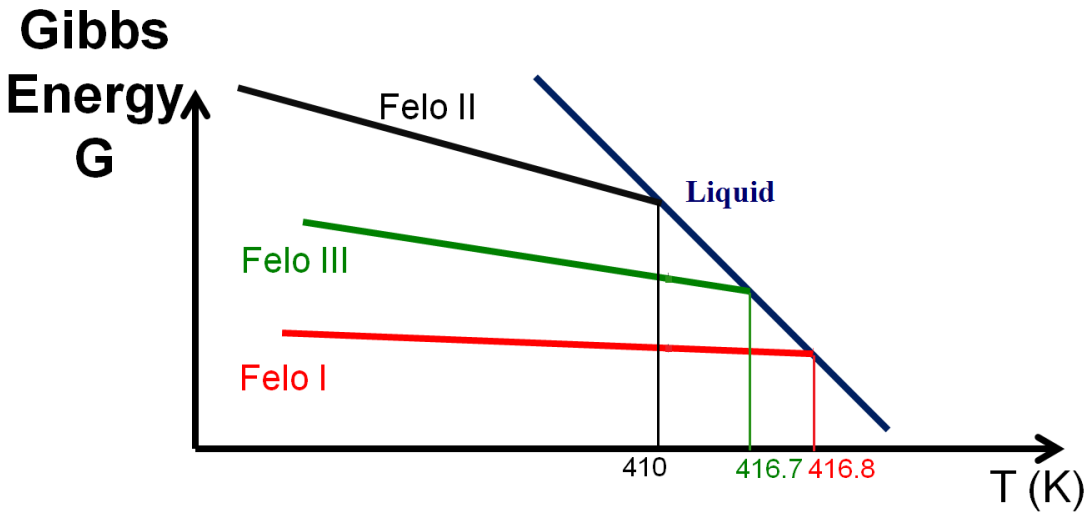

Fig.4.3: A schematic representation of the phase diagram of felodipine polymorphs based on the results from ref.[4].

Two polymorphs are currently well established and have been reported to be produced from the melt: the metastable F II that grows preferentially at all temperatures and the most stable F I that may also grow close to heterogeneities[242]. The most stable F I grows faster than the metastable F II at all temperatures[46, 106, 239]. The experimental growth rate of F I was obtained (Kestur et al. [46]) by placing the supercooled liquid in contact with felodipine form I crystals which play the role of the seed for nucleation and growth. The growth rate of F II was determined by developing crystals from the amorphous form in the absence of seeding[46]. Raman spectroscopy was subsequently used to identify each polymorph.

In this work, two felodipine polymorphs were studied (F I, F II). The most thermodynamically stable form (F I) has a melting temperature of 416.8 K (Fig.4.3) and a density of 1.451 g/cm^3 at 123 K while F II has a melting temperature of 407.8 and a density of 1.421 at 150K[4]. The crystalline structure of F I and F II is monoclinic with respective space groups $P2_1/c$ and C2/c.

1.2 Thermodynamical properties

The variations of the density as function of the temperature of each crystalline and amorphous form are represented in Fig.4.4 a) and b). Main crystallographic parameters with their estimated values are summarized in Table 4.1. These densities are compared to the experimental values at 300 K for N_α and N_β, at 120 K for F I and at 150 K for F II . The cell parameters and the densities were reproduced correctly by the force field GAFF with a maximum deviation of 0.02 g/cm^3 in comparison with the experimental values. We were able to superheat N_α, F I and F II to an approximate temperature of 600 K, about 150 K above their experimental melting point. N_β was superheated to an approximate temperature of 550 K, 100 K above its experimental melting point. As mentioned in chapter 3, the

possibility to largely superheat originates from the periodic boundary conditions in MD simulations that stabilize the crystal structure. At temperatures higher than 600 K, the density decreases brutally indicating the disappearance of the crystalline structure in the simulation box.

Cell parameter	N_α	N_β	F I	F II
a Å (exp)	10.92	9.86	12.09	32.39
a Å (sim)	10.97	9.85	12.14	32.37
b Å (exp)	10.33	13.89	12.08	18.71
b Å (sim)	10.37	13.73	12.13	18.70
c Å (exp)	14.81	14.29	13.42	23.77
c Å (sim)	14.86	12.40	12.11	23.75
α° (exp)	90	61.22	90	90
α° (sim)	90	61.22	90	90
β° (exp)	92.7	79.82	116.13	91
β° (sim)	92.7	79.82	116.13	91
γ° (exp)	90	81.78	90	90
γ° (sim)	90	81.78	90	90
Density mg/m^3 (exp)	1.38 (at 300 K)	1.36 (at 300 K)	1.45 (at 123 K)	1.42(at 150 K)
Density mg/m^3 (sim)	1.37 (at 300 K)	1.37 (at 300 K)	1.44 (at 123 K)	1.41(at 150 K)

Table 4.1: Summary of the simulated (sim) and experimental[4, 5] (exp) crystalline properties of nifedpine and felodipine polymorphs along with their densities.

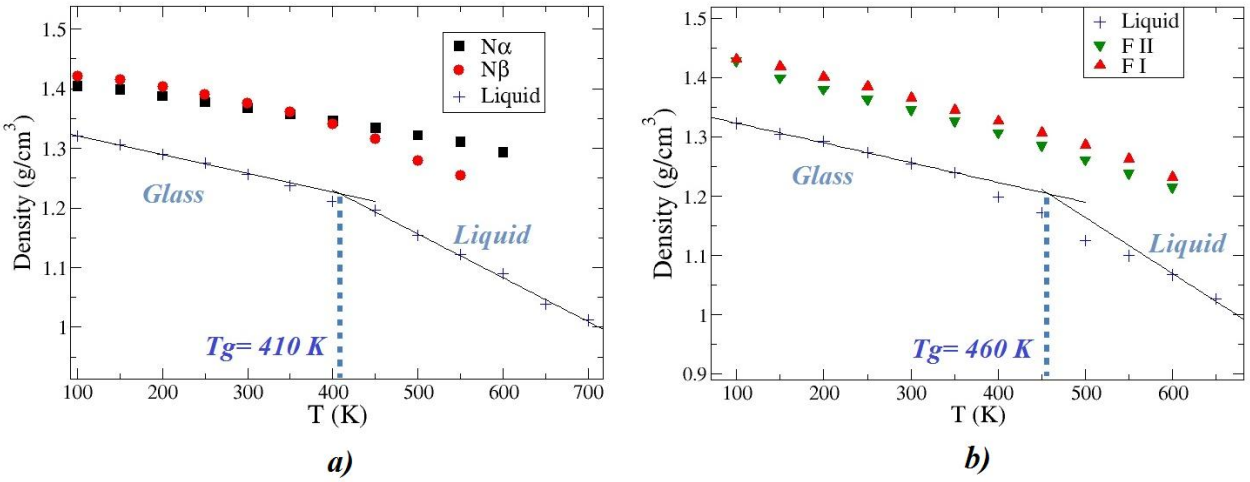

Fig.4.4: Representation of the crystalline and amorphous densities of a) nifedipine and b) felodipine polymorphs versus T(K). A linear adjustment at high and low temperature (straight lines) enabled the estimation of the glass transition temperature $T_g(sim)$.

The liquid densities of nifedipine and felodipine were not reported experimentally. As a consequence, we were unable to compare our simulation results with experimental values. However, the liquid density values at low temperature (the glassy state) are reasonable in comparison to the density of the crystalline forms $\left(\frac{\rho_{cx}-\rho_{glass}}{\rho_{cx}} \approx 10\%\right)$. The evolution of the amorphous densities, in the glass and in the liquid state, as function of the temperature enabled us to determine the simulated glass transition temperature for both compounds. The simulated T_g was equal to 410 K and 460 K for nifedipine and felodipine respectively with a respective overestimation of 90 K and 140 K compared to the experimental T_g that was found to be about 318-319 K[45] for both compounds. The overestimations were expected since the cooling rate in MD simulations is extremely fast (~10^{11} °C/sec) compared to experimental usual rates (~ 10°C/min).

The fast cooling rate used in MD simulations originates from the intrinsic small time-step of the order of the femtosecond required to integrate the Newton's equation of motions (see details in chapter 2).

The calculated $T_g(sim)$ is expected to be always higher than the experimental one $T_g(exp)$. The difference between the simulated values and the experimental ones (T_g(sim)- T_g(exp)) can be understood using the Williams-Landel-Ferry[243] (WLF) $log_{10}\left[\frac{\tau(T_g(\text{sim}))}{\tau(T_g(\text{exp}))}\right] = \frac{-C_1(T_g(\text{sim})-T_g(\text{exp}))}{C_2+(T_g(\text{sim})-T_g(\text{exp}))}$. Assuming reasonable values $\tau(T_g(\text{exp})) \approx 100$ s, $\tau(T_g(\text{sim})) \approx 100$ ps and using the so-called universal values $C_1 \approx 17.44$ and $C_2 \approx 51.6$ K, it is possible to estimate that T_g(sim)- T_g(exp) ≈ 115 K which is well in line with the differences found for liquid nifedipine and felodipine.

Fig.4.5 shows an example of the evolution of the total density of a biphasic system of the crystalline N_α polymorph in contact with its melt at different temperatures. The numerical melting temperatures T_m(sim) were estimated to be 448 K, 445 K, 426 K and 410 K for N_α, N_β, F I and F II respectively. The overestimations ranged from 4 K to 10 K compared to the experimental values[4, 5, 45] (see Table 4.2). The uncertainties on the melting point values were estimated to be +/- 10 K. This error bars were deducted from the density versus time plots where a difference of 10 K was needed to distinguish between the crystallization of the system (increasing density) or the melting of the system (decreasing density).

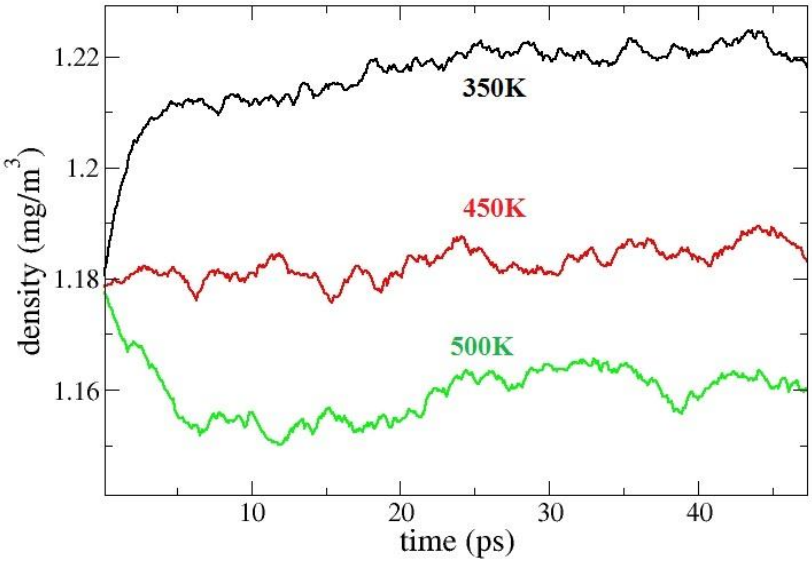

Fig.4.5: Evolution of the density of the biphasic crystal/liquid of N_α system as function of time at three different temperatures. The increase or decrease of density indicates crystallization and melting respectively.

Fig.4.6 a) and b) present the evolution of the enthalpies as function of temperature for the crystalline and the liquid phases for nifedipine and felodipine polymorphs. The enthalpies of fusion ΔH_m were estimated to be 43.9 kJ/mol, 43.5 kJ/mol, 31.8 kJ/mol and 29.3 kJ/mol for N_α, N_β, F I and F II respectively (see Table 4.2). The overestimations were between 0.3 kJ/mol and 3 kJ/mol compared to the experimental values[4, 45]. We were unable to compare the simulated value of N_β to experience since the polymorphism of nifedipine is not yet completely understood[5]. The calculation of the enthalpy of fusion of the N_α polymorph was performed using three different simulation boxes (with different sizes: 4644, 55040 and 110080 atoms) in order to check the possible size effects and validate the accuracy of the method. The error bars were estimated at +/- 3 kJ/mol.

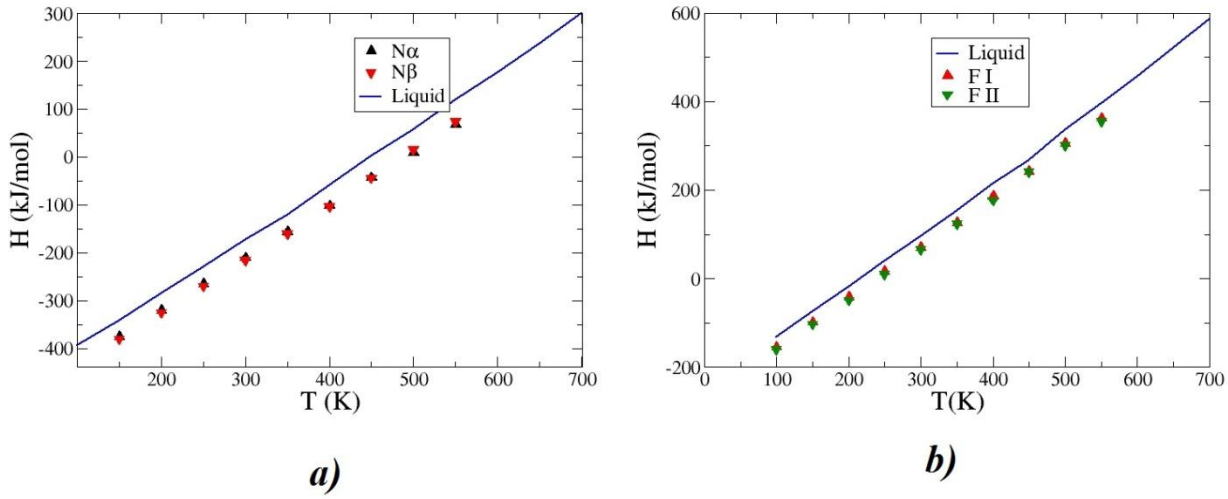

Fig.4.6: Evolution of the enthalpy for the different polymorphic forms and the liquid of a) nifedipine and b) felodipine.

In order to estimate the Gibbs free energy difference ΔG between the liquid and crystal states as function of temperature for the different investigated systems, we used the Hoffman equation[35]. It is given by:

$$\Delta G = \Delta H_m \frac{(T_m - T)T}{T_m^2} \qquad 4.1$$

where ΔH_m and T_m are the simulated melting enthalpy and temperature obtained as described previously. This equation was already shown to reproduce with good agreement the experimental data for nifedipine and felodipine respectively[45]. Fig.4.7 shows the evolution of the driving force ΔG as function of temperature. The expected tendency is obtained for the different systems and their respective polymorphs[4, 5, 45]. It is a direct consequence of the fair agreement obtained for ΔH_m and T_m compared to the experimental data as reported in Table 4.2. In Fig.4.7, one particularly may notice that we were able to reproduce the experimental tendencies of all the systems from the most to the less stable

following this order: N_α, N_β, F I and F II. The greater this number, the greater the tendency for crystallization confirms that the thermodynamic driving force for crystallization of nifedipine is greater than that for felodipine. However, if we compare two polymorphs from the same compound, the crystallization tendency is not reproduced since the metastable phase has a lower ΔG. Hence, the driving force alone cannot be used to predict the crystallization tendencies. Other parameters should also be considered like the interfacial free energy γ and the coefficient of diffusion D as it will be shown in the following.

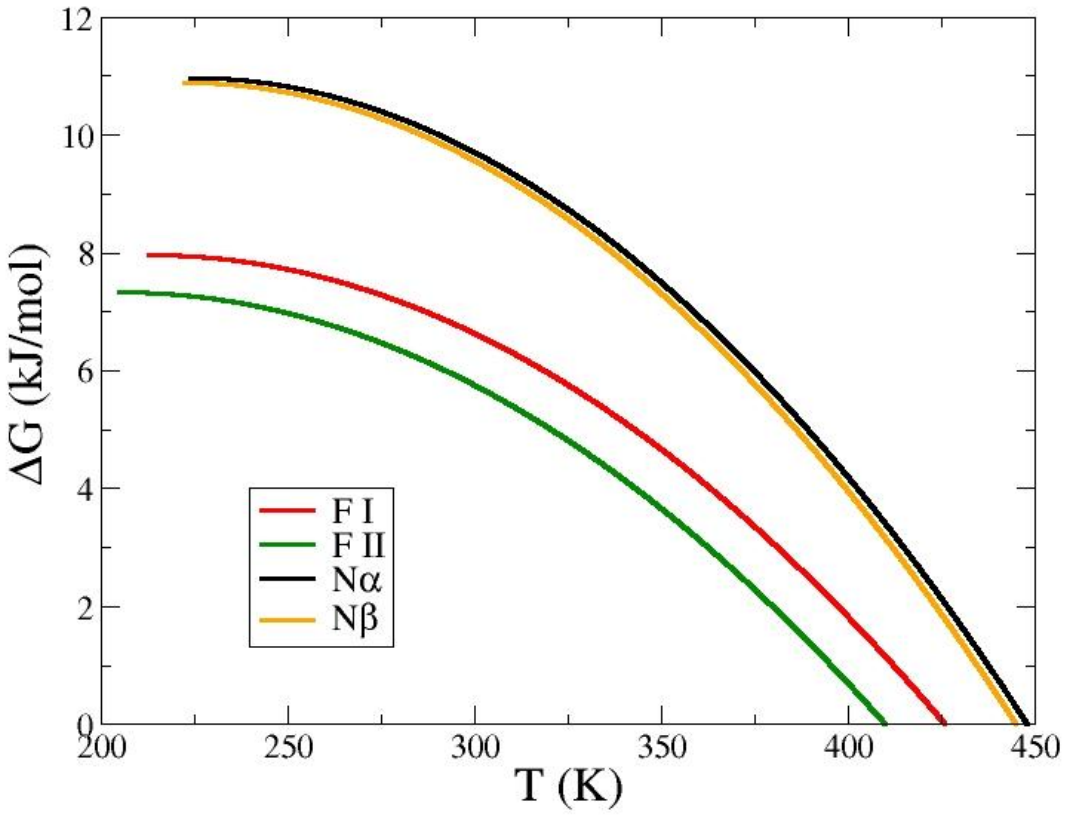

Fig.4.7: The free energy difference between the liquid state and the crystal state as predicted by the Hoffman equation using T_m and ΔH_m determined from MD simulations for the different investigated nifedipine and felodipine polymorphs (see table 4.2).

The value of the interfacial free energy was obtained by using the capillary fluctuation method described in Chapter 2. This method consists on the simulation of the interface at equilibrium and at the melting point and the calculation of the fluctuations of the position of the crystal-liquid interface (see Fig.4.8). An order parameter (q_6 as described in Chapter 2) is used in order to distinguish between the liquid and solid molecules and thus determining the height function $h(x)$. Subsequently, by the intercepts of the plots of $< |h(q)|^2 >$ (the power spectrum of $h(x)$) versus q, the interfacial free energy is determined. Fig.4.9 a) and b) shows the linear behavior of $ln(< |h(q)|^2 >)$ as function of $ln(q)$ at small q for felodipine and nifedipine polymorphs respectively which indicates that the interface is indeed rough[178]. At larger q, the values of $< |h(q)|^2 >$ deviates from this linear behavior; we can conclude that in this region the values are sensitive to the method used to identify the height function while for the small q region the values are not. Therefore, our fits are performed in the small q region only. The interfacial free energy at the melting temperature γ_m obtained by the fitting curves was found to be γ_m= 21.5, 14.4, 28.7 and 15.5 mJ/m^2 for N_α, N_β, F I and F II respectively. The error bars are calculated taking into consideration the uncertainties on the temperature and the fitting procedure (Table 4.2).

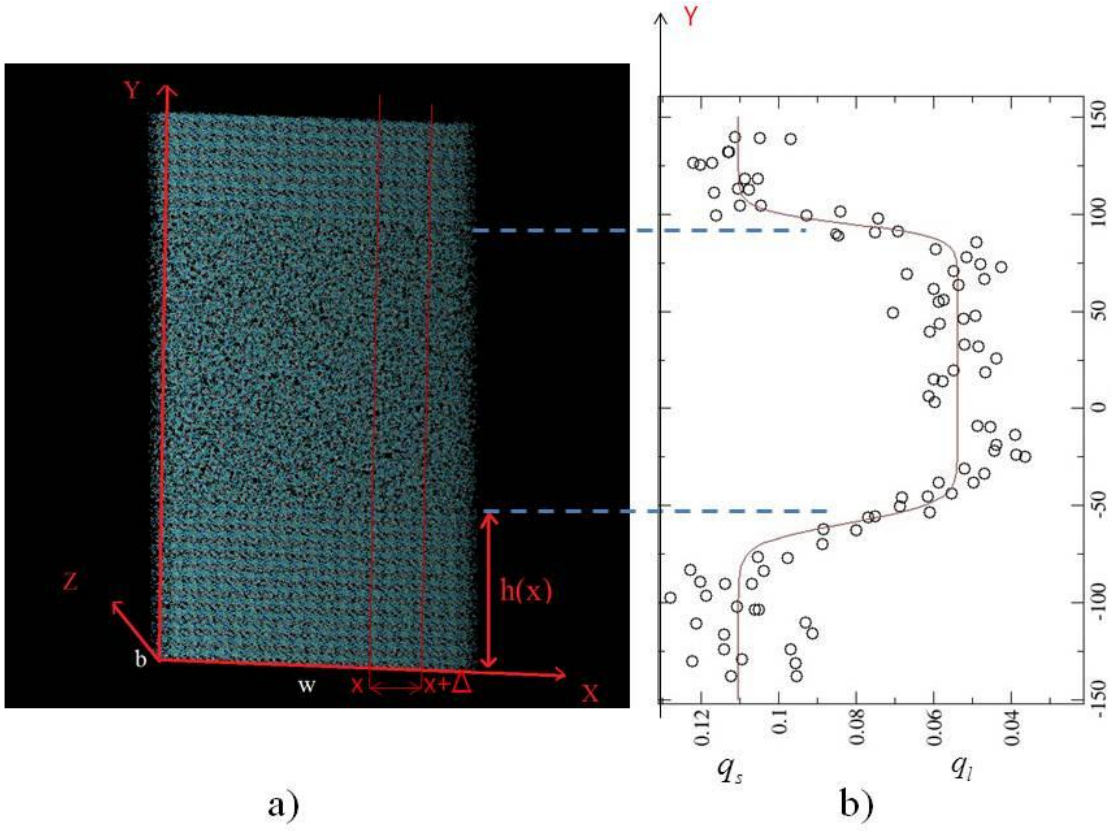

Fig.4.8: a) A snapshot of a simulation box used to determine the interfacial stiffness of felodipine F II. The interface is parallel to the (xz) plane. The system size is as follow: $w = Lx = = 224.31$ *Å,* $b = Lz = 26.05$ *Å and* $Ly = 283.20$ *Å.* Lx*,* Ly *and* Lz *are the dimensions of the whole simulation box along the* x*,* y *an z directions. b) Evolution of the order parameter* $< q_6 >$ *along the direction orthogonal to the interface (y). The line indicates the fitting using equation 2.33.*

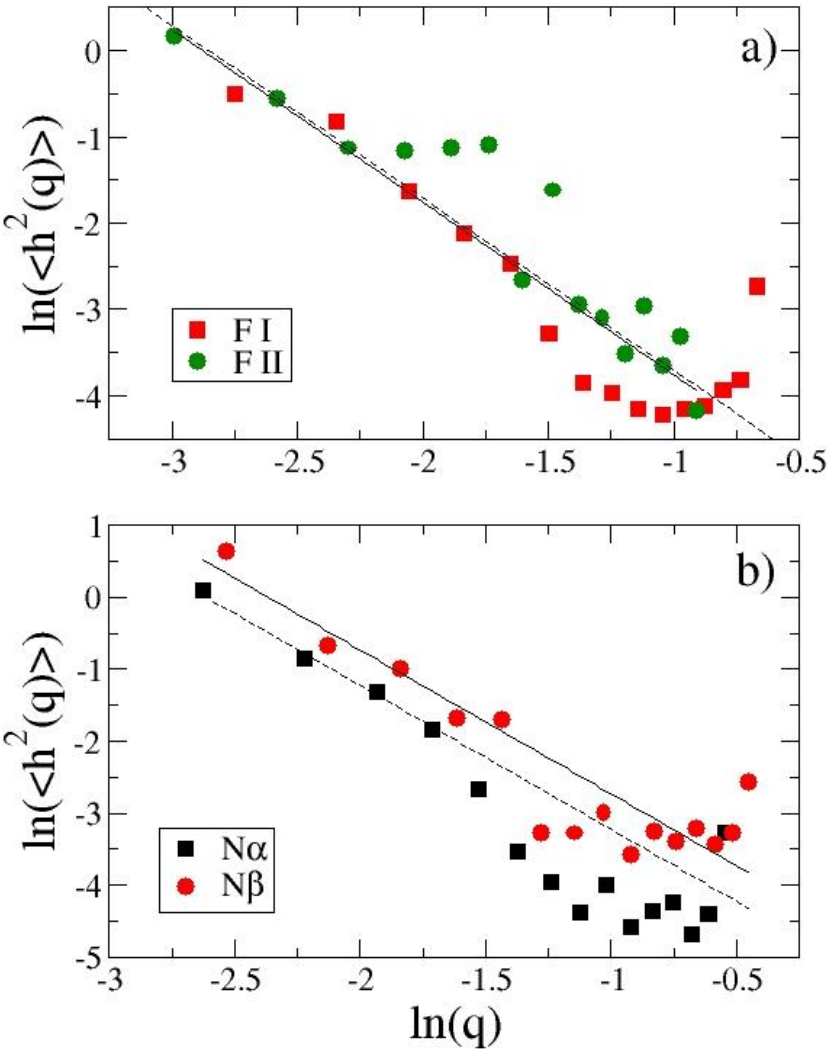

Fig.4.9: The fluctuation spectrum $< |h(q)|^2 >$ of the interface height $h(x)$ for felodipine F I and F II (a) and nifedipine N_α and N_β (b). The solid lines represent fits to the simulation results using equation 2.28. The fit is limited to the small q range. It corresponds to the domain where equation 2.28 is valid and thus in which the plot $ln(< |h(q)|^2 >)$ vs $ln(q)$ has a slope with the value -2. For larger values of q, this equation is no longer valid since the wave length becomes commensurate with the crystal lattice spacing. For larger values of q, the straight line thus deviates significantly with data points.

For both nifedipine and felodipine compounds, the interfacial free energy are clearly the highest for the more stable polymorph (see Fig.4.7). Indeed, since at the crystal-liquid interface, the surface of a less stable phase is likely to be more disordered than the surface of a most stable one, hence the interfacial free energy is likely to be smaller. This trend is also well in line with the well-known Ostwald rule of stage [75] suggesting that the crystal phase that nucleates is not the most thermodynamically stable phase but rather another metastable phase that is closest in Gibbs free energy to the parent phase. Moreover, in Table 4.2 one may notice that the interfacial free energy of the metastable nifedipine N_β is significantly smaller than the values obtained for all felodipine polymorphs. Such result appears very reasonable in explaining why nifedipine may crystallize more easily than felodipine as reported in many investigations[45]. We were unfortunately unable to compare our simulated values to experimental ones since no data are available for nifedipine and felodipine. However, the present obtained values are of the same order of reported data on other similar molecular compounds [39, 244]. For example, for indomethacin polymorphs, Andronis and Zografi[30] estimated using nucleation rates, the interfacial free energy 27 mJ/m^2 and 17 mJ/m^2 for the stable γ form and the metastable α form respectively. They also found that the interfacial free energy follows the Oswald rule of stages: γ is higher for the stable polymorph than the metastable one. It can be also noted in the present numerical study that the trend of the crystal-liquid interfacial free energies between the different polymorphs is not completely consistent with the evolution of the melting entropies $\Delta S_m = \frac{\Delta H_m}{T_m}$. Indeed, for the metastable polymorph, one finds a significant smaller value of the interfacial free energy compared to the most stable one but the melting entropy is roughly the same for the two polymorphs (see Fig.4.7). Some additional investigations are being performed at the moment to understand this discrepancy.

To our knowledge, no other values of the interfacial free energy were determined for pharmaceuticals. Few values have been reported for molecular compounds such as 7.0 mJ/m^2 for succinonitrile [38], 7.9 mJ/m^2 for neopentylglycol [39], 2.8 mJ/m^2 for pivalic acid [245], 4.6 mJ/m^2 for cyclohexane [246] and 10 mJ/m^2 for carbon tetrabromide [89].

Polymorph	ρ_{cx}(exp) [4, 5] /ρ_{cx} (sim) (at T(K)) (g/cm^3)	T_m (exp) [4, 5] /T_m(sim) (K)	ΔH_m(exp) [4, 5, 45] / ΔH_m (sim) (kJ/mol)	γ_m (sim) (mJ/m^2)
Nifedipine α (N_α)	1.38 /1.37 (283-303)	444/ 448	39.9 / 43.9	21.5±1.6
Nifedipine β (N_β)	1.39-1.36 /1.37 (296-298)	- / 445	- / 43.5	14.4±1.0
Felodipine I (F I)	1.45/1.44(123)	416/426	31.5 / 31.8	28.7±2.5
Felodipine II (F II)	1.42/1.40(150)	416/410	29.1 / 29.3	15.5±1.2

Table 4.2: Comparison between experimental data (exp) and simulation data (sim) obtained using the GAFF[135] force-field for nifedipine α and β and felodipine I and II crystal polymorphs. The exp and sim between parentheses indicate the experimental and the simulated values respectively. ρ_{cx},T_m,ΔH_m and γ_m represents the density, the melting temperature, the enthalpy and the interfacial free energy at the melting temperature respectively. Uncertainties of the interfacial free energy γ_m have been estimated from taking into consideration the uncertainties on the melting temperature (10K) and the fitting procedure of equation 2.28.

1.3 Transport properties (D and η)

The diffusion coefficient D, which is the translational diffusion of the center of mass of molecules, and the shear viscosity η of nifedipine and felodipine in the equilibrated liquid state as a function of temperature T are shown in Fig.4.10. Upon decreasing temperature, both transport properties show the classical deviation from an Arrhenius behavior which is a typical behavior of the so-called fragile glass-formers[108]. A fair agreement is found with experimental data for viscosity[25]. Very similar mobility for both nifedipine and felodipine liquids, as measured by values of D and η, are found at all temperatures covered by MD simulations which is in line with data reported in the literature[45]. This result is consistent with the same experimental glass transition temperature $T_g \approx$ 304-318 K that has been particularly found for both pharmaceuticals[25]. However, in the high temperature range investigated from MD simulations, molecular mobility of nifedipine is found a bit lower than felodipine. It is opposite to the trend observed experimentally at lower temperatures either from viscosity measurements or dielectric relaxation spectroscopy data for which felodipine relaxation times are about one decade longer than nifedipine ones. This disagreement between the simulation and the experiments can be a consequence of the inability of the GAFF force field to reproduce dynamics with sufficient accuracy. However, from the trend reported from experimental viscosity measurements (see Fig.4.10 a) one may reasonably also speculate about a possible crossover between felodipine and nifedipine dynamics that may occur from high to low temperatures.

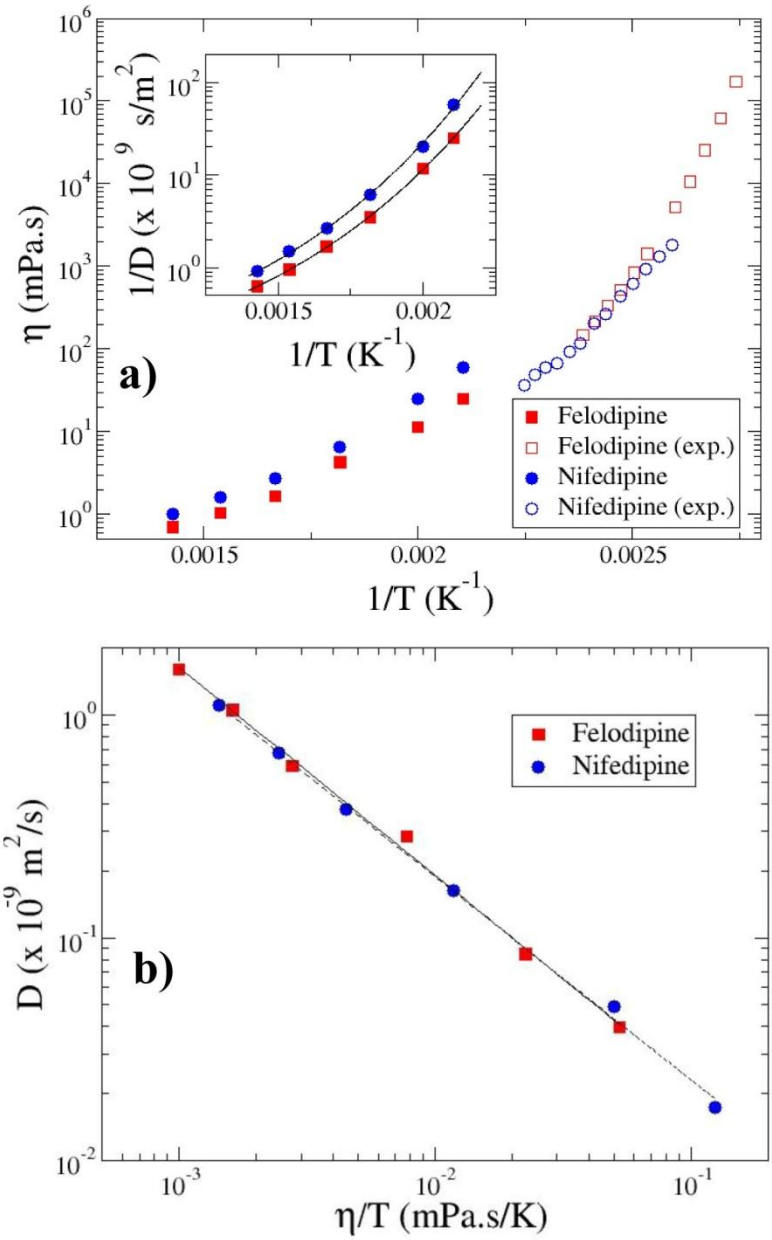

Fig.4.10: a) Evolution of the shear viscosity and diffusivity (in inset) as a function of the inverse of temperature for nifedipine and felodipine in the liquid state. The diffusion coefficients are determined from the long term evolution of the mean square displacement ($< r^2(t) > \sim 6Dt$ see Chapter 2). Shear viscosity η has been computed from the stress-stress autocorrelation functions (See chapter 2). In inset, solid lines indicate fits using equ. 2.34 ($ln\left(\frac{1}{D}\right) = A_1 + \frac{A_2}{T} exp\left(\frac{A_3}{T}\right)$) A_1 = 18.17, A_2 = 491.37 K and A_3 = 874.81 K are obtained for nifedipine while A_1 = 18.03, A_2 = 445.84 K and A_3 = 874.81 K are obtained for felodipine. b) The linear behavior with a slope equal to -1 of D vs η/T shows the validity of the Stokes-Einstein relation at high temperatures.

In the simulated high temperature range, both diffusion coefficient and shear viscosity follow similar temperature dependence. This link between these two transport properties is well described by the Stokes-Einstein relation $D \sim \eta/T$ [247] which was shown to be perfectly valid in our case (Fig.4.10 b)). Inspired by this similarity and in order to fit the diffusion coefficient as a function of temperature, a similar approach as described in reference[142] for viscosity was used (using equation 2.34). It has been suggested that this alternative relation to the usual Vogel-Tamman-Fulcher-Hesse (VFTH) equation was particularly able to reproduce very well both high and low temperatures ranges[247]. It thus provides a possibility to estimate diffusivity in the low temperature range below the melting temperature required to estimate the kinetic pre-factor involved in the CNT. Results of the fitting procedure are shown in the inset of Fig.4.10 for which very similar fitting parameters are obtained for both compounds (see caption Fig.4.10).

1.4 Nucleation and growth of nifedipine and felodipine

In this section, the nucleation and growth of N_α , N_β , F I and F II will be studied and compared to the experience since only these polymorphs have been reported to appear from the melt[46, 48]. As mentioned before, the main parameters involved in nucleation as described by the CNT, i.e. ΔG_v ,γ, D and the liquid and crystal densities were calculated from the present MD simulations (see above).

Prediction of the nucleation tendencies

The steady-state nucleation rate N can be thus estimated from the expression (as mentioned in Chapter 2):

$$N = A_N(T) \cdot exp\left[-\frac{\Delta G^*}{k_b T}\right] \qquad 4.2$$

where $A_N(T)$ is the kinetic pre-factor and $\Delta G^* = \frac{16\pi}{3}\left[\frac{\gamma^3}{\Delta G_v^2}\right]$ is the nucleation barrier. ΔG_v is the Gibbs energy difference between the liquid and crystal states per unit volume. The pre-factor is usually expressed as $A_N(T) = Z \cdot n_{lq} \cdot \frac{24\mathrm{D}n^{*2/3}}{\lambda^2}$ where λ is the atomic jump distance approximated to ${1/n_{lq}}^{1/3}$ in the following, n^* is the number of atoms in the critical nucleus, n_{lq} is the number density of liquid, $Z = (\Delta G_v/6\pi k_B T n^* n_{cx})^{1/2}$ is the Zeldovich factor and n_{cx} is the number density of solid. We could write as well $n^* = (4/3)(\pi {r^*}^3 n_{cx})$ and $r^* = 2\gamma/\Delta G_v$where r^* is the critical radius of the nucleus.

In table 4.2, both the melting enthalpy and the interfacial free energy of nifedipine and felodipine polymorphs are reported. At first glance, by comparing melting enthalpy and interfacial free energies of both compounds, it seems difficult to reconcile the higher values of the melting enthalpy found for nifedipine with their lower interfacial free energies. Polymorphs of the same compound show similar melting enthalpy but quite different interfacial free energies although the trend seems in agreement with Turnbull law $\gamma_m = C_T \cdot \Delta H_m \cdot \rho_{cx}^{2/3}$considering a similar density for both polymorphs. In other words, it thus seems that Turnbull relation may not be applicable in our case with the same Turnbull coefficient C_T which was found to be about 0.45 for most metals, 0.32 for semi metals and water[38]. Other studies showed that this coefficient, for metallic alloys, ranges from 0.13 to 1[77] or from 0.21 to 0.77[39] for other variety of materials (camphene, benezene, lauric acid, stearic acid, dibromobenzene…). In our calculations, we have estimated C_T values for each compound to be 0.28, 0.40, 0.44 and 0.75 for N_β, N_α, F II and F I respectively. A similar calculation made for the indomethacin polymorphs using data taken from[30] would give us C_T values of about 0.43 for the

α polymorph and 0.59 for the γ polymorph close to the values obtained in the present study.

Several works have mentioned the possible temperature dependence of the crystal-melt interfacial free energy[248] and the need to use an effective temperature dependent interfacial free energy has been shown from MD simulations to reproduce nucleation rates in the framework of the CNT[79, 80, 249-253]. There are good reasons, related to the entropy loss due to ordering of the liquid near the interface, suggesting that the interfacial free energy could increase with T [7]. In the following, we have assumed the arbitrary following form suggested in ref.[80] which has been inspired from the Turnbull law for the temperature dependence of the interfacial free energy:

$$\gamma(T) = \gamma_m \cdot \left[\frac{\rho_{cx}(T)}{\rho_{cx}(T_m)}\right]^{2/3} \cdot \left[\frac{\Delta H(T)}{\Delta H_m}\right] \qquad 4.3$$

Using this form, the parameter C_T is different for each investigated compound. Fig.4.11 shows the steady state nucleation rate N obtained from the CNT as function of temperature for the different investigated polymorphs. Nucleation rates N are represented as function of the undercooling $\Delta T = T_m - T$ in order to facilitate the comparison between the different polymorphs. This representation also allows correcting from the slight disagreement between the experimental and numerical melting temperature.

All nucleation curves show the same expected behavior. The nucleation rate N can be first described by a sharp increase upon cooling due to the increasing driving force and then a decrease upon further cooling to low temperatures due to the decreasing molecular mobility (diffusivity). Curves thus show a clear maximum. The value of this maximum significantly increases in the following order: F I, F II,

N_α and N_β. The present results thus confirm the much more favorable nucleation tendency of nifedipine with respective to felopidine as observed experimentally [45].

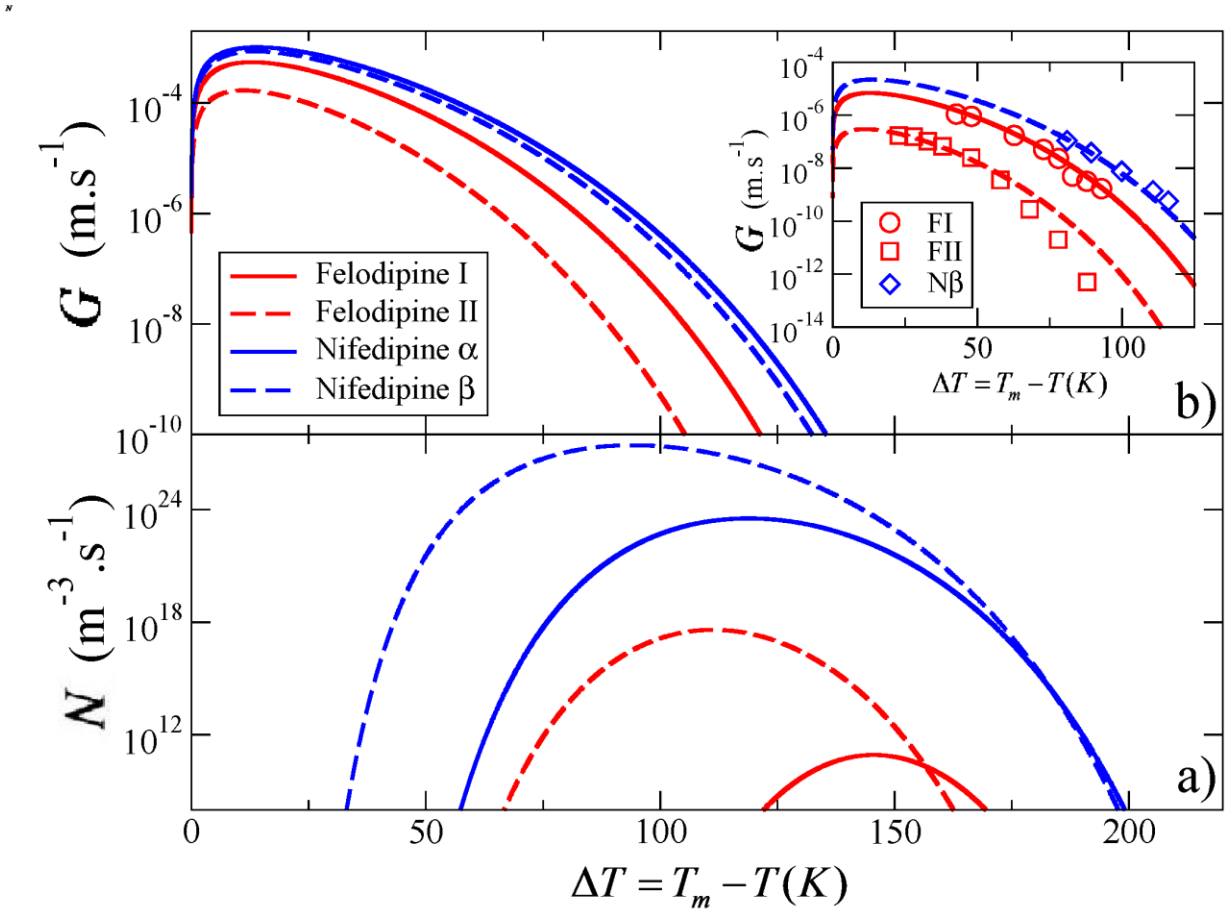

Fig.4.11: Predicted evolution of the nucleation N (a) and growth G (b) rate as function of temperature of the different investigated nifedipine and felodipine polymorphs. A comparison between experimental (symbols) and numerical data is also given in inset (b). Constant parameters 1/k = 60, 570 and 39 have been used to rescale numerical growth rate in order to fit with experimental values using a growth model with f = 1. (See equation 4.5) Experimental data for nifedipine N_β and felodipine F I and F II were extracted respectively from[48] and [46].

Fig.4.11 also clearly suggests nucleation of the predominant metastable nifedipine β polymorph as observed in spontaneous crystallization[5] and well in line with the Oswald rule of stage. The fact that nifedipine crystallizes more readily

than felodipine was mainly attributed to the higher driving force for crystallization for nifedipine than felodipine since both molecules have a very similar mobility and glass transition temperature [45]. The same argument cannot be applied while comparing polymorphs of the same molecule since, for monotropic systems, the driving force of the more stable phase is higher than the metastable phase for all temperatures. Our results show clearly an inverse correlation between the increasing value of γ and the decreasing maximum nucleation rate (see Fig.4.11) for each polymorph. The order observed for the maxima of nucleation (F I, F II, N_α and N_β) can be mainly explained by the influence of the interfacial free energy that acts as a barrier for nucleation.

However, the nucleation tendencies cannot be determined only by the interfacial free energy since γ of N_α is higher than γ of F II but the nucleation rate of N_α is much higher. In that case, the higher driving force of N_α should explain its higher nucleation rate. For other compounds having approximately the same mobility but different crystallization rates[19, 232] as felodipine and nifedipine, it could be suggested that crystallization is controlled by the interplay between ΔG_v and γ. This result is well in line with the nucleation barrier ($\Delta G^* \sim \frac{\gamma^3}{\Delta G_v^2}$) as predicted by the CNT.

Prediction of the growth tendencies

The general mathematical form for the crystal growth rate can be summarized as follows (as mentioned in Chapter 1):

$$G = k \cdot A_G(T) \cdot f(T) \cdot \left[1 - exp\left(-\frac{\Delta G}{k_b T}\right)\right] \qquad 4.4$$

where k is a temperature independent constant, $A_G(T)$ (unit : m.s^{-1}) describes the molecular mobility and has been approximated by $\frac{\mathrm{D}\cdot\mathrm{a}}{\lambda^2}$ in the following where a is the average width of the crystal lattice spacing ($\mathrm{a} \approx 1/{n_{cx}}^{1/3}$). The last two terms represents thermodynamics of the growth process. $f(T)$ is a dimensionless function depending on the growth mechanism at the interface. The last term represents the probability of attachment/detachment of molecules to the crystal nucleus. It only plays a significant role at relatively small undercooling and it approaches unity at large undercooling.

Experimentally, an adapted plot representing the reduced growth $G/\left[A_G(T)\cdot\left(1-e^{-\Delta G/k_bT}\right)\right]$ against undercooling $\Delta T = T_m - T$ may allow discriminating between these three models [2, 30, 33, 58, 242]. In most cases, the inverse of the liquid viscosity $1/\eta(T)$ instead of diffusivity D is supposed to provide a reliable description of the molecular mobility $A_G(T)$. For indomethacin, growth by two-dimensional nucleation has been found to be applicable[30] from such approach. However, recent works by Wu and Yu[58] have also shown that viscosity may not accurately reproduce molecular mobility upon deep cooling owing the breakdown of the Stokes-Einstein relation. Use of a fractional Stokes-Einstein relation[36] where η^{ξ} ($\xi < 1$) is used instead of η particularly allow to show that growth is diffusion-controlled at larger undercooling ($f \approx 1$). Same behavior has been also found for other molecular materials such as ortho-terphenyl[58].

The growth rate G as function of the temperature has been calculated from the present simulations for the different models of growth suggested above. The simplest model $f \approx 1$ (normal growth see Chapter 2) is found to reproduce better the experimental data as represented in inset of Fig.4.11 for three different

polymorphs: F I & F II and N_β at relatively deep undercooling. It is interesting to notice that this simple model particularly allows reproducing the decreasing order of the growth rate: F I, F II, and N_β. Moreover, it is also consistent with the approach used to calculate the interfacial free energy which assumes that the interface is rough on a microscopic scale. However, it should be also noted that the interface free energy has no explicit effect on the growth rate in this case. Dislocation-controlled growth cannot be also totally discarded although agreement is less good. Growth by two-dimensional nucleation has not been found to be applicable even though it seemed the most reasonable. Indeed, it has been suggested [2, 30, 33] that for most materials with high melting entropies like felodipine $\Delta S_m = \Delta H_m/T_m$ = 9.10 R and nifedipine 10.80 R, the mechanism of growth occurs by two dimensions nucleation. The use of the expression $f = exp\left[-\frac{\pi \cdot a \cdot \gamma^2}{k_b T \cdot \Delta G_v}\right]$ associated with this type of growth is strongly dependent on the interfacial free energy γ. It is not thus possible to reconcile the decreasing order determined value of the interfacial free energy γ_m for the F I, F II and N_β polymorph: 28.7, 15.5 and 14.4 mJ/m^2 with the decreasing order of the growth rate. As already mentioned above, same behavior relative to the entropies of fusion has been also reported by Wu and Yu[58] on both indomethacin polymorphs.

Fig.4.11 shows the growth rate for the different investigated polymorphs including polymorph N_α for which experimental data are not available. This figure evidently shows the expected well-expressed maximum in the growth rate G originating from the increase of the thermodynamical driving force on one hand and the decrease of the mobility on the other hand. It can be noted that the maximum growth is localized at small undercooling as classically observed and

offers an interesting parameter to compare crystallization of various compounds as shown in [28].

Interestingly, and perhaps more importantly, is the comparison between both nucleation N and growth G rate. Taking into account the exponential dependence of both N and G upon temperature and the distance between maxima, glass-forming or crystallization capability can be discussed. Fig.4.11 a) and b) clearly confirm that glass-formation is to be expected for felodipine since the curves representing the temperature dependencies of nucleation and growth do not significantly overlap. In contrast, crystallization of the melt is favored for nifedipine since the nucleation and growth curves significantly overlap compared to the curves of felodipine. In other words, both nucleation and growth are favorable in a wider range of temperature for nifedipine which enables the crystallization of this compound and explains the fact that it crystallizes more readily than felodipine.

1.5 Conclusion

By means of MD simulations, the liquid and the crystalline state of felodipine and nifedipine as well as the crystal-liquid interface have been investigated in order to predict their nucleation and growth tendencies from the melt. Two polymorphs of nifedipine (N_β, N_α) and felodipine (F I, F II) have been studied. Calculations were performed on liquid and crystal systems separately in order to determine their main physical properties: density, enthalpy and diffusivity. Biphasic crystal-liquid simulations enabled the calculation of the melting temperatures and the interfacial free energies γ_m at the melting temperatures of the different polymorphs.

A fair agreement was found between the simulation results and the known experimental data such as the crystal densities, the melting temperatures, the enthalpies and the molecular mobility confirming the ability of the force field GAFF to reproduce accurately the experimental data of both compounds. Similarity of the molecular mobility of felodipine and nifedipine is particularly confirmed. The driving force for crystallization has been estimated showing a higher driving force for nifedipine with respect to felodipine as suggested in experiments.

The values of the crystal-liquid interfacial free energy at the melting temperature have been determined. Using the capillary fluctuation method, γ_m = 21.5, 14.4, 28.7 and 15.5 mJ/m^2 have been obtained for N_α, N_β, F I and F II respectively. The interfacial free energy γ was found to increase with the polymorph stability where the metastable forms have always a smaller interfacial free energy than the stable forms in agreement of the Ostwald rule of stage and the melting entropies.

From the estimation of D, γ and ΔG, the nucleation and the growth rates were calculated in the frame work of the CNT and by using different growth modes (normal, 2D and screw dislocation). Having a similar mobility (D), the nucleation and growth rates seem mainly controlled by the interplay between γ and ΔG which is consistent with the amplitude of the nucleation barrier ($\Delta G^* \sim \frac{\gamma^3}{\Delta G_v^2}$) as predicted by the CNT. We found that the higher interfacial free energy of felodipine polymorphs might be an additional reason for its resistance to crystallization compared to nifedipine, other than its lower driving force. The low value of γ of N_β compared to the other polymorphs seems the origin of its higher

nucleation rate and to its larger overlapping of nucleation and growth curves. However, the nucleation tendencies are not only controlled by the interfacial free energy since γ of N_α is higher than γ of FII but the nucleation rate of N_α is much higher. In that case, the higher driving force of N_α should explain its higher nucleation rate. A fair agreement was found between numerical and experimental growth rates suggesting a mechanism of normal growth as already shown for indomethacin assuming a fractional Stokes-Einstein dependency between viscosity and diffusivity in that case. Other growth mechanisms do not seem able to fit the experimental growth rate order (N_β < F I < F II) owing the present calculated interfacial free energy.

Despite a reasonable trend in the nucleation order it can be also noted that the nucleation rate for the different polymorphs predicted from simulations deviates by several decades from the experimental ones[45] (see below). Moreover, the predicted nucleation rates for the different polymorph are also separated by several decades which does not seem to be the case experimentally as reported in[45].

The present absolute value of the predicted nucleation rates should be thus considered with caution. An ideal situation certainly far from reality is considered in the framework of the CNT where homogeneous bulk nucleation is assumed. Moreover, a direct comparison between numerical and experimental values is also difficult since it is not clear which polymorph is nucleated in the experimental study.

As mentioned previously significant deviations between CNT predictions and experimentally measured nucleation rate are expected[81, 226]. Many checks of the CNT have been reported in the literature ranging from fair agreement to severe

disagreement [81]. Nevertheless, because of the simplicity of its formalism, it is still commonly used to analyze crystal nucleation in experiments and simulations. Origin of the discrepancies has been mostly attributed to the kinetic pre-factor rather than the nucleation barrier which is approximately correct in most cases [7]. For certain glass-formers such as sodium metasilicate glasses[226] differences by more than ten orders of magnitude have been reported. The direct determination of the kinetic prefactor from MD simulation in the nucleation rate is found to be some two orders of magnitude larger than predicted by classical nucleation theory[227]. In the present investigation, the nucleation rate is strongly influenced by the value of the interfacial free energy. In contrast, we checked that a small change in the diffusivity D or the driving force ΔG have more less influence on the nucleation rate than γ.

As reported in ref. [253], a small change of a few percent in the value of the interfacial free energy γ can significantly alter by several decades the nucleation rates N. In order to evaluate the sensitivity of the interfacial free energy on the nucleation rate N, we have recalculated the nucleation rate N owing the $\Delta\gamma/\gamma_m \approx$ 7-8% uncertainties obtained on the value of the interfacial free energy γ_m determined in the present study using the present fluctuation methods. In other words, we have computed nucleation rate using either an estimated maximum or minimum of the interfacial free energy using $(\gamma + \Delta\gamma)$ and $(\gamma - \Delta\gamma)$ respectively. We have also compared the nucleation rate N previously determined with the mathematical form given in equation 4.2 with a behavior using a constant value $\gamma(T) = \gamma_m$ owing the same uncertainties.

Figures 4.12 a) and b) show the nucleation rate N obtained using the two different models $\gamma(T)$. The general trend of the nucleation rates is found similar using both models following the order of decreasing maximum nucleation rate: N_β,

N_α, F II, and F I. One may particularly notice the overall higher nucleation rate of the metastable β polymorph of nifedipine due to its lower value of the interfacial free energy 14.4 mJ/m^2. In contrast, using the $\gamma(T) = \gamma_m$ model, the nucleation rate of felopidine FI polymorph becomes so low that it cannot be represented on the Fig.4.12 a) since this polymorph possesses the highest value of the interfacial free energy 28.8 mJ/m^2.

Despite same trends, significant shifts by several orders or magnitude are obtained using the different models depending on the absolute value of the interfacial free energy. Evidently, compounds having a higher interfacial energy are more impacted. For example, an increase of about a factor 10^3 in the maximum nucleation rate is obtained between the present temperature-dependent interfacial free energy model (equation 4.3) with respect to the use of a constant value ($\gamma(T) = \gamma_m$) for the most metastable (lower γ) N_β and F II polymorphs. An increase of about 10^9 is obtained for the most stable (higher γ) N_α and F I polymorphs.

Figures 4.12 a) and b) also show the nucleation rate N obtained taking into account the uncertainties on the values of the interfacial free energy. Since a small variation of the interfacial free energy values causes a large variation in the nucleation rates, the difference between the lower limit and the upper limit at the maximum varies significantly from 2 decades (N_β in Fig.4.12 b) to 8 decades (F II in Fig.4.12 a)). This may cause a crossing between the nucleation rates curves where in some cases the nucleation rate tendency will considerably change. For example the change in the nucleation tendency can be observed in Fig.4.12 a) where the lower limit of the nucleation rate of N_α is smaller than the upper limit of that of F II. In all considered cases, despite the interfacial free energy

uncertainties, the nucleation rate of N_β is always greater than the other polymorphs confirming its higher crystallization tendency.

To conclude, it can be noted that calculation of the nucleation rate N using a third alternative form for the interfacial free energy $\gamma(T) = \gamma_m \cdot \frac{T}{T_m}$ [79, 80] has been also performed (Table 4.3). This latter form roughly produces the same trend for felodipine and nifedipine polymorphs as obtained from equation 4.3. Table 4.3 presents a comparison of the maximum values of the nucleation rate N_{max} for three different models: $\gamma(T) = \gamma_m$, $\gamma(T) = \gamma_m \cdot \frac{T}{T_m}$ and $\gamma(T) = \gamma_m \cdot \left[\frac{\rho_{cx}(T)}{\rho_{cx}(T_m)}\right]^{2/3} \cdot \left[\frac{\Delta H(T)}{\Delta H_m}\right]$. It can be noticed that the differences in the values reported in the column 2 and 3 do not exceed 2 orders of magnitude.

Polymorph	$N_{max}(m^{-3}.s^{-1})$ with $\gamma(T) = \gamma_m$	$N_{max}(m^{-3}.s^{-1})$ with $\gamma(T) = \gamma_m \cdot \frac{T}{T_m}$	$N_{max}(m^{-3}.s^{-1})$ with $\gamma(T) = \gamma_m \cdot \left[\frac{\rho_{cx}(T)}{\rho_{cx}(T_m)}\right]^{2/3} \cdot \left[\frac{\Delta H(T)}{\Delta H_m}\right]$
Nifedipine α (N_α)	$2{,}10.10^{15}$	$6{,}01.10^{23}$	$3.34.10^{23}$
Nifedipine β (N_β)	$7{,}72.10^{15}$	$3{,}22.10^{28}$	$3{,}23.10^{27}$
Felodipine I (F I)	8.10^{-50}	$8{,}18.10^{11}$	$3{,}83.10^{10}$
Felodipine II (F II)	$5{,}45.10^{10}$	$8{,}81.10^{19}$	$8{,}84.10^{17}$

Table 4.3: A comparison of the maximum values of the nucleation rates N_{max} of the different investigated polymorphs using different models of $\gamma(T)$.

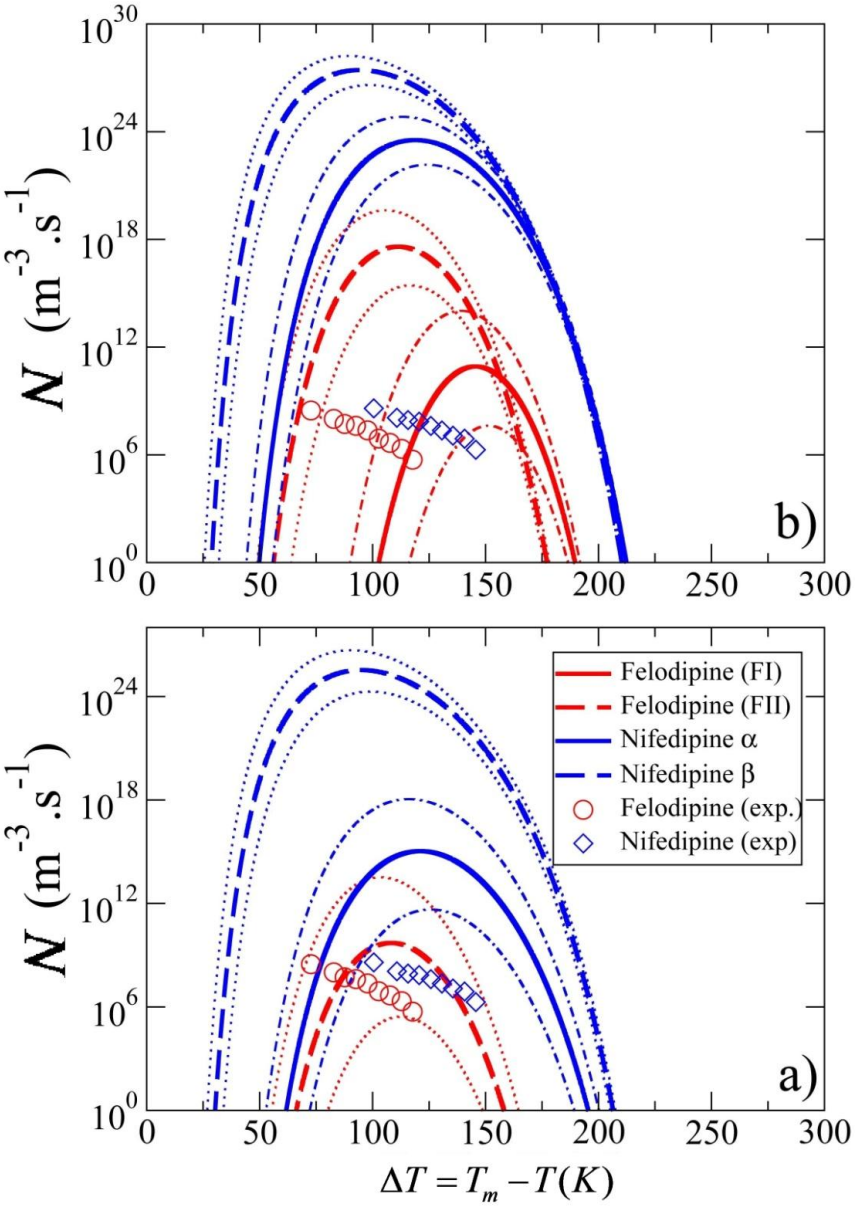

Fig.4.12: Comparison of the predicted evolution of the nucleation rate N for two temperature-dependent models of the interfacial free energy γ as function of temperature of the different investigated nifedipine and felodipine polymorphs: constant value $\gamma(T) = \gamma_m$ (a) and $\gamma(T) = \gamma_m \cdot [\rho_{cx}(T)/\rho_{cx}(T_m)]^{2/3} \cdot [\Delta H(T)/\Delta H_m]$ (b) Experimental data (symbols) extracted from[45] are also given for comparison. For each polymorphs, either dotted or dotted-dashed line indicates prediction of the nucleation rate [N] using values of the interfacial free energy $(\gamma + \Delta\gamma)$ and $(\gamma - \Delta\gamma)$. This calculation takes into the uncertainties of the calculated interfacial free energy γ of the order of $\Delta\gamma/\gamma_m \approx$ 7-8%. Using the $\gamma(T) = \gamma_m$ model, the nucleation rate of felopidine FI polymorph is so low that it is not represented on the figure (a).

2 Crystallization tendencies of Indomethacin

2.1 Description of the system

Indomethacin $C_{19}H_{16}ClNO_4$ [1-(4-chlorobenzoyl)-5-methoxy-2-methyl-1*H*-indole-3-acetic acid] (Fig.4.13) is a non-steroidal, anti-inflammatory agent with anti-pyretic and analgesic properties[254] used as a prescription medication to reduce fever, pain and swelling. It is a hydrophobic poorly water soluble drug[255], which make it a subject to different studies[30, 256, 257]. Indomethacin is a monotropic system that has two structurally solved polymorphs: the α and γ forms[258]. The γ form (I_γ) has the highest melting temperature (434 K)[30, 255] with a density of 1.38 g/cm^3 [259] and the lowest solubility making it the most thermodynamically stable polymorph[254]. While the α form (I_α) has a melting temperature of 428 K[30] with a density of 1.40 g/cm^3 [259]. Thus this system represents an inversion between the stability and the density where the metastable phase (I_α) is denser than the stable phase (I_γ) (Fig.4.13).

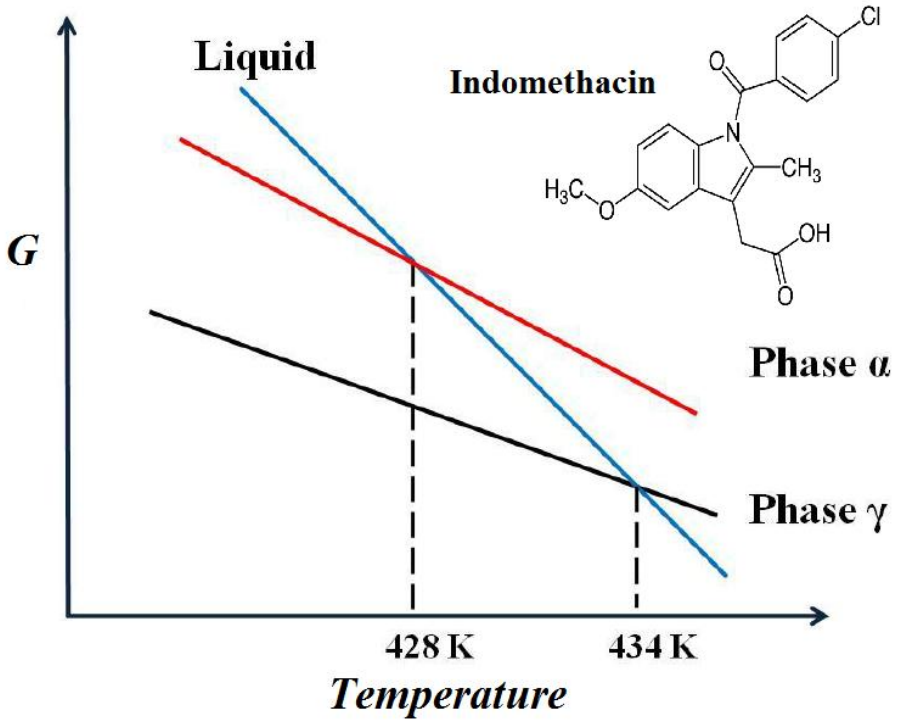

Fig.4.13: Schematic representation of the phase diagram of indomethacin using data from ref.[30].

This inversion is attributed to the local organization of the molecules of each polymorph which limits the chemical activity of the less dense phase[30, 260]. The molecules of I_γ form dimers by linking their carboxylic groups with hydrogen bonds while the molecules of I_α form trimers with two molecules linked via their carboxylic groups by hydrogen bonds and the third molecule linked via its carboxylic group to the ketone group of the closest neighbor (see Fig.4.14). This supplementary association of I_α generates a more compact crystalline arrangement and thus presents a higher density of the possible arrangement of I_γ.

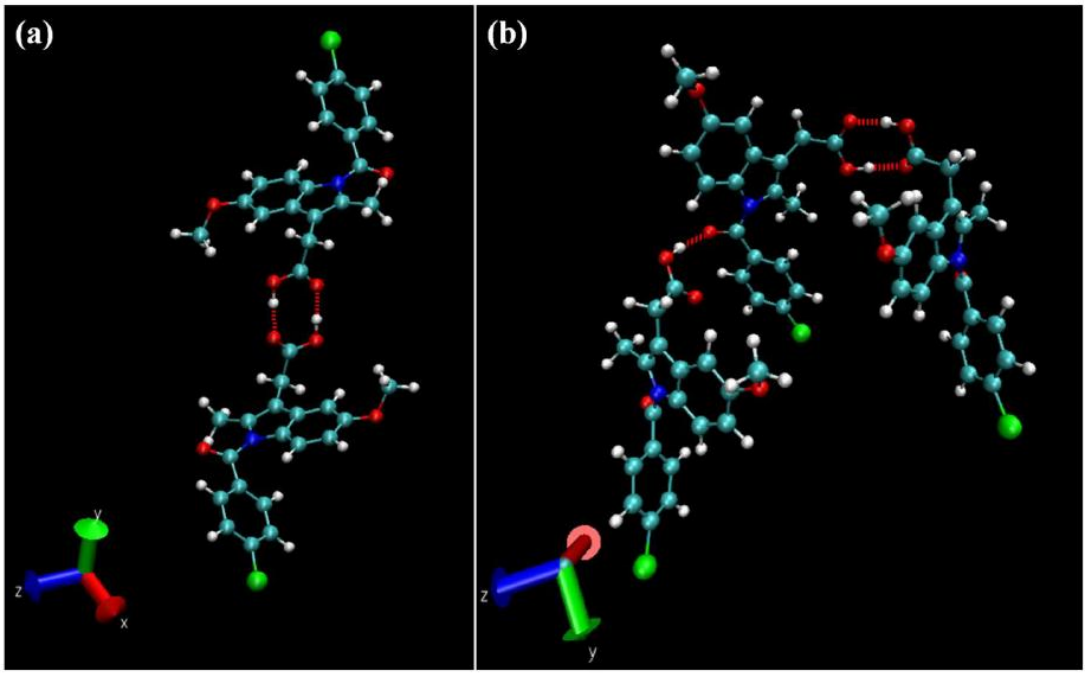

Fig.4.14: A representation of the conformations of the two polymorphs of indomethacin; a) represents the conformation of I_γ (dimer conformation) and b) represents the conformation of I_α (trimer conformation). The hydrogen bonds linking two molecules of indomethacin are represented by dotted lines.

These two polymorphs crystallize from the melt[30]. A third polymorph was mentioned in literature (δ)[58]; it was reported for a sample crystallized from a methanol solution. Indomethacin crystallizes below its glass transition temperature to from I_γ while at higher temperatures, the formation of I_α is predominant[259].

2.2 Simulation and results

The variations of the density as function of the temperature of each crystalline and liquid form are represented in Fig.4.15. Main crystallographic parameters are summarized in Table 4.4. The obtained densities are compared to the experimental values at room temperature (300 K). The OPLS force field was

able also to reproduce the density inversion of the indomethacin polymorphs that was found in literature[259] with a deviation of 0.06 g/cm^3 and 0.05 g/cm^3 for γ and α form respectively in comparison with the experimental values. The systems were heated to an approximate temperature of 500 K before observing the melt, 70 K above the experimental melting point.

Cell parameter	I_γ	I_α
a Å (exp)	9.23	5.46
a Å (sim)	9.23	5.46
b Å (exp)	9.62	25.31
b Å (sim)	9.14	25.77
c Å (exp)	10.88	18.15
c Å (sim)	10.37	18.42
α° (exp)	69.89	90
α° (sim)	69.89	90
β° (exp)	87.32	94.38
β° (sim)	87.32	94.38
γ° (exp)	69.50	90
γ° (sim)	69.50	90
Density mg/m^3 (exp)	1.38 (at 300 K)	1.40 (at 300 K)
Density mg/m^3 (sim)	1.32 (at 300 K)	1.35 (at 300 K)

Table 4.4: Summary of the simulated (sim) and experimental (exp)[259, 261, 262] crystalline properties of indomethacin polymorphs along with their densities.

The evolution of the liquid density as function of the temperature enabled us to determine the simulated glass transition temperature of indomethacin. The T_g simulated was equal to 470 K with an overestimation of 156 K compared to the

experimental T_g that was found to be 314 K[30]. This overestimation was expected as mentioned earlier.

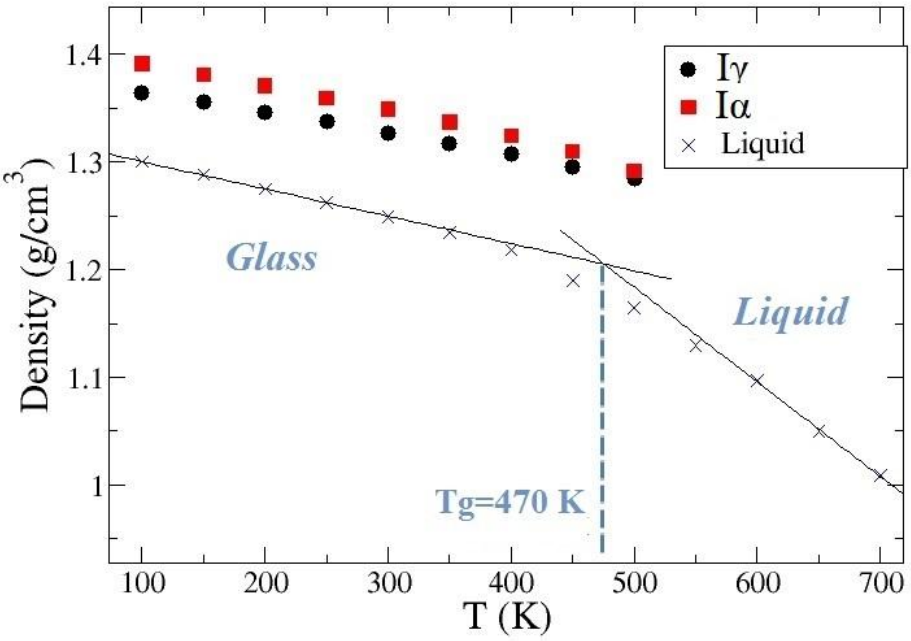

Fig.4.15: Representation of the crystalline and amorphous densities of indomethacin versus T (K). The inversion of the density/stability is well reproduced by the OPLS force field where the most stable phase (I_γ) is less dense than the metastable phase (I_α). A linear adjustment of the amorphous density at high and low temperatures (straight lines) enabled the estimation of the glass transition temperature T_g to be 470 K.

The melting temperatures were estimated by simulating the system at the coexistence temperature as described in Chapter 2. Fig.4.16 presents the biphasic system used to determine the melting temperature of I_γ along with its density variation as function of time at different temperatures. The melting temperatures of I_γ and I_α were estimated at 425 K and 420 K with an underestimation of 9 K and 8 K respectively.

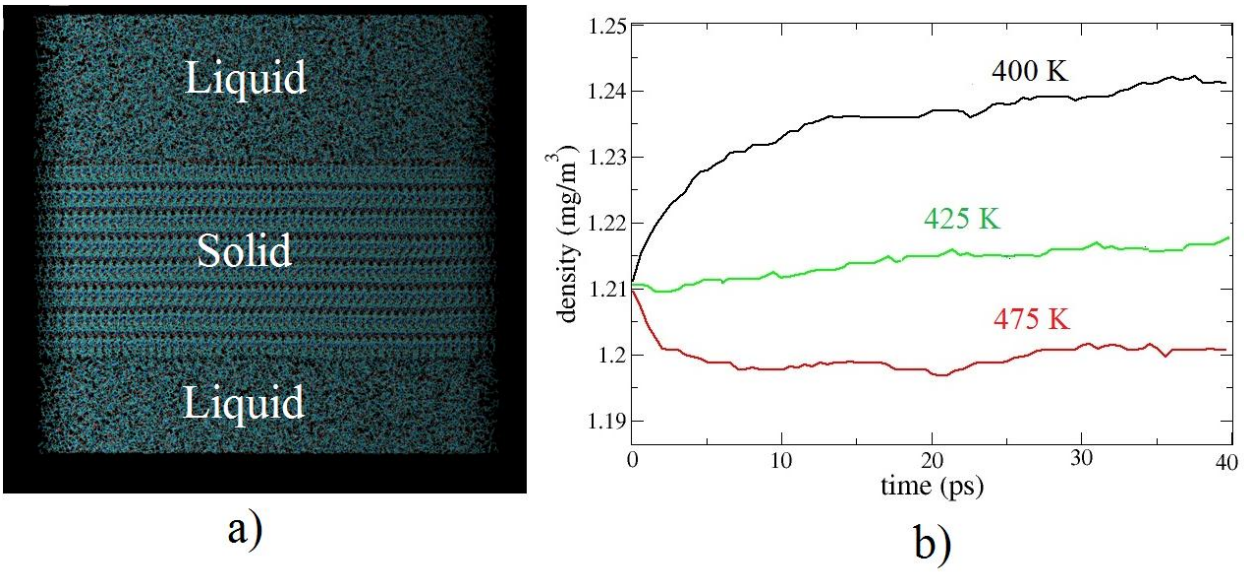

Fig.4.16: The biphasic system a) that was used to determine the melting temperature of I_γ with b) the evolution of its density as function of time at three different temperatures. The increase/decrease of the density indicates the crystallization/melting of the system respectively. The melting temperature T_m was found to be 425 K for I_γ.

Fig.4.17 represents the evolution of the enthalpies of the crystalline and the amorphous forms as function of the temperature. The enthalpy of fusion of I_γ was estimated at 37.11 kJ/mol with an underestimation of 2 kJ/mol compared to the experimental value[30]. While the enthalpy of fusion of I_α was estimated to be 18.91 kJ/mol with an underestimation of 12 kJ/mol (see Table 4.5).

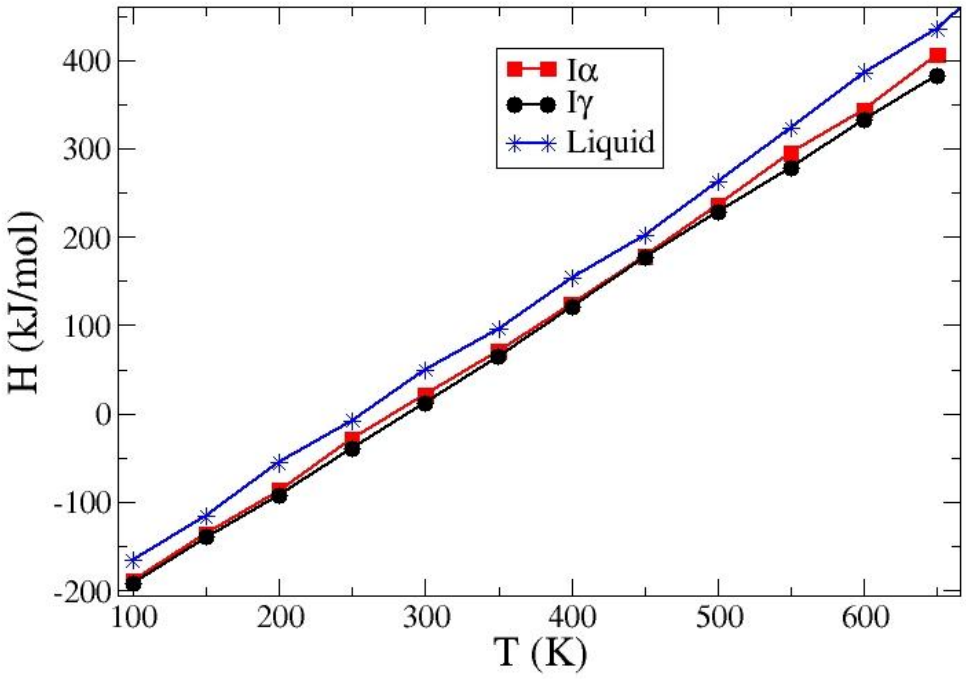

Fig.4.17: Evolution of the enthalpy for the different polymorphic forms and the liquid state of indomethacin.

Fig.4.18 shows the difference in the Gibbs free energy between the liquid and the crystalline phases (γ and α) as a function of temperature calculated from the Hoffman equation (see equation 4.1) using T_m and ΔH_m determined from MD simulations for the investigated Indomethacin polymorphs. This equation gave the same result as the Thompson-Spaepen[263] equation and did accurately predict the ΔG for small molecular weight organic glass formers for which heat capacity data exist[30, 263]. Fig.4.18 shows clearly that the system is monotropic, where the γ-form has a larger ΔG_v and thus it is the stable phase.

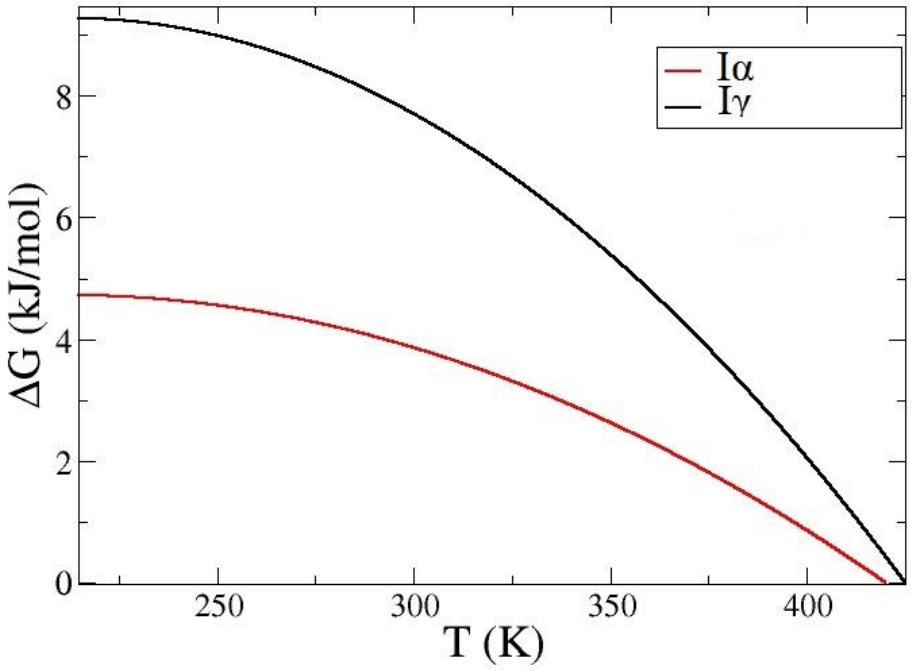

Fig.4.18: The temperature dependence of the Gibbs free energy difference between the liquid and the crystal obtained using the Hoffman equation for the two indomethacin polymorphs.

The interfacial free energy obtained by the fitting curves (Fig.4.19) was found to be 24.6 ± 1.5 mJ/m^2 for the γ polymorph and 14.4 ± 1.2 mJ/m^2 for the α polymorph. We were able to compare our values to the experimental data reported by Andronis and Zografi[30]. In their study[30], the experimental interfacial free energies were obtained from fitting the expression of the steady state rate of homogeneous nucleation as predicted by the CNT to experimental data (Fig.4.20). Thus, the interfacial free energy was taken as a fitting parameter in this analysis. The homogeneous nucleation rates were estimated by using a single stage isothermal technique that consists on melting the pure crystal on pre-cleaned microscope slides and then store the sample inside desiccators placed in ovens maintained at different temperatures. Subsequently, the sample is removed for

microscopic examination in order to calculate the particle number density that enables the determination of the homogeneous nucleation rates. The values obtained were 27 mJ/m^2 for the stable polymorph and 17 mJ/m^2 for the metastable polymorph.

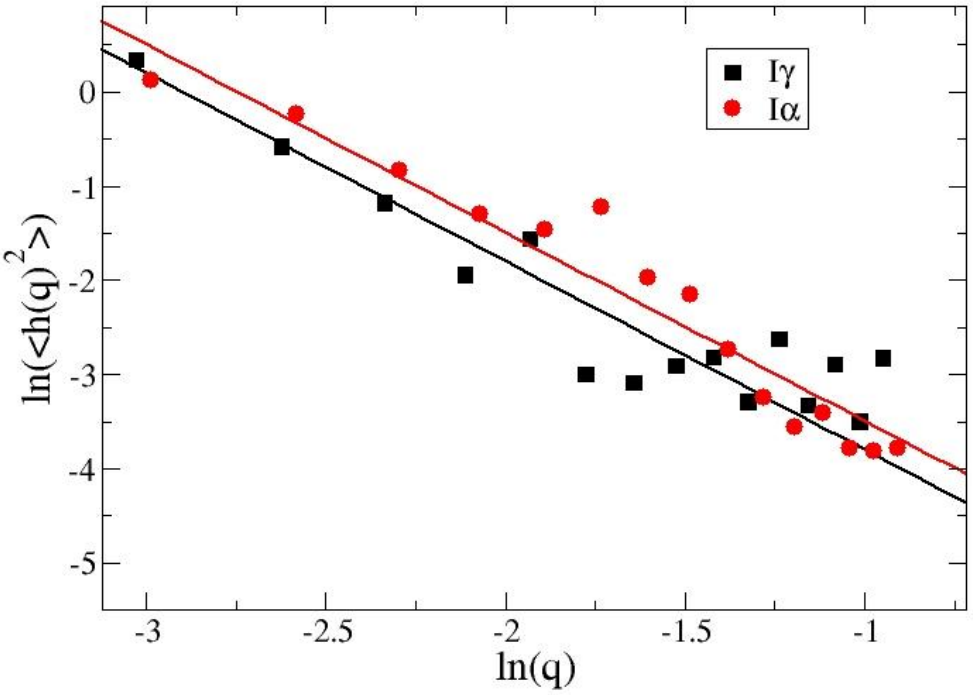

Fig.4.19: The fluctuation spectrum of the interface height for indomethacin γ (black squares) and indomethacin α (red circles). The solid lines are fits to the simulation results using equ. 2.28.

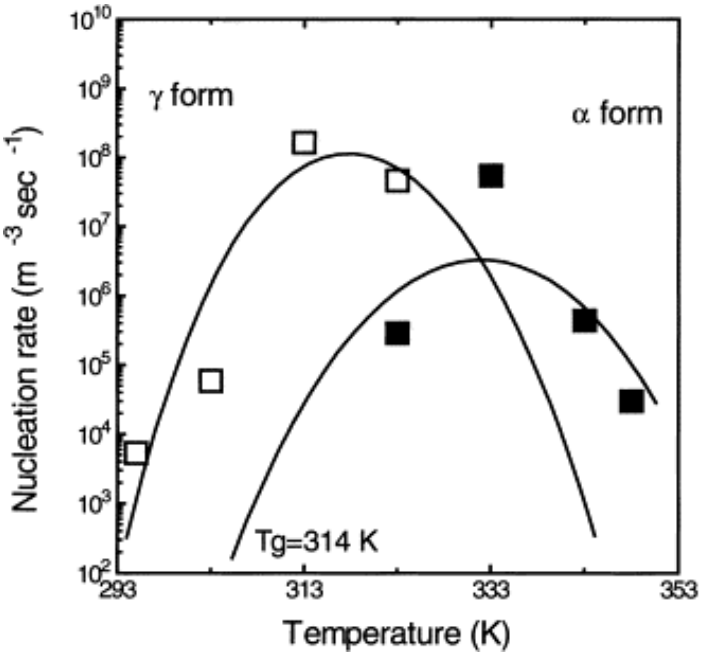

Fig.4.20: Nucleation rates of the γ and α forms of indomethacin as function of temperature determined by Andronis et Zografi[30]. The solid lines represent the fits using the expression of the steady state rate of homogeneous nucleation as predicted by the CNT.

Furthermore, in order to minimize the difference between the theoretical and experimental nucleation rates, Andronis and Zografi considered a temperature dependent interfacial free energy $\gamma(T)$. To obtain the evolution of the interfacial free energy as function of the temperature, the value of γ was varied at each temperature until the experimental nucleation rates agreed with theoretical ones. Fig.4.21 shows the temperature dependent interfacial free energy for the two polymorphs. It can be noticed that each polymorph has different temperature dependence. The metastable polymorph α has a negative slop signifying that the interface free energy is primarily energetic suggesting that it could become more diffuse as the temperature increases. Contrarily, the γ polymorph has a positive slop suggesting a primarily entropic interface free energy[30].

A linear fit was done giving two equations to the temperature dependent interfacial free energy:

$$\gamma_\gamma(T) = 0.06T + 0.85$$
$$\gamma_\alpha(T) = -0.02T + 22.02 \qquad 4.5$$

If we considered that these equations will still be valid at the melting temperature, they will give us a value of 26.9 mJ/m^2 for the γ form and a value of 13.5 mJ/m^2 for the α form (Fig.4.21). The capillary fluctuation method was thus fairly accurate in estimating the interfacial free energies with underestimation of 2 mJ/m^2 for the γ form and an overestimation of 1 mJ/m^2 for the α form.

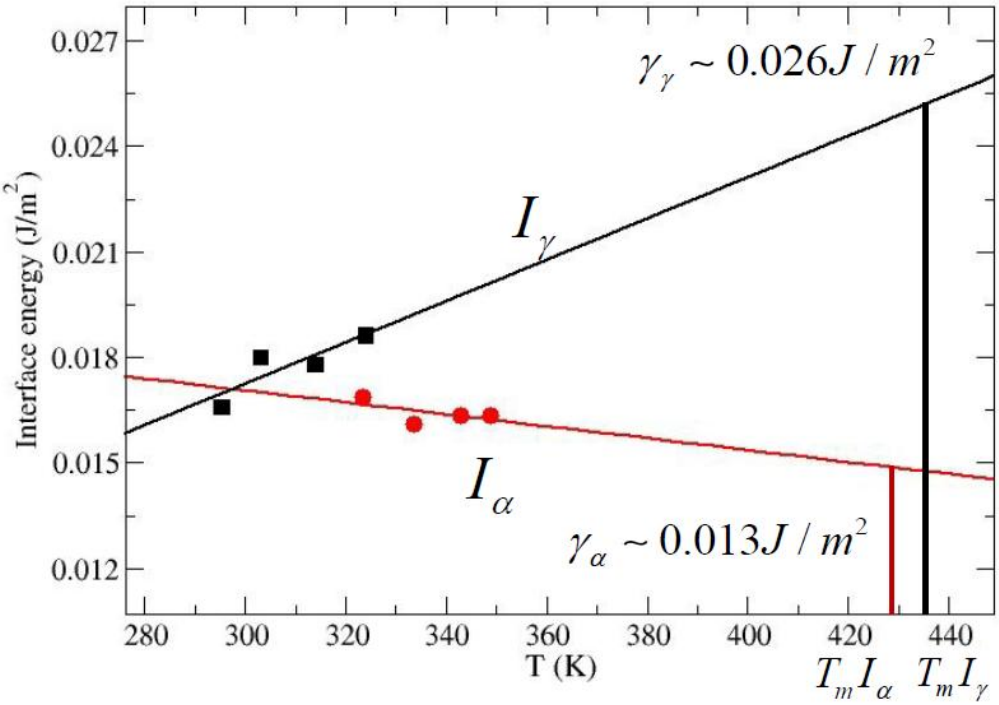

Fig.4.21: The temperature dependent interfacial free energy $\gamma(T)$ for the two crystal forms of Indomethacin, γ polymorph (black squares) and the α polymorph (red circles). The solid lines are the linear fits (see equ. 4.5)[30]. If we assume that equation 4.5 holds at the melting temperature, the crystal-melt interfacial free energy of I_γ and I_α would be approximately 0.026 J/m^2 and 0.013 J/m^2 respectively.

The diffusion coefficient D was determined using the mean squared displacement of molecules $< r^2(t) >$ and fitted using equ. 2.34 (same method used to determine D for nifedipine and felodipine; see Fig.4.22). The estimated shear viscosity as a function of temperature obtained from the stress-stress autocorrelation functions and using the OPLS force field is in a fair agreement with the experimental data obtained from ref.[30] and ref.[25] (Fig.4.23).

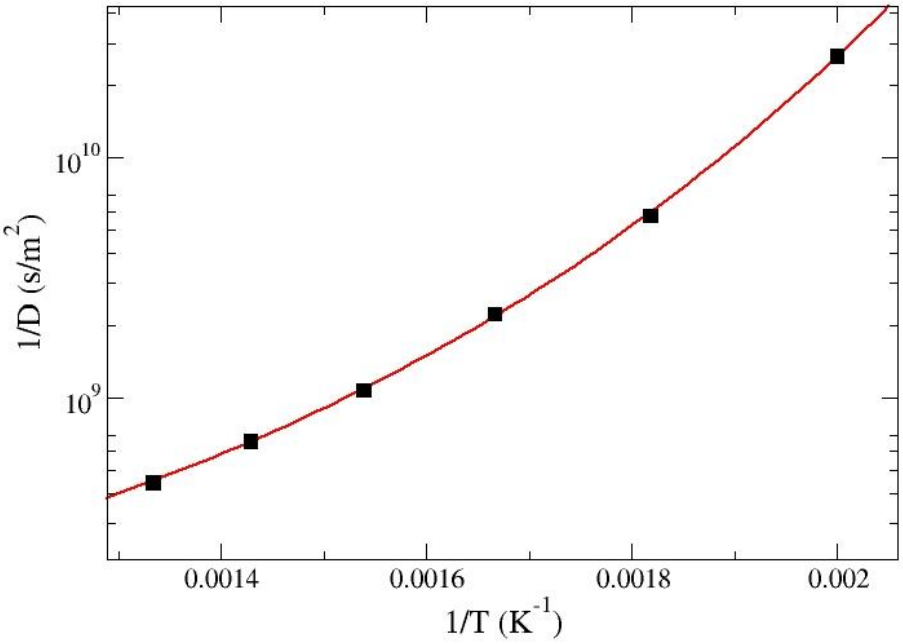

Fig.4.22: The estimated coefficient of diffusion D using the long term evolution of the mean square displacement ($< r^2(t) > \sim 6Dt$ see chapter 2) (black squares) and the fitting using equation 2.34 (solid red line) as a function of the inverse of the temperature for indomethacin in the liquid state.

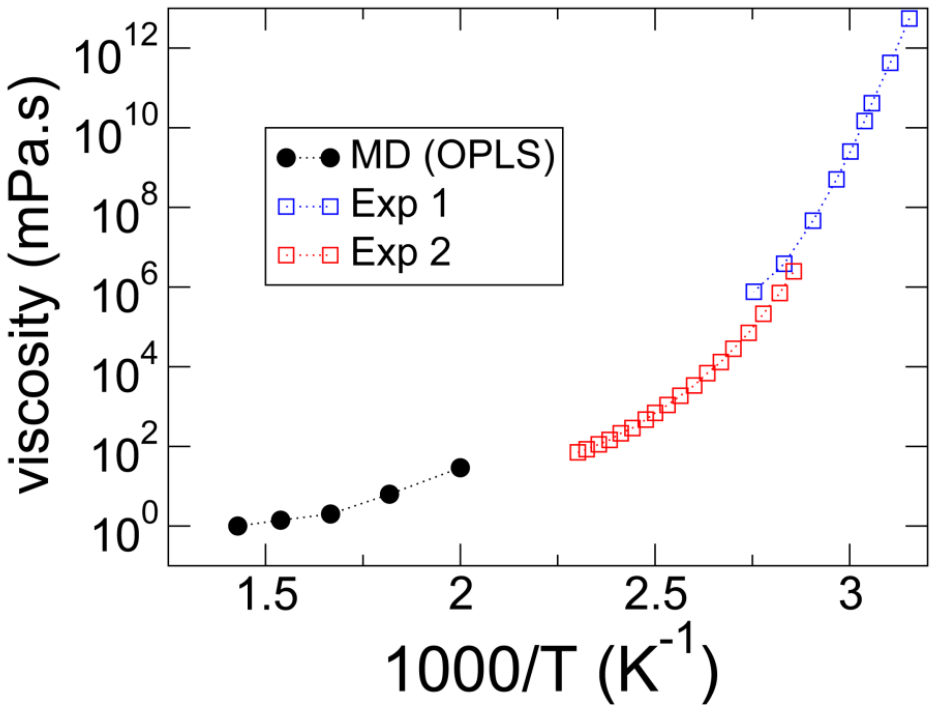

Fig.4.23: Evolution of the shear viscosity as a function of the inverse of temperature for indomethacin in the liquid state compared to the experimental data from ref.[30] (blue squares) and ref.[25] (red squares). The shear viscosity η has been computed from the stress-stress autocorrelation function (see Chapter 2).

Polymorph	ρ_{cx}(exp) [259]/ρ_{cx} (sim) (at T(K)) (g/cm^3)	T_m (exp)[30] /T_m(sim) (K)	ΔH_m(exp)[30] / ΔH_m (sim) (kJ/mol)	γ_m (exp) / γ_m (sim) (mJ/m^2)
Indomethacin γ (I_γ)	1.38 /1.32 (300 K)	434/ 425	39.35 / 37.11	26.9/24.6 $\pm$ 1.5
Indomethacin α (I_α)	1.40 /1.35 (300 K)	428 / 420	32.55 / 18.91	13.4/14.4 $\pm$ 1.2

Table 4.5: Comparison between experimental (exp) and simulation (sim) data obtained using the OPLS force-field for indomethacin γ and α crystal polymorphs. ρ_{cx}, T_m, ΔH_m and γ_m represents the density, the melting temperature, the enthalpy and the interfacial free energy at the melting temperature respectively. Uncertainties of the interfacial free energy γ_m have been estimated from taking into consideration the uncertainties on the melting temperature (10K) and the fitting.

2.3 Prediction of the nucleation and the growth tendencies of Indomethacin

The nucleation and growth were determined in a similar way than nifedipine and felodipine polymorphs. Once the main parameters (D, ΔG and γ) were estimated via MD simulations (see previous section), nucleation and growth of both indomethacin polymorphs were estimated using equations 4.2 and 4.4 respectively.

As mentioned before, the validity of the CNT is frequently questioned because of a lack of agreement between these predictions with measured nucleation rates either from experiments or from direct determination of these rates from simulation. Disparities between predicted and fitted pre-factors can be greatly reduced by using the interfacial free energy γ as a fit parameter, i.e. temperature dependent parameter, or by changing the assumptions in using the viscosity instead of the diffusivity which is usually treated via the questionable validity of the Stokes–Einstein relation[36]. In this work, a temperature dependent interfacial free energy was considered (equ. 4.3).

Fig.4.24 a) shows the steady state nucleation rate N as function of the undercooling for the two studied polymorphs. The nucleation curves show the expected behavior, a bell shaped curve with a sharp increase upon cooling due to the increasing driving force followed by a decrease due to the decreasing diffusivity. The maximum varies notably between the two polymorphs favoring the nucleation of the metastable phase α. In the same figure, we compared the curves obtained from the CNT to the experimental values in ref. [30]. As mentioned before, the nucleation rates predicted from simulation are different from those estimated experimentally by few decades. Even the predicted separation of the two polymorphs is much bigger than the experimental separation. Furthermore, in ref.[30], the fits of the experimental values give a slightly higher nucleation rate for the γ form than α, which is not the case in our prediction.

Andronis and Zografi[30] determined the growth rate G of γ and α indomethacin polymorphs from the melt of a purified alpha crystal. The temperature range was from 293 K to 373 K where two different morphologies were encountered: a needle like grow for the γ form and compact spherules grow for the α form. The behavior of the growth was found to be favorable of a two dimensional growth[30, 58],

and the use of the following function of $f = exp\left[-\frac{\pi \cdot a \cdot \gamma^2}{k_b T \cdot \Delta G_v}\right]$ was applicable since Indomethacin has a high entropy of fusion (~11R), and as mentioned before that the model of a two-dimensional growth is applicable to similar materials[2, 30, 33]. But, these determinations were made just at a small range of temperature (near T_g) and the model assumes that $\frac{1}{\eta}$ represents accurately the effect of the mobility (i.e. $D \sim \frac{1}{\eta}$) which is not always the case[58] (as it will be discussed below). It was also mentioned that more investigation is needed to understand the crystallization process of the γ form since its crystallization is not consistent with what was shown in too many materials (and the α form) where the maximum of the nucleation rate is located above T_g and the maximum of the growth rate is placed at a higher temperature between T_g and T_m (Fig.4.24).

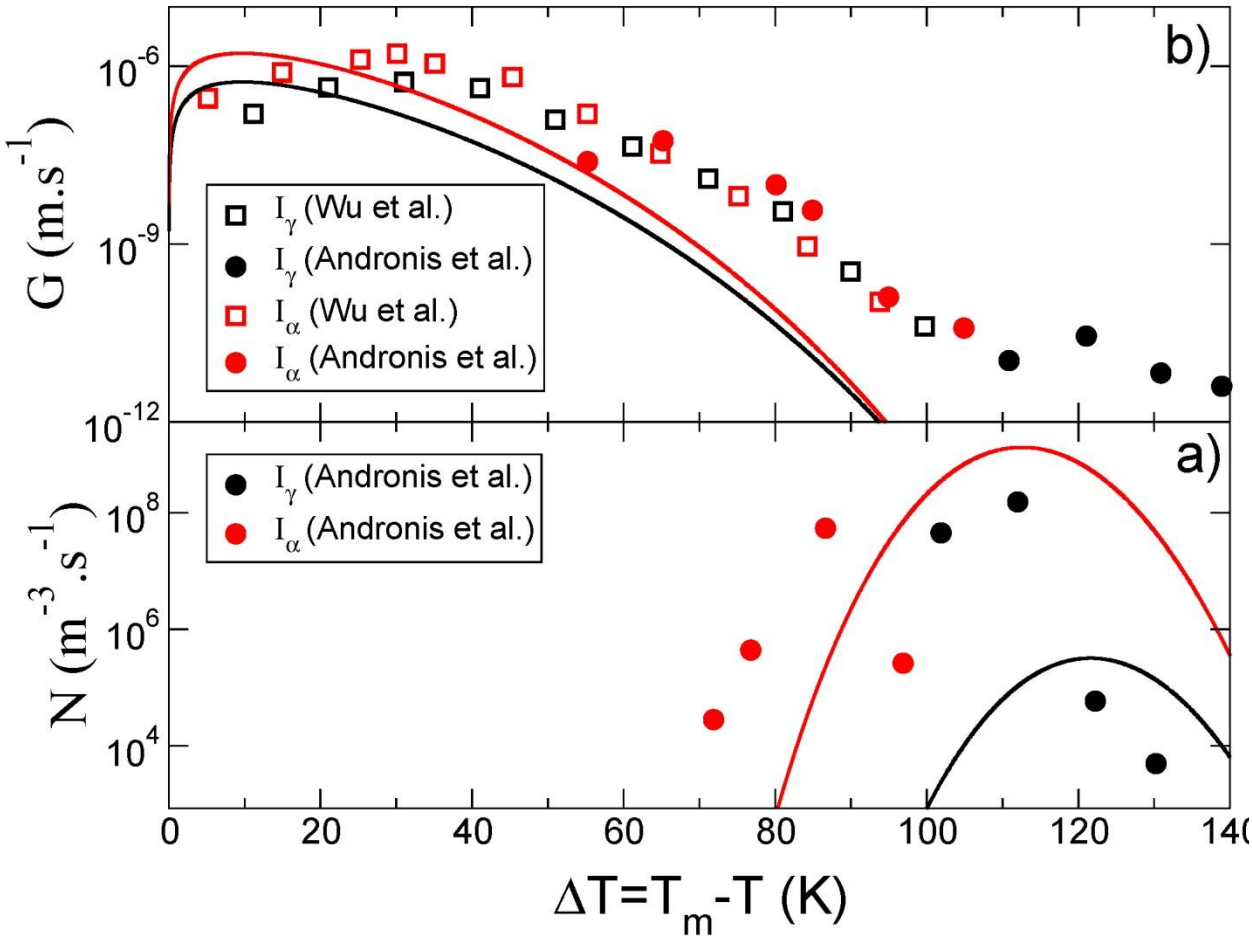

Fig.4.24: Predicted evolution of the nucleation N (a) and growth G (b) rate as function of the undercooling of the different investigated indomethacin polymorphs. A comparison between experimental (symbols) and numerical (solid lines) data is also given. The experimental nucleation data are taken from ref.[30] since they are the only available data. The estimated growth rates are compared to experimental data obtained from ref. [30] and ref. [58]. Constant parameters 1/k = 125 and 14 for γ and α respectively have been used to rescale numerical growth rate in order to fit with experimental values using a growth model with f = 1.

Wu and Yu[58] studied the crystallization from a melt of γ indomethacin for temperatures ranging from 323 K to 423 K (Fig.4.24). They found that γ and α indomethacin grow in different morphologies as function of temperature. At high temperatures ($T > T_g$+19 K) polycrystalline growth was observed and at low temperatures ($T < T_g$+ 19 K) a randomly oriented fibers were detected. In their study, they assume a normal growth mode taking into consideration the break-down of the Stokes-Einstein relation and replacing it by $\sim\frac{1}{\eta^{-\xi}}$. The estimated growth rates were compared to the experimental ones obtained from this reference (Wu and Yu[58]) assuming a normal mode growth ($f = 1$) since the growth rate near T_g seems to have different mechanisms that are not taken into account in this study. Our simulated values (see Fig.4.24) reproduce fairly the experimental growth rate with a slight disagreement of both polymorphs showing the expected bell shaped curve of the growth rate G derived from the respective increase and decrease of the thermodynamical driving force and the mobility. In this case too, the maximum growth is localized at small undercoolings which has been presented as a comparative parameter for the crystallization tendencies [28].

The simple model used in the present study allowed reproducing the decreasing order of the growth rate of indomethacin polymorphs (α and γ). Furthermore, the nucleation and growth curves in Fig.4.24 do not significantly overlap which indicates that indomethacin is a good glass former. This behavior is well in line with experimental data that showed that indomethacin exhibits a very low crystallization tendency during cooling and reheating compared to several glass formers[25, 28]. Based on our results, I_α has a higher nucleation and growth tendency at all temperatures enabling the predominance of this form. This is not

the case in experience since indomethacin crystallizes as I_γ below the glass transition temperature and as I_α at higher temperature[30, 259].

2.4. Comparison between nifedipine, felodipine and indomethacin crystallization tendencies

In order to compare the crystallization tendency of the different investigated pharmaceuticals, we represented the nucleation rates N and the growth rates G of the metastable polymorphs of nifedipine, felodipine and indomethacin in Fig. 4.25. The higher growth rate is obtained for nifedipine followed by felodipine and indomethacin. Even thought the nucleation tendency follows the same trend the crystallization tendency cannot always be predicted just by knowing N or G alone because the growth rate might be high in a certain temperature range where the nucleation rate is not favorable which will not lead to a crystallzation. On the other hand, if we examined the position of the maximum of N and G, we can easily extract the crystallization tendency. In Fig.4.25, N and G curves of indomethacin do not overlap significantly which indicates that indomethacin should have the lowest crystallization tendency (good glass forming ability). The highest crystallization tendency as predicted from Fig. 4.25 should be attributed to nifedipine followed by felodpine. Thus, the crystallization tendency as predicted by the CNT and the normal mode of growth is as follow: nifedipine, felodipine, indomethacin which is well in line with experimental data[25, 28, 45].

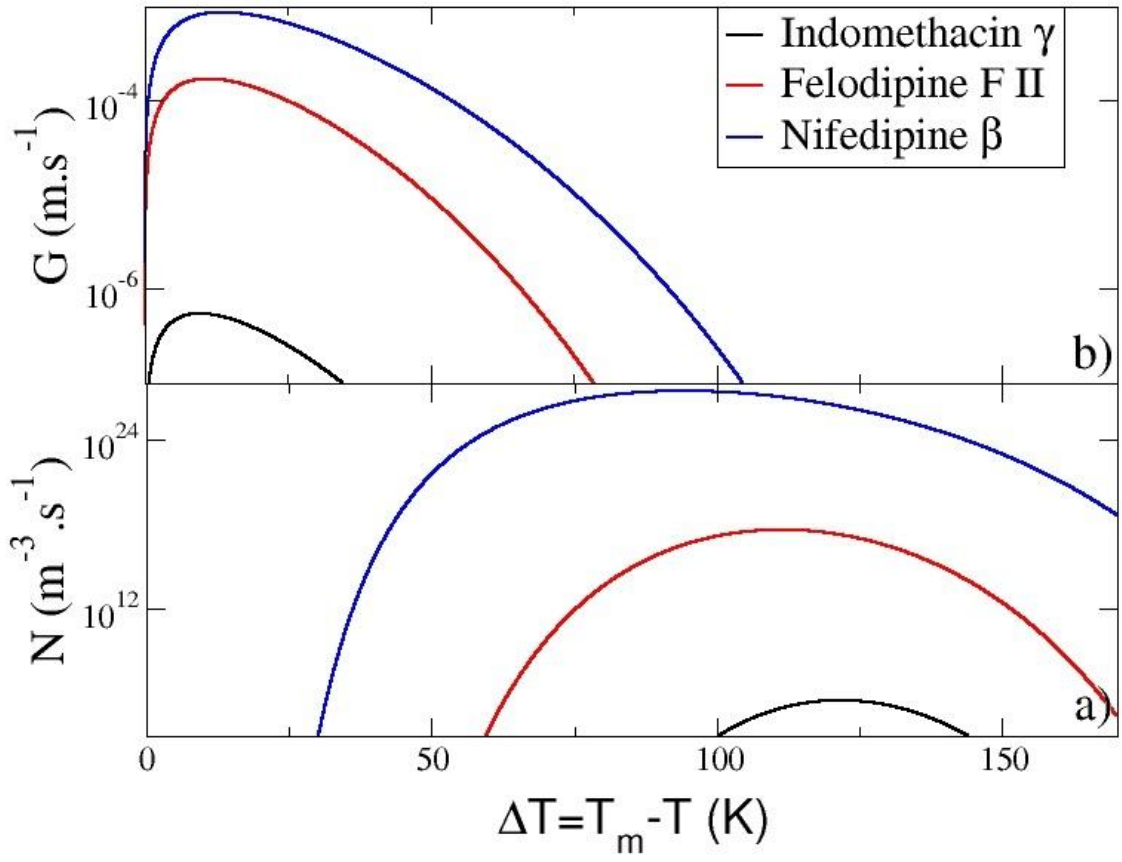

Fig.4.25: Comparison of the nucleation a) and growth b) rates of the three studied systems (nifedipine, felodipine and indomethacin) as predicted by the CNT.

2.5 Conclusion

Nucleation and growth tendencies from the melt were predicted for indomethacin polymorphs based on the investigation of the liquid state, the crystalline state and the crystal-melt interface via MD simulations. Separate calculations were performed on the crystal and the liquid state in order to obtain their main physical properties like the density, the enthalpy and the coefficient of diffusion. The simulation of biphasic systems enabled the determination of the melting temperatures and the crystal-liquid interfacial free energies of both indomethacin polymorphs.

The OPLS force field was able to fairly reproduce the crystallographic as well as the thermodynamic quantities of indomethacin polymorphs. However, it failed of reproducing the enthalpy of fusion of the metastable α form accurately (an underestimation of 12 kJ/mol). In this chapter, we were particularly able to compare the estimated interfacial free energy values obtained by the capillary fluctuation method to the experimental values obtained in ref. [30]. We found a small underestimation of the interfacial free energies compared to the data extracted from the homogeneous nucleation or form the linear approximation proposed in ref. [30]. The interfacial free energy at the melting temperature γ_m was estimated in a good agreement by the capillary fluctuation method to be 24.6 $\pm$ 1.5 mJ/m^2 for I_γ (experimental value 26.9 mJ/m^2) and 14.4 $\pm$ 1.2 mJ/m^2 for I_α (experimental value = 13.4 mJ/m^2).

The nucleation rate of the indomethacin polymorphs was estimated. A difference of several orders of magnitude was obtained compared to the experimental data as usually observed from the CNT predictions. The estimated nucleation rate of I_α is higher than the estimated nucleation rate of I_γ by several orders of magnitude. This behavior was not observed in experiments[30] where the nucleation rates of both polymorphs are roughly the same as shown for nifedipine and felodipine. The normal mode (f =1) was found to be the most suitable mode to reproduce the growth rate of indomethacin polymorphs. A higher growth rate for the metastable phase α at all temperatures was found as observed in experiments. The large gap between the maximum of the nucleation rate and the growth rate of both polymorphs indicates that indomethacin is a good glass former as observed in many experiments[36, 53]. This study clearly confirms the need to determine both nucleation and growth rates in order to predict the crystallization/vitrification tendencies.

Conclusions and perspectives

In summary, by means of MD simulations, the liquid and the crystalline states of some simple LJ liquids and pharmaceutical materials (felodipine, nifedipine and indomethacin) as well as the crystal-liquid interface have been investigated in order to predict their nucleation and growth tendencies from the melt.

In this thesis, as a preliminary step before investigations of complex molecular compounds, we investigated simple models composed of monoatomic Lennard-Jones atoms. Tunable potentials were constructed in which the attractive part may vary while keeping constant the repulsive part. It allowed us to investigate the specific influence of attractive forces on different parameters such as driving force ΔG, interfacial free energy γ and diffusivity D and then to predict nucleation rates in the framework of the classical nucleation theory (CNT).

Our results have particularly highlighted the importance of the often overlooked attractive part of the interaction potential with respect to hard core repulsion. We have pointed out that a change in the attractive part of the interaction potential slightly influences the crystallization times which decrease with the attractiveness of the potential. This trend matches well with the evolution of the driving force ΔG but not with the interfacial free energy γ which behaves in an opposite trend. It thus shows the importance of the relative interplay of both parameters on the nucleation barrier $\Delta G^* \sim \gamma^3 / \Delta G_v^2$. The driving force seems to dominate in the present study. Since LJ simple monoatomic liquids crystallize easily, the direct measurement of nucleation rates can be done. These latter can be compared with CNT predictions. Calculation of both characteristic times of the

transient and steady-state regimes allowed providing a thorough analysis of the directly determined crystallization times. Two different behaviors of the crystallization times were observed as function of the undercooling. For small undercoolings, the steady state nucleation time dominates while at intermediate and deep undercooling it is the transient time that dominates. This result could provide a track to explain some of the disagreements found between predictions from CNT and direct measurements of the crystallization times. An overall fair agreement is found between the direct estimation of the crystallization times and prediction of the nucleation times from the CNT but the need for a temperature-dependent interfacial free energy $\gamma(T)$ is clearly revealed from different tests performed.

Two polymorphs of nifedipine (N_α, N_β), felodipine (FI, FII) and indomethacin (α and γ) have been studied. Calculations were performed on liquid and crystal systems separately in order to determine their main physical properties: density, enthalpy and diffusivity. Biphasic crystal-liquid simulations enabled the calculation of the melting temperatures and the interfacial free energies γ_m at the melting temperatures of the different polymorphs. A fair agreement was found between the simulation results and the known experimental data such as the crystal densities, the melting temperatures, the driving force for crystallization ΔG and the molecular mobility (diffusivity D) confirming the ability of the force fields GAFF used for nifedipine and felodipine and OPLS used for indomethacin to reproduce accurately the experimental data.

In this thesis, we validated the application of the capillary fluctuation method on complex pharmaceutical systems that exhibit polymorphism in order to determine their crystal-melt interfacial free energy at the melting temperature. The

crystal-liquid interfacial free energy has been determined for the first time for the investigated nifedipine, felodipine and indomethacin polymorphs. The values γ_m= 21.5, 14.4, 28.7 and 15.5 mJ/m^2 have been obtained for N_α, N_β, FI and FII respectively. For the indomethacin polymorphs, the interfacial free energy at the melting temperature γ_m was estimated in a good agreement with experimental data. We obtained 24.6 $\pm$ 1.5 mJ/m^2 for I_γ (experimental value 26.9 mJ/m^2) and 14.4 $\pm$ 1.2 mJ/m^2 for I_α (experimental value = 13.4 mJ/m^2). For all studied pharmaceuticals, the interfacial free energy γ_m was found to increase with the polymorph stability where the metastable forms have always a smaller interfacial free energy than the stable forms in agreement with the Ostwald rule of stages.

From the estimation of D, γ_m and ΔG, the nucleation and the growth rates were calculated in the frame work of the CNT and by using different growth modes (normal, 2D and screw dislocation). The nucleation rates seem mainly controlled by the interplay between γ and ΔG which is consistent with the amplitude of the nucleation barrier as predicted by the CNT. A fair agreement was found between numerical and experimental growth rates suggesting a mechanism of normal growth in which growth at deep undercooling is mainly controlled by dynamics as already shown experimentally for indomethacin assuming a fractional Stokes-Einstein dependency between viscosity and diffusivity in that case. Other growth mechanisms do not seem able to fit the experimental growth rate order between the different investigated polymorphs owing the present calculated interfacial free energy. We particularly obtained the increasing order of growth rate: N_β > FI > FII and I_α > I_γ as seen experimentally.

Similarity between the molecular mobility of felodipine and nifedipine is particularly confirmed. The driving force for crystallization has been estimated

showing a higher driving force for nifedipine with respect to felodipine as suggested in experiments. We found that the higher interfacial free energy of felodipine polymorphs might be an additional reason for its resistance to crystallization compared to nifedipine, other than its lower driving force. The low value of γ_m of N_β compared to the other polymorphs seems the origin of its higher nucleation rate and to its larger overlapping of nucleation and growth curves. However, the nucleation tendencies are not only controlled by the interfacial free energy since γ of N_α is higher than γ of FII but the nucleation rate of N_α is much higher. In that case, the higher driving force of N_α should explain its higher nucleation rate.

Our results also pointed out that the interfacial free energy γ cannot be used alone as a parameter to predict the polymorph or the crystal selection. For indomethacin polymorphs, the metastable form possesses the lowest interfacial free energy but crystallizes more readily than the stable form. Furthermore, the nucleation rates alone cannot predict the final crystal phase. For indomethacin, the nucleation rates of the various crystal forms were the same but the crystal growth rates were completely different. Hence, it is clear that both nucleation and growth rates (including driving force, interfacial free energy and diffusivity) should be taken into consideration when trying to predict the phase selection or the crystallization tendencies.

It is clear that the present study is a preliminary work and several perspectives can be considered by improving the approximations and the simplifications. A few directions of additional research are given below.

First, different approximations for the determination of the crystal-liquid interfacial free energy have been made. As confirmed in the present work, a small variation of the γ may strongly impact the nucleation tendencies. In order to reduce the computational effort, the anisotropy of the interface was not taken into account since the interfacial stiffness was identified as the interfacial free energy. Even for small anisotropies, the value of γ might change with the orientation of the crystalline phase in contact with the parent liquid. Additional calculations taking into account different crystallographic orientations should thus be done. Moreover, the curvature of the interface is not considered in the capillary fluctuation method where the interface is considered as a fluctuating quasi-one dimensional interface. This curvature causes the decrease of the melting point during solidification (the Gibbs-Thomson undercooling[95]). A simple correction of the curvature could be applied as described in ref. [2]. The present numerical approach only allowed us to determine γ at the melting temperature and a simple temperature dependent model was also employed. This suggests the use of a recent alternative developed numerical technique that allows calculating this parameter at different temperatures[264].

Secondly, the use of the CNT can be questionable. It is well accepted that the CNT reproduces fairly the overall shape of the experimental nucleation rate (i.e. bell curve) meaning that the theory contains the physical ingredients of the nucleation process but fails to reproduce quantitatively the experimental data. Our model particularly considers an ideal situation where nucleation is purely homogeneous. This is generally not the case in experiments where heterogeneous nucleation occurs. The presence of impurities catalyzes the nucleation and it decreases the nucleation barrier ΔG^*. Hence, our calculations certainly overestimate the nucleation rate. In order to consider catalyzed nucleation

mechanisms from the melt due to impurities, it would require a description of the foreign substrate which is far from being trivial and so far beyond our possibilities[2]. Several alternative models were elaborated in order to minimize the lack of agreement between the CNT predictions and the experiments. Two promising models were excessively used to replace the CNT. On one hand, the Generalized Gibb's Approach (GGA)[265, 266] that lies on the fact that the structure of the initial germ is different than the structure of the final crystal. In this case the germ will follow several transformations before attending the final form (this concept agrees with the Ostwald rule of stage). On the other hand, the two-step model[266-268] considers that a pre-nucleation phase occurs before the formation of a nucleus. In this phase a more concentrated state will appear (but still fluid) in the liquid leading to the formation of a crystal nucleus. It will be interesting to test the alternative methods in future investigations.

Thirdly, in addition to the steady state nucleation rate N and the growth rate G, there is a non-steady-state nucleation regime. The importance of this transient regime was clearly highlighted in the investigations on simple LJ liquids but it was not unfortunately studied in the case of pharmaceuticals. Generally, a rapidly cooled system requires time, called the time-lag or the transient time, before attending a steady state nucleation. In deep undercooling, the transient time was shown to be much longer than the time predicted while using only the steady-state rate[79, 80]. Since the same parameters that are calculated in the present study (driving force ΔG, diffusivity D and interfacial free energy γ) are also linked to the time-lag, it should not be difficult to get an estimation of this time as described in the CNT [2, 79-81].

Finally, it has been shown [46, 48, 58] for nifedipine, felodipine and indomethacin, that i) below T_g materials may experience a sudden jump in crystal growth rate labeled as a diffusionless mode of growth which has been related to the oscillatory motions in the glasses and the liquid[46]; and ii) the surface crystal growth rate is faster than the bulk crystal growth rate i.e. surface induced crystallization. Indeed, the mobility at free surfaces can exceed the bulk mobility by many orders of magnitudes[46, 269, 270]. Obviously, these two important phenomena were not simulated in our approach and it clearly motivates additional numerical developments in order to take them into account.

Annex

Bonded interactions

The intramolecular contributions are V_{Bond}, $V_{angular}$, $V_{Dihedral}$ and $V_{Improper}$.

The V_{bond}, which represents the chemical bond between two atoms i and j, can be modeled by the harmonic oscillator approximation by considering the bond between the 2 atoms i and j as a spring. Hence the bond potential V_{Bond} can be written as follow:

$$V_{Bond} = \sum_{i,j} \frac{1}{2} k_{ij} (r_{ij} - r_{ij}^{0})^2 \qquad 1$$

where k_{ij} is the spring constant associated to the bond, r_{ij}^{0} is the reference distance and r_{ij} is the length of the bond. The summation is done over all pair of atoms i & j having a covalent bond between them. Note that k_{ij} can be obtained experimentally via Raman or Infra-red spectroscopy.

The $V_{Angular}$ contribution takes into consideration the interactions with the nearest neighbors. To do so the deformation of the angles of the covalent bonds between 3 atoms is described using the harmonic approximation:

$$V_{Angular} = \sum_{i,j,k} \frac{1}{2} k_{ijk} (\Theta_{ijk} - \Theta_{ijk}^{0})^2 \qquad 2$$

where Θ_{ijk} is the angle between the 3 atoms i,j & k, Θ^{0}_{ijk} is the reference angle and k_{ijk} is the angular spring constant. The summation is held over all triplets of atoms (i,j & k) where the pairs (i,j) and (j,k) form between them a covalent bond. This contribution is smaller than the first one knowing that one needs less energy to deform a covalent angle than deforming a covalent bond.

The diehedral terms ($V_{Dihedral}$ & $V_{Improper}$) describes the interactions between 4 atoms. The $V_{Dihedral}$ term (or proper dihedral) represents the flexibility and the rigidity (torsion). It is represented as a sinusoidal function:

$$V_{Dihedral} = \sum_{i,j,k,l} k_{ijkl}[1+\cos(\mathrm{m}\varphi_{ijkl} + \delta_{ijkl})] \qquad 3$$

where k_{ijkl} is the energetic barrier between 2 positions at equilibrium of the torsion linked to the dihedral angle φ_{ijkl} formed between the 2 atom groups (i,j & k) and (j,k &l), δ_{ijkl} is a phase shift associated with the molecules geometry and m is an integer representing the multiplicity of the torsion potential. The summation covers all the quadruples of atoms (i,j,k,l) forming respectively a covalent bond between each pair (i,j),(j,k)and (k,l).

On the other hand, the improper dihedral potential ($V_{Improper}$) is used to impose and conserve the chirality or the planarity around certain atoms. It is represented as an harmonic potential as follow:

$$V_{Improper} = \sum_{i,j,k,l} k_{ijkl}(\omega - \omega_{ijkl}^{0})^2 \qquad 4$$

In this contribution, k_{ijkl} is the spring constant of the torsion, ω is the angle between the plane formed by the central atom and 2 peripheral atoms and the plane formed by the peripheral atoms and ω_{ijkl}^{0} is the equilibrium angle.

Non-bonded interactions

The two remaining contributions ($V_{L\text{-}J}$ and V_{elec}) are considered as intermolecular interactions. They intervene between two pairs of atoms from two different molecules, or within the same molecule but separated by more than 3 covalent bonds.

The $V_{L\text{-}J}$ potential represents the combination of two opposite forces, a repulsive and an attractive force (Fig.1), and it's represented as follow:

$$V_{L-J} = \sum_{ij} 4\varepsilon[(\frac{\sigma}{r_{ij}})^{12} - (\frac{\sigma}{r_{ij}})^{6}] \qquad 5$$

where r_{ij} is the distance separating the atoms i and j, ε is the depth of the potential well and σ is the equilibrium distance. The repulsive part of the potential is represented in the $1/r^{12}$ term and is caused by the superposition of the electronic clouds of two atoms described by the exclusion law of Pauli. The second term, $1/r^{6}$, represents the attractive part of the potential resulting from the existence of van der waals forces generated by the different types of dipolar interactions (permanent dipole-induced dipole, permanent dipole- permanent dipole, and between instantaneous dipoles)[271].

In order to reduce the calculation time, the terms in equation 5 can be reduced by introducing a truncation sphere having a radius of Rc. All interactions beyond this sphere will be neglected. This truncation seems reasonable since the van der Waals forces decrease by a factor of $1/r^{6}$. Usually Rc is chosen equal to 2.5σ or 3σ but always smaller than the half of the elementary cell.

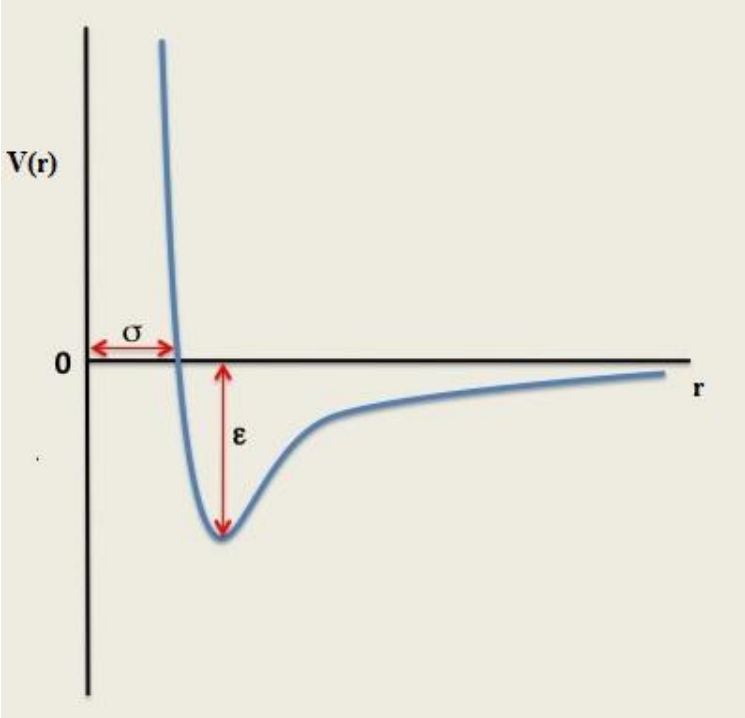

Fig. 1 A typical Lennard-Jones potential as function of r

The potential between two charged atoms i and j is expressed as a Coulomb potential:

$$V_{elec} = \sum_{ij} \frac{1}{4\pi\varepsilon_0} \frac{q_i q_j}{r_{ij}} \qquad 6$$

where r_{ij} is the distance between the atoms i and j with the charges q_i and q_j respectively and ε_0 is the vacuum permittivity. To minimize calculation time, two techniques are generally used which are the reaction field method and the Ewald summation. The Ewald summation is used in this work (see below). For more information, check the following references[272, 273].

Ewald summation was first introduced in 1921[274] as an efficient tool to sum the long range interactions between particles and their infinite periodic images[275]. The

contribution of the potential energy of all the images can be taken into consideration with changing the equation 6 into

$$V_{elec} = \sum_{\vec{n}} \sum_{ij} \frac{1}{4\pi\varepsilon_0} \frac{q_i q_j}{|\overrightarrow{r_{ij}} + \overrightarrow{n}|} \qquad 7$$

where the sum over n is the sum over all simple cubic lattice point and the vector sign reflects the shape of the basic box. The equation 7 as it is cannot be used directly to calculate the electrostatic contributions because of its divergence[120]. Therefore Ewald[274] proposed a method that consists of adding for each point charge q, a charge distribution of opposite sign –q. A screening effect is thus created on the point charge q which is now surrounded by a charge density of equal magnitude and opposite sign. This density is represented as a Gaussian charge distribution:

$$\rho(r) = -q \frac{\alpha^3}{\pi^{\frac{3}{2}}} \exp(-\alpha^2 r^2) \qquad 8$$

where α is a parameter that determines the width of the distribution and r is the position relative to the center of the distribution. Introducing this contribution screens the interactions between the neighboring point charges reducing their range. As a result the sum over all charges and their images in real space converges rapidly and can be calculated like the LJ potential. A second Gaussian distribution with the same sign and magnitude of the original distribution is then added to each point charge in order to cancel out the first induced Gaussian distribution. The resulting Poisson equation can be solved in the reciprocal space using Fourier transforms. A third contribution should be added as a correction term that counteracts the interaction of each of the introduced artificial counter-charges with

itself. The total electrostatic energy can then be written as the sum of the three contributions mentioned above:

$$V_{elec} = V_{real\,space} + V_{reciprocal\,space} + V_{correction} \quad (9)$$

$$V_{elec} = \frac{1}{4\pi\varepsilon_0}\sum_{n}\sum_{i<j}^{N}\frac{q_i q_j erfc(\alpha\,|\,r_{ij}+n\,|)}{|\,r_{ij}+n\,|} + \frac{1}{\pi\varepsilon_0 L^3}\sum_{i<j}\sum_{k\neq 0}^{\infty}\frac{e^{-k^2/4\alpha^2}}{k^2}\,|\sum_{m=1}^{N} q_i e^{-ikr_i}\,|^2 - \frac{\alpha}{\sqrt{\pi}\sum_i q_i^2} \quad (10)$$

The convergence of the Ewald sum depends essentially of 3 parameters. Rc (the truncation sphere radius) that is considered equal to Rc of the LJ potential due to simplicity reasons, α and the number of periodic replicas taken into account. In order to optimize the convergence in the real and the reciprocal spaces with a fair precision, the relative error is considered in the order of 10^{-6} for a cubic simulation box (L^3), with Rc=L/2, the maximal value of k is then 14π/L [136].

Algorithms and principles

Integration algorithm and the 2nd law of Newton

As mentioned above, the classic MD simulations determines the trajectory of each atom i of a system containing N atoms by integrating the equation obtained by the 2nd law of Newton. Each atom i is considered as a mass point (m_i):

$$m_i \frac{d^2\vec{r_i}(t)}{dt^2} = \vec{f_i}(t) \quad (11)$$

$$\vec{f_i}(t) = \frac{-\partial V(\vec{r^N})}{\partial \vec{r_i}(t)} \quad (12)$$

where $\vec{r_i}$ is the position of the atom, $\vec{f_i}$ is the force applied on the atom i and $V(\vec{r^N})$ is the potential of interaction obtained by the force field of the system. This equation cannot be solved as it is since it consists of solving 3N coupled equations

of the 2nd order. These equations are hence an N-body problem that has not an analytical solution. However this equation can be solved numerically using the finite difference method:

$$\vec{r_i}(t+\Delta t) = \vec{r}_i(\mathrm{t}) + \Delta \mathrm{t}\, \vec{v}_i(t) + \frac{\Delta t^2}{2}\frac{\vec{f_i}(t)}{m_i} + \ldots \qquad 13$$

where Δt is the time step and $\vec{\boldsymbol{v}}_{\mathbf{i}}$ is the velocity of the atom i. Verlet algorithm[137] is generally used to solve equation 13 in a microcanonical ensemble (NVE) where the total energy is conserved. This algorithm needs the knowledge of the force at the instant t:

$$\vec{r_i}(t+\Delta t) = 2\vec{r}_i(\mathrm{t}) - \vec{r_i}(t-\Delta t) + \Delta t^2 \frac{\vec{f_i}(t)}{2m_i} + 0(\Delta t^4) \qquad 14$$

Even though this algorithm is simple, its use remains effective and stable. Another algorithm that is widely used in MD simulations is the Verlet Leapfrog algorithm[138]. In order to obtain the position of an atom at t+Δt, this algorithm needs the values of the position and the forces at the instant t as well as the values of the velocities at t-1/2Δt. The first step consists of determining the value of the velocities of the particles:

$$\vec{v_i}(t+\frac{1}{2}\Delta t) = \vec{v_i}(t-\frac{1}{2}\Delta t) + \Delta t \frac{\vec{f_i}(t)}{m_i} \qquad 15$$

Then the positions are calculated using the new velocities:

$$\vec{r_i}(\mathrm{t}+\Delta\,\mathrm{t}) = \vec{r_i}(\mathrm{t}) + \Delta t \vec{v_i}(t+\frac{1}{2}\Delta t) \qquad 16$$

To obtain the velocities at the instant t, an average of two intermediate velocities is calculated as follow:

$$\vec{v_i}(t) = \frac{1}{2}[\vec{v_i}(t+\frac{1}{2}\Delta t) + \vec{v_i}(t-\frac{1}{2}\Delta t)] \quad 17$$

On the other hand, the velocity Verlet algorithm[276] enable the user to skip the last part assuming that the positions, the velocities and the forces are known at each time step. Like the Verlet Leapfrog algorithm, the first 2 steps consist of determining the velocities at t+1/2Δt in order to obtain the positions at t+Δt:

$$\vec{v_i}(t+\frac{1}{2}\Delta t) = \vec{v_i}(t) + \frac{1}{2}\Delta t\frac{\vec{f_i}(t)}{m_i} \quad 18$$

$$\vec{r_i}(\mathrm{t}+\Delta\mathrm{t}) = \vec{r_i}(\mathrm{t}) + \Delta t\vec{v_i}(t+\frac{1}{2}\Delta t) \quad 19$$

The forces acting on the particle i are recalculated using the following equation:

$$\vec{v_i}(t+\Delta t) = \vec{v_i}(t+\frac{1}{2}\Delta t) + \frac{1}{2}\Delta t\frac{\vec{f_i}(t+\Delta t)}{m_i} \quad 20$$

Once the equations are solved, the trajectory can be deduced in the microcanonical ensemble NVE where the number of particles, the volume and the energy are constant. The Hamiltonian of the system is then written as:

$$H_{NVE} = \sum_i \frac{1}{2}mv_i^2 + U \quad 21$$

For practical reasons, sometimes the pressure and/or the temperature are fixed also. Therefore the ensemble of the system will be the canonical ensemble NVT or the canonical isotherme-isobar ensemble NPT. Those two ensembles are obtained by using barostats and thermostats (next paragraph).

Additional algorithms should be used such as constraint algorithms in order to satisfy the Newtonian motion of rigid molecules. This algorithm insures

that the distance between mass points is maintained constant. In this study, the SHAKE[196] algorithm is used as a constraint algorithm to maintain the geometry of the system by satisfying the bond-length constraints.

Thermostats and Barostats

In order to run MD simulations in other ensembles than the microcanonical ensemble NVE, thermostats and/or barostats must be introduced. In this work, the Berendsen thermostat and barostat was used in all MD simulations.

A weak coupling method was introduced by Berendsen[139] to an external bath to correct the fluctuations of the actual temperature T from the desired temperature T_0. To do so, the velocities are multiplied by a scaling factor $\lambda = \sqrt{(1+\frac{\Delta t}{\tau_T}(\frac{T_0}{T(t)}-1))}$ to push the system towards the temperature T_0. Hence, the velocities are scaled at each time step in a way that the rate of change of temperature is proportional to the difference in temperature:

$$\frac{dT(t)}{dt} = \frac{T_0 - T(t)}{\tau_T} \qquad 22$$

where τ_T represents the relaxation time of the temperature fluctuations and the instantaneous temperature $T(t)=\sum_i \frac{1}{2} m_i v_i^2\,(t)$ obtained using the instantaneous velocities. This method generates a force on the system to converge towards the desired temperature:

Berendsen's Barostat on the other hand is an extended version of the method used in the thermostat in which the thermodynamic value to correct is the volume of the elementary volume. To do so, the atomic positions should be

changed. The motion equations are changed as function of the instantaneous pressure P(t) determined by the theorem of Viriel[277] so that P(t) converges towards the desired pressure P_0:

$$\frac{dP(t)}{dt} = \frac{P_0 - P(t)}{\tau_p} \qquad 23$$

where τ_p is the relaxation time of the pressure's fluctuations. While readjusting the atomic coordinates and the dimensions of the periodic box by a factor of ς, the box volume will be modified to $\Delta V=(\varsigma^3-1)V$

$$\varsigma = 1 - \frac{\beta \delta t}{\tau_p}(P_0 - P(t)) \qquad 24$$

where β is the isothermal compressibility and ς will be written as:

Periodic boundary conditions

Periodic boundary conditions allow the performance of an MD simulation of a large (infinite) system by using a relatively small number of particles (10^4-10^6). The particles experience forces as if they were in a bulk solution by replicating the elementary simulation box in all the 3 Cartesian directions (Fig. 2). Therefore, each particle i of the elementary box interacts with all the particles j in the same box and interacts as well with all the particles in the replicated boxes. In fact when a particle comes into or leaves the simulation region, an image particle leaves or enters this region conserving the number of particles. The surface effects are hence eliminated and the position of the box boundaries has no role.

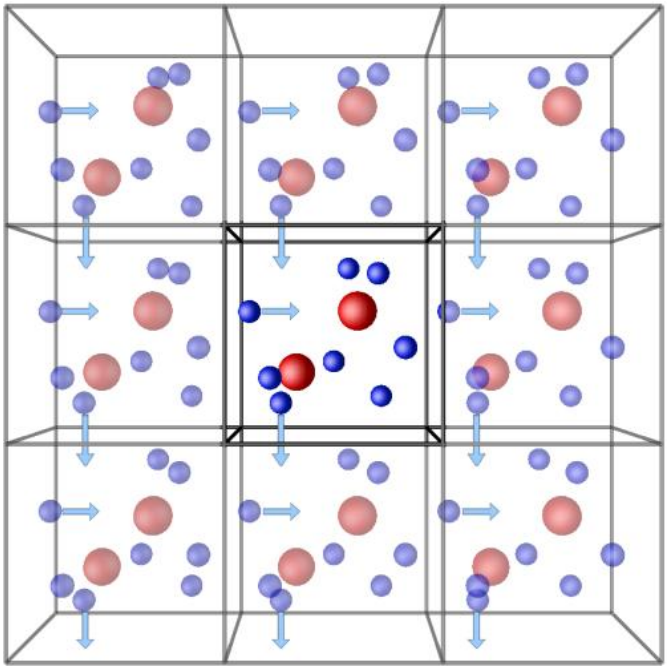

Fig. 2: Schematic representation of the periodic boundary condition concept.

The λ-integration approach:

In order to construct the transformation path between the liquid and the solid state, three separate reversible steps must be executed. Step 1 consists of the transition from the initial liquid state to a weakly attractive fluid. Step 2 consists of the transition to a solid constrained fluid and the final step will lead to the final solid state (see Fig. 3)

The main goal of the first step is to reversibly obtain a weakly attractive fluid state while contracting the cell volume. The volume contraction is necessary since the reference liquid state has a higher volume than the final crystalline state. The weakly attractive fluid is generated by progressively turning off the corresponding potential using a linear λ-integration where the potential is multiplied by a scaling function $f_1(\lambda)$ (equ. 25). λ starts from a value of 0 at first

and goes to 1.0 at the end of this step. The potential energy H of the first step can be represented as:

$$H(\lambda) = \sum_{i,j} \frac{1}{2} f_1(\lambda) E_l(r_{ij)} \quad 25$$

where $f_1(\lambda) = 1 - 0.9\lambda$ and $E_l(r)$ is the potential described in the previous section. When f depends only on the parameter λ (that varies from 0 to 1), we can write:

$$\Delta F_1 = \int_0^1 \frac{\partial F}{\partial \lambda} d\lambda = \int_0^1 \langle \frac{\partial H}{\partial \lambda} \rangle \, d\lambda \quad 26$$

This equation establishes the link between the free energy F, and the total energy H that is accessible at each molecular dynamics step.

Once the arbitrary weakly attractive fluid is created, a Gaussian well is gradually turned on using λ-integration in order to constrain the fluid to a solidlike structure. The Gaussian function can be written as follow:

$$E_{Gauss} = \sum_{i,k} a exp(-b r_{ik}^2) \quad 27$$

where r_{ik} is the distance of the ith atom from the Gaussian well at the kth lattice position, a and b are optimized constants so that the intermediate state of the solid constraint fluid resembles to the solid reference state. Hence the potential energy of the second step can be written as:

$$H(\lambda) = 0.1 \sum_{i,j} \frac{1}{2} E_l(r_{ij)} + \lambda E_{Gauss} \quad 28$$

where λ runs again from 0 to 1. The total Helmholtz free energy change during this step can be calculated similarly to the first step:

$$\Delta F_2 = \int_0^1 \frac{\partial F}{\partial \lambda} d\lambda = \int_0^1 \langle \frac{\partial H}{\partial \lambda} \rangle \, d\lambda \quad 29$$

The third step consists of turning on the main LJ potential while turning off the Gaussian potential at the same time in order to obtain the final reference solid state. The potential energy can be written as:

$$H(\lambda) = \sum_{i,j} \frac{1}{2} f_3(\lambda) E_l(r_{ij)} + (1-\lambda) E_{Gauss} \qquad 30$$

where $f_3(\lambda) = 0.1 + 0.9\lambda$.

The total Helmholtz free energy of the three steps described above will be thus:

$$\Delta F = \Delta F_1 + \Delta F_2 + \Delta F_3 \qquad 31$$

The Gibbs free energy is then obtained using the following relation:

$$\Delta G = \Delta F + P(V_c - V_l) \qquad 32$$

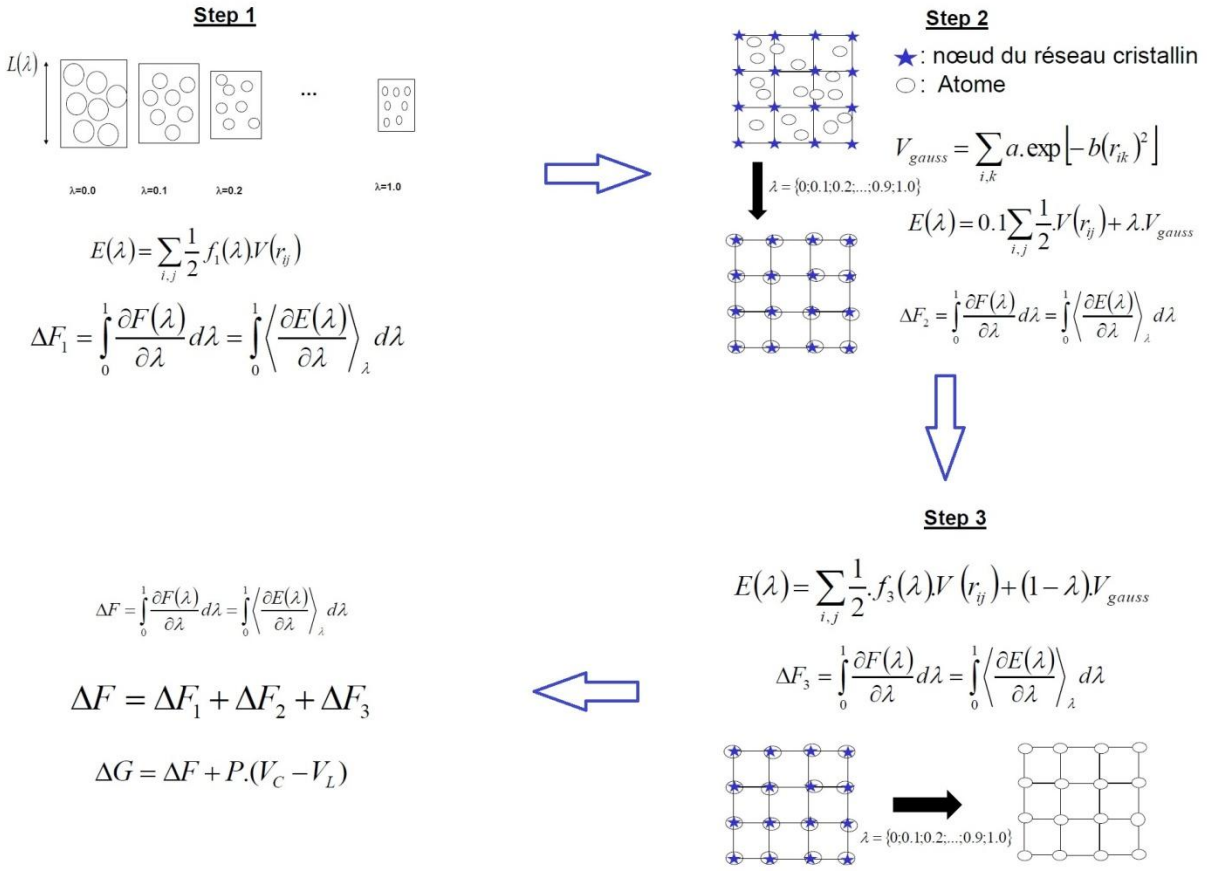

Fig 3: A schematic representation of the λ-integration approach[224] used to determine the Gibbs free energy between the crystal and the liquid (see text)

References

1. Debenedetti, P. G., *Metastable Liquids: Concepts and Principles.* Princeton University Press: Princeton, New jersey, 1996.
2. Gutzow, I.; Schmelzer, J. W. P., *The Vitreous State Thermodynamics, Structure, Rheology, and Crystallization.* 2 ed.; Springer Berlin, Heidelberg, 2013.
3. Deb, B.; Ghosh, A., Crystallization Kinetics in Selenium Molybdate Molecular Glasses. *Europhys. Lett.* **2011,** *95*, 26002-1-26002-5.
4. Surov, A. O.; Solanko, K. A.; Bond, A. D.; Perlovich, G. L.; Bauer-Brandl, A., Crystallization and Polymorphism of Felodipine. *Cryst. Growth Des.* **2012,** *12*, 4022-4030.
5. Gunn, E.; Guzei, I. A.; Cai, T.; Yu, L., Polymorphism of Nifedipine: Crystal Structure and Reversible Transition of the Metastable B Polymorph. *Cryst. Growth Des.* **2012,** *12*, 2037-2043.
6. Kang, D. H.; Zhang, H.; Yoo, H.; Lee, H. H.; Lee, S.; Lee, G. W.; Lou, H.; Wang, X.; Cao, Q.; Zhang, D.; et al., Interfacial Free Energy Controlling Glass-Forming Ability of Cu-Zr Alloys. *Sci. Rep.* **2014,** *4*, 5167-1-5167-5.
7. Wu, D. T.; Gránásy, L.; Spaepen, F., Nucleation and the Solid–Liquid Interfacial Free Energy. *MRS Bull.* **2004,** *29*, 945-950.
8. Zhang, K.; Wang, M.; Papanikolaou, S.; Liu, Y.; Schroers, J.; Shattuck, M. D.; O'Hern, C. S., Computational Studies of the Glass-Forming Ability of Model Bulk Metallic Glasses. *J. Chem. Phys.* **2013,** *139*, 124503-1-124503-8.
9. Zhang, K.; Liu, Y.; Schroers, J.; Shattuck, M. D.; O'Hern, C. S., The Glass-Forming Ability of Model Metal-Metalloid Alloys. *J. Chem. Phys.* **2015,** *142*, 104504-1-104504-5.
10. Shen, J.; Chen, Q.; Sun, J.; Fan, H.; Wang, G., Exceptionally High Glass-Forming Ability of an Fe Co Cr Mo Cb Y Alloy. *Appl. Phys. Lett.* **2005,** *86*, 151907-1-151907-3.
11. Alba, C.; Busse, L. E.; List, D. J.; Angell, C. A., Thermodynamic Aspects of the Vitrification of Toluene, and Xylene Isomers, and the Fragility of Liquid Hydrocarbons. *J. Chem. Phys.* **1990,** *92*, 617-624.
12. Ngai, K. L., *Relaxation and Diffusion in Complex Systems.* Springer Science & Business Media: New York, U.S.A., 2011.
13. Tanaka, H., Relationship among Glass-Forming Ability, Fragility, and Short-Range Bond Ordering of Liquids. *J. Non-Cryst. Solids* **2005,** *351*, 678-690.
14. Busch, R.; Liu, W.; Johnson, W. L., Thermodynamics and Kinetics of the $Mg_{65}cu_{25}y_{10}$ Bulk Metallic Glass Forming Liquid. *J. Appl. Phys.* **1998,** *83*, 4134-4141.
15. Kawakami, K.; Harada, T.; Yoshihashi, Y.; Yonemochi, E.; Terada, K., Correlation between Glass-Forming Ability and Fragility of Pharmaceutical Compounds. *J. Phys. Chem. B* **2015,** *119*, 4873-4880.
16. Baird, J. A.; Van Eerdenbrugh, B.; Taylor, L. S., A Classification System to Assess the Crystallization Tendency of Organic Molecules from Undercooled Melts. *J. Pharm. Sci.* **2010,** *99*, 3787-3806.
17. Wang, L.-M.; Richert, R., Glass Transition Dynamics and Boiling Temperatures of Molecular Liquids and Their Isomers. *J. Phys. Chem. B* **2007,** *111*, 3201-3207.
18. Kaminski, K.; Adrjanowicz, K.; Wojnarowska, Z.; Dulski, M.; Wrzalik, R.; Paluch, M., Do Intermolecular Interactions Control Crystallization Abilities of Glass-Forming Liquids? *J. Chem. Phys. B* **2011,** *115*, 11537-11547.

19. Zhou, D.; Zhang, G. G.; Law, D.; Grant, D. J. W.; Schmitt, E. A., Physical Stability of Amorphous Pharmaceuticals, Importance of Configurational Thermodynamic Quantities and Molecular Mobility. *J. Pharm. Sci.* **2002,** *91*, 1863-1872.
20. Sanz, A.; Nogales, A.; Ezquerra, T. A., Influence of Fragility on Polymer Cold Crystallization. *Macromolecules* **2010,** *43*, 29-32.
21. Ping, W.; Paraska, W. P. D.; Baker, R.; Harrowell, P.; Angell, C. A., Molecular Engineering of the Glass Transition: Glass-Forming Ability across a Homologous Series of Cyclic Stilbenes. *J. Phys. Chem. B* **2011,** *115*, 4696–4702.
22. Kauzmann, W., The Nature of the Glassy State and the Behavior of Liquids at Low Temperatures. *Chem. Rev.* **1948,** *43*, 219-256.
23. Turnbull, D., Under What Conditions Can a Glass Be Formed? *Contemp. Phys.* **1969,** *10*, 473-488.
24. Belieres, J.-P.; Angell, C. A., Protic Ionic Liquids: Preparation, Characterization, and Proton Free Energy Level Representation. *J. Phys. Chem. B* **2007,** *111*, 4926-4937.
25. Baird, J. A.; Santiago-Quinonez, D.; Rinaldi, C.; Taylor, L. S., Role of Viscosity in Influencing the Glass-Forming Ability of Organic Molecules from the Undercooled Melt State. *Pharm. Res.* **2012,** *29*, 271-284.
26. Descamps, M.; Dudognon, E., Crystallization from the Amorphous State: Nucleation–Growth Decoupling, Polymorphism Interplay, and the Role of Interfaces. *J. Pharm. Sci.* **2014,** *103*, 2615–2628.
27. Pedersen, U. R.; Harrowell, P., Factors Contributing to the Glass-Forming Ability of a Simulated Molecular Liquid. *J. Phys. Chem. B* **2006,** *115*, 14205-14209.
28. Trasi, N. S.; Baird, J. A.; Kestur, U. S.; Taylor, L. S., Factors Influencing Crystal Growth Rates from Undercooled Liquids of Pharmaceutical Compounds. *J. Phys. Chem. B* **2014,** *118*, 9974−9982.
29. Jackson , K. A., The Interface Kinetics of Crystal Growth Processes. *Interface Sci.* **2002,** *10*, 159–169.
30. Andronis, V.; Zografi, G., Crystal Nucleation and Growth of Indomethacin Polymorphs from the Amorphous State. *J. Non-Cryst. Solids* **2000,** *271*, 236-248.
31. Porter, D. A.; Easterling, K. E., *Phase Transformations in Metals and Alloys*. CRC Press: Boca Raton, U.S.A., 1992.
32. Kirkpatrick, R. J., Crystal Growth from the Melt: A Review. *Am. Mineral.* **1975,** *60*, 798-614.
33. Woodruff, D. P., *The Solid-Liquid Interface*. Cambridge University Press: London, U.K., 1973.
34. Turnbull, D., Formation of Crystal Nuclei in Liquid Metals. *J. Appl. Phys.* **1950,** *21*, 1022-1028.
35. Hoffman, J. D., Thermodynamic Driving Force in Nucleation and Growth Processes. *J. Chem. Phys.* **1958,** *29*, 1192-1193.
36. Becker, S. R.; Poole, P. H.; Starr, F. W., Fractional Stokes-Einstein and Debye-Stokes-Einstein Relations in a Network-Forming Liquid. *Phys. Rev. Lett.* **2006,** *97*, 055901-1-055901-4.
37. Wang, J.; Tang, Y. W.; Zeng, X. C., Solid-Liquid Interfacial Free Energy of Water: A Molecular Dynamics Simulation Study. *J. Chem. Theory Comput.* **2006,** *3*, 1494-1498.
38. Feng, X.; Laird, B. B., Calculation of the Crystal-Melt Interfacial Free Energy of Succinonitrile from Molecular Simulation. *J. Chem. Phys.* **2006,** *124*, 044707-1-044707-5.

39. Ocak, Y.; Akbulut, S.; Keslioglu, K.; Marasli, N., Solid-Liquid Interfacial Energy of Neopentylglycol. *J. Colloid Interface Sci.* **2008,** *320*, 555-562.
40. Roazas, R. E.; Horbach, J., Capillary Wave Analysis of Rough Solid-Liquid Interfaces in Nickel. *Europhys. Lett.* **2011,** *93*, 26006-1-26006-6.
41. Bai, X.; Li, M., Calculation of Solid-Liquid Interfacial Free Energy: A Classical Nucleation Theory Based Approach. *J. Chem. Phys.* **2006,** *124*, 124707-1-124707-12.
42. Lu, Z. P.; Liu, C. T., Glass Formation Criterion for Various Glass Forming Systems. *Phys. Rev. Lett.* **2003,** *91*, 115505.
43. Andronis, V.; Zografi, G., Molecular Mobility of Supercooled Amorphous Indomethacin, Determined by Dynamic Mechanical Analysis. *Pharm. Res.* **1997,** *14*, 410-414.
44. Fukuoka, E.; Makita, K. R.; Yamamura, S., Glassy State of Pharmaceuticals. Iii. Thermal Properties and Stability of Glassy Pharmaceuticals and Their Binary Glass Systems. *Chem. Pharm. Bull* **1989,** *37*, 1047-1050.
45. Marsac, P. J.; Konno, H.; Taylor, L. S., A Comparison of the Physical Stability of Amorphous Felodipine and Nifedipine Systems. *Pharm. Res.* **2006,** *23*, 2306-2316.
46. Kestur, U. S.; Taylor, L. S., Evaluation of the Crystal Growth Rate of Felodipine Polymorphs in the Presence and Absence of Additives as a Function of Temperature. *Cryst. Growth Des.* **2013,** *13*, 4349−4354.
47. Gnutzmann, T.; Kahlau, R.; Scheifler, S.; Friedrichs, F.; Rossler, E. A.; Rademann, K.; Emmerling, F., Crystal Growth Rates and Molecular Dynamics of Nifedipine. *CrystEngComm* **2013,** *15*, 4062-4069.
48. Ishida, H.; Wu, T.; Yu, L., Sudden Rise of Crystal Growth Rate of Nifedipine near Tg without and with Polyvinylpyrrolidone. *J. Pharm. Sci.* **2007,** *96*, 1131-1138.
49. Porter, D. A.; Easterling, K. E., *Phase Transformations in Metals and Alloys*. Chapman & Hall: London, U.K., 1992.
50. Veesler, S.; Puel, F.; Fevotte, G., Polymorphisme Dans Les Procédés De Cristallisation En Solution. *Pharma Pratiques* **2003,** *13* (2).
51. Puel, F.; Vessler, S.; Mangin, D., Cristallisation Industrielle : Aspects Théoriques. *Techniques de l'Ingénieur* **2005,** *J2710*.
52. Saridakis, W.; Chayen, N. E., Towards a 'Universal' Nucleant for Protein Crystallization. *Trends Biotechnol.* **2009,** *27*, 99-106.
53. Zhou, D.; Zhang, G. G. Z.; Law, D.; Grant, D. J. W.; Schmitt, E. A., Thermodynamics, Molecular Mobility and Crystallization Kinetics of Amorphous Griseofulvin. *Mol. Pharm.* **2008,** *5*, 927-936.
54. Ediger, M. D.; Harrowell, P.; Yu, L., Crystal Growth Kinetics Exhibit a Fragility-Dependent Decoupling from Viscosity. *J. Chem. Phys.* **2008,** *128*, 034709-1-034709-6.
55. Kashiev, D., *Nucleation: Basic Theory with Applocations*. Butterworth-Heinemann: Oxford, 2000.
56. Volmer, M.; Weber, A., Keimbildung in Übersättigten Gebilden. *Z. Phys. Chem.* **1926,** *119*, 277.
57. Farkas, L., Keimbildungsgeschwindigkeit in Übersättigten Dämpfen. *Z. Phys. Chem.* **1927,** *125*, 239.
58. Wu, T.; Yu, L., Origin of Enhanced Crystal Growth Kinetics near Tg Probed with Indomethacin Polymorphs. *J. Phys. Chem. B* **2006,** *110*, 15694-15699.
59. Gutzow, I., The Mechanism of Crystal Growth in Glass Forming Systems. *J. Cryst. Growth* **1977,** *42*, 15-23.

60. Masuhr, A.; Waniuk, T. A.; Busch, R.; Johnson, W. L., Time Scales for Viscous Flow, Atomic Transport, and Crystallization in the Liquid and Supercooled Liquid States of $Zr_{41.2}Ti_{13.8}Cu_{12.5}Ni_{10.0}Be_{22.5}$. *Phys. Rev. Lett.* **1999,** *82*, 2290-2293.
61. Rao, K. J., *Structural Chemistry of Glasses.* Elsevier Science Oxford, U.K., 2002.
62. B. Rodriguez-Spong, C. P. P., A. Jayasankar, A. J. Matzger, N. Rodrıguez-Hornedo, General Principles of Pharmaceutical Solid Polymorphism a Supramolecular Perspective. *Advanced Drug Delivery Reviews* **2003,** *56*, 241–274.
63. Makoto Otsuka , T. O., Yoshihisa Matsuda, Effect of Environmental Humidity on the Transformation Pathway of Carbamazepine Polymorphic Modifications During Grinding. *Colloids and Surfaces B: Biointerfaces* **1999,** *13*, 263-273.
64. Byrn, S. R., *Solid-State Chemistry of Drugs*. Academic Press: New York, U.S., 1982.
65. Haleblian, J. K., Characterization of Habits and Crystalline Modification of Solids and Their Pharmaceutical Applications. *J. Pharm. Sci.* **1975,** *64*, 1269-1288.
66. Defossemont, G.; Randzio, S.; Legendre, B., Identification of an Enantiotropic System with Hindered Multiphase Transitions Reexamination of Polymorphism in Carbamazepine. *J. Therm. Anal. Calorim.* **2007,** *89*, 751–755.
67. Hu, Y.; Wikström, H.; Byrn, S. R.; Taylor, L. S., Estimation of the Transition Temperature for an Enantiotropic Polymorphic System from the Transformation Kinetics Monitored Using Raman Spectroscopy. *J. Pharm. Biomed. Anal.* **2007,** *45*, 546–551.
68. Crowley, K. J.; Zografi, G., The Use of Thermal Methods for Predicting Glass-Former Fragility. *Thermochim. Acta* **2001,** *380*, 79-93.
69. Debenedetti, P. G.; Truskett, T. M.; Lewis, C. P.; Stillinger, F. H., Theory of Supercooled Liquids and Glasses: Energy Landscape and Statistical Geometry Perspectives. *Advances in Chemical Engineering* **2003,** *28*, 21-79.
70. Angell, C. A., *Strong and Fragile Liquids, In: Relaxations in Complex Systems*. National Technical Information Service: N.Y., U.S, 1985 (National Technical Information Service, U.S. Dept. of Commerce, Springfield, 1985). .
71. Vogel, H., Das Temperatur-Abhängigkeitsgesetz Der Viskosität Von Flüssigkeiten. *Phys. Zeit.* **1921,** *22*, 645.
72. Tammann, G.; Hesse, W., Die Abängigkeit Der Viskosität Von Der Temperature Bei Unterkühlten Flüssigkeiten. *Z. Anorg. Allg. Chem.* **1926,** *156*, 245.
73. Fulcher, G. S., Analysis of Recent Measurements of the Viscosity of Glasses. *J. Am. Ceram. Soc.* **1925,** *8*, 339.
74. Wang, L.-M.; Angell, C. A.; Richert, R., Fragility and Thermodynamics in Nonpolymeric Galss-Forming Liquids. . *J. Chem. Phys.* **2006,** *125*, 074505-1-074505-6.
75. Ostwald, W., Studien Uber Die Bildung Und Umwandlung Fester Korper. *Z. Phys. Chem.* **1897**, 289-330.
76. Spaepen, F., A Structural Model for the Solid-Liquid Interface in Monatomic Systems. *Acta Metall.* **1975,** *23*, 729-743.
77. Ozer, A.; Bayram, U.; Aksoz, S.; Marasli, N., Solid-Liquid Interfacial Energy of Neopentylglycol Solid Solution in Equilibrium with Succinonitrile-Neopentylglycol-Aminomethylpropanediol Liquid. *J. Cryst. Growth* **2013,** *364*, 34-39.
78. Laird, B. B., The Solid-Liquid Interfacial Free Energy of Close-Packed Metals: Hard-Spheres and the Turnbull Coefficient. *J. Chem. Phys.* **2001,** *115*, 2887-2888.

79. Peng, L. J.; Morris, J. R.; Aga, R. S., A Parameter-Free Prediction of Simulated Crystal Nucleation Times in the Lennard-Jones System: From the Steady-State Nucleation to the Transient Time Regime. *J. Chem. Phys.* **2010,** *133*, 084505-1-084505-6.
80. Aga, R. S.; Morris, J. R.; Hoyt, J. J.; Mendelev, M., Quantitative Parameter-Free Prediction of Simulated Crystal-Nucleation Times. *Phys. Rev. Lett.* **2006,** *96*, 245701-1-45701-4.
81. Kelton, K. F.; Ehrenreich, H.; Turnbull, D., *Solid State Physics*. Academic Press: Boston, U.S.A., 1991.
82. Turnbull, D., Kinetics of Solidification of Supercooled Liquid Mercury Droplets. *J. Chem. Phys.* **1952,** *20*, 411-424.
83. Jones, D. R. H.; Chadwick, G. A., Experimental Measurement of the Solid-Liquid Interfacial Energies of Transparent Materials. *Philos. Mag.* **1970,** *22*, 291-300.
84. Gunduz, M.; Hunt, J. D., The Measurement of Solid-Liquid Surface Energies in the Al-Cu, Al-Si and Pb-Sn Systems. *Acta Metall.* **1985,** *33*, 1651-1672.
85. Gunduz, M.; Hunt, J. D., Solid-Liquid Surface Energy in the Al-Mg System. *Acta Metall.* **1989,** *37*, 1839-1845.
86. Glicksman, M. E.; Vold, C. L., Determination of Absolute Solid-Liquid Interfacial Free Energies in Metals. *Acta Metall.* **1969,** *17*, 1-11.
87. Glicksman, M. E.; Vold, C. L., Establishment of Error Limits on the Solid-Liquid Interfacial Free Energy of Bismuth. *Scripta Metall.* **1971,** *5*, 493-498.
88. Herring, C.; Kingston, W. E., *The Physics of Powder Metallurgy*. McGraw-Hill: New York, U.S., 1953.
89. Jones, D. R. H., Review the Free Energies of Solid-Liquid Interfaces. *J. Mater. Sci.* **1974,** *9*, 1-17.
90. Jones, H., An Evaluation of Measurements of Solid/Liquid Interfacial Energies in Metallic Alloy Systems by the Groove Profile Method. *Metallurgical and Materials Transactions A* **2007,** *38*, 1563-1569.
91. Broughton, J. Q.; Gilmer, G. H., Molecular Dynamics Investigation of the Crystal-Fluid Interface. Vi. Excess Surface Free Energies of Crystal-Liquid Systems. *J. Chem. Phys.* **1986,** *84*, 5759-5768.
92. Davidchack, R. L.; Laird, B. B., Direct Calculation of the Hard-Sphere Crystal/Melt Interfacial Free Energy. *Phys. Rev. Lett.* **2000,** *85*, 4751-4754.
93. Davidchack, R. L.; Laird, B. B., Direct Calculation of the Crystal-Melt Interfacial Free Energies for Continuous Potentials: Application to the Lennard-Jones System. *J. Chem. Phys.* **2003,** *118*, 7651-7657.
94. Handel , R.; Davidchack, R. L.; Anwar, J.; Brukhno, A. V., Direct Calculation of Solid-Liquid Interfacial Free Energy for Molecular Systems: Tip4p Ice-Water Interface. *Phys. Rev. Lett.* **2008,** *100*, 036104-1036104-4.
95. Shibuta, Y.; Watanabe, Y.; Suzuki, T., Growth and Melting of Nanoparticles in Liquid Iron: A Molecular Dynamics Study. *Chem. Phys. Lett.* **2009,** *475*, 264-268.
96. Hoyt, J. J.; Asta, M., Atomistic Computation of Liquid Diffusivity, Solid-Liquid Interfacial Free Energy, and Kinetic Coefficient in Au and Ag. *Phys. Rev. B* **2002,** *65*, 214106-1-214106-11.
97. Hoyt, J. J.; Asta, M.; Karma, A., Method for Computing the Anisotropy of the Solid-Liquid Interfacial Free Energy. *Phys. Rev. Lett.* **2000,** *86*, 5530-5533.
98. Davidchack, R. L.; Morris, J. R.; Laird, B. B., The Anisotropic Hard-Sphere Crystal-Melt Interfacial Free Energy from Fluctuations. *J. Chem. Phys.* **2006,** *125*, 094710-1-094710-7.

99. Amini, M.; Laird, B. B., Crystal-Melt Interfacial Free Energy of Binary Hard Spheres from Capillary Fluctuations. *Phys. Rev. E* **2008,** *78*, 144112-1-144112-6.
100. Morris, J. R., Complete Mapping of the Anisotropic Free Energy of the Crystal-Melt Interface in Al. *Phys. Rev. B* **2002,** *66*, 144104-1-144104-7.
101. Becker, C. A.; Olmsted, D. L.; Asta, M.; Hoyt, J. J.; Foiles, S. M., Atomistic Simulations of Crystal-Melt Interfaces in a Model Binary Alloy: Interfacial Free Energies,Adsorption Coefficients, and Excess Entropy. *Phys. Rev. B* **2009,** *79*, 054109-1-054109-13.
102. Benet, J.; MacDowell, L. G.; Sanz, E., A Study of the Ice-Water Interface Using the Tip4p/2005 Water Model. *Phys. Chem. Chem. Phys.* **2014,** *16*, 22159-22166.
103. Van den Mooter, G.; Wuyts, M.; Blaton, N.; Busson, R.; Grobet, P.; Augustijns, P.; Kinget, R., Physical Stabilisation of Amorphous Ketoconazole in Solid Dispersions with Polyvinylpyrrolidone K25. *Eur. J. Pharm Sci.* **2001,** *12*, 261-269.
104. Tantishaiyakul, V.; Kaewnopparat, N.; Ingkatawornwong, S., Properties of Solid Dispersions of Piroxicam in Polyvinylpyrrolidone. *Int. J. Pharm.* **1999,** *181*, 143-151.
105. Vasconcelos, T.; Sarmento, B.; Costa, P., Solid Dispersions as Strategy to Improve Oral Bioavailability of Poor Water Soluble Drugs. *Drug Discov. Today* **2007,** *12*, 1068-1075.
106. Kestur, U. S.; Taylor, L. S., Role of Polymer Chemistry in Influencing Crystal Growth Rates from Amorphous Felodipine. *CrystEngComm* **2010,** *12*, 2390–2397.
107. Niraj S. Trasi, J. A. B., Umesh S. Kestur, and Lynne S. Taylor, Factors Influencing Crystal Growth Rates from Undercooled Liquids of Pharmaceutical Compounds *the journal of physical Chemistry B* **2014,** *118*, 9974−9982.
108. Hancock, B. C.; Zografi, G., Characteristics and Significance of the Amorphous State in Pharmaceutical Systems. *J. Pharm. Sci.* **1996,** *86*, 1-12.
109. Gross, E. K. U.; Dreizler, R. M., *Density Functional Theory*. Springer Science+Business Media: New York, U.S.A., 1995.
110. Rapaport, D. C., *The Art of Molecular Dynamics Simulation.* Cambridge University Press: Cambridge, U.K., 1995.
111. Groot, R. D., Mesoscopic Simulation of Polymer−Surfactant Aggregation. *Langmuir* **2000,** *16*, 7493-7502.
112. Reddy, J. N., *An Introduction to the Finite Element Method*. McGraw-Hill: 2006.
113. Karplus, M.; McCammon, J. A., Molecular Dynamics Simulations of Biomolecules. *Nature Structural & Molecular Biology* **2002,** *9*, 646 - 652.
114. Harvey, M. J.; Giupponi, G.; De Fabritiis, G., Acemd: Accelerating Biomolecular Dynamics in the Microsecond Time Scale. *J. Chem. Theory Comput.* **2009,** *5*, 1632–1639.
115. Hong, C.; Tieleman, D. P.; Wang, Y., Microsecond Molecular Dynamics Simulations of Lipid Mixing. *Langmuir* **2014,** *30* 11993-12001.
116. Matsumoto, M.; Saito, S.; Ohmine, I., Molecular Dynamics Simulation of the Ice Nucleation and Growth Process Leading to Water Freezing. *Nat. Biotechnol.* **2002,** *416*, 409-413.
117. Wang, J.; Hou, T., Application of Molecular Dynamics Simulations in Molecular Property Prediction. 1. Density and Heat of Vaporization. *J. Chem. Theory Comput.* **2011,** *7*, 2151–2165.
118. Cui, S. T.; Gupta, S. A.; Cummingsand, P. T.; Cochran, H. D., Molecular Dynamics Simulations of the Rheology of Normal Decane,Hexadecane, and Tetracosane. *J. Chem. Phys.* **1996,** *105*, 1214-1220.

119. Jabbarzadeh, A.; Tanner, R. I., Molecular Dynamics Simulation and Its Application to Nano-Rheology. *Rheology Reviews* **2006**, 165-216.
120. Allen, M. P.; Tildesley, D. J., *Computer Simulation of Liquids*. Oxford University Press: New York, U.S., 1991.
121. Monticelli, L.; Tieleman, D. P., Force Fields for Classical Molecular Dynamics. *Methods Mol. Biol.* **2013,** *924*, 197-213.
122. Gavezzotti, A., *Molecular Aggregation Structure Analysis and Molecular Simulation of Crystals and Liquids*. Oxford University Press: 2007.
123. Lifson, A.; Warshel, A., Consistent Force Field for Calculations of Conformations Vibrational Spectra and Enthalpies of Cycloalkane and N-Alkane Molecules. *J. Chem. Phys.* **1968,** *49*, 5116.
124. Margottin-Maclou, M., Calcul Du Champ De Force Et Interprétation Des Spectres De Vibration De L'alcool Méthylique ($C-H_3$ O-H, $C-H_3$ O-D, $C-D_3$ O-H & $C-D_3$ O-D). *J. Phys. Rad.* **1960,** *21*, 634-644.
125. McCammon , J. A.; Gelin, B. R.; Karplus, M., Dynamics of Folded Proteins. *Nature* **1977,** *267*, 585-590.
126. Levitt, M.; Warshel, A., Computer Simulation of Protein Folding. *Nature* **1975,** *253*, 694-698.
127. Warshel, A.; Levitt, M., Theoretical Studies of Enzymic Reactions: Dielectric, Electrostatic and Steric Stabilization of the Carbonium Ion in the Reaction of Lysozyme. *J. Mol. Biol.* **1976,** *102*, 227-249.
128. Case, D. A.; Babin, V.; Berryman, J. T.; Betz, R. M.; Cai, Q.; Cerutti, D. S.; Cheatham III, T. E.; Darden, T. A.; Duke, R. E.; Gohlke, H.; et al., Amber 14 University of California, San Francisco. **2014**.
129. Brooks, B. R.; Brucolleri, R. E.; Olafson, B. D.; States, D. J.; Swaminathan, S.; Karplus, M., Charmm: A Program for Macromolecular Energy, Minimization, and Dynamics Calculations. *J. Comput. Chem.* **1983,** *4*, 187-217.
130. Jorgensen, W. L.; Maxwell, D. S.; TiradoRives, J., Development and Testing of the Opls All-Atom Force Field on Conformational Energetics and Properties of Organic Liquids. *J. Am. Chem. Soc.* **1996,** *118*, 11225-11236.
131. T., S., *Molecular Modeling and Simulation: A Interdisciplinary Guide.* Springer: New York, U.S., 2010; Vol. 21.
132. Leach, A. R., *Molecular Modelling: Principles and Applications.* Prentice Hall: 2001.
133. Ponder, J. W.; D.A., C., Force Fields for Protein Simulations. *Adv. Protein Chem.* **2003,** *66*, 27-85.
134. Wang, J.; Wolf, R. M.; Caldwell, J. W.; Kollman, P. A.; Case, D. A., Development and Testing of a General Amber Force Field. *J. Comput. Chem.* **2004,** *25*, 1157-1174.
135. Caleman, C.; Van Maaren, P. J.; Hong, M.; Hub, J. S.; Costa, L. T.; Van der Spoel, D., Force Field Benchmark of Organic Liquids: Density, Enthalpy of Vaporization, Heat Capacities, Surface Tension, Isothermal Compressibility, Volumetric Expansion Coefficient, and Dielectric Constant. *J. Chem. Theory Comput.* **2011,** *8*, 61-74.
136. Todorov, I. T.; Smith, W.; Trachenko, K.; Dove, M. T., Dl_Poly_3: New Dimensions in Molecular Dynamics Simulations Via Massive Parallelism. *J. Mater. Chem.* **2006,** *16*, 1911-1918.
137. Verlet, L., Computer "Experiments" on Classical Fluids. I. Thermodynamical Properties of Lennard-Jones Molecules. *Physical Review* **1967,** *159*, 98-103.

138. Hockney, R. W., The Potential Calculation and Some Applications. *Methods in Computational Physics* **1970,** *9*, 136-211.
139. Berendsen, H. J. C.; Postma, J. P. M.; van Gusteren, W. F.; DiNola, A.; Haak, J. R., Molecular Dynamics with Coupling to an External Bath. *J. Chem. Phys.* **1984,** *81*, 3684-3690.
140. Philibert, J., One and a Half Century of Diffusion: Fick, Einstein,before and Beyond. *The Open-Access Journal for the Basic Principles of Diffusion Theory, Experiment and Application* **2005**.
141. Rousseau, B.; Petravic, J., Transport Coefficients of Xylene Isomers. *J. Chem. Phys. B* **2002,** *106*, 13010-13017.
142. Mauro, J. C.; Yue, Y.; Ellison, A. J.; Gupta, P. K.; Allan, D. C., Viscosity of Glass-Forming Liquids. *PNAS* **2009,** *106*, 19780-19784.
143. Cleri, F.; Rosato, V., Tight-Binding Potentials for Transition Metals and Alloys. *Phys. Rev. B* **1993,** *48* (1), 22-33.
144. Morris, J. R.; Song, X., The Melting Lines of Model Systems Calculated from Coexistence Simulations. *J. Chem. Phys.* **2002,** *116*, 9352-9358.
145. Frenkel, D.; Smit, B., *Understanding Molecular Simlation*. Academic: San Diego, U.S., 1996.
146. Lai, P.-K.; Hsieh, C.-M.; Lin, S.-T., Rapid Determination of Entropy and Free Energy of Mixtures from Molecular Dynamics Simulations with the Two-Phase Thermodynamic Model. *Phys. Chem. Chem. Phys.* **2012,** *14*, 15206-15213.
147. Morris, J. R.; Wang, C. Z.; Ho, K. M.; Chan, C. T., Melting Line of Aluminum from Simulations of Coexisting Phases. *Phys. Rev. B* **1993,** *49*, 3109-3115.
148. Fernández, R. G.; Abascal, J. L. F.; Vega, C., The Melting Point of Ice Ih for Common Water Models Calculated from Direct Coexistence of the Solid-Liquid Interface. *J. Chem. Phys.* **2006,** *124*, 144506.
149. Harafuji, K.; Tsuchiya, T.; Kawamura, K., Molecular Dynamics Simulation for Evaluating Melting Point of Wurtzite-Type Gan Crystal. *J. Appl. Phys.* **2004,** *96*, 2501.
150. Agrawal, P. M.; Rice, B. M.; Thompson, D. L., Molecular Dynamics Study of the Melting of Nitromethane. *J. Chem. Phys.* **2003,** *119*, 9617.
151. Noya, E. G.; Vega, C.; de Miguel, E., Determination of the Melting Point of Hard Spheres from Direct Coexistence Simulation Methods. *J. Chem. Phys.* **2008,** *128*, 154507.
152. Liu, J.; Davidchack, R. L.; Dong, H. B., Molecular Dynamics Calculation of Solid-Liquid Interfacial Energy and Its Anisotropy During Iron Solidification. *Computational Materials Science* **2013,** *74*, 92.
153. Alfè, D., First-Principles Simulations of Direct Coexistence of Solid and Liquid Aluminum. *Phys. Rev. B* **2003,** *68*, 064423.
154. Belonoshko, A. B.; Ahuja, R.; Johansson, B., Quasi–Ab Initio Molecular Dynamic Study of Fe Melting. *Phys. Rev. Lett.* **2000,** *84*, 3638.
155. Sibug-Aga, R.; Laird, B. B., Simulations of Binary Hard-Sphere Crystal-Melt Interfaces: Interface between a One-Component Fcc Crystal and a Binary Fluid Mixture *J. Chem. Phys.* **2002,** *116*, 3410.
156. Lanning, O. J.; Shellswell, S.; Madden, P. A., Solid–Liquid Coexistence in Ionic Systems and the Properties of the Interface. *Molecular Physics: An International Journal at the Interface Between Chemistry and Physics* **2007,** *102* (9-10), 839-855.
157. Abascal, J. L. F.; Fernández, R. G.; Vega, C.; Carignano, M. A., The Melting Temperature of the Six Site Potential Model of Water. *J. Chem. Phys.* **2006,** *125*, 166101.

158. Bryk, T.; Haymet, A. D. J., Ice 1h/Water Interface of the S P C/E Model: Molecular Dynamics Simulations of the Equilibrium Basal and Prism Interfaces *J. Chem. Phys.* **2002,** *117*, 10258.
159. Mastny, E. A.; De Pablo, J. J., Melting Line of the Lennard-Jones System, Infinite Size, and Full Potential. *J. Chem. Phys.* **2007,** *127*, 104504-1-104504-8.
160. Kirkwood, J. G., Statistical Mechanics of Fluid Mixtures. *J. Chem. Phys.* **1935,** *3*, 300.
161. Harvey, J.-P.; Gheribi, A. E.; Chartrand, P., Accurate Determination of the Gibbs Energy of Cu–Zr Melts Using the Thermodynamic Integration Method in Monte Carlo Simulations. *J. Chem. Phys.* **2011,** *135*, 084502-084513.
162. Zhang, Y.; Maginn, E. J., A Comparison of Methods for Melting Point Calculation Using Molecular Dynamics Simulations. *J. Chem. Phys.* **2012,** *136*, 144116-1-144116-12.
163. Lin, S.-T.; Blanco, M.; Goddard, W. A., The Two-Phase Model for Calculating Thermodynamic Properties of Liquids from Molecular Dynamics: Validation for the Phase Diagram of Lennard-Jones Fluids. *J. Chem. Phys.* **2003,** *119*, 11792-11805.
164. Lin, S.-T.; Maiti, P. K.; Goddard, W. A., Two-Phase Thermodynamic Model for Efficient and Accurate Absolute Entropy of Water from Molecular Dynamics Simulations. *J. Phys. Chem. B* **2010,** *114*, 8191–8198.
165. Pascal, T. A.; Lin, S.; Goddard, W. A., Thermodynamics of Liquids: Standard Molar Entropies and Heat Capacities of Common Solvents from 2pt Molecular Dynamics. *PCCP* **2011,** *13*, 169–181.
166. Pirzadeh, P.; Beaudoin, E. N.; Kusalik, P. G., Interfacial Free Energy: An Entropy Portent to Energy Changes. *Cryst. Growth Des.* **2012,** *12*, 124-128.
167. Uberti, S. A.; Ceriotti, M.; Lee, P. D.; Finnnis, M. W., Solid-Liquid Interface Free Energy through Metadynamics Simulations. *Phys. Rev. B* **2010,** *81*, 125416-1-125416-11.
168. Luo, S. N.; Strachan, A.; Swift, D. C., Deducing Solid-Liquid Interfacial Energy from Superheating or Supercooling: Application to H2o at High Pressures. *Modell. Simul. Mater. Sci. Eng.* **2005,** *13*, 321-328.
169. Laird, B. B.; Davidchack, R. L.; Yang, Y.; Asta, M., Determination of the Solid-Liquid Interfacial Free Energy Along a Coexistence Line by Gibbs-Cahn Integration. *J. Chem. Phys.* **2009,** *131*, 114110-1-114110-8.
170. Zhou, H.; Lin, X.; Wang, M.; Huang, W., Calculation of Crystal-Melt Interfacial Free Energies of Fcc Metals. *J. Cryst. Growth* **2012,** *366*, 82-87.
171. Zhou, H.; Lin, X.; Wang, M.; Huang, W., Calculation of Solid-Liquid Interfacial Free Energy of Cu by Two Different Methods. *J. Cryst. Growth* **2013,** *377*, 107-111.
172. Benjamin, R.; Horbach, J., Crystal-Liquid Interfacial Free Energy Via Thermodynamic Integration. *J. Chem. Phys.* **2014,** *141*, 044715-1-044715-11.
173. Benjamin, R.; Horbach, J., Crystal-Liquid Interfacial Free Energy of Hard Spheres Via a Thermodynamic Integration Scheme. *Phys. Rev. B* **2015,** *91*, 032410-1-032410-10.
174. Espinosa, J. R.; Vega, C.; Sanz, E., The Mold Integration Method for the Calculation of the Crystal-Fluid Interfacial Free Energy from Simulations. *J. Chem. Phys.* **2014,** *141*, 134709-1-134709-14.
175. Safran, S. A., *Statistical Thermodynamics of Surfaces, Interfaces, and Membranes.* Westview Press: Colorado, USA, 2003.
176. Morris, J. R.; Napolitano, R. E., Developments in Determining the Anisotropy of Solid-Liquid Interfacial Free Energy. *JOM* **2004,** *56*, 40-44.

177. Potter, A. A.; Hoyt, J. J., A Molecular Dynamics Simulation Study of the Crystal-Melt Interfacial Free Energy and Its Anisotropy in the Cu-Ag-Au Ternary System. *J. Cryst. Growth* **2011,** *327*, 227-232.
178. Morris, J. R.; Song, X., The Anisotropic Free Energy of the Lennard-Jones Crystal-Melt Interface. *J. Chem. Phys.* **2003,** *119*, 3920-3925.
179. Hoyt, J. J.; Trautt, Z. T.; Upmanyu, M., Fluctuations in Molecular Dynamics Simulations. *Mathematics and Computers in Simulation* **2010,** *80*, 1382.
180. Vink, R. L. C.; Horbach, J.; Binder, K., Capillary Waves in a Colloid-Polymer Interface. *J. Chem. Phys.* **2005,** *122*, 134905.
181. Karma, A., Fluctuations in Solidification. *Phys. Rev. E* **1993,** *48* (5).
182. Landau, L. D.; Lifshitz, E. M., *Physique Theorique Physique Statistique*. Edition Mir 1994: 1984.
183. Boal, D., *Mechanics of the Cell.* Cambridge University press: Cambridge, 2002.
184. Reinhardt, A.; Doye, J. P. K.; Noya, E. G.; Vega, C., Local Order Parameters for Use in Driving Homogeneous Ice Nucleation with All-Atom Models of Water. *J. Chem. Phys.* **2012,** *137*, 194504-1-194504-9.
185. Steinhardt, P. J.; Nelson, D. R.; Ronchetti, M., Bond-Orientational Order in Liquids and Glasses. *Phys. Rev. B* **1983,** *28*, 784-805.
186. Lechner, W.; Dellago, C., Accurate Determination of Crystal Structures Based on Averaged Local Bond Order Parameters. *J. Chem. Phys.* **2008,** *129*, 114707-1-114707-5.
187. Mickel, W.; Kapfer, S. C.; Schröder-Turk, G. E.; Mecke, K., Shortcomings of the Bond Orientational Order Parameters for the Analysis of Disordered Particulate Matter. *J. Chem. Phys.* **2013,** *138*, 044501-1-044501-7.
188. Chushak, Y.; Bartell, L. S., Crystal Nucleation and Growth in Large Clusters of Sef_6 from Molecular Dynamics Simulations. *J. Phys. Chem. A* **2000,** *104*, 9328-9336.
189. Santiso, E. E.; Trout, B. L., A General Set of Order Parameters for Molecular Crystals. *J. Chem. Phys.* **2011,** *134*, 064109.
190. J. J. Hoyt, M. A., A. Karma, *Physical Review Letters* **2001,** *86*, 24.
191. Mishin, Y., Calculation of the Gamma/Gamma' Interface Free Energy in the Ni-Al System by the Capillary Fluctuation Method. *cond-mat.mtrl-sci* **2013,** *2*.
192. Heinonen, V.; Mijailovic, A.; Achim, C. V.; Ala-Nissila, T.; Rozas, R. E., Bcc Crystal-Fluid Interfacial Free Energy in Yukawa Systems. *J. Chem. Phys.* **2013,** *138*, 044705.
193. Hoyt, J. J.; Asta, M., *Phys. Rev. B* **2001,** *65*, 214106.
194. Todorov, I. T.; Smith, W., *The Dl_Poly_4 User Manual, 4.07*. STFC Daresbury Laboratory: Daresbury, U.K., 2015.
195. Frisch, M. J.; Trucks, G. W.; Schlegel, H. B.; Scuseria, G. E.; Robb, M. A.; Cheeseman, J. R.; Zakrzewski, V. G.; Montgomery, J. A.; Stratmann, R. E.; Burant, J. C., *Gaussian 98*. Gaussian, Inc: Pittsburg, PA, USA, 1998.
196. Ryckaert, J. P.; Ciccotti, G.; Berendesen, H. J. C., Numerical Integration of the Cartesian Equations of Motion of a System with Constraints: Molecular Dynamics of N-Alkanes. *Journal of Computational Physics* **1977,** *23*, 327-341.
197. Cambridge Structural Database *www. ccdc.cam.ac.uk*.
198. Davidchack, R. L.; Handel , R.; Anwar, J.; Brukhno, A. V., Ice Ih–Water Interfacial Free Energy of Simple Water Models with Full Electrostatic Interactions. *J. Chem. Theory Comput.* **2012,** *8*, 2383–2390.

199. Bordat, P.; Affouard, F.; Descamps, M.; Ngai, K. L., Does the Interaction Potential Determine Both the Fragility of a Liquid and the Vibrational Properties of Its Glassy State? *Phys. Rev. Lett.* **2004,** *93*, 105502.
200. Shi, Z.; Debenedetti, P. G.; Stillinger, F. H.; Ginart, P., Structure, Dynamics, and Thermodynamics of a Family of Potentials with Tunable Softness. *J. Chem. Phys.* **2011,** *135*, 084513.
201. Angell, C. A., Glass Formation and Glass Transition in Supercooled Liquids, with Insights from Study of Related Phenomena in Crystals. *J. Non-Cryst. Solids* **2008,** *354*, 4703-4712.
202. Rahman, A., Correlations in the Motion of Atoms in Liquid Argon. *Phys. Rev. B* **1964,** *136*, A405.
203. Morris, J. R.; Dahlborg, U.; Calvo-Dahlborg, M., Recent Developments and Outstanding Challenges in Theory and Modeling of Liquid Metals. *J. Non-Cryst. Solids* **2007,** *353*, 3444-3453.
204. Luo, S.-N.; Strachan, A.; Swift, D. C., Nonequilibrium Melting and Crystallization of a Model Lennard-Jones System. *J. Chem. Phys.* **2004,** *120*, 11640.
205. Lynden-Bell, R. M.; Debenedetti, P. G., Computational Investigation of Order, Structure, and Dynamics in Modified Water Models. *J. Phys. Chem. B* **2005,** *109*, 6527–6534.
206. Vollmayr, K.; Kob, W.; Binder, K., How Do the Properties of a Glass Depend on the Cooling Rate? A Computer Simulation Study of a Lennard-Jones System. *J. Chem. Phys.* **1996,** *105*, 4714.
207. Kob, W.; Anderson, H. C., Testing Mode-Coupling Theory for a Supercooled Binary Lennard-Jones Mixture I: The Van Hove Correlation Function. *Phys. Rev. E* **1995,** *51*, 4626.
208. Ryltsev, R. E.; Chtchelkatchev, N. M.; Ryzhov, V. N., Superfragile Glassy Dynamics of a One-Component System with Isotropic Potential: Competition of Diffusion and Frustration. *Phys. Rev. Lett.* **2013,** *110*, 025701.
209. Weeks, D.; Chandler, D.; Andersen, H. C., Role of Repulsive Forces in Determining the Equilibrium Structure of Simple Liquids. *J. Chem. Phys.* **1971,** *54*, 5237.
210. De Michele, C.; Sciortino, F.; Coniglio, A., Scaling in Soft Spheres: Fragility Invariance on the Repulsive Potential Softness. *J. Phys.: Condens. Matter* **2004,** *16*, L489.
211. Sengupta, S.; Vasconcelos, F.; Affouard, F.; Sastry, S., Dependence of the Fragility of a Glass Former on the Softness of Interparticle Interactions. *J. Chem. Phys* **2011,** *135*, 194503
212. Berthier, L.; Tarjus, G., Nonperturbative Effect of Attractive Forces in Viscous Liquids. *Phys. Rev. Lett.* **2009,** *103*, 170601.
213. Banerjee, A.; Sengupta, S.; Sastry, S.; Bhattacharyya, S. M., Role of Structure and Entropy in Determining Differences in Dynamics for Glass Formers with Different Interaction Potentials. *Phys. Rev. Lett.* **2014,** *113*, 225701.
214. Coslovich, D.; Roland, C. M., Heterogeneous Slow Dynamics and the Interaction Potential of Glass-Forming Liquids. *J. Non-Cryst. Solids* **2011,** *357*, 397-400.
215. Ahmed, A.; Sadus, R. J., Solid-Liquid Equilibria and Triple Points of N-6 Lennard-Jones Fluids. *J. Chem. Phys.* **2009,** *131*, 174504.
216. Khrapak, S. A.; Chaudhuri, M.; Morfill, G. E., Universality of the Melting Curves for a Wide Range of Interaction Potentials. *J. Chem. Phys.* **2011,** *134*, 241101.
217. Hsu, C. S.; Rahman, A., Interaction Potentials and Their Effect on Crystal Nucleation and Symmetry. *J. Chem. Phys.* **1979,** *71*, 4974.

218. Davidchack, R. L.; Laird, B. B., Crystal Structure and Interaction Dependence of the Crystal-Melt Interfacial Free Energy. *Phys. Rev. Lett.* **2005,** *94*, 086102.
219. Molinero, V.; Sastry, S.; Angell, C. A., Tuning of Tetrahedrality in a Silicon Potential Yields a Series of Monatomic (Metal-Like) Glass Formers of Very High Fragility. *Phys. Rev. Lett.* **2006,** *97*, 075701.
220. Auer, S.; Frenkel, D., Crystallization of Weakly Charged Colloidal Spheres:A Numerical Study. *J. Phys.: Condens. Matter* **2002,** *14*, 7667-7680.
221. Zhang, K.; Fan, M.; Liu, Y.; Schroers, J.; Shattuck, M. D.; O'Hern, C. S., Beyond Packing of Hard Spheres: The Effects of Core Softness, Non-Additivity, Intermediate-Range Repulsion, and Many-Body Interactions on the Glass-Forming Ability of Bulk Metallic Glasses. *cond-mat.mtrl-sci* **2015**.
222. Jones, L., On the Determination of Molecular Fields. *Proc. R. Soc. Lond. A* **1924,** *106* (738), 463-477.
223. Toxvaerd, S., Role of Attractive Forces in Determining the Equilibrium Structure and Dynamics of Simple Liquids. *Condens. Matter Phys.* **2015,** *18*, 13002:1-11.
224. Grochola, G., Constrained Fluid Λ-Integration: Constructing a Reversible Thermodynamic Path between the Solid and Liquid State. *J. Chem. Phys.* **2004,** *120*, 2122-2126.
225. W. R. Fehlner, S. H. V., A Product Representation for Cubic Harmonics and Special Directions for the Determination of the Fermi Surface and Related Properties. *Can. J. Phys.* **1976,** *54* (21), 2159-2169.
226. Sen, S.; Mukerji, T., A Generalized Classical Nucleation Theory for Rough Interfaces: Application in the Analysis of Homogeneous Nucleation in Silicate Liquids. *J. Non-Cryst. Solids* **1999,** *246*, 229-239.
227. Rein ten Wolde, P.; Ruiz-Montero, M. J.; Frenkel, D., Numerical Calculation of the Rate of Crystal Nucleation in a Lennard-Jones System at Moderate Undercooling. *J. Chem. Phys.* **1996,** *104*, 9932-9947.
228. Hilfiker, R., *Polymorphism: In the Pharmaceutical Industry.* Wiley-VCH: Weinheim, Germany, 2006.
229. Zhou, D.; Schmitt, E. A.; Zhang, G. G.; Law, D.; Vyazovkin, S.; Wight, C. A.; Grant, D. J. W., Crystallization Kinetics of Amorphous Nifedipine Studied by Model-Fitting and Model-Free Approaches. *J. Pharm. Sci.* **2003,** *92*, 1779-1792.
230. Hypertension: Management of Hypertension in Adults in Primary Care. *Clinical guideline CG34. National Institute for Health and Clinical Excellence* **2006**.
231. Vater, W.; Schlossmann, K.; Stoepel, K.; Hoffmeister, F.; Kroneberg, G.; Puls, W.; Kaller, H.; Oberdorf, A.; Meng, K., *Arzneim-Forsch* **1972,** *22*, 1.
232. Miyazaki, T.; Yoshioka, S.; Aso, Y.; Kawanishi, T., Crystallization Rate of Amorphous Nifedipine Analogues Unrelated to the Glass Transition Temperature. *Int. J. Pharm.* **2006,** *336*, 191-195.
233. Burger, A.; Koller, K. T., Polymorphism and Pseudopolymorphism on Nifedipine. *Sci. Pharm* **1996,** *64*, 293-301.
234. Ekert, T.; Muller, J., On Polymorphic Forms of Nifedipine from Supercooled Melts. *J. Arch. Pharm* **1977,** *310*, 116-118.
235. Grooff, D.; De Villiers, M. M.; Liebenberg, W., Thermal Methods for Evaluating Polymorphic Transitions in Nifedipine. *Thermochim. Acta* **2006,** *454*, 33-42.

236. Chan, K. L. A.; Fleming, O. S.; Kazarian, S. G.; Vassou, D.; Chryssikos, G. D.; Gionis, V. J., Polymorphism and Devitrification of Nifedipine under Controlled Humidity: A Combined Ft-Raman, Ir and Raman Microscopic Investigation. *J. Raman Spectroscopy.* **2004,** *35*, 353-359.
237. Edgar, B.; Lundborg, P.; Regårdh, C. G., Clinical Pharmacokinetics of Felodipine. A Summary. *C. G. Drugs* **1987,** *34*, 16-27.
238. Srčič, S.; Kerč, J.; Urleb, U.; Zupančič, I.; Lahajnar, G.; Kofler, B.; Smid-Korbar, J., Investigation of Felodipine Polymorphism and Its Glassy State. *International Journal of Pharmaceutics.* **1992,** *87*, 1-10.
239. Rollinger, J. M.; Burger, A., Polymorphism of Racemic Felodipine and the Unusual Series of Solid Solutions in the Binary System of Its Enantiomers. *J. Pharm. Sci.* **2001,** *90*, 949–959.
240. Mishra, M. K.; Desiraju, G. R.; Ramamurty, U.; Bond, A. D., Studying Microstructure in Molecular Crystals with Nanoindentation: Intergrowth Polymorphism in Felodipine. *Angew. Chem. Int. Ed.* **2014,** *53*, 13102-13105.
241. Lou, B.; Boström, D.; Velaga, S. P., Polymorph Control of Felodipine Form Ii in an Attempted Cocrystallization. *Journal of Crystal Growth & Design* **2009,** *9*, 1254–1257.
242. Kestur, U. S.; Lee, H.; Santiago, D.; Rinaldi, C.; Won, Y.; Taylor, L. S., Effects of the Molecular Weight and Concentration of Polymer Additives, and Temperature on the Melt Crystallization Kinetics of a Small Drug Molecule. *Cryst. Growth Des.* **2010,** *10*, 3585–3595.
243. Ferry, J. D., *Viscoelastic Properties of Polymers.* John Wiley & Sons Inc.: New York, USA, 1980.
244. Lu, H. M.; Wen, Z.; Jiang, Q., The Solid-Liquid Interface Energy of Organic Crystals. *J. Phys. Org. Chem.* **2007,** *20*, 236-240.
245. Singh, N. B.; Glicksman, M. E., Determination of the Mean Solid-Liquid Interface Energy of Pivalic Acid. *J. Cryst. Growth* **1989,** *98*, 573-580.
246. Jackson, C. L.; Mckenna, G. N., The Melting Behavior of Organic Materials Confined in Porous Solids. *J. Chem. Phys.* **1990,** *93*, 9002-9011.
247. Affouard, F.; Descamps, M.; Valdes, L.-C.; Habasaki, J.; Bordat, P.; Ngai, K. L., Breakdown of the Stokes–Einstein Relation in Lennard-Jones Glassforming Mixtures with Different Interaction Potential. *J. Chem. Phys.* **2009,** *131*, 104510 -1-104510 -18.
248. Gránásy, L.; Iglói, F., Comparison of Experiments and Modern Theories of Crystal Nucleation. *J. Chem. Phys.* **1997,** *107*, 3634-3644.
249. Baidakov, V. G.; Tipeev, A. O., Crystal Nucleation and the Solid–Liquid Interfacial Free Energy. *J. Chem. Phys.* **2012,** *136*, 074510-1-074510-9.
250. Fokina, V. M.; Zanottob, E. D.; Yuritsync, N. S.; Schmelzerd, J. W. P., Homogeneous Crystal Nucleation in Silicate Glasses: A 40 Years Perspective. *J. Non-Cryst. Solids* **2006,** *352*, 2681–2714.
251. Baidakov, V. G.; Protsenko, S. P.; Tipeev, A. O., Temperature Dependence of the Crystal-Liquid Interfacial Free Energy and the Endpoint of the Melting Line. *J. Chem. Phys.* **2013,** *139*, 224703-1-2240703-11.
252. Wilson, S. R.; Mendelev, M. I., Dependence of Solid–Liquid Interface Free Energy on Liquid Structure. *Modell. Simul. Mater. Sci. Eng.* **2014,** *22*, 065004-1-065004-12.
253. Kelton, K. F.; Greer, A. L., *Nucleation in Condensed Matter: Applications in Materials and Biology*. Elsevier: 2010.
254. O'Brien, M.; McCauley, J.; Cohen, E., Indomethacin. *Analytical Profiles of Drug Substances* **1984,** *13*, 211-238.

255. Hancock, B. C.; Parcks, M., What Is the True Solubility Advantage for Amorphous Pharmaceuticals? *Pharm. Res.* **1999,** *17* (4), 397-404.
256. Jambhekar, S.; Casella, R.; Maher, T., The Physicochemical Characteristics and Bioavailability of Indomethacin from B-Cyclodextrin, Hydroxyethyl-B-Cyclodextrin, and Hydroxypropyl-B-Cyclodextrin Complexes. *Int. J. Pharm.* **2003,** *270*, 149-166.
257. Hamada, Y.; Nambu, N.; Nagai, T., Interactions of A- and B-Cyclodextrin with Several Non-Steroidal Antiinflammatory Drugs in Aqueous Solution. *Chem. Pharm. Bull.* **1975,** *23*, 1205-1211.
258. Aubrey-Medendorp, C.; Swadley, M. J.; Li, T., The Polymorphism of Indomethacin: An Analysis by Density Functional Theory Calculations. *Pharm. Res.* **2007,** *24* (4), 953-959.
259. Yoshioka, M.; Hancock, B. C.; Zografi, G., Crystallization of Indomethacin from the Amorphous State Below and above Its Glass Transition Temperature. *J. Pharm. Sci.* **1994,** *83* (12), 1700-1705.
260. Legendre, B.; Feutelais, Y., Polymorphic and Thermodynamic Study of Indomethacin. *J. Therm. Anal. Calorim.* **2004,** *76*, 255-264.
261. Cox, P. L.; Manson, P. L., Γ-Indomethacin at 120k. *Acta Crystallographica Section E Structure Reports Online* **2003,** *59*, o986-o988.
262. Chen, X.; Morris, K. R.; Griesser, U. J.; Byrn, S. R.; Stowell, J. G., Reactivity Differences of Indomethacin Solid Forms with Ammonia Gas. *J. Am. Chem. Soc.* **2001,** *124*, 15012-15019.
263. Thompson, C. V.; Spaepen, F., On the Approximation of the Free Energy Change on Crystallization. *Acta Metall.* **1979,** *27*, 1855-1859.
264. Pedersen, U. R., Direct Calculation of the Solid-Liquid Gibbs Free Energy Difference in a Single Equilibrium Simulation. *J. Chem. Phys.* **2013,** *139*, 104102-1-104102-9.
265. Schmelzer, J. W. P.; Gokhman, A. R.; Fokin, V. M., Dynamics of First Order Phase Transitions in Multicomponent Systems: A New Theoretical Approach. *J. Colloid. Interface* **2004,** *272*, 109-133.
266. Neuville, D. R.; Cormier, L.; Caurant, D.; Montagne, L., *Du Verre Au Cristal Nucléation, Croissance Et Démixtion, De La Recherche Aux Applications.* EDP Sciences: Les Ulis, France, 2013.
267. Demichelis, R.; Raiteri, P.; Gale, J. D.; Quigley, D.; Gebauer, D., Stable Prenucleation Mineral Clusters Are Liquid-Like Ionic Polymers. *Nat. Commun.* **2011,** *2*, 590-1-590-8.
268. Kovácsa, T.; Christenson, H. K., A Two-Step Mechanism for Crystal Nucleation without Supersaturation. *Faraday Discuss.* **2012,** *159*, 123-138.
269. Swallen, S. F.; Ediger, M. D., Self-Diffusion of the Amorphous Pharmaceutical Indomethacin near Tg. *Soft Matter* **2011,** *7*, 10339-10344.
270. Zhu, L.; Brian, C. W.; Swallen, S. F.; Straus, P. T.; Ediger, M. D.; Yu, L., Surface Self-Diffusion of an Organic Glass. *Phys. Rev. Lett.* **2011,** *106*, 256103-1-256103-4.
271. Atkins, P. W.; Beran, J. A., *General Chemistry.* Scientific American Books: 1992.
272. Barker, J. A.; Watts, R. O., Monte Carlo Studies of the Dielectric Properties of Water-Like Models. *Mol. Phys.* **1973,** *26* (3), 789-792.
273. Watts, R. O., Monte Carlo Studies of Liquid Water. *Mol. Phys.* **1974,** *28* (4), 1069-1083.
274. Ewald, P., Evaluation of Optical and Electrostatic Lattice Potentials. *Ann.Phys. Leipzig* **1921,** *64*, 253-287.
275. Toukmaji, A. Y.; Board Jr., J. A., Ewald Summation Techniques in Perspective: A Survey. *Comput. Phys. Commun.* **1996,** *95*, 73-92.

276. Swope, W. C.; Anderson, H. C.; Berens, P. H.; Wilson, K. R., A Computer Simulation Method for the Calculation of Equilibrium Constants for the Formation of Physical Clusters of Molecules: Application to Small Water Clusters. *J. Chem. Phys.* **1982,** *76*, 637-649.
277. Munster, A., *Statistical Thermodynamics*. John Wiley & Sons Inc: 1970.